37th conference with international participation

COMPUTATIONAL MECHANICS 2022

PROCEEDINGS OF COMPUTATIONAL MECHANICS 2022

November 7 - 9, 2022

HOTEL SRNÍ
CZECH REPUBLIC

FACULTY
OF APPLIED SCIENCES
UNIVERSITY
OF WEST BOHEMIA

PILSEN REGION

IFToMM

Central European Association
for Computational Mechanics

PROCEEDINGS OF COMPUTATIONAL MECHANICS 2022

ISBN 978-80-261-1116-0

Published by
University of West Bohemia, Univerzitní 8, 301 00 Plzeň, Czech Republic, IC 49777513

Edited by
Vítězslav Adámek
Alena Jonášová
Stanislav Plánička
Martin Zajíček

Conference secretariat
Jana Nocarová
Department of Mechanics
Faculty of Applied Sciences
University of West Bohemia
Univerzitní 8
301 00 Plzeň
Czech Republic

phone: +420 377 632 301
e-mail: vm@kme.zcu.cz

PREFACE

The proceedings contain 56 conference papers presented at the 37th conference **Computational Mechanics 2022**, which was held at the Hotel Srní in Srní, Czech Republic, on November 7 – 9, 2022. This annual conference, which was attended by nearly eighty participants from the Czech Republic, Slovakia and from abroad, was organised by the Department of Mechanics, Faculty of Applied Sciences of the University of West Bohemia under the auspices of

- Miloš Železný, the Dean of the Faculty of Applied Sciences,
- Rudolf Špoták, the President of the Pilsen Region,
- Czech Society for Mechanics,
- Czech National Committee of IFToMM,
- Central European Association for Computational Mechanics.

The main objective of this traditional conference is to bring together academicians, researchers and industrial partners interested in relevant disciplines of mechanics including

- solid mechanics,
- dynamics of mechanical systems,
- mechatronics and vibrations,
- reliability and durability of structures,
- fracture mechanics,
- mechanics in civil engineering,
- fluid mechanics and fluid-structure interaction,
- thermodynamics,
- biomechanics,
- heterogeneous media and multiscale problems,
- experimental methods in mechanics,

to create an opportunity for meeting, discussion and collaboration among the participants. As in the previous years, the three best papers presented at this conference were awarded the Czech Society for Mechanics Award for young researchers under 35 years of age.

To all conference participants, we offer the possibility to publish their peer-reviewed full papers in the international journal **Applied and Computational Mechanics** indexed by Scopus. This journal has been published by the University of West Bohemia since 2007 (see `https://www.kme.zcu.cz/acm/`).

We would like to express our gratitude to all the invited speakers for their significant contribution to the conference and the time and effort they put. Considerable acknowledgement belongs also to the members of the Organising Committee for their important work.

We strongly believe that all participants of the CM2022 enjoyed their stay in the beautiful nature of the Šumava region in a meaningful way. Finally, we would like to invite you all to come to the next conference CM2023.

Jan Vimmr
University of West Bohemia
Chairman of the Scientific
Committee

Vítězslav Adámek
University of West Bohemia
Chairman of the Organising
Committee

SCIENTIFIC COMMITTEE

Chairman:

Jan Vimmr
  University of West Bohemia, Faculty of Applied Sciences, Czech Republic

Members:

Miroslav Balda
  Research and Testing Institute Plzeň, Czech Republic

Jiří Burša
  Brno University of Technology, Faculty of Mechanical Engineering, Czech Republic

Jan Dupal
  University of West Bohemia, Faculty of Applied Sciences, Czech Republic

Václav Dvořák
  Technical University of Liberec, Faculty of Mechanical Engineering, Czech Republic

Jiří Fürst
  Czech Technical University in Prague, Faculty of Mechanical Engineering, Czech Republic

Miroslav Holeček
  University of West Bohemia, Czech Republic

Jaromír Horáček
  Institute of Thermomechanics, Czech Academy of Sciences, Czech Republic

Michal Kotoul
  Brno University of Technology, Faculty of Mechanical Engineering, Czech Republic

Jiří Křen
  University of West Bohemia, Faculty of Applied Sciences, Czech Republic

Vladislav Laš
  University of West Bohemia, Faculty of Applied Sciences, Czech Republic

Justín Murín
  Slovak University of Technology in Bratislava, Faculty of Mechanical Engineering, Slovak Republic

Milan Naď
  Slovak University of Technology in Bratislava, Faculty of Materials Science and Technology in Trnava, Slovak Republic

Jiří Náprstek
  Institute of Theoretical and Applied Mechanics, Czech Academy of Sciences, Czech Republic

Miloslav Okrouhlík
  Institute of Thermomechanics, Czech Academy of Sciences, Czech Republic

Luděk Pešek
  Institute of Thermomechanics, Czech Academy of Sciences, Czech Republic

Jindřich Petruška
  Brno University of Technology, Faculty of Mechanical Engineering, Czech Republic

Jiří Plešek
  Institute of Thermomechanics, Czech Academy of Sciences, Czech Republic

František Pochylý
  Brno University of Technology, Faculty of Mechanical Engineering, Czech Republic

Pavel Polach
  Research and Testing Institute Plzeň, Czech Republic

Eduard Rohan
University of West Bohemia, Faculty of Applied Sciences, Czech Republic
Josef Rosenberg
University of West Bohemia, Faculty of Applied Sciences, Czech Republic
Milan Růžička
Czech Technical University in Prague, Faculty of Mechanical Engineering, Czech Republic
Milan Sága
University of Žilina, Faculty of Mechanical Engineering, Slovak Republic
Petr Sváček
Czech Technical University in Prague, Faculty of Mechanical Engineering, Czech Republic
Zbyněk Šika
Czech Technical University in Prague, Faculty of Mechanical Engineering, Czech Republic
Michael Valášek
Czech Technical University in Prague, Faculty of Mechanical Engineering, Czech Republic
Jaroslav Zapoměl
VŠB – Technical University of Ostrava, Faculty of Mechanical Engineering, Czech Republic
Vladimír Zeman
University of West Bohemia, Faculty of Applied Sciences, Czech Republic

Table of Contents

COMPUTATIONAL MECHANICS 2022
37th conference with international participation
Srní
November 7 - 9, 2022

Model reduction in aeroservoelasticity

A. Balon, P. Beneš, Z. Šika

Department of Mechanics, Biomechanics and Mechatronics, Faculty of Mechanical Engineering, Czech Technical University in Prague, Technicka 4, Praha 6, Czech Republic

1. Introduction

Aeroservoelasticity is a field focusing on interaction between aerodynamic forces, elastic forces, and control forces acting on a body [4]. To correctly predict these interactions complex numerical models are often used. The complexity of the numerical models can vary however the resulting numerical model is usually nonlinear and of high order. At this stage the model cannot be used for control law design and model reduction is required. Essentially there are two approaches to reduce the order of a model [2]. First approach is to project the dynamics of high-dimensional system onto a low-dimensional subspace. Second approach is system identification which uses collected data, either from experiment or simulation, to construct low order models that match the input-output relationship of the data [2], [3]. Due to the ease of implementation, system identification is often preferred for control law design. The rest of this extended abstract focuses on methods which produce linear models such as eigensystem realization algorithm or dynamic mode decomposition [2].

Eigensystem realization algorithm (ERA) was first introduced in 1985 to identify modal parameters and reduce dynamic systems from experimental data [3]. The method is based on obtaining Markov parameters from impulse response experiment, which are then used to construct a generalized Hankel matrix. Singular value decomposition (SVD) of the Hankel matrix is then performed to reduce the order of the model and obtain the state matrices of linear dynamic system. If the data is collected from a simulation, then obtaining impulse response of the system is quite simple. If the data is collected from an experiment where impulse response might not be possible to perform, then a pseudo random input can be used and subsequently observer Kalman filter identification (OKID) can be used to extract impulse response of the system from the collected data [2].

2. Example: 2D flow over a flat plate with single control input

The data input-output impulse response data is collected from a simulation of unsteady vortex lattice method (UVLM) coupled with linear finite element model. The input is the control force and outputs are coefficient of lift C_L and vertical displacement velocity $\dot{z}$ at the trailing edge of the plate (Fig. 1). ERA is used to extract linear dynamic model from the data. Order of the reduced model is determined by a choice based on singular values of the Hankel matrix (Fig. 2). Fig. 3 shows both simulation model response and reduced model response to a ramp and sine wave inputs. This reduced order model is now suitable for control engineering applications. It should be noted that the states of ERA model are not physical states such as position or velocity. Therefore, use of control techniques which rely on model output is necessary, for example model predictive control, LQR with output feedback, or SHAVO [1].

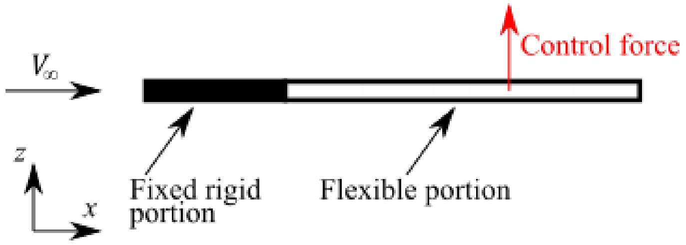

Fig. 1. Illustration of the flow over partially flexible flat plate with a control force input

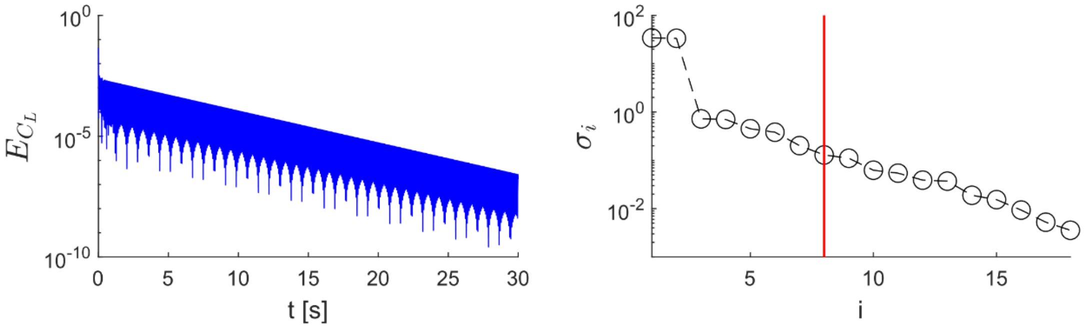

Fig. 2. Lift coefficient error between simulation and ERA outputs for impulse response (left). Several singular values of Hankel matrix and selected model order (right)

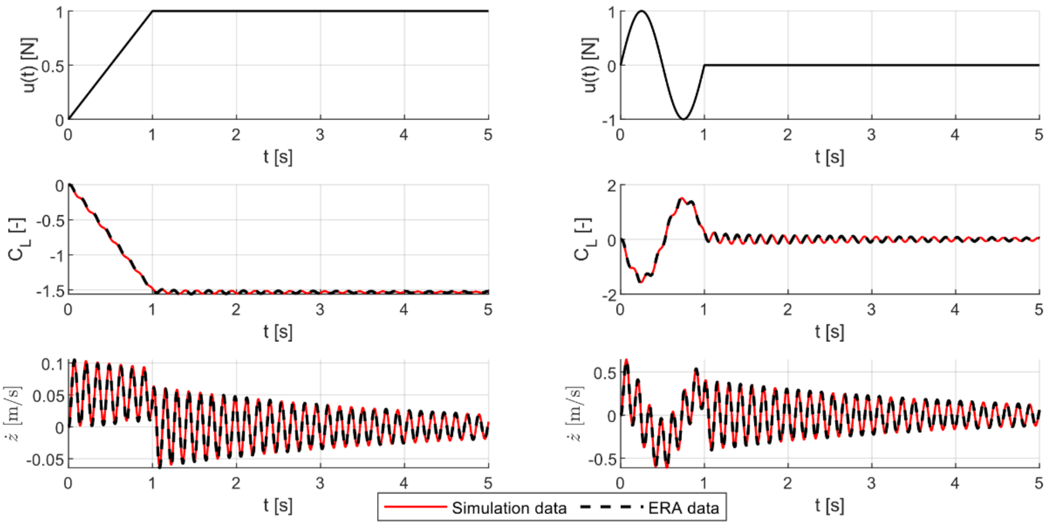

Fig. 3. Model responses to ramp and sine wave inputs

Acknowledgements

The work has been supported by the project SGS22/150/OHK2/3T/12 "Mechatronics and adaptronics 2022" of Czech Technical University in Prague.

References

[1] Beneš, P., Valášek, M., Šika, Z., Zavřel, J., Pelikán, J., SHAVO control: The combination of the adjusted command shaping and feedback control for vibration suppression, Acta Mechanica 230 (5) (2019) 1891-1905.

[2] Brunton, S. L., Kutz, J. N., Data-driven science and engineering: Machine learning, dynamical systems, and control, Cambridge University Press, 2022.

[3] Juang, J. N., Pappa, R. S., An eigensystem realization algorithm for modal parameter identification and model reduction. Journal of guidance, control, and dynamics 8 (5) (1985) 620-627.

[4] Tewari, A., Aeroservoelasticity, modeling and control, Springer New York, 2015.

COMPUTATIONAL MECHANICS 2022
37th conference with international participation
Srní
November 7 - 9, 2022

Assessment of various computational approaches for airfoil stability analysis with two degrees of freedom

M. Bělohoubek, M. Hajžman, J. Vimmr

Faculty of Applied Sciences, University of West Bohemia, Univerzitní 8, 301 00 Plzeň, Czech Republic

The paper deals with the solution of fluid-structure interaction (FSI) problems, specifically the external aerodynamics of airfoils and turbine blades. This problem is of high importance since structural instabilities may occur if the flow field's input parameters and the airfoil's properties are not properly configured. A typical example of such instability is flutter, a self-excited oscillation of the structure induced by the flowing fluid. A long-term problem in solving FSI tasks with classical numerical approaches (FVM, FEM) is their high computational complexity, which does not allow solving these tasks in real-time. This deficit is usually compensated by using semi-empirical methods, which, however, do not offer comparable accuracy compared to numerical techniques. This paper aims to compare the two mentioned approaches and their advantages and disadvantages in the context of the two degrees of freedom (DoF) airfoil wrapping problems.

For the analysis, a 2D perfectly rigid airfoil model with 2 DoF, namely in heave h and pitch θ, was chosen, a sketch of which can be seen in Fig. 1. Based on the Lagrange equations, the system's equations of motion were then derived, which have the following form

$$\left.\begin{aligned} &m\ddot{h} - m\ddot{\theta}e_{MS}\cos(\theta+\tilde{\varphi}_0) + m\dot{\theta}^2 e_{MS}\sin(\theta+\tilde{\varphi}_0) + k_h h = mg - L_{\text{dyn}},\\ &(me_{MS}^2 + I_{M_C})\,\ddot{\theta} - m\ddot{h}e_{MS}\cos(\theta+\tilde{\varphi}_0) + k_\theta\theta = -mge_{MS}\cos(\theta+\tilde{\varphi}_0) + M_{\text{dyn}},\end{aligned}\right\} \quad (1)$$

where m is the mass of the body, k_h is the stiffness of the vertical spring, k_θ is the stiffness of the torsion spring, g is the gravitational acceleration and I corresponds to the moment of inertia, the form of the aerodynamic force effects L_{dyn} and M_{dyn} depends on the choice of the particular solver.

The first approach to solving the problem was a complex CFD analysis using the ANSYS Fluent software, which is based on solving a nonlinear Reynolds-averaged Navier-Stokes equa-

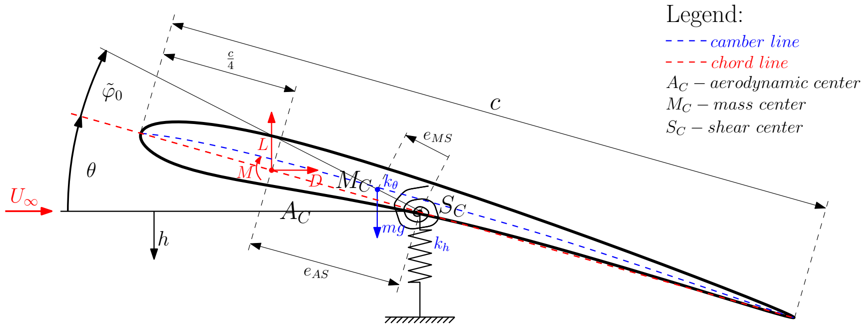

Fig. 1. Sketch of the analyzed airfoil profile with 2 DoF, including force effects on the system

tions (RANS) using the finite volume method (FVM). In this problem, a computational domain of type C was chosen, and the airfoil was the symmetric profile NACA0012. In addition, a pressure-based solver and a single-equation Spalart-Allmaras (SA) turbulence model were used to solve the external aerodynamics problems. To minimize the resulting numerical calculation errors, a mesh resolution study was calculated, especially in the boundary layer region of the airfoil where $y^+_{\max} \sim 1$. The influence of the choice of the turbulent model (specifically SA, SST k–ω, and LES) was also investigated. Further specifications of the chosen domain, the quality of the discretization, and the settings of other parameters are given in the paper [2].

The main disadvantage of the numerical model based on the FVM is its high computational cost, where several tens of hours of machine time of a standard desktop computer are needed to obtain a solution of one-time response to initial conditions with a total length of 6 s. On the other hand, the advantage of this approach is the high complexity of the obtained outputs and their accuracy. The graphical outputs demonstrate this in Fig. 2, which offer a comparison with the experimental data available in the literature [5]. The plots show comparisons in the time and frequency domain for four cases of initial-boundary conditions for the flow field and airfoil. The time-domain output quantity is the vertical displacement z_w located at the top of the airfoil at a distance of $0.7c$ from the wing's leading edge.

Comparisons with the experiment are made for both the one and two DoF cases, the first three cases with zero flow field velocity, and the last case (bottom right) shows a comparison of the time domain response, which the author of the experiment refers to as the limiting cyclic oscillation, i.e., the limit of instability (flutter) directly. Except for the last case, the time domain responses achieved a good agreement, and the higher amplitude of the experimental data is seen in the last case. More importantly, however, the stability limit has been reached in the numerical calculation for the same flow field velocity. Thus, despite the mentioned differences, the outputs of ANSYS Fluent software represent a suitable reference to which the outputs from the application of other methods can be related.

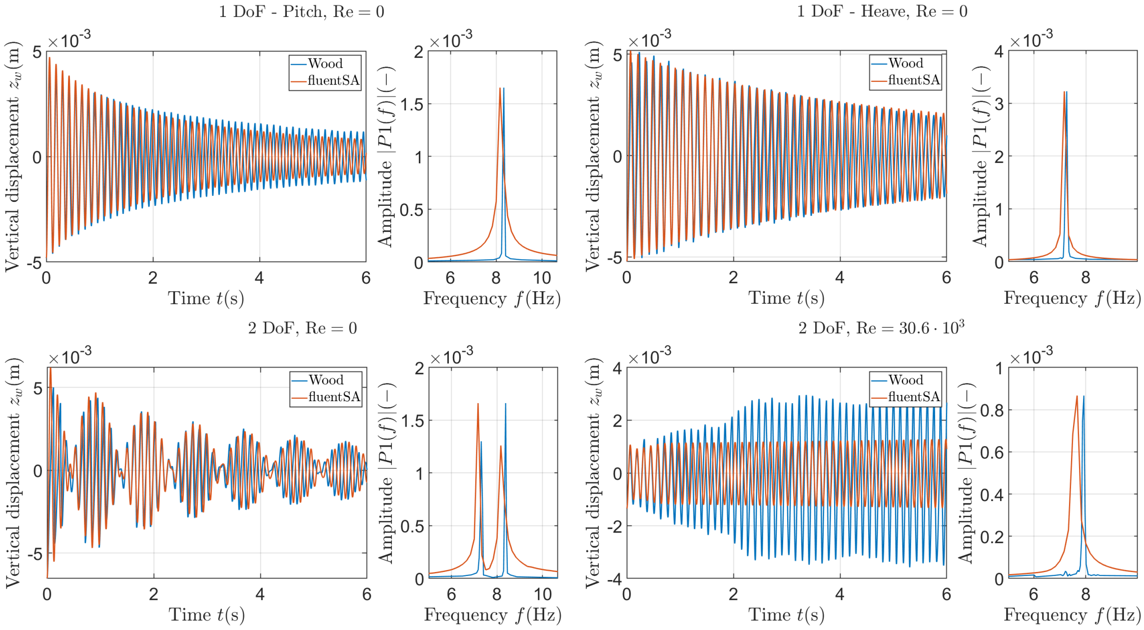

Fig. 2. Comparison of ANSYS Fluent generated outputs with experimental data presented in literature [5]. Top left case with 1 DoF in pitch and for Re = 0, the top right case with 1 DoF in heave and Re = 0, the bottom left case with 2 DoF and for Re = 0 and bottom right case with 2 DoF and Re = 30.6×10^3 corresponding to the flutter limit

As far as semi-empirical methods are concerned, they offer an advantage over the complex CFD approach in terms of much lower computational cost (for the identical problem described above, the solution is computed in higher units of seconds). However, the disadvantage is the lower accuracy of the results obtained. The popular Quasi steady theory approach and the Theodorsen theory approach were selected for comparison from several possible variants. The definition of the aerodynamic force effects L_{dyn} and M_{dyn} from Eq. (1) including their detailed derivation is given in the literature [3]. Both methods were implemented in MATLAB, and the more complex approach of Theodorsen theory was verified on the outputs reported in the literature [1]. As with the ANSYS Fluent software, a time-step resolution study was performed.

The analyses show that for the case of both semi-empirical approaches, there is higher damping of the model oscillations across different variations of the structural parameter settings and initial conditions. This is well illustrated in Fig. 3 showing the values of the dynamic force effects L_{dyn} and M_{dyn} over time for the approaches represented by Fluent, Quasti steady theory and Theodorsen theory. In addition to the noticeably higher dissipation of the two semi-empirical models, on closer examination, the plots show a good indication of the evolution of the quantities of interest. This shows that although greater damping is typical of both semi-empirical methods, only the curve corresponding to the Theodorsen theory calculation follows the Fluent outputs in a trend direction. We note here that a similar result can be observed for the outputs of both displacements over time and also for other settings of the model input.

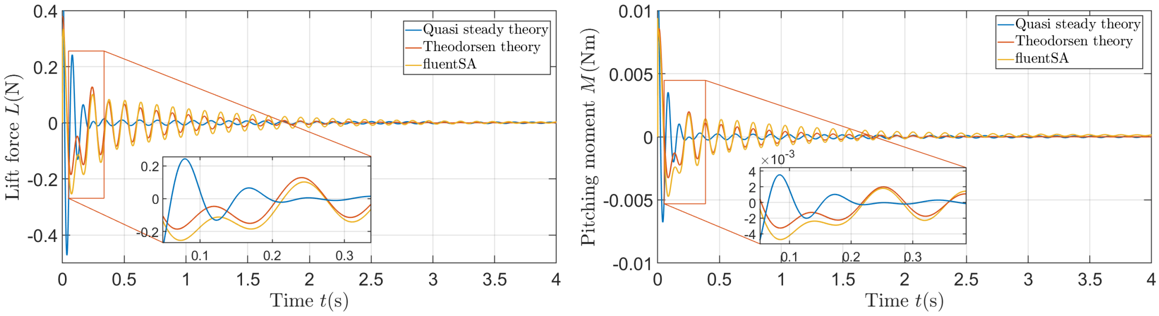

Fig. 3. Comparison of the dynamic force effects of the lift force L_{dyn} (*left*) and pitching moment M_{dyn} (*right*) for three different numerical approaches. In the zoom-in, the trend of the individual force effects can be seen, in which there is an agreement between Thedorsen theory and the results of the Fluent

The phenomenon of the higher damping of Theodorsen theory compared to the Fluent software outputs is evident even when directly comparing the value of the flutter threshold for a particular choice of input parameters. This fact is well illustrated in Fig. 4, which shows the time responses to the flutter limit for Theodorsen theory (top left) and Fluent (top right). It is also possible to find the stability limit directly using methods based on modal analysis. A variety of approaches based on modal analysis principles have been developed for airfoil problems, of which the p method (see, e.g., [4] for a derivation) and the U–g method (e.g., [1]) have been implemented here. These methods do not need to iterate solutions for different levels of input flow field velocity U_∞ and thus have the potential to streamline the flutter limit detection process further. Outputs of the modal analysis in Fig. 4 (bottom) operate with the definition of force effects based on Theodorsen theory, and the resulting values of the limiting velocity of the flow field U_∞ should be comparable to the outputs of Theodorsen theory.

As the presented paper shows, complex CFD numerical methods can be used to solve real problems of complex FSI external aerodynamics tasks. However, despite the currently available computational performance, their high computational cost remains a disadvantage. On the other

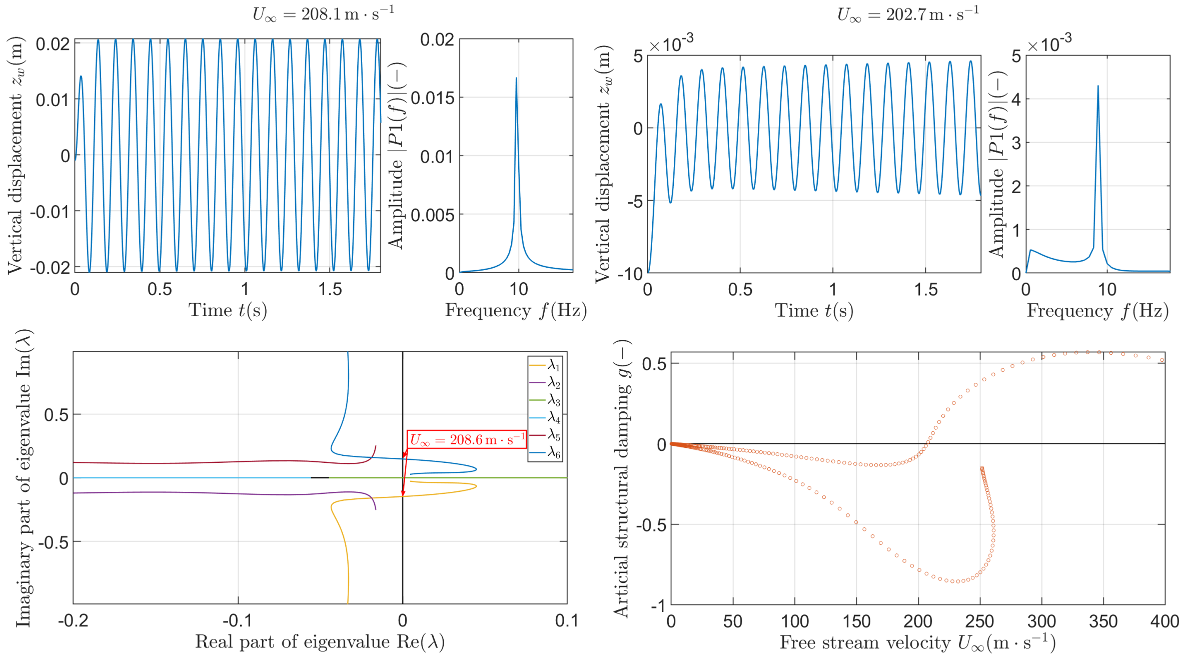

Fig. 4. Comparison of different approaches for flutter limit detection for a specific set of the 2 DoF rigid airfoil problem. Top left output for Theodorsen theory ($U_\infty = 208.1\,\mathrm{m\cdot s^{-1}}$), top right for ANSYS Fluent software ($U_\infty = 202.7\,\mathrm{m\cdot s^{-1}}$), bottom left for p method ($U_\infty = 208.6\,\mathrm{m\cdot s^{-1}}$) and bottom right for U–g method ($U_\infty = 207.1\,\mathrm{m\cdot s^{-1}}$)

hand, semi-empirical approaches to solving this problem offer lower computational costs but at the loss of a certain accuracy of the solution. Of the semi-empirical approaches investigated, the one based on Theodorsen theory appears to be the most appropriate approach. Despite still significant differences in the outputs shows trend-like characteristics with the Fluent outputs. Eliminating the differences between the Theodorsen approach and the Fluent outputs would provide an accurate and efficient tool for flutter limit detection. This elimination is the subject of further investigation.

Acknowledgements

This research work was supported by project SGS-2022-008 of the Czech Ministry of Education, Youth and Sport, and by the Czech Science Foundation project number 20-26779S. I would also like to thank Techsoft Engineering for helping me debug the model in ANSYS Fluent.

References

[1] Alighanbari, H., Flutter analysis and chaotic response of an airfoil accounting for structural nonlinearities, McGill University, Canada, 1995.

[2] Bělohoubek, M., Hajžman, M., Vimmr, J., Comparison of computational approaches for the efficient analysis of airfoil dynamics, Proceedings of the conference Computational Mechanics 2021, Srní, 2021, pp. 9-12.

[3] Fung, Y. C., An introduction to the theory of aeroelasticity, Dover Publications, USA, 1969.

[4] Latif, R., Khan, M., Javed, A., Shah, S., Rizvi, S., A semi-analytical approach for flutter analysis of a high-aspect-ratio wing, The Aeronautical Journal 125 (2021) 410-429.

[5] Wood, J. N., Breuer, M., De Nayer, G., Experimental investigations on the dynamic behavior of a 2-DOF airfoil in the transitional Re number regime based on digital-image correlation measurements, Journal of Fluids and Structures 96 (2020) No. 103052.

COMPUTATIONAL MECHANICS 2022
37th conference with international participation
Srní
November 7 - 9, 2022

Mechanical properties of 3D printed composite material

A. Boualleg, D. Cirkl

Faculty of Mechanical Engineering, Technical University of Liberec, Studentská 2, 46117 Liberec, Czech Republic

1. Introduction

Additive manufacturing (AM), become widely used in engineering prototyping, complex geometry, and multi-purpose. The PolyJet 3D printing method is photopolymer jetting that deposits of voxel-based droplets of photopolymer resins onto a print bed, after which the resins are cured using ultraviolet (UV) lamps. The development of novel photopolymer resins, for instance, Agilus30 and Tango+ have become accessible to PolyJet technology. The mechanical flexibility of PolyJet elastomers has made them mainly useful for applications like soft robotic active hinges, actuators, and building a complex geometry [1], [2].

The paper is intended to determine the mechanical properties of Additive Manufacturing of the Digital Material DM40 (Agilus30 and VeroClear) in terms of selecting the appropriate hyperplastic model. The work aim is to compare the simulation of two hyperelastic materials Mooney-Rivlin (MR) and Ogden with the experiment. The DM40 material behavior is visco-hyperelastic, therefore the viscoelastic part of the material response will be considered.

2. Constitutive model

2.1. Hyperelastic model

The tension test was performed on a dumbbell sample under a strain rate of 4×10^{-2} s^{-1} to define the material constants.

The experimental data were used to fit the Ogden and Mooney-Rivlin models by using MSC Marc software, the strain energy function of the Ogden model is expressed by Eq.1 and data fitting, as well as the material constants, are shown in Fig.1 and Table 1 respectively [3]

$$W = \sum_{i=1}^{N} \frac{\mu_i}{\alpha_i}\left(\lambda_1^{\alpha_i} + \lambda_2^{\alpha_i} + \lambda_3^{\alpha_i} - 3\right) + \frac{K}{2}(J-1)\,, \tag{1}$$

where λ_1, λ_2, and λ_3 are principal stretches, μ_i are moduli and α_i are non-dimensional material constants. J and K are the elastic volume ratio and the material bulk modulus, respectively. The Mooney-Rivlin Strain energy function is as follows [3]

$$W = C_{10}(I_1 - 3) + C_{01}(I_2 - 3) + C_{11}(I_1 - 3)(I_1 - 3)\,, \tag{2}$$

where C_{10}, C_{01} and C_{11} are material constants while I_1 and I_2 are invariants. Fig. 2 illustrates the fitting results and the material constants are presented in Table 2.

Table 1. Ogden model constant

Terms	Moduli	Exponents
1	2.21514	0.167737
2	0.055668	5.20789
3	0.768557	0.147847

Table 2. Mooney-Rivlin model constant

Material constant	
C_{10}	0.100513
C_{01}	0.102029
C_{11}	0.0782547

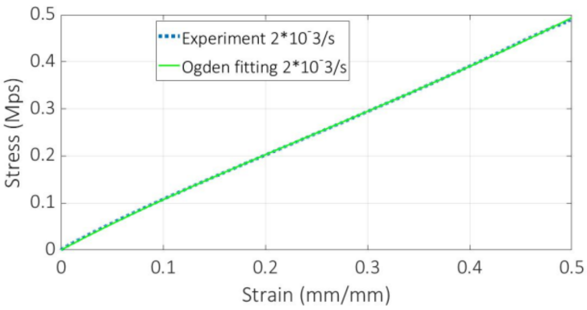

Fig. 1. Ogden model - fitting to experiment

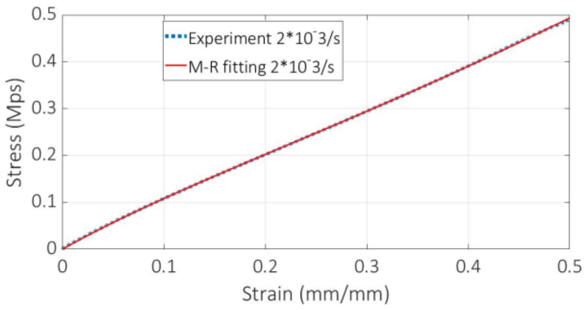

Fig. 2. MR model - fitting to experiment

2.2. Viscoelastic model

The stress relaxation was investigated on a cylindrical sample (height 25 mm and diameter 17.9 mm) at strain 0.5 with a ramp time of 1.5 s to investigate the viscoelastic properties of the material. The relaxation moduli are presented by the Prony series in Eq. (3), [3],

$$E(t) = E^{\infty} + \sum_{n=1}^{N} E^{n}\, exp(\frac{-t}{\tau_n}) \,, \tag{3}$$

where t is time, E^n is the relaxation modulus, τ_n is the relaxation time constant, and E^{∞} is the long-term modulus. The relaxation data fitted with the Prony series is in Fig. 3 and the four terms of viscoelastic material constants are presented in Table 3.

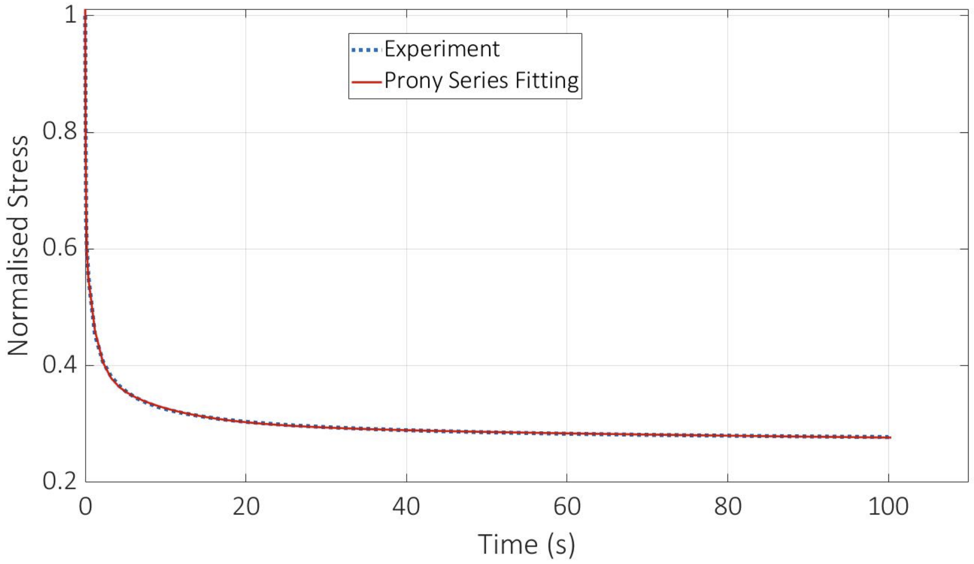

Fig. 3. The experimental fitting of the Prony series

3. Results and discussion

The hyper-viscoelastic material was validated using the cylinder sample compressed to 50 % with a strain rate of 4×10^{-2} s^{-1}. In this work, the friction between the compression plates

Table 3. Viscoelastic Prony series constant

Terms	Relaxation time	Relaxation coefficient
1	0.0657	0.38702
2	1.11	0.21787
3	8.238	0.0968119
4	100.029	0.0387605

and the sample was measured using a tribometer and considered for the simulation. The friction coefficient is $\mu = 0.8$. It is clearly shown from the results that the Ogden model has a good agreement with the experiment data, whereas the Mooney-Rivlin has a high deviation from the experiment. This indicates that for the description of mechanical properties of the composite material DM40 (Agilus30 and VeroClear) the Ogden model with three terms can be a suitable choice.

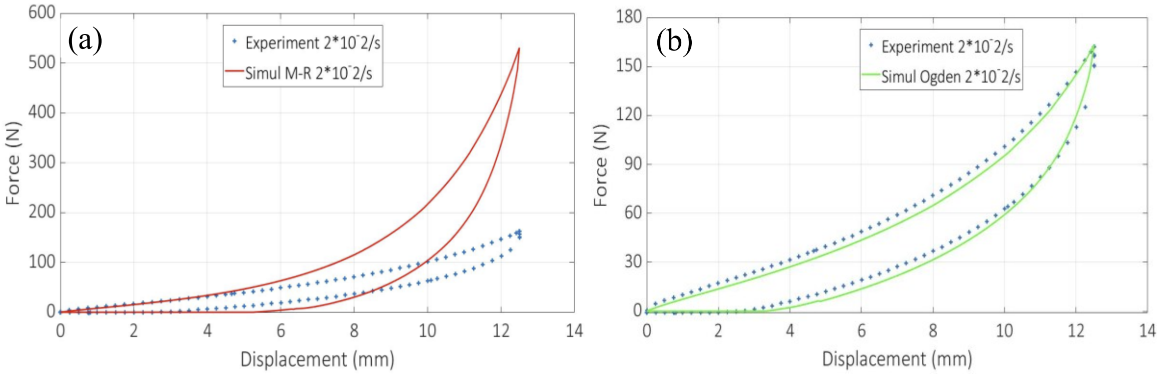

Fig. 4. The experiment validation with (a) Mooney-Rivlin and (b) Ogden models

Acknowledgements

This publication was written at the Technical University of Liberec as part of the project "Research of advanced materials, and application of machine learning in the area of control and modelling of mechanical systems" nr. SGS-2022-5072 with the support of the Specific University Research Grant, as provided by the Ministry of Education, Youth and Sports of the Czech Republic in the year 2022.

References

[1] Abayazid, F.F., Ghajari, M., Material characterisation of additively manufactured elastomers at different strain rates and build orientations, Additive Manufacturing 33 (2020) 101160.

[2] Hossain, M., Navaratne, R., Perić, D., 3D printed elastomeric polyurethane: Viscoelastic experimental characterizations and constitutive modelling with nonlinear viscosity functions, International Journal of Non-Linear Mechanics 126 (2020) 103546.

[3] Holzapfel, G.A., Nonlinear solid mechanics : A continuum approach for engineering, John Wiley & Sons, Chichester, 2000.

COMPUTATIONAL MECHANICS 2022
37th conference with international participation
Srní
November 7 - 9, 2022

Solution of incompressible viscid fluid flow using a physical informed neural network

O. Bublík

Faculty of Applied Sciences, University of West Bohemia, Univerzitní 8, 301 00 Plzeň, Czech Republic

A physical informed neural network (PINN) is the novel approach for solving a partial differential equation using a neural network. This concept was firstly introduced in the paper [3], where the PINN was used for the solution of various partial differential equations. Since then, many papers have been published dealing with the solution of a wide range of partial differential equations [1, 2].

The principle of this novel method is quite simple. It considers a solution of an equation as a non-linear function defined by a neural network. In other words, the neural network is used as the mapper from the space-time variables into unknowns. This contrasts sharply with classical methods, where the solution is considered as a linear combination of basis functions. The crucial part of the PINN approach lies in constructing a loose function, see Fig. 1. Firstly, the automatic differentiation process is used to find the exact space and time derivatives of a solution with arbitrary orders, see green layer. Then the solution, with its derivatives, is put into the equations in the classical or weak form, see the red box. If we assume that the exact solution satisfies the equations together with boundary conditions, we can think of the value after substitution directly as the loss function.

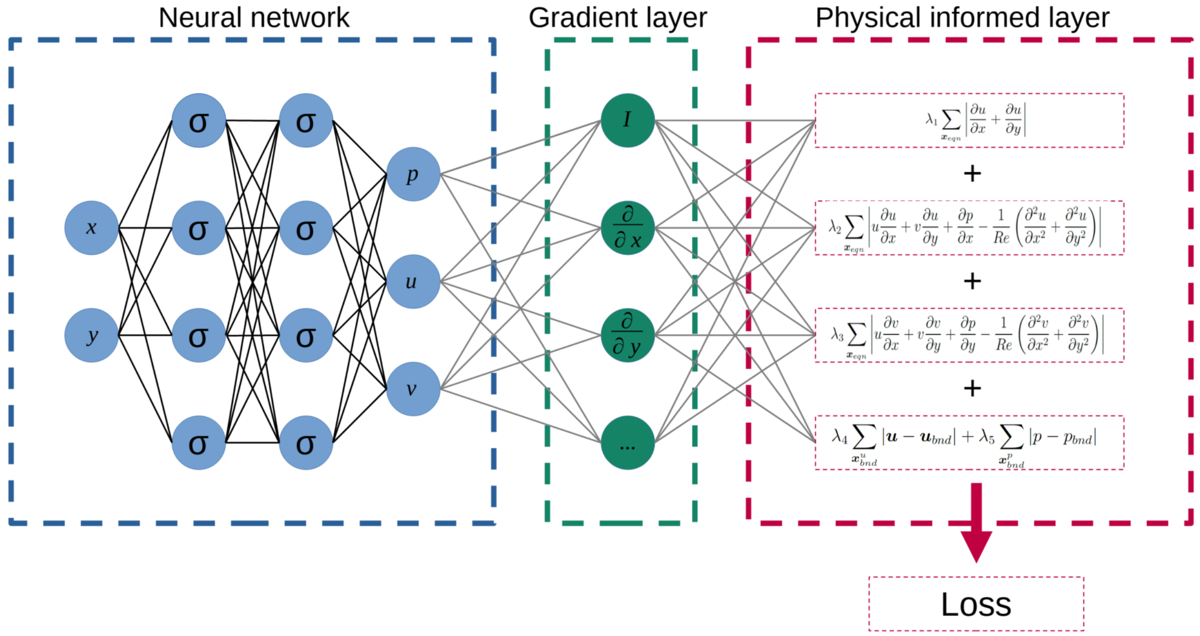

Fig. 1. Example of physical informed neural network for solution of Navier-Stokes equations

The training process starts by choosing points inside and on the boundary of the computational domain. The training algorithm tries to minimize the loss function evaluated for selected points. Suppose the loss function is minimized to zero. In that case, the function described by the neural network will be satisfying boundary conditions at the boundary points and the equation at the inner points.

The methodology is demonstrated in the solution of the flow field of incompressible viscid fluid in the channel for various Reynolds numbers. Figs. 2 and 3 show the comparison between PINN predicted solution and solution computed by discontinuous Galerkin finite element method (DGFEM).

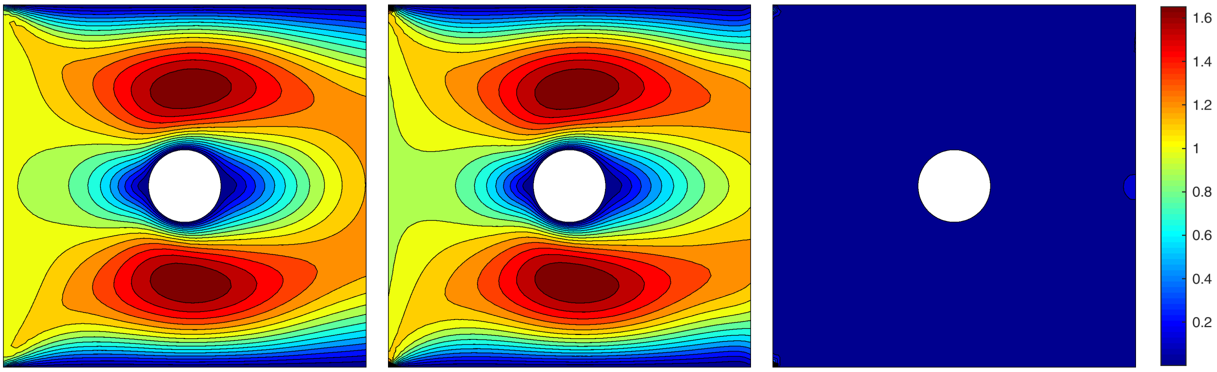

Fig. 2. Comparison of PINN predicted solution (*left*) with a solution computed by DGFEM (*middle*) for Reynolds number 10. The figure on the right shows the error between solutions

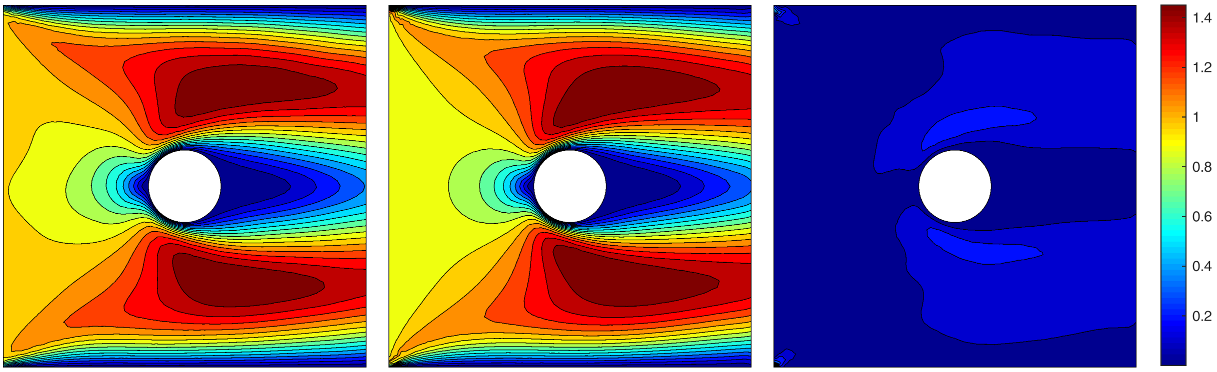

Fig. 3. Comparison of PINN predicted solution (*left*) with a solution computed by DGFEM (*middle*) for Reynolds number 100. The figure on the right shows the error between solutions

References

[1] Giampaolo, F., De Rosa, M., Qi, P., Izzo, S., Cuomo, S., Physics-informed neural networks approach for 1D and 2D Gray-Scott systems, Advanced Modeling and Simulation in Engineering Sciences 9 (1) (2022) No. 5.

[2] Haghighat, E., Raissi, M., Moure, A., Gomez, H., Juanes, R., A physics-informed deep learning framework for inversion and surrogate modeling in solid mechanics, Computer Methods in Applied Mechanics and Engineering 379 (2021) No. 113741.

[3] Raissi, M., Perdikaris, P., Karniadakis, G. E., Physics-informed neural networks: A deep learning framework for solving forward and inverse problems involving nonlinear partial differential equations, Journal of Computational Physics (378) (2019) 686-707.

COMPUTATIONAL MECHANICS 2022
37th conference with international participation
Srní
November 7 - 9, 2022

Modelling of gear couplings in the framework of multibody systems

R. Bulín, M. Hajžman, M. Byrtus

NTIS – New Technologies for the Information Society, Faculty of Applied Sciences, University of West Bohemia, Univerzitní 8, 301 00 Plzeň, Czech Republic

A computational investigation of multibody systems dynamics [2] is widely applied in various practical and research problems. Since the multibody system is composed of rigid or flexible bodies, interconnected with multiple joints, and loaded by different types of forces, all relevant parts must be included in the mathematical model of such a system. In general, the bodies can perform large motions and are driven by drives, that are often controlled by a human operator or by some autonomous control strategy. The gear couplings (GC) are the most common parts of the drive trains for various multibody systems, such as robotic manipulators, wind power plants, vehicles, and other systems with rotating parts. The purpose of the GC is to transfer the rotary motion of a drive (motor, engine, etc.) to another body with desired rotation ratio. This also applies to robotic manipulators based on tensegrity structures, where the length of cables is adjusted using motors. The motor rotation needs to be transferred with proper ratio to a cable winch to achieve stable motion of the whole tensegrity structure and also to achieve good dexterity and controllability. This paper deals with the summary of standard approaches of gear and gear coupling modelling in the framework of multibody system dynamics. The most common gear coupling types are spur, helical, bevel, hypoid and worm.

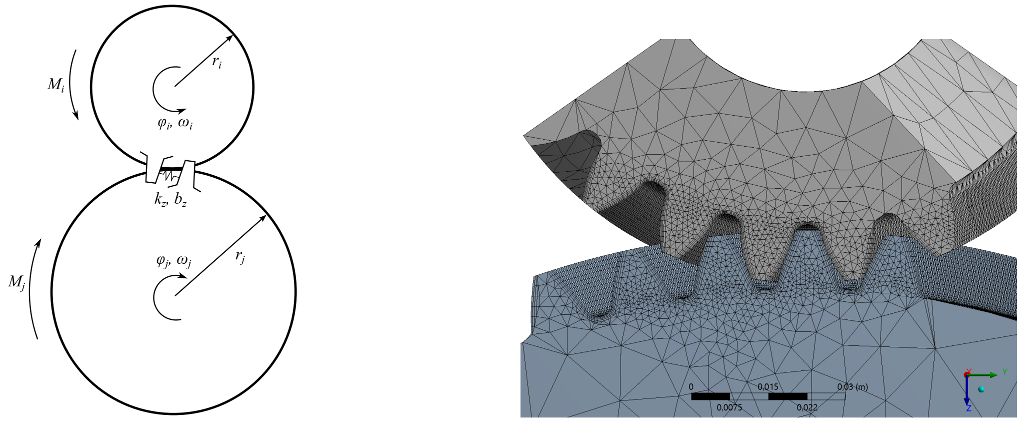

Fig. 1. Simplified scheme of the gear coupling (*left*) and the example of gear stiffness estimation using a software based on the finite element method (*right*)

There are several possible approaches for including the GC in mathematical models of multibody systems, and they can be divided by their complexity. The simplest approach is based on the kinematic constraint formulation in the form of an algebraic equation. Considering the gear coupling from Fig. 1, the algebraic equation that fully constrains the rotation of the gears can be expressed as

$$r_i\varphi_i - r_j\varphi_j = 0, \tag{1}$$

where r_i, r_j are gear pitch circle diameters and φ_i, φ_j are the gear angles of rotation. Since algebraic constraints are commonly used in problems of multibody system dynamics, several methods exist to solve the resulting differential-algebraic equations. On the other hand, this basic approach does not reflect any flexibility of the coupling and also no transverse vibrations of gears are considered, which limits the possible usage of this simple model.

Another approach to describe the GC is the force-based model of the coupling. The basic version couples only the rotational motion of the gears by using appropriately defined moments. Considering the gear coupling from Fig. 1 again, the gear coupling moments M_j and M_i can be expressed as

$$\begin{aligned} F_z &= k_z(r_i\varphi_i - r_j\varphi_j) + b_z(r_i\omega_i - r_j\omega_j), \\ M_i &= F_z \cdot r_i, \\ M_j &= F_z \cdot r_j, \end{aligned} \tag{2}$$

where F_z is the gear force, k_z is the gear stiffness coefficient, and b_z is the tooth damping coefficient. This model allows a flexible transition of the rotational vibrations from one gear to another. The estimation of the gear stiffness can be performed using analytical approaches [3], or the software for structural analysis based on the finite element method can be used; see Fig. 1. This simple force model can be enhanced by varying gear stiffness, kinematic transmission error and teeth backlash that further affects the dynamic behaviour of the whole system [1]. For another improvement of this model, it is possible to include transverse, axial and tilting motion of gears into the expression for teeth deformation, see [1], which makes this approach sufficiently accurate and still computationally effective. This approach can be extended by teeth normal and axial forces together with friction forces, which makes it more detailed.

The most complex force-based method utilizes the general contact of two bodies. In problems of multibody system dynamics, the contact model is most often formulated based on the modified Hertz theory that includes damping in contact. This approach is the most computationally demanding because some algorithm for a contact of solid bodies needs to be employed; thus, its usage in large systems is limited.

The typical software for simulations of multibody systems, such as Adams, Simpack, or Recurdyn, often includes some GC modelling modules, which employ all mentioned methods. Regarding Adams, its force-based approach does not include phenomena such as varying gear stiffness and kinematic transmission error, and its kinematics is based only on the gear rotation angles. Thus, there is still a possibility to extend this kind of modelling tool with the more detailed GC force models, which are needed to be used when the motor-induced vibrations can amplify through the GC to other system parts. This may lead to an increase in noise during mechanism operation. The adequately chosen GC modelling approach helps to analyse possible causes of highly vibrating parts that produce undesired noise.

Acknowledgement

The work was supported by the Czech Science Foundation project number 20-21893S.

References

[1] Byrtus, M., Hajžman, M., Zeman, V., Dynamics of rotating systems, University of West Bohemia, Plzeň, 2010. (in Czech)

[2] Shabana, A. A., Dynamics of multibody systems, 5th edition, Cambridge University Press, Cambridge, 2020.

[3] Tuplin, W. A., Gear stress, SNTL, Praha, 1964. (in Czech)

COMPUTATIONAL MECHANICS 2022
37th conference with international participation
Srní
November 7 - 9, 2022

Supplementary aeroelastic analysis of modified LSA-category aircraft

J. Čečrdle

Czech Aerospace Research Centre (VZLU), Beranových 130, 199 05 Praha Letňany, Czech Republic

Aircraft are required to have a reliability certificate including the aeroelastic (flutter) stability. Flutter analysis must include all applicable configurations of an aircraft in terms of fuel or payload. In the case of the aircraft modification, the appropriate aeroelastic assessment and supplementary analyses are required. Considering the general aviation aircraft, aeroelastic certification is usually based on the ground vibration test (GVT) and on the follow-on analyses using directly the GVT results [1]. The advantage of this approach is its simplicity and cost effectivity. On the other hand, the possibilities for the supplementary analyses in the case of an aircraft modification are limited. Submitted paper presents the practical application of such supplementary analysis.

Subjected aircraft is a two-seat all-composite low-wing LSA-category aircraft. The wingspan is 8.0 m, length is 6.5 m, maximal take-off weight is 600 kg. The design velocity is set as V_D = 300 km/h.

Aeroelastic analysis is based on the experimental data gained by the previously performed GVT of the unmodified aircraft. The changes of the structure and their influence on the structural characteristics are summarised in Table 1.

Table 1. Structure changes and their influence on structural characteristics

Structure change description	Influence on mass and stiffness description
Flap (simple hinge flap instead of a split flap)	No influence on the wing stiffness. Only mass change to be considered.
Aileron (installation of balance weight including the arm)	Control surfaces are considered rigid. No influence on the wing stiffness. Only mass change to be considered.
Wing (reinforced spar web in the central part – inside fuselage)	Influences the wing stiffness. The influence on the appropriate modes to be assessed. Mass change to be considered as well.
Payload increase (pilots, fuel, luggage, parachute)	No influence on the wing and fuselage stiffness. Only mass change to be considered.

The item with the influence on the structural stiffness is the wing spar reinforcement. Therefore, the influences on the appropriate wing and fuselage vibration modes were assessed as summarised in Table 2.

Considering the expected increase in the 1st symmetric wing bending mode frequency, very simple measurement of this mode was performed. Tested aircraft was suspended using a rubber hanger. Sensor instrumentation included two pairs of accelerometers on both sides of the wing and a single accelerometer on the fuselage. The symmetric excitation was realised by a weight release. Measured vibrational time domain response was evaluated. The correct mode was identified within the expected frequency range by the evaluation of the phase

Table 2. Wing spar reinforcement – influence on vibration modes

Mode	GVT freq. (Hz)	Influence description
1st symmetric wing bending	8.57	Symmetric bending deformation of the wing is mainly in the central part of the wing (inside fuselage). Thus, increase in the natural frequency is expected.
1st lateral fuselage bending	10.57	Main bending deformation of the fuselage is at the rear part (behind the cabin). Thus, no significant influence on the fuselage deformation is expected.
1st vertical fuselage bending	11.17	Main bending deformation of the fuselage is at the rear part (behind the cabin). Thus, no significant influence on the fuselage deformation is expected.
1st antisymmetric wing bending	15.03	Antisymmetric bending deformation of the wing is mainly in the out-of fuselage part. Thus, no significant influence is expected.
1st symmetric wing torsion	32.33	Torsional deformation of the wing is mainly in the out-of fuselage part. Thus, no significant influence is expected.

relations among the sensors. The frequency (f), logarithmic decrement (υ) and damping ratio (ζ) were evaluated using standard equations.

As regards to mass changes, the empty weight of the aircraft increased from 280.5 kg to 300 kg (structural changes, parachute) and payload increased from 169.5 kg to 300 kg (pilots, fuel, luggage). The maximal take-of weight increased from 450 kg to 600 kg.

Flutter analyses were performed using g-method. This method transforms aerodynamic matrix into the stiffness matrix (real part) and into the damping matrix (imaginary part). The method generates real physical damping prediction directly at the specified velocities. Analyses were performed at several flight altitudes within the certification envelope (from H = 0 to 3000 m). Velocities were ranging from V = 10 m/s to 200 m/s. Non-matched analysis was employed, i.e., a single (reference) Mach number (M_{REF}) was used within the whole range of velocities. $M_{REF} = 0$, i.e., incompressible flow was considered. This fact must be considered in the result evaluation. Flutter results up to the certification velocity ($1.2{*}V_D = 100$ m/s) may be considered as physically correct as the effect of compressibility is negligible up to this velocity. The results for higher velocities represent just artificial results for evaluation of the rate of reserve with respect to the certification velocity. This is the ordinary practice in aeroelastic analysis. Structural damping was considered using viscous model and common damping ratio (g) of 0.02. This is the realistic estimation of the damping with respect to the results of the GVT. Optionally, g = 0.03, which represents the maximal value acceptable by the regulation standards was used.

Aerodynamic model included the wing, horizontal tail, and vertical tail surfaces. Aerodynamic panels were divided with respect to the geometry including control surfaces and tabs. Interpolation between the structural and aerodynamic model (transfer of displacements

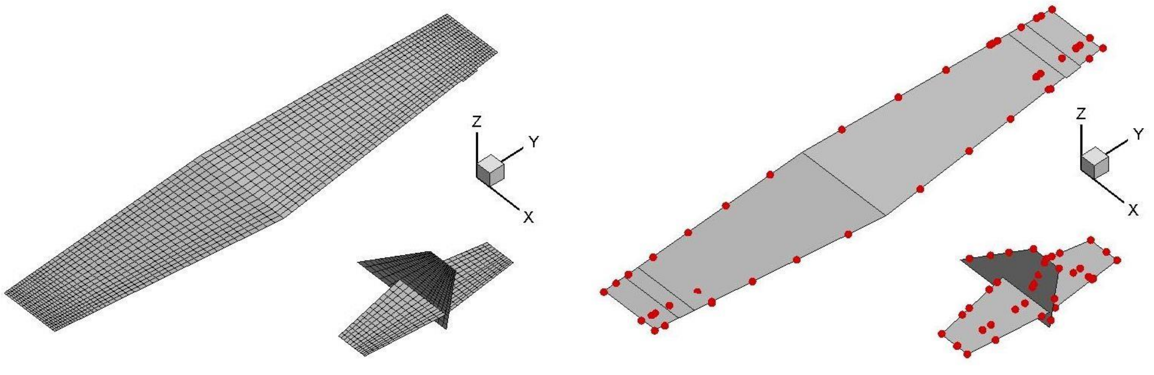

Fig. 1. (a) Aerodynamic mesh, (b) interpolation points

and load between both parts) was realised using Infinite Plate Splines. Appropriate structural points (wing, aileron, aileron tab, etc.) were connected to the appropriate aerodynamic elements. Fig. 1 shows the aerodynamic mesh and the interpolation points.

GVT data (modal model) included 30 modes in total with the frequencies up to 90 Hz. These modes represent vibration modes of the main structural parts (wing, fuselage, vertical tail, horizontal tail) and control surface flapping modes. Full-span model was used, thus both symmetric and antisymmetric modes were included to analysis. Control surface flapping modes were considered for fixed stick (pedals) condition. The reason is that the frequency of the mode with the free stick (pedals) condition is either very close to the frequency of the mode with the fixed stick (pedals) condition (for elevator) or was not measured (otherwise).

Additional mass points representing the structure changes were added into the flutter solution as mass perturbation matrices, which are added into the unperturbed generalized mass matrix. The mass perturbation option provides a change in the mass distribution of the structure without any change within the GVT data.

Analyses included two variants of the fuel load: 26 lt (25 %) and 104 lt (100 %). Identified flutter states are summarised in Table 3 (ordered by the flutter frequency).

Flutter speeds for both analysed configurations are summarised in Fig. 2. It is obvious from the figure that the states of rudder flutter and of aileron flutter are appearing within the certification envelope, i.e., below the velocity of 100 m/s. Considering the structural damping of g = 0.03, which is the maximal value acceptable by regulation standards, the aileron flutter with the character of a hump can be eliminated. Contrary to that, the rudder flutter instability is remaining within the certification envelope even for g = 0.03 (dotted line in the figure).

Due to the above-mentioned fact, the detailed assessment into the rudder flutter instability was performed. First, the flutter primary modes and the main contributing modes were evaluated. Seven modes were evaluated as contributing. From these modes a pair of primary modes (Rudder Flapping, Fuselage Lateral Bending) and a one more significantly contributing mode (Empennage Rolling) were evaluated. Next, the effect of a change in the frequencies of these three modes were evaluated. From this evaluation, the maximal positive effect onto the flutter speed was found for an increase in the Fuselage Lateral Bending mode. However, it is not feasible to make a simple structure change to provide this.

Table 3. Flutter states

Title	Abbr.	~ f_{FL} (Hz)	Description
Rudder flutter	RUDD	9.5	Rudder flapping mode coupling with the empennage rolling mode and with the fuselage lateral bending mode which both induce the fin bending and torsional deformation respectively.
Antisymmetric wing aileron flutter	AILA	11.5	Aileron antisymmetric flapping mode coupling with the wing antisymmetric bending mode, also the lateral engine vibration mode including the wing torsional deformation is contributing.
Wing unsymmetrical flutter	WLA	14.5	This is the wing aileron flutter with the dominant deformation at the port side only. It is caused by the structure unsymmetry.
Symmetric elevator flutter	ELEVS	15.0	Symmetric elevator flapping mode coupling with the fuselage vertical bending and with the tailplane bending deformations. It has a character of a hump instability
Antisymmetric wing aileron flutter	AILA2	16.3	This is another type of the wing bending torsional aileron flutter. It has a character of a hump instability
Wing and elevator flutter	W+E	20.5	Flutter with the dominant deformation at the starboard wing and at the port tailplane. It is caused by the structure unsymmetry.
Antisymmetric elevator flutter	ELEVA	30.6	Antisymmetric elevator flapping mode coupling with the tailplane antisymmetric bending deformations.

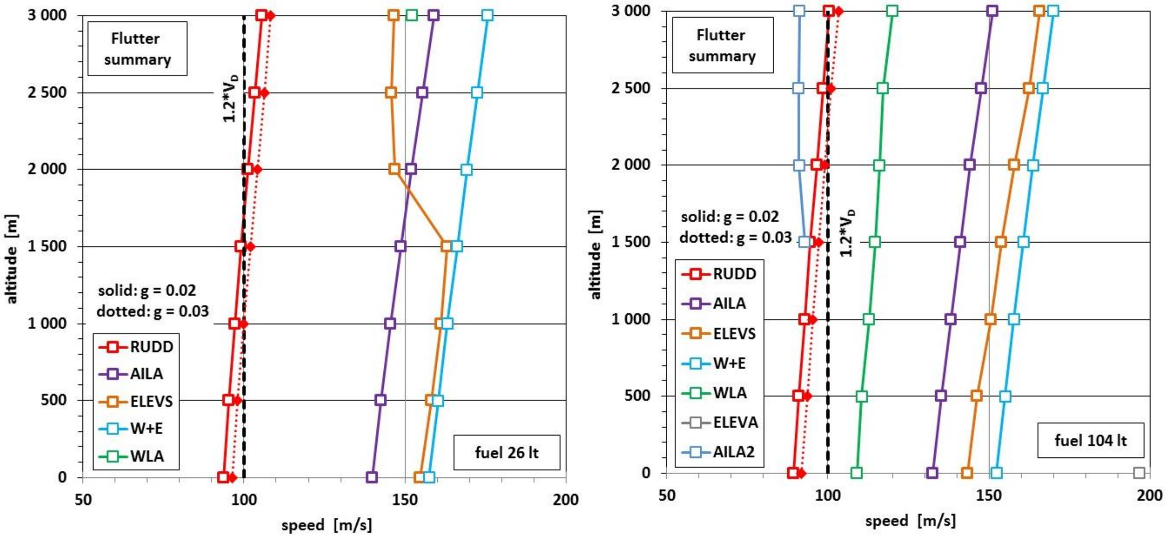

Fig. 2. Flutter speeds (a) fuel 26 lt, (b) fuel 104 lt

Further, the effect of the rudder massbalance was assessed. Note that rudder was not massbalanced. Mass parameters of the rudder structure considering two options of rudder (made of glass-fibre or of carbon-fibre composites) were evaluated. Massbalance weight was simulated at the leading edge of the rudder between both attachment points. Three variants of weight layout (full-length, lower-half, upper-half) were considered. The massbalance weights for a static balance were calculated for these six options. In addition, the conditions of the rudder dynamic balance with respect to the major flutter-contributing modes (Fuselage Lateral Bending and Empennage Rolling) were assessed. In both cases, the static balancing was found to be sufficient also for the dynamic balancing. Next, flutter analyses considering statically balanced rudder were performed for the above-mentioned options. Flutter speeds of the rudder flutter were found sufficiently above the certification velocity. Finally, the optimization of the massbalance weights were performed, i.e., the minimal massbalance weights to keep the flutter speed above the certification threshold were calculated for the above-mentioned options. These calculations were performed for the most critical case, i.e., fuel of 104 lt and H = 0.

To conclude, it may be stated that the requirement of the regulation standard for the design velocity of $V_D = 300$ km/h is fulfilled provided that the appropriate rudder massbalance weight is applied. Otherwise, the reduced value of V_D must be applied for the subjected aircraft.

References

[1] Čečrdle, J., Hlavatý, V., Aeroelastic analysis of light sport aircraft using ground vibration test data proceedings of the institution of mechanical engineers, Part G: Journal of Aerospace Engineering 229 (12) (2015) 2282-2296.

COMPUTATIONAL MECHANICS 2022
37th conference with international participation
Srní
November 7 - 9, 2022

p-Adaptive simulations of Richards’ equation with discontinuous Galerkin method

J.-B. Clément

Department of Technical Mathematics, Faculty of Mechanical Engineering, Czech Technical University in Prague, Prague, Czechia

1. Introduction

Richards’ equation is widely used to study groundwater dynamics of saturated/unsaturated porous media, with problems ranging from oil industry and geotechnical engineering to agriculture and earth science. The numerical solution of Richards’ equation can be troublesome and costly because of abrupt changes in the nonlinear hydraulic properties [1]. Typically, Richards’ equation exhibits sharp wetting fronts moving dynamically in the unsaturated zone while the saturated zone remains relatively smooth. Wetting fronts may be so sharp that spurious oscillations (overshoots/undershoots) appear. Increasing mesh discretization with local adaptation (h-adaptation) is one well-known remedy [1]. High-order methods are known to reach accuracy with a reduced cost compared to low-order methods. In that context, the use of local space order approximation (p-adaptation) is a quite natural direction to be explored in order to assess the possible gains for the solution of Richards’ equation. However, there have been few attempts of high-order applications to Richards’ equation in the literature [2, 3, 5]. Besides, their conclusions have remained unclear about what high-order accuracy can specifically achieve for Richards’ equation because these studies applied general-purpose strategies where mesh and order adaptations are used in combination (hp-adaptation). Firstly, this makes the benefits of high-order accuracy difficult to evaluate. Secondly, these general strategies imply many numerical and computational tools making them difficult to implement and costly to compute. This last statement is even more questionable in regards of Richards’ equation which is known to be quite challenging to solve numerically and whose solvers need to be as robust and efficient as possible. Thereby, there is room to explore high-order methods applied to Richards’ equation.

To this end, discontinuous Galerkin (DG) methods will be employed in this paper. DG methods are particularly suitable for high-order accuracy. Indeed, they rely on an element-wise weak formulation which can be seen as a generalization of the Finite Element or the Finite Volume frameworks. This makes DG methods flexible and attractive to design high-order schemes which can be locally adapted. In this study, the p-adaptive algorithm is kept simple in order to prevent computational complexity and, if needed in the future, to make the extension to hp-adaptation as easy as possible.

Firstly, Richards’ equation and hydraulic properties are briefly introduced. Then, Richards’ equation is discretized with a DG method for space and with Backward Differentiation Formula (BDF) methods for time. The adaptivity algorithm is also outlined. Finally, a test-case is presented to show the abilities of the numerical methods.

2. Model problem

Richards' equation is a degenerate nonlinear parabolic equation which models flows in variably-saturated porous media [1]

$$\partial_t \theta(\psi) - \nabla \cdot (\mathbb{K}(\psi)\nabla(\psi + z)) = 0, \tag{1}$$

where $\mathbb{K}$ is the hydraulic conductivity [L·T^{-1}] and z is the elevation [L]. This equation can be rewritten in terms of hydraulic head $h = \psi + z$ [L], a more common variable in hydrology

$$\partial_t \theta(h - z) - \nabla \cdot (\mathbb{K}(h - z)\nabla h) = 0. \tag{2}$$

Solving Richards' equation (1) requires two constitutive laws: one for water content and one for hydraulic conductivity. For practical purposes, it is assumed that

$$\mathbb{K}(\psi) = \mathbb{K}_{\mathrm{s}} K_{\mathrm{r}}(\psi) \qquad \text{and} \qquad S_{\mathrm{e}}(\psi) = \frac{\theta(\psi) - \theta_{\mathrm{r}}}{\theta_{\mathrm{s}} - \theta_{\mathrm{r}}}, \tag{3}$$

where $\mathbb{K}_{\mathrm{s}}$ denotes the intrinsic or saturated hydraulic conductivity tensor [L · T^{-1}], K_{r} the relative hydraulic conductivity [-], θ_{s} the saturated water content [-] and θ_{r} the residual water content [-], corresponding to the maximal and minimal saturations, respectively. S_{e} and K_{r} are monotonic increasing functions of pressure head ψ in the unsaturated zone ($\psi < 0$) and constant in the saturated zone ($\psi \geq 0$). Several relations exist to model these hydraulic properties. In this paper, the van Genuchtem-Mualem relations will be used

$$\text{if } \psi \geq 0, \text{ then } S_{\mathrm{e}}(\psi) = K_{\mathrm{r}}(\psi) = 1, \tag{4}$$

$$\text{if } \psi < 0, \text{ then } S_{\mathrm{e}}(\psi) = (1 + (\alpha|\psi|)^n)^{-m} \quad \text{and} \quad K_{\mathrm{r}}(\psi) = {S_{\mathrm{e}}}^{0.5}\Big(1 - \Big(1 - {S_{\mathrm{e}}}^{\frac{1}{m}}\Big)^m\Big)^2, \tag{5}$$

where α the parameter linked to air entry pressure inverse [L^{-1}], $n > 1$ the pore-size distribution [-] and $m = 1 - \dfrac{1}{n}$ the pore-size distribution [-].

3. Numerical methods

3.1 Discontinuous Galerkin discretization

DG methods rely on an element-wise weak formulation which share properties from both the Finite Element and the Finite Volume frameworks which makes them flexible and attractive to design high-order schemes and local adaptation. Extensive introduction can be found in Rivière [4]. In this paper, Richards' equation is discretized in space by a DG method called incomplete interior penalty Galerkin (IIPG) because it is the simplest one. For time discretization, BDF methods with variable time step are chosen because they provide high-order implicit schemes in time which are needed if one wants to take advantage of high-order accuracy in space. For further developments about DG and BDF methods for Richards' equation, the reader is referred to Clément *et al.* [1].

Careful considerations should be given to the choice of the basis for the expansion of the solution when using high-order DG approximations. Indeed, modal bases which are orthogonal and hierarchical present enjoyable properties compared to other bases like nodal bases. Their hierarchical design helps the implementation along and their orthogonality provides better numerical behaviour at high-order like a low condition number for the matrices of the discrete system. In addition, integration quadrature formula should be in accordance with the maximum order of used polynomials. In this study, the Legendre's polynomials are used because this is one of the simplest and most suitable basis for high-order. For quadrangle elements, a tensor product is performed in each direction.

3.2 Adaptivity algorithm

The adaptivity algorithm is made of three main steps which are sketched in Fig. 1. The first step is the evaluation of a criterion η, or better an error estimator, on each element to indicate the area of interest. In this study, the criterion is heuristically-based and aims at measuring the numerical smoothness of the solution through the volume residual, the solution jump and the flux jump, see [1]. The second step is the selection of the elements where the approximation order will be increased or decreased. To do this, the criterion is compared to user-defined threshold values $0 < \beta_\mathrm{d} \leq \beta_\mathrm{i}$. For $\beta_\mathrm{d} \leq \eta < \beta_\mathrm{i}$, the element order remains unchanged. For $\beta_\mathrm{i} \leq \eta$, the element order is increased by one. For $\eta < \beta_\mathrm{d}$, the element order is decreased by one. The last step consists in transferring the solution from the previous order approximation to the new one. Since the employed basis is hierarchical, the corresponding degrees of freedom in the solution expansion are truncated in case of order decrease, or extended by zero values in case of order increase. The adaptation process is not performed at each time step but according to a user-defined frequency.

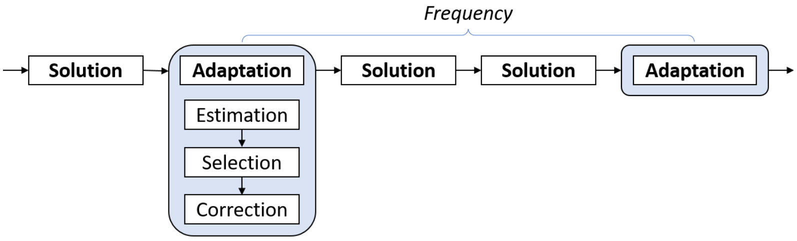

Fig. 1. Adaptivity algorithm for the present *p*-adaptive strategy

4. Numerical results

Numerical results are evaluated with a 1D vertical downward infiltration problem called Polmann's test-case which is described in [1]. The computational domain is a rectangle $(0, 20) \times (0, 100)$ cm. The test-case is solved for pressure head ψ during $T = 48$ h with a constant time step $\tau = 120$ s. The initial condition is $\psi_0 = -1000$ cm. The implicit Euler scheme is used (1-step BDF method). The parameters of Van Genuchten-Mualem relations are $K_s = 9.22 \times 10^{-3}$ cm·s^{-1}, $\theta_\mathrm{s} = 0.368$, $\theta_\mathrm{r} = 0.102$, $\alpha = 3.35 \times 10^{-2}$ cm^{-1} and $n = 2$. Three computations are carried out: one for a mesh M100 of 100 elements of order one, one for mesh M400 of 400 elements of order one, and one for *p*-adaptive mesh of 100 elements. In the latter case, order varies from 1 to 3, $\beta_\mathrm{d} = \beta_\mathrm{i} = 0.05$ and adaptation is done every 5 time steps.

Results are presented in Fig. 2. The left and middle figures show the abilities of the *p*-adaptive computation to follow the wetting front in time. The right figure compares the different computations. For the mesh M100, the solution holds an undershoot ahead of the wetting front. For the mesh M400 and *p*-adaptation, the oscillations in the solution vanish.

5. Conclusions

The paper shows that Richards' equation solution can benefit from high-order DG methods. One finding is that high-order approximation can suppress oscillations at the wetting front.

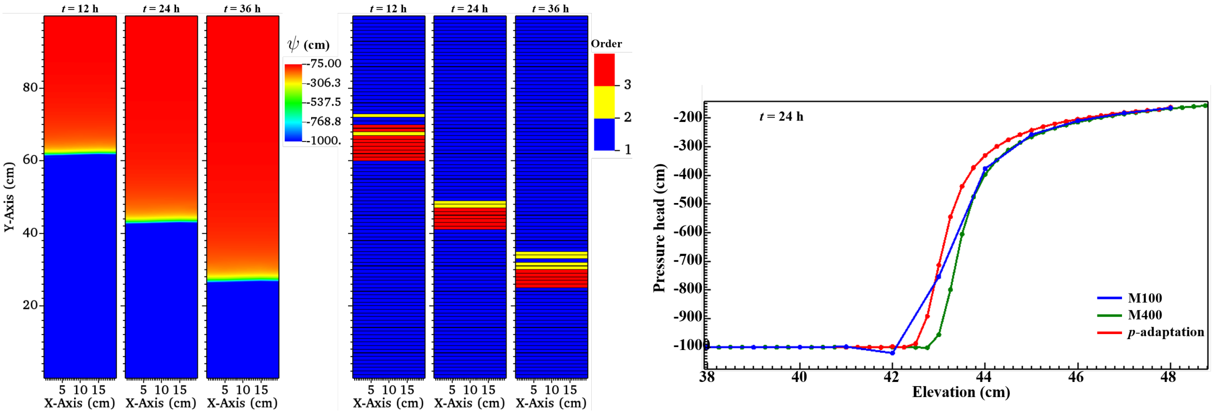

Fig. 2. Wetting front evolution (*left*), element order adaptation (*middle*) and comparison of pressure head profiles (*right*)

This is quite unexpected because wetting fronts are sharp features lacking smoothness. Since high-order approximation everywhere is costly, p-adaptation is necessary. A simple adaptivity algorithm was designed to follow dynamically the wetting fronts of Richards' equation where the approximation order is locally increased to remove the oscillations.

In order to take the most of high-order methods, especially in case of adaptation, lots of numerical and computational tools must be implemented. This is a challenging task and the computational cost may be increased. The choice of DG methods with orthogonal and hierarchical modal bases allows to alleviate some efforts. High-order time accuracy is needed if one wants to use high-order space accuracy. That is why BDF methods with variable time step are employed.

This study raises an interesting question to know whether p-adaptation is worthy in case of Richards' equation because previous studies in the literature [2, 3, 5] do not use p-adaptation at the wetting front but in smooth regions. In addition, p-adaptation is often used in combination with h-adaptation to make hp-adaptation. Toward this direction, further research is needed to assess p-adaptive simulations of Richards' equation.

Acknowledgement

The Czech Technical University in Prague supported this work under the “Program Postdoc”.

References

[1] Clément, J.-B., Golay, F., Ersoy, M., Sous, D., An adaptive strategy for discontinuous Galerkin simulations of Richards' equation: Application to multi-materials dam wetting, Advances in Water Resources 151 (2021) No. 103897.

[2] Dolejší, V., Kuraz, M., Solin, P., Adaptive higher-order space-time discontinuous Galerkin method for the computer simulation of variably-saturated porous media flows 72 (2019) 276-305.

[3] Li, H., Farthing, M. W., Miller, C. T., Adaptive local discontinuous Galerkin approximation to Richards' equation, Advances in Water Resources 30 (9) (2007) 1883-1901.

[4] Rivière, B., Discontinuous Galerkin methods for solving elliptic and parabolic equations, Society for Industrial and Applied Mathematics, 2008.

[5] Solin, P., Kuraz, M., Solving the nonstationary Richards equation with adaptive hp-FEM, Advances in Water Resources 34 (9) (2011) 1062-1081.

COMPUTATIONAL MECHANICS 2022
37th conference with international participation
Srní
November 7 - 9, 2022

Periodical solution of *n*-DOF parametric system vibration

J. Dupal

Faculty of Applied Sciences, University of West Bohemia in Pilsen, Univerzitní 8, 301 00 Plzeň, Czech Republic

1. Introduction

The contribution deals with usage of periodic Green´s function (PGF) to periodic solution of linear vibrating systems described by time dependent coefficient matrices. The PGF enables to transfer system of 2nd order ODE to the system of integral [1, 2, 4] and integer-differential equations [3] and its analytical solution. Behaviour of several mechanical objects such as non-symmetrical rotors can be described by system of linear ordinary differential equations of the 2nd order. This system in matrix form is represented by matrices of mass, damping, stiffness and excitation force vector. The mentioned matrices especially for non-symmetrical rotors have time dependent periodic form. Assuming the excitation is periodic too, the equation of motion can take a form

$$\left[\mathbf{M}_0-\tilde{\mathbf{M}}(t)\right]\ddot{\mathbf{q}}(t)+\left[\mathbf{B}_0-\tilde{\mathbf{B}}(t)\right]\dot{\mathbf{q}}(t)+\left[\mathbf{K}_0-\tilde{\mathbf{K}}(t)\right]\mathbf{q}(t)=\mathbf{f}(t), \tag{1}$$

where

$$\tilde{\mathbf{M}}(t)=\tilde{\mathbf{M}}(t+T),\ \tilde{\mathbf{B}}(t)=\tilde{\mathbf{B}}(t+T),\ \tilde{\mathbf{K}}(t)=\tilde{\mathbf{K}}(t+T),\ \mathbf{f}(t)=\mathbf{f}(t+T), \tag{2}$$

T is period and $\omega=2\pi/T$ is basic angular frequency. For the reason of periodicity the matrices and force vector can be expressed by Fourier series (let us mark $e_k(t)=e^{ik\omega t}$)

$$\tilde{\mathbf{M}}(t)=\sum_{k=-N}^{N}\mathbf{M}_k e_k(t),\ \tilde{\mathbf{B}}(t)=\sum_{k=-N}^{N}\mathbf{B}_k e_k(t),\ \tilde{\mathbf{K}}(t)=\sum_{k=-N}^{N}\mathbf{K}_k e_k(t),\ \mathbf{f}(t)=\sum_{k=-N}^{N}\mathbf{f}_k e_k(t). \tag{3}$$

2. Periodic Green’s function

Periodic Green’s function is matrix function whose *j*-th column is system response to excitation in the *j*-th place to force in the form of Dirac train with period *T*. This excitation in *j*-th place and Dirac train [1] can be written in form

$$\frac{1}{T}\mathbf{i}_j\delta_T(t)=\frac{1}{T}\mathbf{i}_j\sum_{k=-N}^{N}e_k(t), \tag{4}$$

where $\mathbf{i}_j$ is *j*-th column of identity matrix. The response taken into account corresponds to the stationary part of left hand side of Eq. (1)

$$\mathbf{M}_0\ddot{\mathbf{q}}^{(j)}(t)+\mathbf{B}_0\dot{\mathbf{q}}^{(j)}(t)+\mathbf{K}_0\mathbf{q}^{(j)}(t)=\frac{1}{T}\mathbf{i}_j\sum_{k=-N}^{N}e_k(t). \tag{5}$$

The PGF after some arrangements has form

$$\mathbf{H}_T(t)=\frac{1}{T}\sum_{k=-N}^{N}\mathbf{L}_k e_k(t),\ \mathbf{L}_k=\left(-k^2\omega^2\mathbf{M}_0+ik\omega\mathbf{B}_0+\mathbf{K}_0\right)^{-1}\in\mathbf{C}^{n,n}. \tag{6}$$

N corresponds to the number of respected terms in Fourier series. Solution of (1) is identic with solution of integer-differential equation

$$\begin{aligned}\mathbf{q}(t) &= \int_0^T \mathbf{H}_T(t-s)\tilde{\mathbf{M}}(s)\ddot{\mathbf{q}}(s)\,ds + \int_0^T \mathbf{H}_T(t-s)\tilde{\mathbf{B}}(s)\dot{\mathbf{q}}(s)\,ds + \\ &+ \int_0^T \mathbf{H}_T(t-s)\tilde{\mathbf{K}}(s)\mathbf{q}(s)\,ds + \int_0^T \mathbf{H}_T(t-s)\mathbf{f}(s)\,ds.\end{aligned} \tag{7}$$

The last equation can be rewritten after some arrangements into form

$$\mathbf{q}(t) = \mathbf{E}(t)\boldsymbol{\gamma} + \mathbf{E}(t)\boldsymbol{\beta} + \mathbf{E}(t)\boldsymbol{\alpha}, \tag{8}$$

where $\mathbf{E}(t) = \left[e_{-N}(t)\mathbf{I},\ \ e_{-N+1}(t)\mathbf{I},\ \ \ldots,\ \ e_N(t)\mathbf{I}\right] \in \mathbf{C}^{n,(2N+1)n}$, $\mathbf{I} \in \mathbf{R}^{n,n}$ is identity matrix. Vectors of coefficients are result of solution to Eq. (7).

3. Conclusion

The results and detailed procedure of solution of Eq. (7) will be presented during oral presentation. This result relation (8) enables next possibilities for the solution of equation of motion (1), e.g. response to random excitation on the right hand side of Eq. (1) or solution to the same equation whose matrices on the left hand side contain random parameters.

References

[1] Babitsky, V.I., Krupenin, V.L., Vibration of strongly nonlinear discontinuous systems, Springer, Berlin, 2001.

[2] Dupal, J., Zajíček, M., Analytical periodic solution and stability assessment of 1 DOF parametric systems with time varying stiffness, Applied Mathematics and Computation 243 (2014) 138-15.

[3] Dupal, J., Zajíček, M., Existence of analytical solution, stability assessment and periodic response of vibrating systems with time varying parameters, Applied and Computational Mechanics 14 (2) (2020) 123–144.

[4] Zajíček, M., Dupal, J., Analytical solution of spur gear mesh using linear model, Mechanism and Machine Theory 118 (2017) 154–167.

COMPUTATIONAL MECHANICS 2022
37th conference with international participation
Srní
November 7 - 9, 2022

Local phenomena in tilting-pad journal bearing's pivot

Š. Dyk, J. Rendl, R. Bulín, L. Smolík

NTIS, Faculty of Applied Sciences, University of West Bohemia, Univerzitní 8, 301 00 Plzeň, Czech Republic

Tilting-pad journal bearings (TPJBs) are often used to support rotating machines where high load-carrying capacity is needed. The tilting motion of the pads is secured by various joint types: rocker-back pivots, cylindrical coupling or ball-and-socket. The latter, which we focus on, brings several design advantages. However, it also generates additional friction moments that negatively affect the bearing's behaviour with respect to the static equilibrium path and stability [4, 5].

As shown in the previous research [2], one of the key factors in modelling TPJBs behaviour is a normal force in ball-and-socket coupling. Usually, the Hertz theory is used for the contact force description. However, considering the conforming contact of the ball-and-socket bodies, the assumptions of the Hertz theory are not satisfied, and a theory for conformal contact should be used. Here, we use a Fang theory [1] for the inner contact of two spheres which describes a pressure distribution in such contact.

As noted before, the friction in ball-and-socket coupling plays an essential role in the bearing's performance. For the friction description, we use representatives of both statical and dynamical friction models: the Bengisu-Akay and the LuGre model. The latter allows a description of such phenomena as stick-slip transitions, presliding or frictional lag. However, the dynamic models are tricky from the viewpoint of parameter estimation.

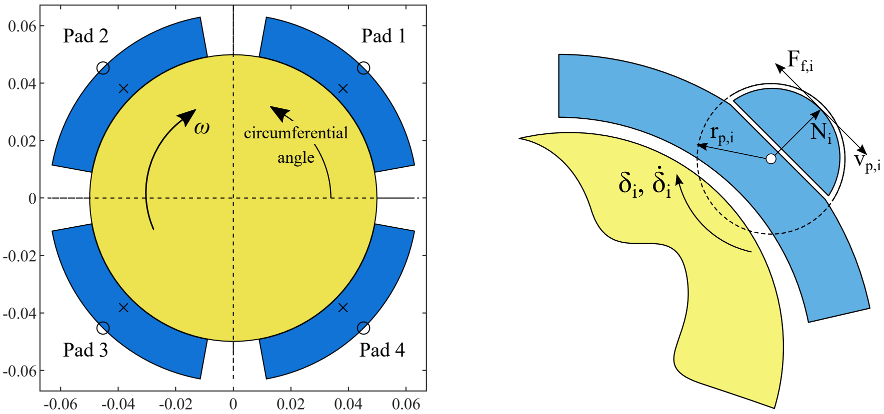

Fig. 1. A scheme of the considered TPJB and a detailed view of the ball-and-socket pivot with emphasised friction force

As a benchmark model, we use four-pad TPJB with the load-between-pads configuration, see Fig. 1. For simplicity, the rotating part is represented by a simple Jeffcott-like rotor: a journal with vertical and horizontal displacements as degrees of freedom. Moreover, since we focus on the local behaviour of pads' pivots, we omit upper pads – the previous analyses [3] showed that they are not carrying a load and are rather subjected to pad fluttering.

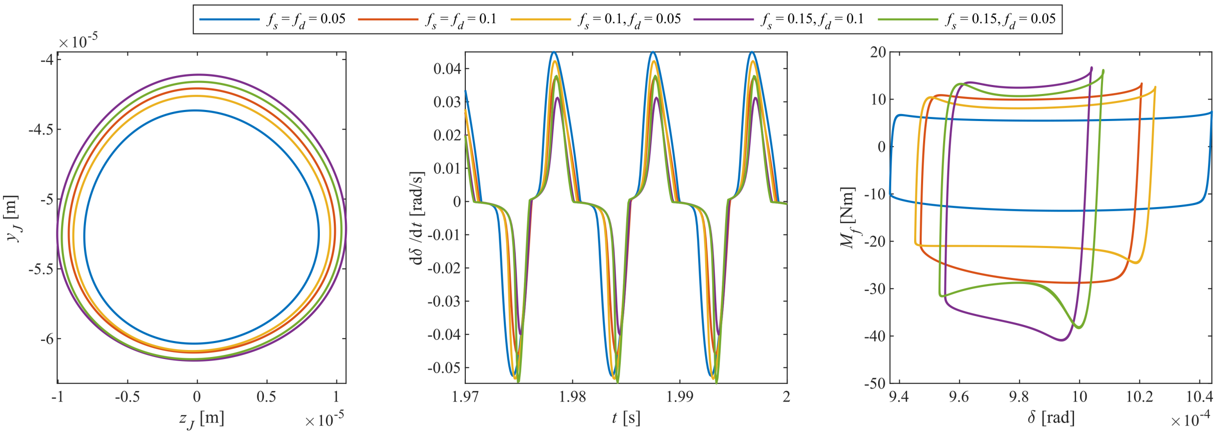

Fig. 2. Journal orbit for various friction coefficients, tilting velocity of one of the lower pads and the hysteresis loops of the considered cases

As shown in Fig. 2, the friction strongly affects the pads' tilting motion concerning velocity amplitudes, stick phases near zero velocity, and dissipation properties, as demonstrated via hysteresis loops. As a consequence, the orbit gets larger with an increasing friction coefficient. We also show a crucial influence of friction parameter settings, e.g., critical velocity, bristle stiffness and damping of the LuGre model, etc.

The proposed model provides a comprehensive basis for further research focusing on the interferences between friction phenomena in ball-and-socket couplings and the unloaded upper pads behaviour.

Acknowledgement

This paper was supported by the Technology Agency of the Czech Republic under the THETA Programme within the TK04020057 project.

References

[1] Fang, X., Zhang, C., Chen, X., Wang, Y., Tan Y., A new universal approximate model for conformal contact and non-conformal contact of spherical surfaces, Acta Mechanica 226 (6) (2015) 1657-1672.

[2] He, F., Including pivot friction in pad motion for a tilting pad journal bearing with ball-socket pivots, Volume 7A: Structures and Dynamics of Turbo Expo: Power for Land, Sea and Air, 2017, pp. 1-11.

[3] Rendl, J., Dyk, Š., Smolík, L., Nonlinear dynamic analysis of a tilting pad journal bearing subjected to pad fluttering, Nonlinear Dynamics 105 (2021) 2133-2156.

[4] Wygant, K. D., Flack, R. D., Barrett L. E., Influence of pad pivot friction on tilting-pad journal bearing measurements–Part II: Dynamic coefficient, Tribology Transactions 42 (1) (1999) 250-256.

[5] Wygant, K. D., Flack, R. D., Barrett L. E., Measured performance of tilting-pad journal bearings over a range of preloads–Part I: Static operating conditions, Tribology Transactions 47 (4) (2004) 576-584.

COMPUTATIONAL MECHANICS 2022
37th conference with international participation
Srní
November 7 - 9, 2022

Device for measuring the stiffness of the tensile nylon springs

V. Goga, Š. Berta, J. Murín, J. Paulech, L. Šarkán

Faculty of Electrical Engineering and Information Technology of Slovak University of Technology in Bratislava, Institute of Automotive Mechatronics, Ilkovičova 3, 812 19 Bratislava, Slovak Republic

1. Introduction

Twisted and coiled nylon fiber actuator represents a soft actuator (also called as an artificial muscle) which is suitable to realize smooth and soft motion of machines and robots. This type of actuator is fabricated by twisting nylon fibres (e.g. fishing line) into helical state and in the final, it looks like a preloaded tensile nylon spring (Fig. 1 left).

Cold nylon spring actuator is stretched due to tensile load and its shortening is realized by heating. Thus, the actuator's operation can be controlled by changing its temperature. Actuator heating is realized by hot air blowing, warm water bypass or by electric Joule heating (Fig. 1 right). The advantage of this actuator is simple and cheap production, outstanding power density and large deformation. These actuators are referred to as Twisted-Polymeric-Fibre Actuators (TPFA), while the nylon fishing line is commonly used to produce them. A more extensive overview of TPFA can be found in [2, 4, 5].

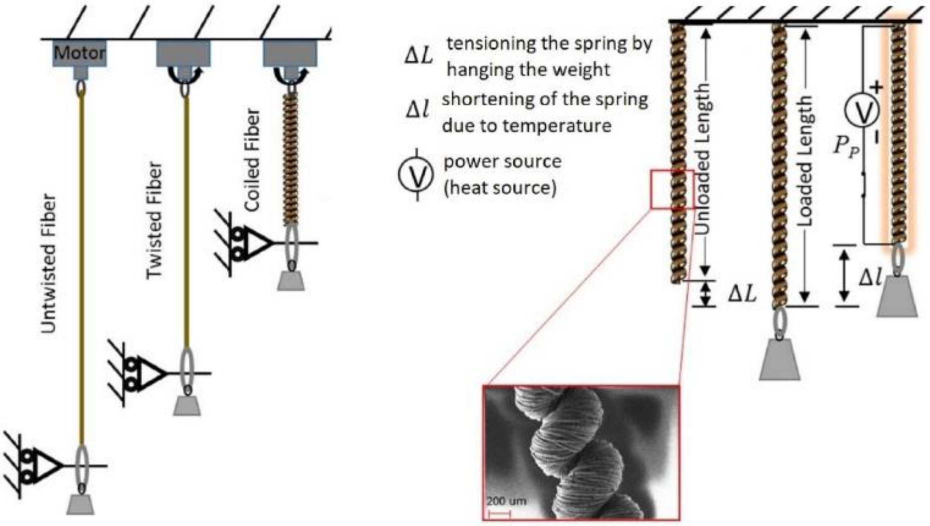

Fig. 1. Twisting process of the nylon fiber into the shape of a spring (left) [2], reaction of nylon fiber spring on adding mass and reaction to temperature change (right) [2]

To analyze the functionality of a nylon spring by the computational methods [3], it is necessary to know its mechanical and thermal properties. This paper presents a device that can be used to measure the basic mechanical property of nylon springs - tensile stiffness. Spring stiffness is measured either by a quasi-static test (stretching of the spring) or a dynamic test (mass vibration) [1]. Data acquisition system is implemented using the Arduino platform.

2. Measuring device

From a technical point of view, the device consists of a supporting structure, two strain gauge load cells, a linear actuator with a built-in potentiometric position sensor, control electronics and a touch screen (Fig. 2). [1]

Linear actuator is used for continuous stretching of the spring and is powered through a driver for DC motor. Load cells measure the tensile force in the spring. Voltage signal from the load cells is converted into digital form using 16-bit sigma-delta analog-to-digital converter (ADC). Arduino Mega controller is used as the control unit for the entire device, which also serves as a data acquisition system. Control of the measurement system is solved using a touch screen, on which the measured graphic curves for individual measurements are also drawn.

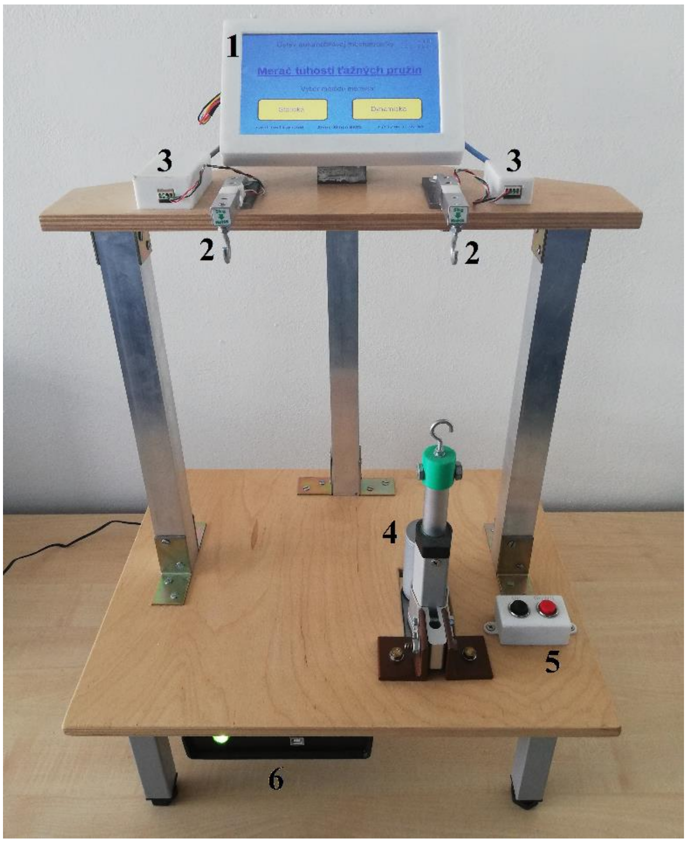

Fig. 2. Measuring device [1]: 1 – touchscreen, 2 – loadcells, 3 – ADC, 4 – linear actuator, 5 – manual control, 6 – electronics and data acquisition system

The basis of the electrical wiring of the device is the so-called shield, i.e. the expansion board with the connection pins located on the underside of the board (Fig. 3 left). These pins connect the shield directly to the Arduino Mega microcontroller board. On the shield's top side, there are connectors for other individual electronic parts and modules of the measuring and control system (Fig. 4). The shield also contains a couple of ceramic filter capacitors, a reset button, a couple of indicator diodes with their resistors, and a screw connector for 5 V power supply from DC-DC converter (Fig. 3 right).

A special voltage transducer was designed and used to measure the force in the dynamic test (Fig. 3 right). This transducer converts low voltage output (0 to 4.6 mV) from load cell linearly to usable range (0 to 5 V) for applied ADC (module ADS1115). This output voltage is proportional to the exerted force on load cell from 0 to 50 N. Both the shield and the voltage transducer were designed in KiCAD software.

For quasi-static measurement method, the load cell in combination with module HX711 is used because it is more precise (24-bit). However, data processing by the HX711 module is slower than that of the ADS1115 module and is therefore not suitable for dynamic measurements.

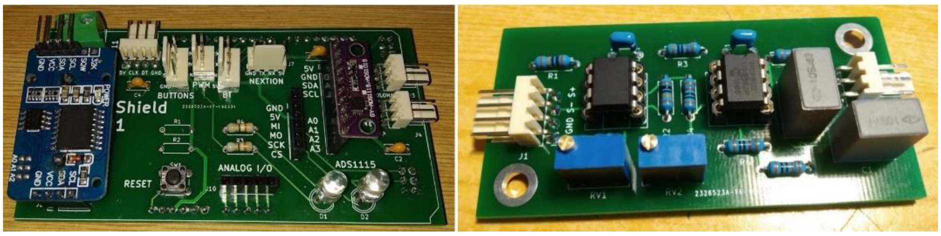

Fig. 3 Expansion board – shield (left), voltage transducer (right) [1]

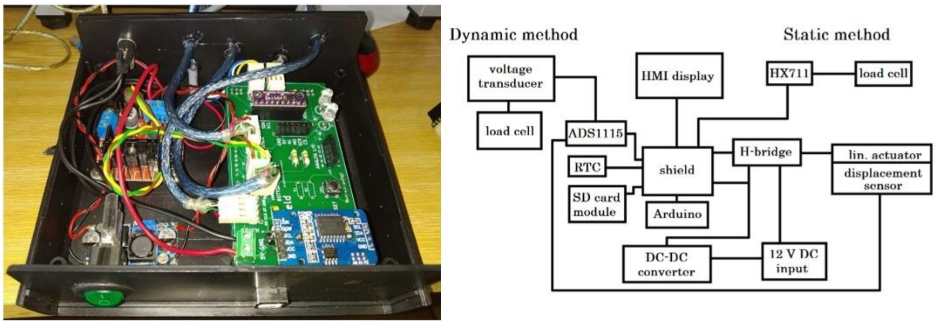

Fig. 4. Measuring and control system: actual wiring (left) and block diagram (right) [1]

3. Spring stiffness measurement procedure

Spring stiffness can be measured using two methods. The first method represents quasi-static stretching of the spring, when the tensile force and spring extension are measured. Spring stiffness in linear area of deformations is then calculated as the ratio of tensile force and spring extension by linear regression using least squares method (Fig. 5). Tensile force is measured by a load cell mounted on the upper fixed console of the device, and the spring extension is measured by a potentiometric position sensor located in the body of the linear actuator that stretches the spring.

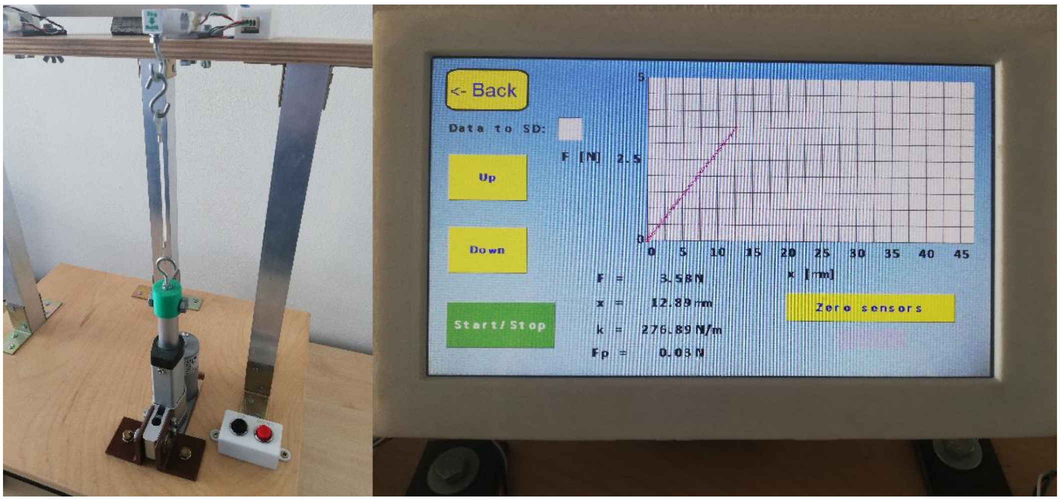

F = 3.58 N
x = 12.89 mm
k = 276.89 N/m
Fp = 0.03 N

Fig. 5. Quasi-static measurement of the spring stiffness

The second method is a dynamic test, when a mass is hung on a spring attached to a load cell and allowed to oscillate (Fig. 6), it represents free vibration of 1-DOF mechanical oscillator. Before the start of the test, the load cell measures the weight of the suspended mass on the spring. Then the spring is manually stretched and released, creating a free vibration of the system. Load cell measures the time course of the force in the spring and natural frequency of the system is calculated using FFT (Fast Fourier Transform). Spring stiffness is then calculated from the known mass weight and system's natural frequency.

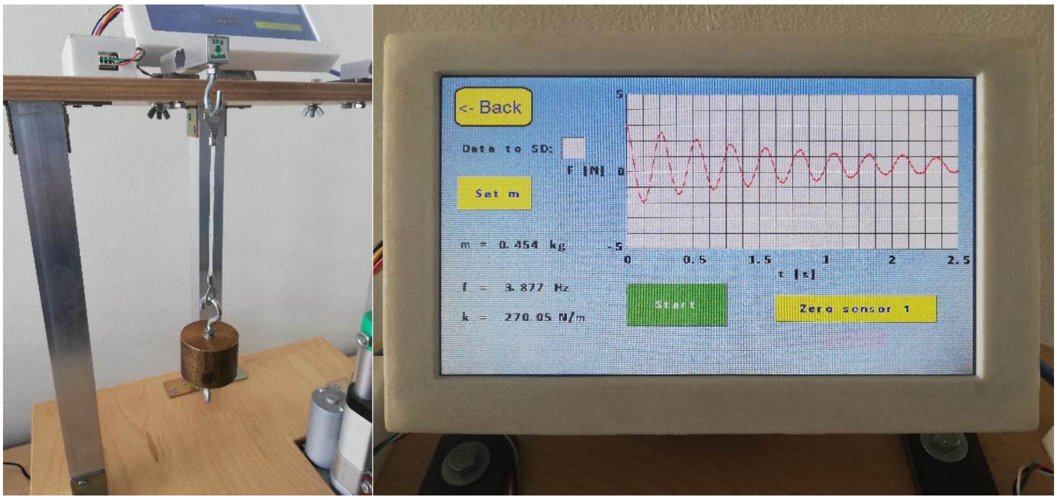

m = 0.454 kg

f = 3.877 Hz

k = 270.05 N/m

Fig. 6. Dynamic measurement of the spring stiffness

4. Conclusions

Due to the relatively large material damping of the nylon springs, the stiffnesses measured by both methods are slightly different. Better agreement is obtained when the steel springs are measured because their material damping is minimal.

The measuring device has the following advantages: it is powered only by 12 V DC power supply, the device is light and easily portable, touch screen control that also displays the measurement results, the possibility of transferring measured data to a PC using SD card, and it is suitable in education process in the mechanics.

Acknowledgements

This work was supported by the Slovak Research and Development Agency under the contract No. APVV-19-0406, by Grant Agency VEGA, grant No. 1/0416/21 and by Grant Agency KEGA, grant No. 011STU-4/2020.

References

[1] Berta, Š., Experimentálne zariadenie pre meranie tuhosti ťažných pružín, Bachelor thesis, FEI STU in Bratislava, 2019. (in Slovak)

[2] Cherubini, A., Moretti, G., Vertechy, R., Fontana, M., Experimental characterization of thermally-activated artificial muscles based on coiled nylon fishing lines, AIP Advances 5 (2015) 067158.

[3] Murín, J., Goga, V., Paulech, J., Hrabovský, J., Sedlár. T., Kutiš, V., Aminbaghai, M., Thermo-elastostatic analyzes of new dampers made of polymer springs with negative thermal expansion, MMS 2021 International Slovak-Polish Scientific Conference on Machine Modelling and Simulations, Bristol: IOP Publishing, 2021. IOP Conference Series: Materials Science and Engineering, Art. no. 01205 [16] (2021).

[4] Suzuki, M., Kamamichi, N., Robust control with disturbance observer for twisted and coiled polymer actuator, Smart materials and Structures 27 (2018) 085006.

[5] Wu, L., De Andrade, M.J., K Saharan, K., Rome, R.S., Baughman, R.H., Tadesse, Y., Compact and low-cost humanoid hand powered by nylon artificial muscles, Bioinspiration and Biomimetics 12 (2017) 026004.

COMPUTATIONAL MECHANICS 2022
37th conference with international participation
Srní
November 7 - 9, 2022

Multibody dynamics simulations of the railway vehicle for heavy loads transport

M. Hajžman, P. Polach, P. Polcar

Research and Testing Institute Pilsen, Tylova 1581/46, 301 00 Plzeň, Czech Republic

Numerical simulations are efficiently used for the evaluation of the design of various mechanical systems in pre-production states. Since the railway industry is very strictly controlled by various standards and codes, the usage of computational models to verify proposed vehicle design according to standards is quite convenient. This paper is aimed at the description of the evaluation process for a special purposed 32-axle wagon (see Figs. 1 and 2) intended for carrying large size and heavy loads.

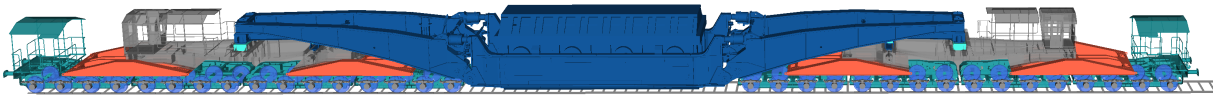

Fig. 1. Visualization of the whole wagon multibody model in the SIMPACK software

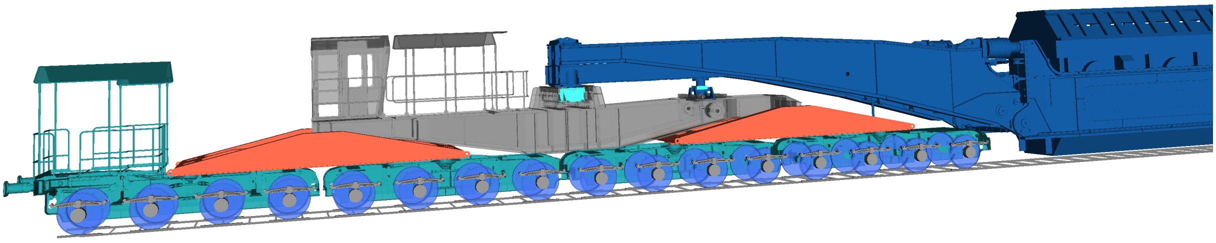

Fig. 2. Visualization of the rear wagon section with two small bridges (red bodies) and one large bridge (gray body) and half of the main bridge with payload

Railway vehicles are typical representatives of multibody systems that are composed of kinematically constrained bodies [2]. The SIMPACK software was used as the main software tool in this modelling task. The modelling methodology is based on the vehicle decomposition into particular design elements characterized as rigid bodies. Except for particular bogies (each with four wheelsets), the modelled wagon is designed with several functional components called bridges carrying payload. The wagon multibody model contains these main rigid bodies: 32 wheelsets, 8 bogie frames, 4 small bridges, 2 large bridges, and 1 main bridge (+payload and/or platforms), see Fig. 3 for the kinematical scheme of the whole model.

The SIMPACK multibody formalism is formulated for relative coordinates between bodies, and therefore each rigid body has exactly one kinematical joint. Other kinematical relations are represented by so-called constraints. Several bodies, which form a functional group and are

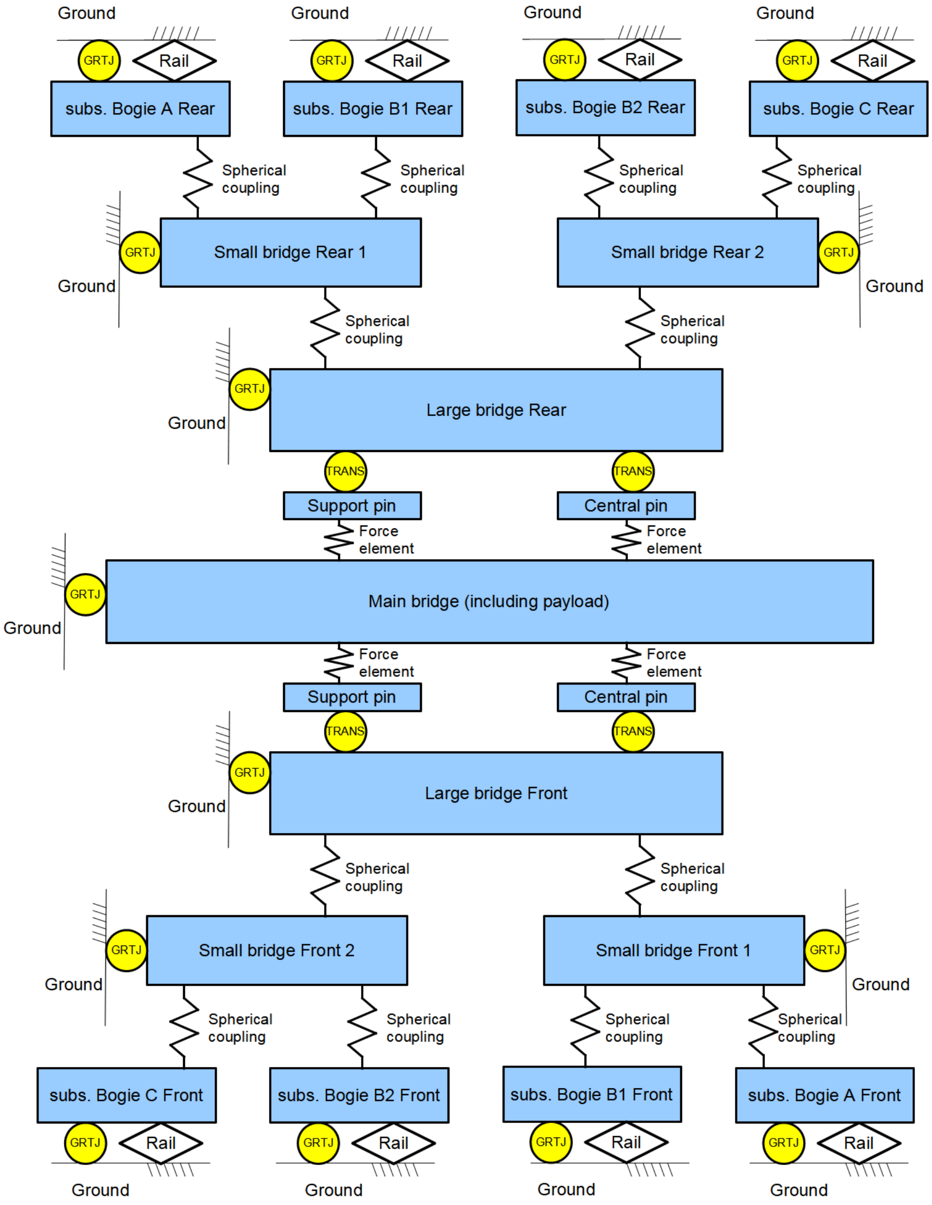

Fig. 3. Kinematical scheme of the wagon multibody model

repeated in the model, could be set as substructures. There are bogie substructures, composed of a rigid body representing a bogie frame and four wheelset substructures. The bogie frame and wheelset bearings are connected by force elements representing leaf springs [3]. Each wheelset substructure contains the wheelset represented by one rigid body with six degrees of freedom and coupled with the ground (basic frame) by so-called General Rail Track joint (GRTJ) related to a defined track. The interaction of wheels and rails is ensured by a complex rail-wheel force element, which represents spatial forces and torques between the wheel and the rail depending on the wheel-rail design parameters and model kinematical variables.

Each two bogies are mutually joined with one small bridge (as it was already mentioned, 4 small bridges in total). The bogies and the bridge are connected using bushing force elements, that substitute real spherical joints. Analogously, each two small bridges are mutually joined with one large bridge (as it was already mentioned, 2 large bridges in total). The last mentioned design element of the wagon is the main bridge carrying possible a payload. The connection of the main bridge and the large bridges is realized using movable support and central pins.

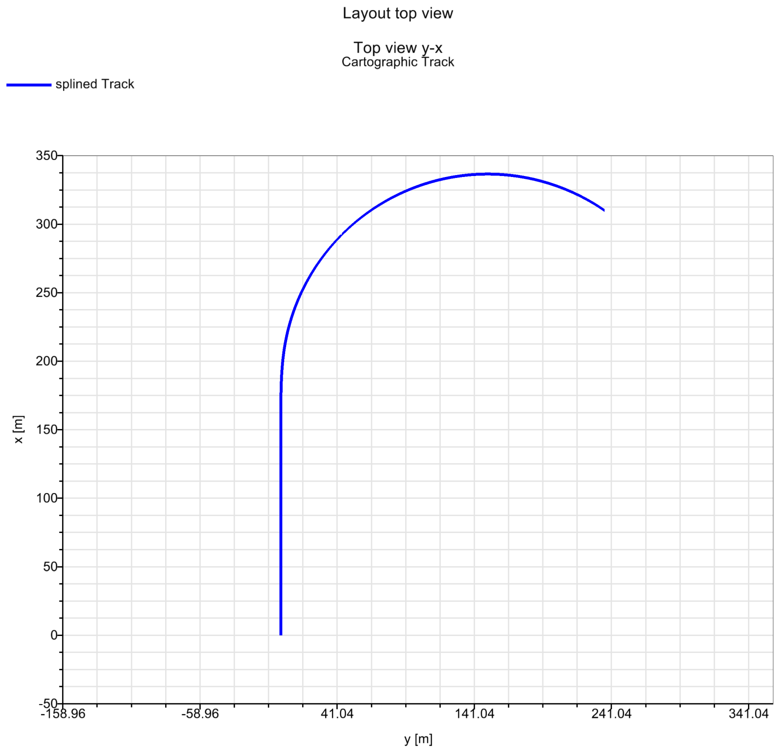

Fig. 4. Twisted track definition — top view

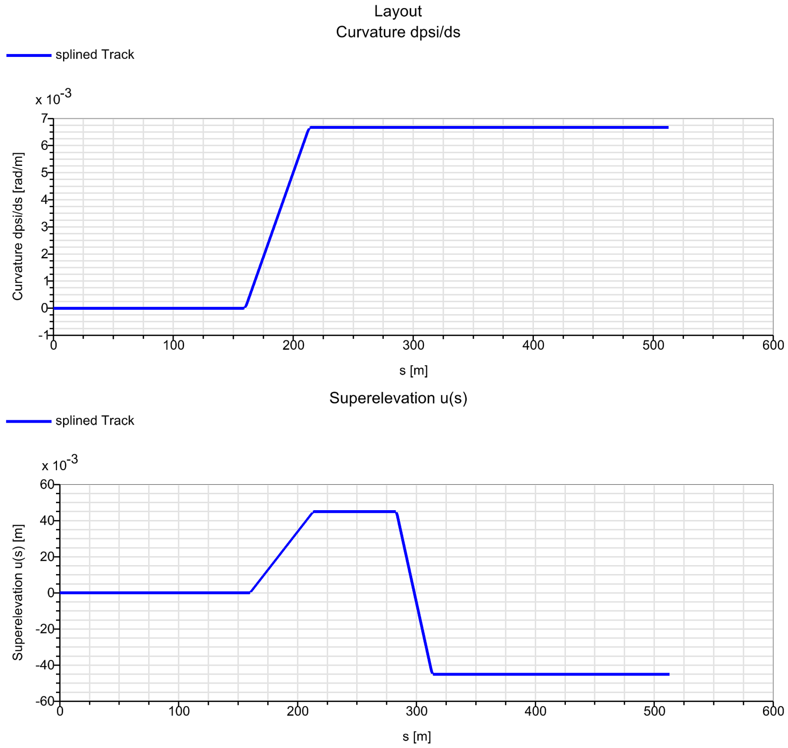

Fig. 5. Twisted track definition — curvature and superelevation

Fig. 6. Time history of the wheel lift on the leading wheelset when running through the twisted track

The computational multibody model of the wagon was implemented to perform various numerical simulations prescribed in railway standards. The main code utilized for railway vehicles is EN 14363 standard ”Railway applications – Testing and simulation for the acceptance of running characteristics of railway vehicles – Running behaviour and stationary tests” [1]. At first, the running of the wagon on a straight track by various velocities was numerically simulated. It was followed by linearized modal analysis to investigate stability properties. The extensive set of numerical simulations was dedicated to running on tracks with prescribed curvature and given velocity. All tests were evaluated based on the standard using derailment coefficient and wheel lateral forces. EN 14363 standard prescribes three possible methods [4] how to evaluate the safety against derailment for railway vehicles running on a twisted track. Method 1 from the standard was chosen as the evaluation method. It is based on the vehicle slowly running on a twisted track with a 150 m radius (see Figs. 4 and 5), while the assessment criterion is the outer wheel lift of the leading wheelset which has to be under 5 mm (see Fig. 6 for illustrative results).

Acknowledgement

The paper originated in the framework of institutional support for the long-time conception development of the research institution provided by Ministry of Industry and Trade of the Czech Republic.

References

[1] EN 14363:2016+A1: Railway applications – Testing and simulation for the acceptance of running characteristics of railway vehicles – Running behaviour and stationary tests, European Standard, CEN, December 2018.

[2] Iwnicki, S., Handbook of railway vehicle dynamics, CRC Press, Boca Raton, 2006.

[3] Polach, P., Hajžman, M., Computer simulations of the freight wagon laboratory excitation, Mechanics Based Design of Structures and Machines 39 (2) (2011) 194-209.

[4] Wilson, N., Fries, R., Witte, M., Haigermoser, A., Wrang, M., Evans, J., Orlova, A., Assessment of safety against derailment using simulations and vehicle acceptance tests: A worldwide comparison of state-of-the-art assessment methods, Vehicle System Dynamics 49 (7) (2011) 1113-1157.

COMPUTATIONAL MECHANICS 2022
37th conference with international participation
Srní
November 7 - 9, 2022

Non-uniform quaternion spline interpolation in vehicle kinematics

V. Houdek[a,b], O. Verlinden[b], M. Hajžman[a]

[a] *Faculty of Applied Sciences, University of West Bohemia, Univerzitní 8, 301 00 Plzeň, Czech Republic*
[b] *Theoretical Mechanics, Dynamics and Vibration, University of Mons, Mons, Belgium 7000*

Interpolation plays an important role in nowadays world. By interpolating data, we save time and money in general. The main areas where interpolation is applied are robotics, automotive, medicine, biology etc. One of the possible basis splines for interpolation are B-splines, which are also used in Computer Aided Geometric Design (CAGD) due to their smoothness and locality properties [5]. To fit a curve to a given set of points, B-spline can be used either in interpolation or in approximation [5]. In this work we consider the application of B-splines (cumulative) for the non-uniform interpolation of quaternions. This requires to overcome some difficulties. Firstly it is necessary to compute control points (sometimes called de Boor points [4]) to fulfil the basic interpolation property. Second problem is hidden in non-uniformity of data points as formulas available for quaternion spline interpolation generally consider uniformly distributed points [4]. The last problem lies in discretization: to achieve desired maximum error of the interpolation we have to choose the proper density of interpolation points.

B-spline is a spline function driven by an independent parameter that will be denoted here by t which usually varies from $t = T_0$ to $t = T_n$, with $\mathbf{T}$ the knot vector (T_0,..., T_n) and n positive integers. The associated B-splines B_i^k of order k (degree = $k-1$) are defined by [4]

$$B_i^1(t) \;= \begin{cases} 1 & T_i \le t \le T_{i+1}, \\ 0 & \text{otherwise} \end{cases} \tag{1}$$

for $k = 1$ and

$$B_i^k(t) \;= \tfrac{t-T_i}{T_{i+k-1}-T_i} B_i^{k-1}(t) + \tfrac{T_{i+k}-t}{T_{i+k}-t_{i+1}} B_{i+1}^{k-1}(t), \;\; k > 1 \text{ and } i = 0, 1, ..., n. \tag{2}$$

We can now define B-spline curve [3]. With a given list of control points (also called de Boor points), $p_i \in R^m$ ($m \ge 1$), $0 \le i \le n$, and a knot vector $\mathbf{T}$, then B-spline interpolation of order k (degree $k-1$) is defined by

$$P(t) = \sum_{i=0}^{n} p_i B_i^k(t) \qquad \text{for } T_0 \le t < T_n. \tag{3}$$

With a given list of data points $P_i \in R^m$, $0 \le i \le n$, corresponding with the knot vector $\mathbf{T}$, we can proceed with the B-spline interpolation of order k. First we need to compute control points so that we ensure

$$P(T_i) = P_i, \tag{4}$$

which can be rewritten into the form

$$p_0 B_0^k(T_i) + p_1 B_1^k(T_i) + ... + p_n B_n^k(T_i) = P_i, \qquad 0 \leq i \leq n. \tag{5}$$

This can be rewritten [5] into condensed matrix form for all rows

$$\mathbf{A}\mathbf{p} = \mathbf{P}, \tag{6}$$

where

$$\mathbf{A} = \begin{pmatrix} B_0^k(T_0) & B_1^k(T_0) & \dots & B_n^k(T_0) \\ B_0^k(T_1) & B_1^k(T_1) & \dots & B_n^k(T_1) \\ \vdots & \vdots & \vdots & \vdots \\ B_0^k(T_n) & B_1^k(T_n) & \dots & B_n^k(T_n) \end{pmatrix}, \text{ where } \begin{cases} \mathbf{p} = [p_0, p_1, ..., p_n]^T, \\ \mathbf{P} = [P_0, P_1, ..., P_n]^T. \end{cases} \tag{7}$$

With respect to the previous definitions we can define B-spline quaternion interpolation of order 4 ($k = 4$, degree = 3), so that we achieve C^2 continuity. We consider unit quaternion definition given by [2] in this work. With a given sequence of data points (data unit quaternions) Q_i (i = 0, 1,...,n), the interpolation can be proceeded by constructing the B-spline quaternion curve $Q(t)$ which interpolates a given sequence of unit quaternions Q_i (i = 0, 1,...,n). The B-spline quaternion curve is defined as

$$Q(t) = q_{-1}^{\tilde{B}_0(t)} \prod_{i=0}^{n+1} (q_{i-1}^{-1} q_i)^{\tilde{B}_i(t)}, \qquad \tilde{B}_i(t) = \sum_{j=i}^{n+1} B_i(t), \tag{8}$$

where q_i are control points ('control quaternions') and $B_i(t) \equiv B_i^4(t)$. To compute the control points from non-uniform knot vector, we have to start with the condition $Q(T_i) = Q_i$, so we get

$$\begin{aligned} & q_0^{\tilde{B}_0(T_i)} (q_0^{-1} q_1)^{\tilde{B}_1(T_i)} (q_1^{-1} q_2)^{\tilde{B}_2(T_i)} ... (q_{i-2}^{-1} q_{i-1})^{\tilde{B}_{i-1}(T_i)} ... \\ & (q_{i-1}^{-1} q_i)^{\tilde{B}_i(T_i)} (q_i^{-1} q_{i+1})^{\tilde{B}_{i+1}(T_i)} (q_{i+1}^{-1} q_{i+2})^{\tilde{B}_{i+2}(T_i)} ... = Q_i. \end{aligned} \tag{9}$$

It holds that $\tilde{B}_x(T_i) = 1, 0 \leq x \leq i-1$ and $\tilde{B}_y(T_i) = 0, i+2 \leq y \leq n+1$, following this rule we get

$$q_0 (q_0^{-1} q_1)(q_1^{-1} q_2) ... (q_{i-2}^{-1} q_{i-1})(q_{i-1}^{-1} q_i)^{\tilde{B}_i(T_i)} (q_i^{-1} q_{i+1})^{\tilde{B}_{i+1}(T_i)} \cdot 1 = Q_i, \tag{10}$$

which can be rewritten as

$$q_{i-1} (q_{i-1}^{-1} q_i)^{\tilde{B}_i(T_i)} (q_i^{-1} q_{i+1})^{\tilde{B}_{i+1}(T_i)} = Q_i, \quad \text{for } i = 0, 1, 2, ..., n, \tag{11}$$

Note that for uniformly distributed knot vector $\mathbf{T}$, we can easily write

$$q_{i-1} (q_{i-1}^{-1} q_i)^{\frac{5}{6}} (q_i^{-1} q_{i+1})^{\frac{1}{6}} = Q_i. \tag{12}$$

Eq. (11) forms $n+1$ equations. Since the dominant term on the left side is $(q_{i-1}^{-1} q_i)^{\tilde{B}_i(t_i)}$ we can use the iterative refinement procedure for the solution from [3] as

$$(q_{i-1}^{-1} q_i)^{\tilde{B}_i(T_i)} = q_{i-1}^{-1} Q_i (q_i^{-1} q_{i+1})^{-\tilde{B}_{i+1}(T_i)}, \tag{13}$$

$$q_i^* = q_{i-1} (q_{i-1}^{-1} Q_i (q_i^{-1} q_{i+1})^{-\tilde{B}_{i+1}(T_i)})^{\frac{1}{\tilde{B}_i(T_i)}}, \tag{14}$$

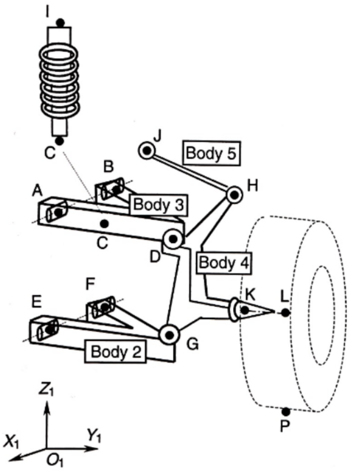

Fig. 1. Double wishbone suspension example [1]

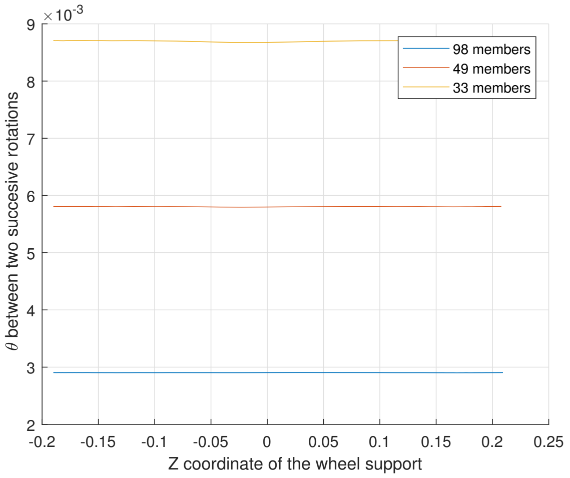

Fig. 2. Angle θ between two successive data points (Q_i and Q_{i+1})

which is the iterative solution of the system of equations, assuming q_i^* is a next iteration step of q_i. Already known formula for uniform B-splines is analogically given by [3]

$$q_i^* = q_{i-1}(q_{i-1}^{-1}Q_i(q_i^{-1}q_{i+1})^{-\frac{1}{6}})^{\frac{6}{5}}. \tag{15}$$

Because there are $n+1$ equations for $n+3$ unknowns q_{-1}, q_0,..., q_{n+1}, two boundary conditions are needed. The end conditions for natural spline are [3]

$$Q''(0) = 0 \quad \text{and} \quad Q''(n) = 0. \tag{16}$$

When these two boundary conditions are applied to previous equation, we obtain non-linear system of equations

$$\begin{aligned} q_{-1} &= Q_0(Q_0^{-1}Q_1)^{-1}, && (17)\\ q_{i-1}(q_{i-1}^{-1}q_i)^{\tilde{B}_i(T_i)}(q_i^{-1}q_{i+1})^{\tilde{B}_{i+1}(T_i)} &= Q_i, \quad \text{for } i = 0, 1, 2, ..., n, && (18)\\ q_{n+1} &= Q_n(Q_{n-1}^{-1}Q_n). && (19) \end{aligned}$$

As far as there is no other known method to compute the exact solution, the proposed iterative method, Eq. (14), is utilized to solve this system. For the initial guess, $q_i = Q_i$ is considered. However, due to the non-linearity of the problem, there are some restrictions for the input values of Q_i, but this is not the topic of this conference paper.

We interpolated the orientations of classical double wishbone suspension support (Fig. 1) in terms of vertical coordinate and we compared it with exact results. We chose the data so that we ensure almost constant angle θ (Fig. 2) between two successive data points (Q_i and Q_{i+1}), considering θ as an angle of axis-angle representation between two orientations. For the interpolation we used 3 different look-up tables which differed in number of data points:$n = 33$,$n = 49$ and $n = 98$ (see Fig. 2), these data were compared with the data set of 500 members, so that we can observe the interpolation error trend. The interpolation relative error was computed as the relative angle between the exact and the interpolated orientation and divided by the constant angle distance value (Fig. 2) and was denoted by θ_e. The results are shown in Fig. 3 and 4, the latter being a zoom of Fig. 3 on the vertical axis.

Figs. 3 and 4 show that we successfully achieved interpolation property, i.e., zero error at data points. The figures show that the highest interpolation error is at the beginning and at the

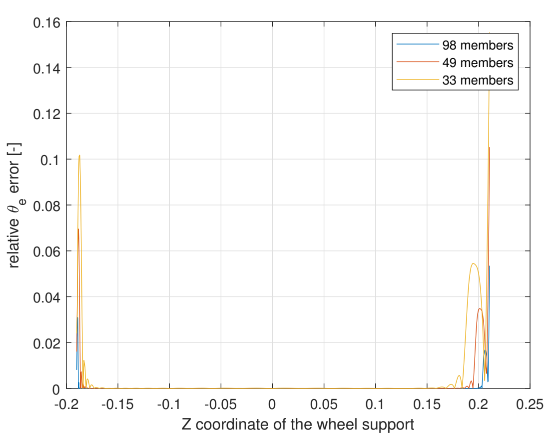

Fig. 3. Interpolation error θ [rad]

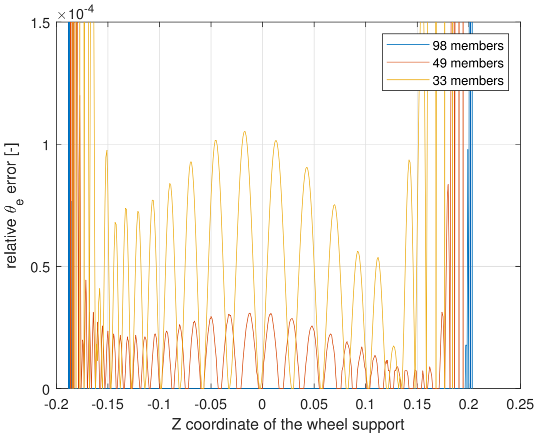

Fig. 4. Interpolation error – zoomed

end of the interpolated interval in our case. Whatever the number of interpolation points the highest interpolation error intervals are always given by the first and last k data points ($k = 4$ is the order of the interpolation). In case of high demand for low interpolation error at the beginning or at the end of the interpolated interval it is possible to add more data points at the beginning and at the end of the look-up table so that higher density of data points is ensured and the high interpolation error interval becomes smaller, or it is possible to change the boundary conditions. However, in practise it is not usual to achieve these end positions.

We can also see that the maximum interpolation error θ_e remains approximately constant inside the interpolated interval, which means that the main impact on the interpolation error has the development of angle θ between the two data points and the precision is not dependent on the relative axis development, considering the axis-angle representation. We can see that for 33 data points (members of look-up table) we achieved $\theta_e \approx 10^{-4}$, for 49 data points $\theta_e = 3 \times 10^{-5}$ and for 98 data points θ_e is equal to zero inside the interpolated interval. As far as the proposed interpolation fulfils C^2 continuity, we found formulas for the first and second derivative to be used for dynamics simulation of the suspension.

Acknowledgement

This research work was supported by the project SGS-2022-008.

References

[1] Bundell, M., Harty, D., Multibody systems approach to vehicle dynamics, Elsevier Butterworth-Heinemann, Oxford, 2004.

[2] Hamilton, W. R., Lectures on quaternions, Hodges and Smith, Dublin, 1853.

[3] Kim, M.-J., Kim M.-S., Shin S. Y., A C_2-continuous B-spline quaternion curve interpolating a given sequence of solid orientations, Proceedings of Computer Animation ’95, 1995, pp. 72-81

[4] Kim, M.-J., Kim, M.-S., Shin, S. Y., A general construction scheme for unit quaternion curves with simple high order derivatives, Proceedings of the 22nd annual conference on Computer Graphics and Interactive Techniques – SIGGRAPH ’95, New York, 1995, pp. 369-376.

[5] Lim, C.-G., A universal parametrization in B-spline curve and surface interpolation, Computer Aided Geometric Design 16 (5) (1999) 407-422.

COMPUTATIONAL MECHANICS 2022
37th conference with international participation
Srní
November 7 - 9, 2022

Optimization of a ducted-fan propulsion unit equipped with an internal combustion engine

T. Jánošík, F. Brož

Faculty of Mechanical Engineering, Czech Technical University Prague, Jugoslávských partyzánů 1580/3, 160 00 Prague 6 – Dejvice, Czech Republic

The idea of using a heat source for increasing the propulsion efficiency an airplane equipped with piston combustion engine first appeared just before the Second World War. F.W. Meredith [1] describes the mechanism of a radiator placed in a duct inside an airplane's structure and expresses the basic relations on the aerodynamic resistance of such a structure.

The issue was further processed by H. Winter [3]. In his article: Contribution to the theory of the heated duct radiator, the author derived simple equations allowing to quantify the drag reduction of a radiator due to additional heat with enough accuracy for practical application. Such a relationship is an expression of the law of conservation of energy, where the heat transferred from radiator to ambient air corresponds to engine power - from this relationship, the flow rate in the channels can be easily estimated. The equation is expressed as follows

$$\rho_0 v_1 F g \left[\left(i_2 + A\frac{v_2^2}{2g}\right) - \left(i_1 + A\frac{v_1^2}{2g}\right)\right] = Q,$$

where $i = \frac{\kappa}{\kappa-1} A \frac{p}{g\rho}$ and $A = \frac{1}{427}\,\mathrm{kcal/mkg}$. The amount of heat can be taken as a fraction of the engine power $Q = A \propto 75N$ (for water cooled engines $\propto \approx 0{,}5$), i is internal energy and N is engine power [hp]. Indices 1 and 2 correspond to sections in front of, behind the radiator respectively, 0 at the entrance to the channel.

In a practical sense, the most famous aircraft using the heat from the radiator for thrust is probably the P-51 Mustang. However, the relevant publication was not available at the time of writing this post.

However, the Me-109E concept described in [2] is also interesting. Small radiators are at Me. 109E and I. 110 are located in each wing. Attached is a sketch of this structure near the trailing edge of the wing (Fig. 1). It includes a mechanism for controlling the outlet flap from the channel, with which it is possible to regulate the flow of the cooler with an increase in local losses in the nozzle ("throttling"), which is important in reducing aerodynamic resistance at higher speeds. The author also caused large potential losses caused by the boundary layer, which in this case is significantly developed, since the entrance is on the underside of the wing.

The cited articles are important in determining the methodology of this study and thesis. To quantify the contribution of residual heat to the reduction of aircraft drag, it is first necessary to describe the task analytically. The system of the following equations will serve the purpose:

1. The energy difference in front of and behind the radiator is equal to the delivered heat Q [W], which can be expressed as a fraction of the engine power

$$\dot{m}\left[\frac{p_1}{\rho_0} - \frac{p_2}{\rho_2} + \frac{1}{2}({v_1}^2 - {v_2}^2)\right] = Q\,.$$

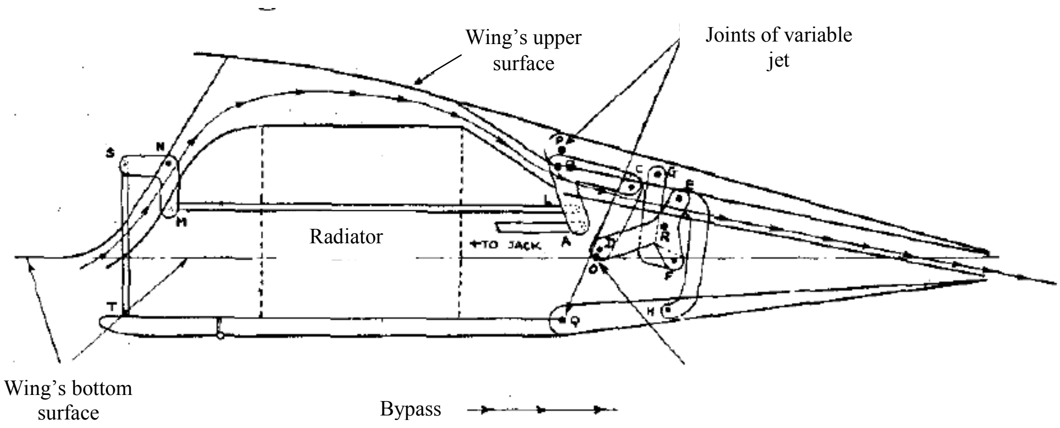

Fig. 1. Radiator duct of Me-109E

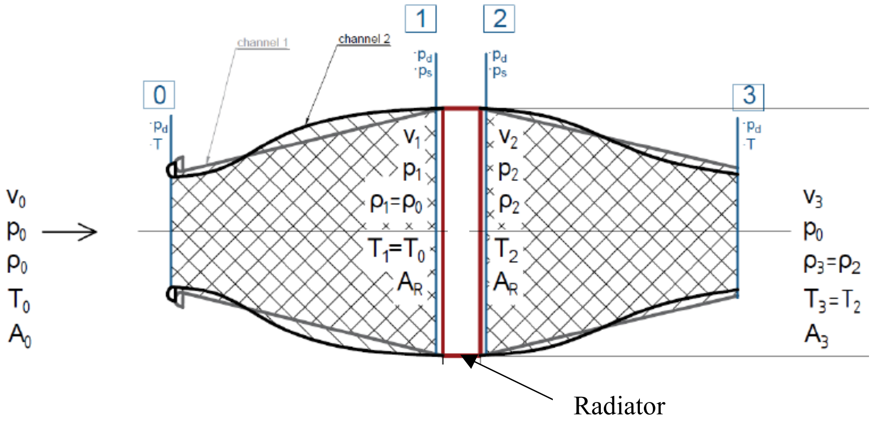

Fig. 2. Reference sections of radiator duct

2. The second important parameter is the pressure loss of the radiator Δp_c. Neglecting the supplied heat (we are talking about a so-called cold radiator), the pressure difference can be expressed by multiplying of the loss coefficient c_w and the dynamic pressure at the inlet to the radiator

$$\Delta p_c = p_1 - p_2 = \frac{\rho_0 {v_1}^2}{2} c_w \,.$$

3. When including the effect of supplied heat, this equation does not apply, because the change in dynamic pressure also plays a significant role here. The pressure loss of the "hot radiator" Δp_h is expressed as the difference of the dynamic pressures in front of and behind the radiator in the sum with $h \cdot c_w = c_{w_h}$ which is the loss coefficient of the hot radiator

$$\Delta p_h = p_1 - p_2 = \rho_2 {v_2}^2 - \rho_0 {v_1}^2 + h \cdot c_w \,.$$

The value of the coefficient h defines the dependence of the pressure loss of the cold and hot radiator. As part of the experiment, the goal is to obtain the value of this coefficient as a function of another known parameter (the literature refers *to* $\frac{1}{2}(\rho_2 {v_2}^2 - \rho_0 {v_1}^2)$, however this is not validated).

4. Remaining equations represent the application of the law of conservation of momentum and the equation of continuity between individual sections of the channel.

$$p_1 - p_0 = \eta_{Di}\frac{\rho_0}{2}({v_1}^2 - {v_0}^2)\,, \qquad \eta_{Di} - \text{ diffuser efficiency}\,,$$

$$p_2 = p_0 + \frac{1}{2}\rho_2 {v_2}^2(\beta^2 - 1)\,, \qquad \beta - \text{ section ratio } \mathrm{A_R}/\,\mathrm{A_0}\,,$$

$$\rho_0 v_1 = \rho_2 v_2\,.$$

The output of the system of these equations is $v_2 = f\,(\rho_0;\, p_0;\, v_0;\, Q;\, c_w;\, \beta;\, \eta_{Di})$. Result can be expressed as decrease in the internal drag of a heated radiator in comparison with the unheated condition as the Function of duct opening ratio *A3/AR* (Fig. 3).

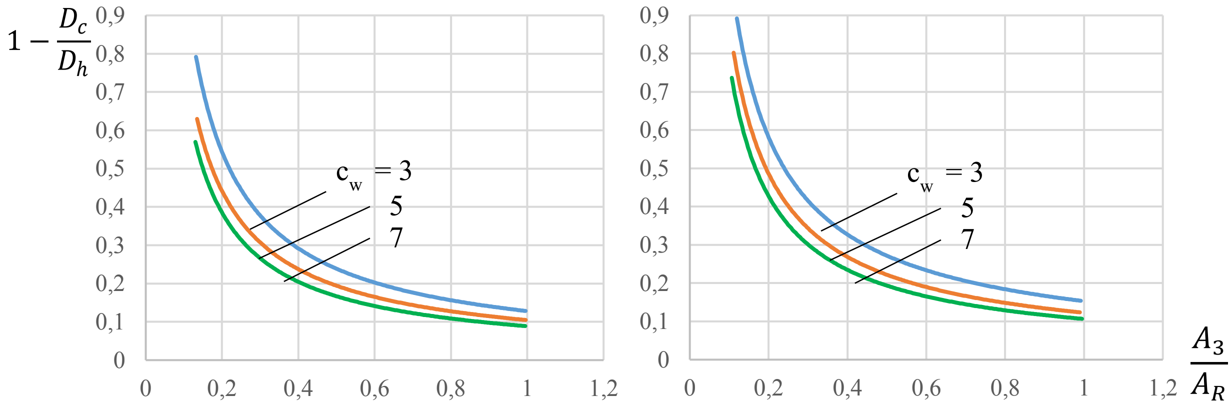

Fig. 3. Decrease in the internal drag of a heated radiator in comparison with the unheated condition as the function of duct opening ratio *A3/AR*

The results of this study were used for designing the flow path of the propulsion unit of the UL-39[1] aircraft developed under the auspices of the Faculty of Mechanical Engineering of the Czech Technical University. Main goal was to optimize the existing structure in order to maximize the efficiency of the drive unit. Inlet part of the unit will be described. The goal was to create an inlet channel with the lowest possible losses and the most uniform flow field on the outlet cross-section (blower inlet).

First, a simulation of the entire aircraft was carried out with the old variant of the drive. The boundary conditions at the inlet were taken from it for further calculations. Furthermore, a multi-criteria optimization was carried out using the adjoint in Fluent, with the help of which a significant improvement was achieved in terms of pressure losses in the channels.

Fig. 4. UL-39 Albi

---

[1] The UL-39 Albi is a Czech project of a world-unique ultralight two-seater aircraft, built according to the model of the L-39 Albatros jet training aircraft. It is the only ultralight in which the engine does not drive the propeller, but the blower. The development version of the aircraft took off for the first time on April 4, 2016 at the airport in České Budějovice.

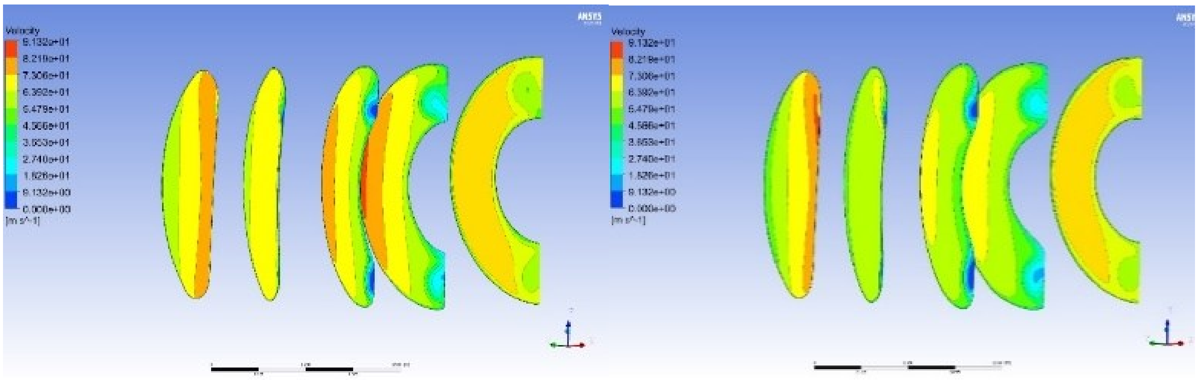

Fig. 5. CFD Analysis of inlet channel of UL-39 Albi

Table 1. Results of CFD analysis of inlet channel - total pressure loss refering to improvement

Velocity [m/s]	Standard deviation of axial velocity	Uniformity index of axial velocity	Total pressure loss	Averange magnitude of tangential velocity
75	4,48%	0,68%	**11,81%**	-1,17%
70	5,46%	0,76%	**15,39%**	-0,67%
55	7,58%	0,91%	**23,96%**	3,92%
40	7,91%	0,95%	**30,78%**	5,82%
25	2,55%	-1,26%	**12,90%**	2,15%

Acknowledgements

The work has been supported by the grant project “Optimization of a ducted-fan propulsion unit equipped with a internal combustion engine”.

References

[1] Meredith, F. W., Cooling of aircraft engines with special reference to ethylene glycol radiators enclosed in ducts, Aeronautical Research Commitee Reports and Memoranda 1683 (1935). Available: http://naca.central.cranfield.ac.uk/reports/arc/rm/1683.pdf

[2] Morgan, M. B., Smelt, R., Aerodynamic features of german aircraft, The Journal of the Royal Aeronautical Society 48 (404) (1944) 271-331.

[3] Winter, H., Contribution to the theory of the heated duct radiator, Technical Memorandums. National Advisory Committee for Aeronautics, Washington, 1939. Available: https://ntrs.nasa.gov/citations/19930094523

COMPUTATIONAL MECHANICS 2022
37th conference with international participation
Srní
November 7 - 9, 2022

Post-processing the results of the topology optimization with the level-set technique

O. Ježek[a,b], J. Kopačka[b], D. Gabriel[b]

[a] *Faculty of Mechanical Engineering, Czech Technical University in Prague, Technická 4, 160 00 Prague 6, Czech Republic*
[b] *Institute of Thermomechanics, Czech Academy of Sciences, Dolejškova 1402/5, 182 00 Prague 6, Czech Republic*

1. Introduction

Topology optimization (TO) is a popular method for designing innovative components. Its goal is to find the optimal material distribution in the design space based on predefined boundary conditions and constraints. TO is most commonly used in the conceptual phase of the design process. However, with the development of additive technology and post-processing methods, the possibilities of using TO results directly for manufacturing are beginning to emerge.

The seminal paper that laid the foundations for the development of topology optimization is considered to be the work of Bendsøe *et al.* [1]. Since then, the development of TO has taken several directions, and nowadays, many different methods can be found in the literature. An overview of known TO methods can be found, e.g., in the review article [2]. Nevertheless, the most common TO approaches are density-based, especially the SIMP method, which stands for Solid Isotropic Material with Penalization. This method's results are unsuitable directly for manufacturing, so post-processing is required.

In this paper, the optimization problem of minimizing compliance with a constraint on the volume fraction will be formulated first. Then the SIMP method will be introduced. This paper's main contribution lies in using the level-set principle combined with RBF for post-processing the results obtained by the SIMP method. In the final part, the proposed method for post-processing of the topologically optimized gripper of an industrial robot will be applied.

2. Compliance minimization problem

A typical topology optimization problem is to find a maximally stiff structure with respect to its loads and supports. The constraint is the volume fraction, i.e., a certain ratio between the volume of the structure and the volume of the design domain in which the optimization is performed. Such a problem can be described by minimizing an objective function c (twice the strain energy) with a constraint on the volume fraction f, i.e.,

$$\begin{aligned} \min_{\rho} : \quad & c(\rho) = \mathbf{U}^T \mathbf{K} \mathbf{U} = \sum_{e=1}^{N} E_e(\rho_e) \mathbf{u}_e^T \mathbf{k}_0 \mathbf{u}_e \\ \text{subjected to :} \quad & V(\rho)/V_0 = f, \\ & 0 \leq \rho \leq 1, \end{aligned} \tag{1}$$

where $\mathbf{U}$ is the global displacement vector, $\mathbf{F}$ is the global stiffness matrix, $\mathbf{u}_e$ is the displacement vector of the element, $\mathbf{k}_0$ is the stiffness matrix of the element with the corresponding

Young's modulus E_e, N indicates the total number of elements, $V(\rho)$ is the current volume of the material, and V_0 is the volume of the design domain.

2.1 Modified SIMP method

The SIMP method belongs to the class of *Density-based* methods and is one of the most used in TO. It employs finite elements to describe the shape, assigning each element a kind of importance known as fictitious density. This fictitious density (design variable) is used to calculate Young's modulus $E_e(\rho_e)$ of each element.

The result of the SIMP method is a scalar field of fictitious densities ρ, where each element is assigned a constant fictitious density ρ_e. This result can be used by the designer to get a basic idea of the shape of the part but cannot be used directly for manufacturing. Post-processing is required to obtain the shape from the TO results. In the case of 2D objects, post-processing can be done by simple sketching in CAD software. For more complex solids, it is necessary to use automated techniques.

3. Post-processing the results with the level-set technique

TO has become integral to many finite element systems and even some CAD programs. These systems usually use *Density-based* methods to obtain the optimal material distribution. The main advantage of these methods is their robustness. However, the results are highly dependent on the quality of the mesh, the filter parameters, and the post-processing type. Conventional post-processing methods average the element densities into nodal values and consequently interpolate them, most frequently with linear polynomials. It yields only C^0 continuous geometry, which is usually unsuitable for downstream processing. Some software uses B-spline curve segments to smooth the geometry, but here the results are of much higher quality. Unfortunately, all available software offers little or no user customization in terms of post-processing.

This section proposes two approaches to construct the level-set (LS) function. Both approaches use radial basis functions (RBFs) to construct the level-set function. RBFs are suitable for post-processing due to their ability to smooth the geometry but still preserve the shape complexity of the optimized shape [3].

3.1 Density in nodes approach

This post-processing approach uses RBFs to construct a LS function. RBFs can only be used in nodes of a regular grid. If the optimization has been performed on an irregular mesh, the entire design space must be packed into a so-called bounding box and this space discretized with a regular grid. The procedure for computing the node densities of a regular grid is as follows. First, the density at the nodes of the original grid has to be computed. This can be done by taking the continuous density in the elements to the geometric center of the elements and then using the least squares method to compute the density at the nodes. Subsequently, the density at the nodes of the regular grid can be calculated using shape functions. By placing the RBFs (2) in the nodes of the regular network with appropriate weights so that the sum of these functions at the nodes of the regular network corresponds to the nodal values, we obtain an implicit LS function. The zero level of this function corresponds to the geometry of the shape.

$$N_i(x) = exp\left[-\left(\frac{\|x - x_i\|}{B}\right)^2\right] \tag{2}$$

The described approach has been tested on a gripper of an industrial robot. From the results shown in Fig. 1, it can be seen that this method gives smooth results, but has the characteristics

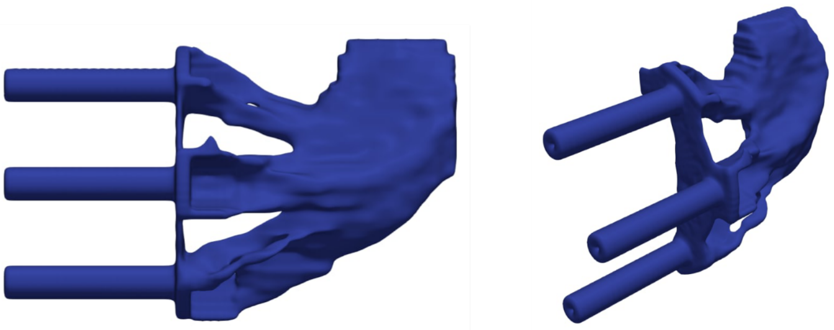

Fig. 1. Post-processing result of the topologically optimized gripper of an industrial robot

of a filter, i.e., it ”blurs” the shape complexity of the component in places where there is a step change in the TO results between empty and full space.

3.2 Approach based on signed distance function

Another approach for post-processing is based on a signed distance function. This function assigns to each point in the control area the shortest distance to the boundary of the solid, including a sign, so it is possible to distinguish whether the point is inside or outside the solid. To construct a discrete form of the distance function, the density field was nested in a regular Cartesian grid, and for each vertex of this grid, the closest point to the boundary of the solid was found. The density isocontour defines the boundary of the solid. This threshold density boundary was computed to respect the volume fraction. The distance field was used as a weighting factor for RBFs to construct the LS function. The zero level of the implicit LS function corresponds to the geometry boundary.

The approach has been tested on a 3D beam. From the results in Fig. 2, it can be seen that a very smooth geometry was achieved, and no complications in the boundary regions.

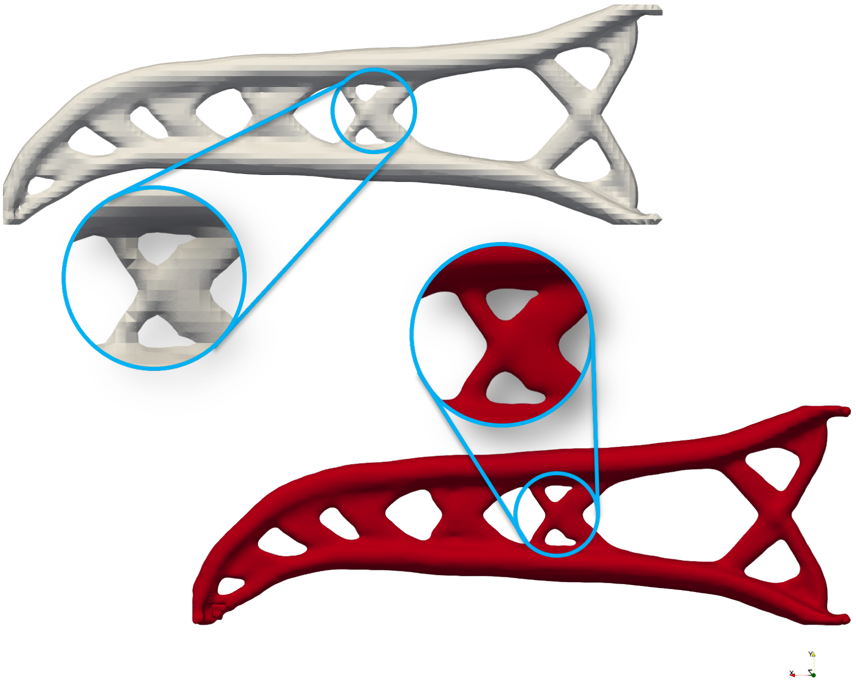

Fig. 2. Example of 3D beam test geometry. Above is the original C^0 continuous geometry and below is the smoothed shape

4. Conclusions

The last part of the paper describes two post-processing procedures using the LS method. The construction of the LS function itself was performed using Radial Basis Functions. The first approach uses the nodal densities as weights of the RBFs, while the second obtain these weights from the distance field. The results from the first approach are very smooth. However, there is a blurring of shape complexity at the points of sharp transition between the elements of the original mesh and the empty space (i.e., high-density elements and empty space). The second post-processing approach seems to be more appropriate because of its ability to describe even shape-complex objects. This capability to describe shape is due to the density of the control region discretization.

Acknowledgements

The work was supported by the Technology Agency of the Czech Republic under grant No TN01000024/08 (National Competence Center-Cybernetics and Artificial Intelligence) – sub-project "Automation and production system optimization" within institutional support RVO:61388998 and by the Grant Agency of the Czech Technical University in Prague, under grant No. SGS21/151/OHK2/3T/12.

References

[1] Bendsøe, M. P., Kikuchi, N., Generating optimal topologies in structural design using a homogenization method, Computer Methods in Applied Mechanics and Engineering 71 (2) (1988) 197-224.

[2] Sigmund, O., Maute, K., Topology optimization approaches: A comparative review, Structural and Multidisciplinary Optimization 48 (2013) 1031-1055.

[3] Swierstra M. K., Post-processing of topology optimized results: A method for retrieving smooth and crisp geometries, Master thesis, Delft University of Technology, 2017.

COMPUTATIONAL MECHANICS 2022
37th conference with international participation
Srní
November 7 - 9, 2022

The comparison of real gas and ideal gas models for compressor design

J. Klesa[a], M. Fukuchi[b]

[a] Faculty of Mechanical Engineering, Czech Technical University, Karlovo náměstí 13, 121 35 Praha, Czech Republic
[b] SIGMA Clermont, 20 avenue Blaise Pascal, 63178 Aubière, France

1. Introduction

This paper is focused on the comparison of the real and ideal gas models for the case of the compressor for the secondary cooling circuit for gas-cooled nuclear reactor developed in the frame of KOBRA project. Real gas model is defined by polynomial model from Baehr and Schwier [1]. Both models are compared and used for the stage design of the axial compressor. The comparison is performed for the case of the isentropic compression corresponding to the parameters of the KOBRA compressor for the secondary cooling circuit. The dependence of the real gas parameters on the temperature is presented and relative error in comparison with the ideal gas model is determined.

2. Methods

Following functions were programmed in the MATLAB environment with the mathematical model from [1]:

- $h\left(T, v\right)$,
- $s\left(T, v\right)$,
- $c_p\left(T, v\right)$,
- $c_v\left(T, v\right)$,
- $p\left(T, v\right)$,
- $v\left(T, p\right)$,
- $T\left(p, v\right)$,

where h [J.kg^{-1}] is the enthalpy, T [K] is the temperature, v [m^3.kg^{-1}] is the specific volume, s [J.K^{-1}] is the entropy, c_p [J.kg^{-1}.K^{-1}] is the specific heat capacity at constant pressure, c_v [J.kg^{-1}.K^{-1}] is the specific heat capacity at constant volume and p [Pa] is the pressure. The accuracy of these functions was tested, see [2]. These functions are used as the base for the other functions needed. Following functions are needed for the case of the isentropic compression:

- $T\left(p, s\right)$,
- $v\left(p, s\right)$,

- $h(p, s)$,
- $c_p(p, s)$,
- $c_v(p, s)$,
- $\kappa(p, s) = \frac{c_p}{c_v}$,
- $r(p, s) = c_p - c_v$,

where r [J.kg^{-1}.K^{-1}] is the specific gas constant and κ [$-$] is the isentropic coefficient, i.e., c_p/c_v. An iterative numerical approach is used for the calculation of all these variables. The Newton-Rapson method is used, ideal gas values are used as the initial guess. Ideal gas and real gas results are compared for the case of isentropic compression both for the single stage (i.e., the first compressor stage) and the whole compressor. Basic parameters for both cases are in Table 1.

Table 1. Compressor parameters

parameter	compressor	the first stage
input pressure p_1 [MPa]	7.5	7.5
input total temperature T_1 [K]	333.15	333.15
pressure ratio Π [$-$]	3	1.246
number of stages	5	1

3. Results

Dependence of real gas parameters on the pressure are presented for the case of the KOBRA secondary cooling circuit compressor, i.e., the specific gas constant r in Fig. 1, the isentropic coefficient (ratio of specific heats) κ in Fig. 2, the heat capacity at constant pressure c_p in Fig. 3 and the heat capacity at constant volume c_v in Fig. 4.

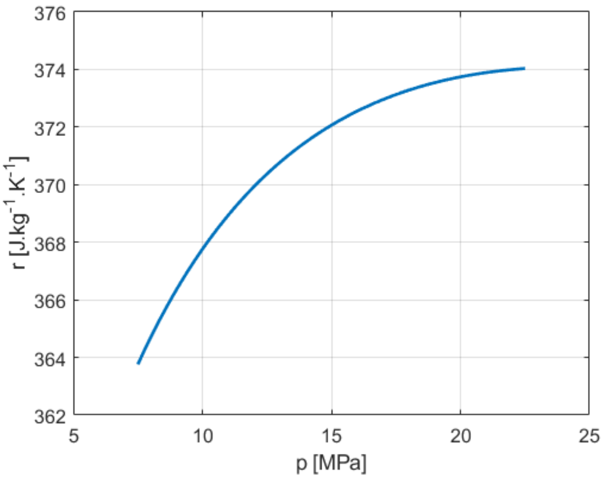

Fig. 1. Specific gas constant r constant on pressure p for the KOBRA compressor

Comparison of the results for the real and ideal gas ($r = 287$ J.kg^{-1}.K^{-1}, $\kappa = 1.4$) are presented in following tables for the case of the whole compressor (see Table 2) and for the single stage (see Table 3). Ideal gas values are used as reference for the computation of the relative error.

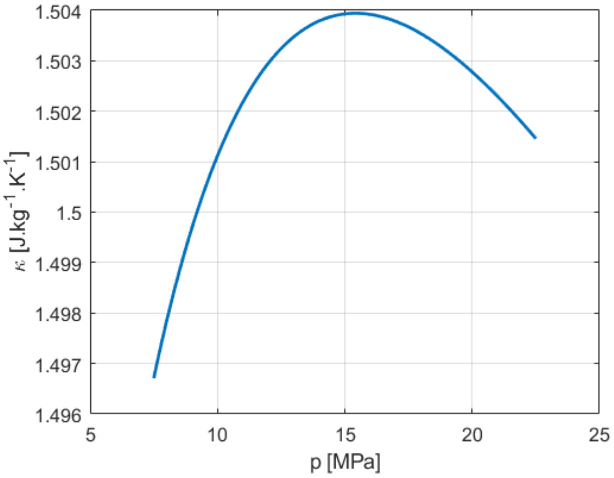

Fig. 2. Isentropic coefficient κ constant on pressure p for the KOBRA compressor

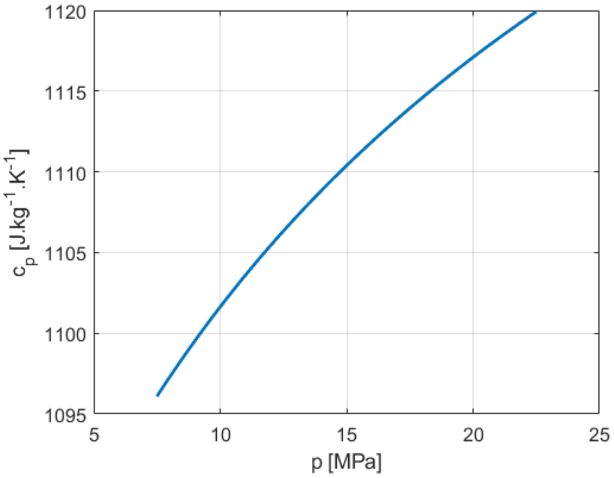

Fig. 3. Specific heat capacity at constant pressure c_p constant on pressure p for the KOBRA compressor

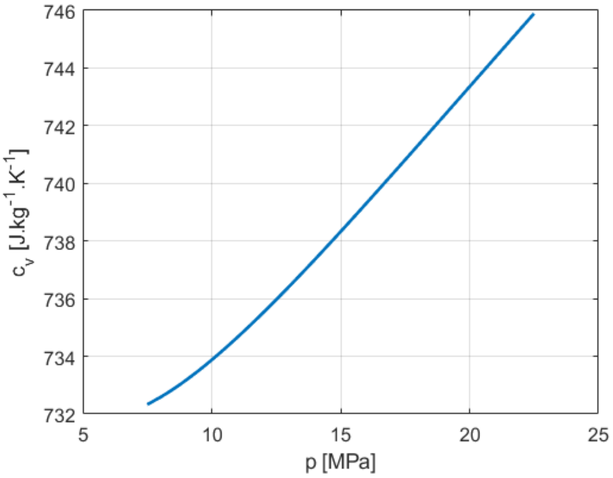

Fig. 4. Specific heat capacity at constant volume c_v constant on pressure p for the KOBRA compressor

Table 2. Comparison real vs. ideal gas for the compressor outlet

parameter	real gas	ideal gas	relative error [%]
T_2 [K]	459.099	455.995	0.68
v_2 [m^3.kg^{-1}]	0.0064	0.0058	10.02
Δh [kJ.kg^{-1}]	129.656	123.398	5.07

Table 3. Comparison real vs. ideal gas for the first stage outlet

parameter	real gas	ideal gas	relative error [%]
T_2 [K]	355.3521	354.757	0.17
v_2 [m^3.kg^{-1}]	0.0111	0.0110	1.36
Δh [kJ.kg^{-1}]	21.960	21.704	1.18

4. Conclusions and future Work

The comparison of the ideal and the real gas models based on the work of Baehr and Schwier [1] is presented for the case of the compressor for the secondary cooling circuit of the KOBRA project. It is shown that the gas parameters change quite strongly with the pressure for this case. The results will be used for the improvement of the compressor design and possibly also for the implementation to the CFD simulation model.

Acknowledgement

This work was supported by the Technology Agency of the Czech Republic, project TK03030121 Conceptual Design of an Innovative Safety System for Gas-cooled Nuclear Reactors.

References

[1] Baehr, H. D., Schwier, K., The thermodynamic properties of air, Springer, Berlin – Göttingen – Heidelberg, 1961. (in German)

[2] Fukuchi, M.,Thermodynamic air modelling, internship report, 2022.

COMPUTATIONAL MECHANICS 2022
37th conference with international participation
Srní
November 7 - 9, 2022

Compressor cascade total pressure loss correlation modelling at design points using artificial neural networks

P. Kovář, J. Fürst

Faculty of Mechanical Engineering, Czech Technical University, Karlovo náměstí 13, 121 35 Praha 2, Czech Republic

1. Introduction

The analysis of the flows by computational fluid dynamics becomes useful design and optimization method during recent years. Despite the advances in the computational power but it could be still very demanding. Therefore empirical models are commonly used as a main tool for design and prediction of basic performance of axial compressor cascades [1]. The empirical correlations are derived from experimental data obtained from two-dimensional measurements. Unfortunately, sufficient amount of data is available only in cases of well-known airfoils as e.g. NACA 65-series or C.4 profiles. Thus, there is en effort to find a similar relation which will serve in the same manner for another family of the airfoils.

Classical profiles as NACA 65-series and C.4 circular-arc are suitable in case of low Mach number corresponding to subsonic flows. Double-circular arc (DCA) and multi-circular arc (MCA) profiles perform well when the flow is accelerated to high subsonic, transonic even to low supersonic velocities [1]. Controlled diffusion (CD) airfoils are designed and optimized specifically for subsonic and transonic cascade applications, thus they can provide better performance than DCA or MCA profiles. The shape construction employs the concept of shaping the blade beyond the point of peak suction of the surface velocity such that the diffusion rate and associated suction boundary layer results in minimum loss for the airfoil section [6] resulting in relatively tight range of acceptable incidence angles [1].

In some complex engineering applications, e.g., nuclear reactor cooling by an axial compressor as a part of the secondary system, it is necessary to ensure reliable operation of the device when off-design conditions occur. Based on desired pressure distribution on the blade surface, camber line of the profile together with thickness distribution are established as described in [4]. A new airfoil family should outperforms NACA 65-series and it should offer performance comparable with the CD airfoils. Furthermore, the range of acceptable incidences should be much wider.

Flow analysis by means of computational fluid dynamics (CFD) could be still very demanding, thus empirical correlations are commonly used as a tool for design and prediction of axial compressor cascade performance. This contribution aims to searching correlation model for design points of the new airfoils family in order to accelerate the design of compressor cascade using artificial neural network (ANN). In contrast to standard deep neural network, the proposed neural network is built using higher order neural units.

2. Objective statement

The basic objective of the empirical modelling process is to predict the fluid turning and total pressure loss for a compressor cascade. From experimental cascade data for NACA 65-series and C.4 circular-arc blades, Lieblein in [5] developed an empirical correlation for a pressure loss PL as a function of the equivalent diffusion factor D_{eq}

$$PL = \frac{\omega \cos \beta_2}{2\sigma} \left(\frac{W_1}{W_2} \right)^2 = 0.004 \left[1 + 3.1 \left(D_{eq} - 1 \right)^2 + 0.4 \left(D_{eq} - 1 \right)^8 \right], \tag{1}$$

where

$$D_{eq} = \left(\frac{W_{max}}{W_1} \right) \frac{W_1}{W_2} = \left(1.12 + 0.61 \frac{\cos^2 \beta_1}{\sigma} \left(\tan \beta_1 - \tan \beta_2 \right) \right) \frac{W_1}{W_2}. \tag{2}$$

As it can be seen in equations above, the dependence between total pressure loss, cascade solidity σ and parameters of the flow is strongly non-linear that is a suitable task for ANN.

3. Methodology

From a mathematical point of view, processing of the information within neuron is consisted of two separated mathematical operations [2]. The first, synaptic operation contains weights of the synapse which represents storage of knowledge and thus the memory for previous knowledge. The second is somatic operation which provides various mathematical operations such as thresholding, non-linear activation, aggregation, etc. Neural output of the unit $\tilde{y}$ is then scalar as it is indicated in Fig. 1 (left) and expressed by the following equation

$$\tilde{y} = \sigma(s). \tag{3}$$

Let us assume N-th order neural unit, then product of synaptic operation can be written as [3]

$$s = w_0 x_0 + \sum_{i=1}^{n} w_i x_i + \sum_{i=1}^{n} \sum_{j=i}^{n} w_{ij} x_i x_j + \cdots + \sum_{i_1=1}^{n} \cdots \sum_{i_N=i_{N-1}}^{n} w_{i_1 i2 \ldots i_n} x_{i_1} x_{i_2} \ldots x_{i_n}, \tag{4}$$

where $x_0 = 1$ denotes threshold and n stands for length of input feature vector.

Since desired outputs are known, machine learning is called as supervised learning which is the task of learning a function that maps input to an output represented with cost function $\vec{\boldsymbol{e}}$. As we could see, the neural output is strongly dependent on the neural memories represented by vector of the weights $\overrightarrow{\boldsymbol{W}}$. Thus, processing of the information should be done in a way which leads neural unit to be learned. Batch Levenberg-Marquardt algorithm for weights updating [2] is employed in this work

$$\overrightarrow{\boldsymbol{W}} = \overrightarrow{\boldsymbol{W}} + \Delta \overrightarrow{\boldsymbol{W}}, \quad \Delta \overrightarrow{\boldsymbol{W}}^T = - \left(\overrightarrow{\overrightarrow{\boldsymbol{J}}}^T \overrightarrow{\overrightarrow{\boldsymbol{J}}} + \frac{1}{\mu} \overrightarrow{\overrightarrow{\boldsymbol{I}}} \right)^{-1} \overrightarrow{\overrightarrow{\boldsymbol{J}}}^T \vec{\boldsymbol{e}}. \tag{5}$$

Coefficient μ is learning rate, $\overrightarrow{\overrightarrow{\boldsymbol{I}}}$ is $n_w \times n_w$ identity matrix, n_w number of weights and $\overrightarrow{\overrightarrow{\boldsymbol{J}}}$ represents $n \times n_w$ Jacobian matrix.

Usually, training data set is divided into three subsets. The first, training set which serves for learning and weights updating. The second is validating set. After each epoch of learning algorithm, error estimation is performed on this subset in order to avoid neural unit overfitting. Training continues until validating error is increasing. Third part is called testing set which measures error after learning is terminated.

In order to obtain training data set for neural network and replace experimental measurement, various numerical simulations with different geometrical setups and inlet boundary conditions were performed. Design incidence angle was found through number of simulations as the flow angle with minimum pressure loss as described in [1].

Designed neural network is consisted of two neurons in the first layer and single neuron in the output layer as it can be seen in Fig. 1 (right). Synaptic operation of all neurons was assumed as quadratic polynomial in the designed ANN. As the activation function $\sigma(\cdot)$, bipolar sigmoid was used in the first layer and linear one in the output layer. Error propagation through the network is performed using multilayer backpropagation algorithm described in [3].

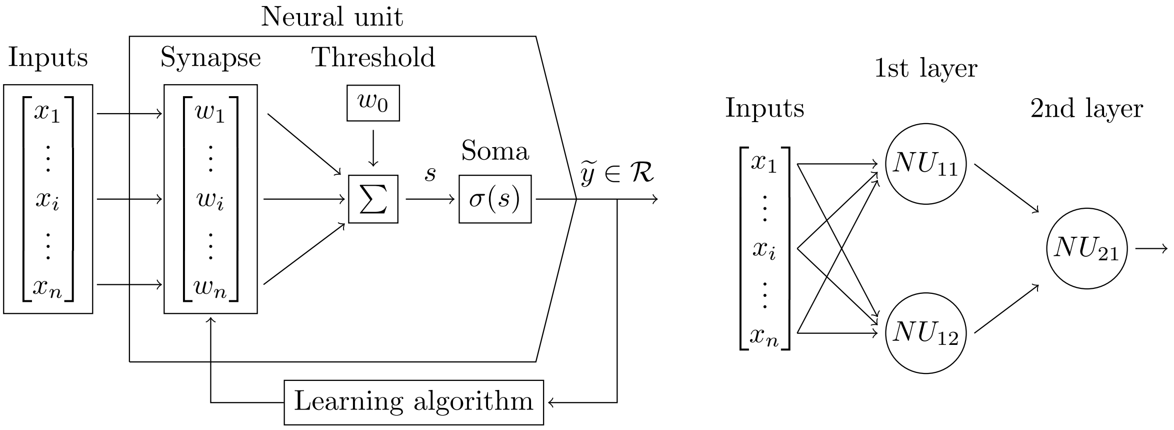

Fig. 1. Neural network: single neural unit (*left*); shallow neural network (*right*)

4. Results

Data set was divided into three aforementioned parts, 80% of samples belongs to training subset and the rest was equally distributed to validating and testing subsets. Learning rate μ in weight updating formula (5) was set to $\mu = 0.4$. Referring to Fig. 2 (left), twenty epochs was sufficient to neural network got learned with testing error 0.0192. Progress of the Lieblein's correlation and the function learned by ANN is shown in Fig. 2 (right).

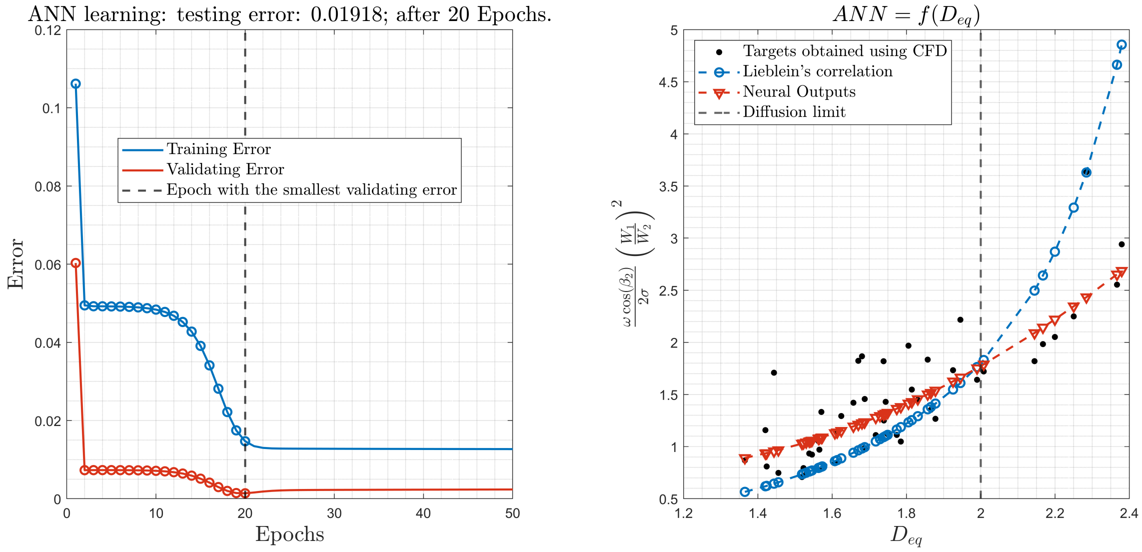

Fig. 2. Results: progress of the learning (*left*); ANN results compared to Lieblein's correlation (*right*)

Deviations performed by artificial neural network and the Lieblein's correlation compared to data obtained by CFD are listed in Table 1, both measured with mean square error (MSE). Approximation using ANN is more than threefold more accurate that Lieblein's correlation model in the whole interval of equivalent diffusion ratio D_{eq}. Although the difference between discussed methods is smaller, it is shown that total pressure loss modelling using ANN offers better approximation than Lieblein correlation in the region under diffusion limit ($D_{eq} < 2$).

Table 1. Mean square error comparison

Interval	Whole interval	$D_{eq} < 2$
MSE: Lieblein's correlation	0.3555	0.1571
MSE: correlation using ANN	0.1096	0.0901

5. Conclusion

An approach for loss correlation was presented in this paper. Based on CFD simulations that was taken as input data set, artificial neural network was learned to predict total pressure loss at design point of axial compressor cascade designed with the new family of the airfoils. Results of the learning are compared against Lieblein's empirical model [5]. Approximation using ANN outperformed available correlation model from the literature as it can be seen in Table 1.

Further work should aim to axial compressor cascade performance predicting at off-design points which will require much larger training data set. Moreover, some geometrical parameters and parameters of the flow probably should be taken into account as inputs to ANN.

Acknowledgements

This work was supported by the grant agency of the Czech Technical University in Prague, grant No. SGS22/148/OHK2/3T/12.

This work was supported by the Technology Agency of the Czech Republic, project TK03030121 Conceptual Design of an Innovative Safety System for Gas-cooled Nuclear Reactors.

References

[1] Aungier, R. H., Axial-flow compressors: A strategy for aerodynamic design and analysis, Applied Mechanics Reviews 57 (4) (2004) B22.

[2] Gupta, M. M., Bukovsky, I., Homma, N., Solo, A. M., Hou, Z. G., Fundamentals of higher order neural networks for modeling and simulation, In: Artificial higher order neural networks for modeling and simulation, M. Zhang (editor), IGI Global, 2013, pp. 103-133.

[3] Gupta, M. M., Liang J., Noriyasu H., Static and dynamic neural networks: From fundamentals to advanced theory, John Wiley & Sons, 2004.

[4] Klesa, J., Aerodynamic design of transsonic compressor airfoil family, Proceedings of the 36th conference with international participation Computational Mechanics, Srn, University of West Bohemia, 2021, pp. 115-118.

[5] Lieblein, S., Loss and stall analysis of compressor cascades, Journal of Basic Engineering 81 (3) (1959) 387-397.

[6] Salunke, N. P., Channiwala S. A., Design and analysis of a controlled diffusion aerofoil section for an axial compressor stator and effect of incidence angle and Mach No. on performance of CDA, International Journal of Fluid Machinery and Systems 3 (1) (2010) 20-28.

COMPUTATIONAL MECHANICS 2022
37th conference with international participation
Srní
November 7 - 9, 2022

Experimental based tuning of active 3-DoF planar absorber

K. Kraus, Z. Šika, J. Krivošej

Department of Mechanics, Biomechanics and Mechatronics, Faculty of Mechanical Engineering, Czech Technical University in Prague, Technická 4, Praha 6, 160 00 Prague, Czech republic

Vibration suppression takes place in many applications and enviroments. In various cases, for example in robotics and industrial enviroment [3], it might be convenient to use absorbers [1] to suppress vibrations of the main structure. Based on application, mass-spring absorber is attached to main structure in point of interest, tuned and actively driven if needed. In order to be able to actively tune and control absorber, some sort of sensors needs to be implemented in the main structure or in the absorber itself, such as accelerometers, encoders, geophones, etc. Depending on absorbers count and the nature of vibrations, various algorithms can be used to drive absorber's actuators, such as PID regulation, H-inf, LQR [4], Delayed resonator [2], etc. Nevertheless, besides mass and stiffness of the absorber, due to many kinds of bearings, usually some sort of damping takes place in the absorber. Lots of real cases of beraing damping are far from linear and thus burdens control algorithms. In this paper we are experimentally tuning real active absorber to be as much undamped (ideal) as possible, so it can be further controlled by superior algorithm.

3-DoF assembly (Fig. 1b) is configured such that active elements lies in mutually perpendicular axes, and enables full planar motion (translation in both directions and rotation). Each active element (based on assembly MGV52 – Fig. 1a) consists of preloaded springs, linear ball bearing, voice-coil actuator and built-in linear encoder. dSpace computer is then used to read sensors and control voice-coil actuators through motor driver (Fig. 2a).

First of all, rough identification must take place in order to get basics characteristics, such as precise mass, stiffness of elements and drive coefficients. Since this identification is based on measurement data from the control pc, ceratin delay of the loop between output and input of the pc (Fig. 2a) is also included among these characteristics. After that it is possible to more closely identify the damping function.

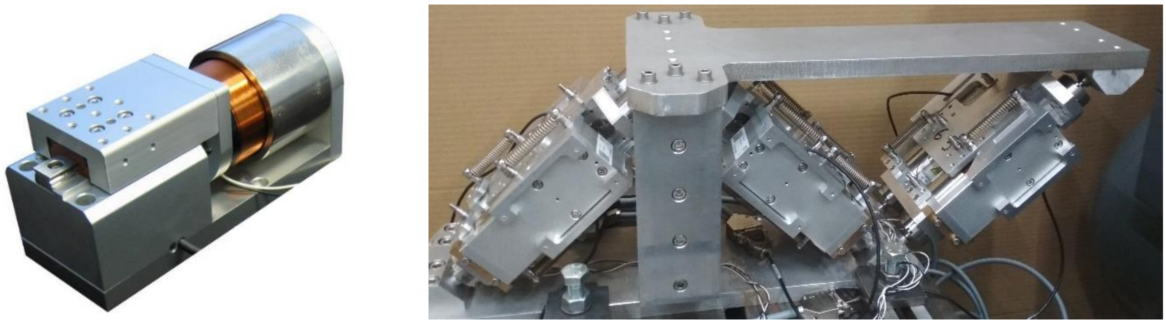

a) active element with linear bearing   b) 3-DoF planar mass-spring configuration

Fig. 1. Absorber design based on MGV52 assembly

Since every planar motion of the whole assembly can be transformed into set of linear motions of every active element, prev to the 3-DoF tuning, tuning of the single element has been performed to get potentionally convinient initial values. Combination of various non-linear functions with tunable coefficients has proven insufficient for the damping identification as well as 1-D look-up table, because results implied the function to be not only the function of velocity, but of the displacement as well – since voice-coil has been chosen as an active absorber's actuator for various advantageous reasons, there are more damping sources apart from bearings. Firstly, its closed-end design with one millimeter wide gap does not allow air to flow effortlessly in and out. Secondly, and more relevantely, electrical characteristic of magnet-coil coupling greatly depends on the mutual position. Therefore, parametrical 1-D look-up table must be at least 2-dimensional. Fig. 2b shows one of more precise idendifications of damping as a function of both, displacement and velocity one of the active elements. It consists of more or less conventional coulomb-viscous area in low speeds and strokes, as well as of great fluctuations (with some sense of symetry) in areas of high strokes. This parametrical plane, when put into positive feedback, is then able to reduce relative damping of the absorber and retain its stability at the same time. When assembled into the final 3-DoF planar configuration, another optimization process takes place in order to adapt initial parameters to increased mass (and therefore forces in bearings). This process is centralized in first half and broken apart in the second half, in order to save optimization time.

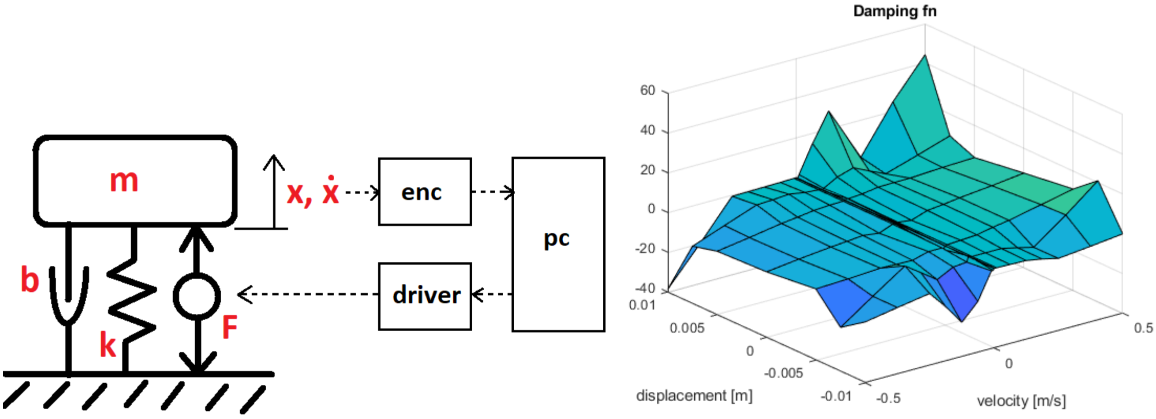

a) Control scheme

b) Damping function included in algorithm

Fig. 2. Absorber control algorithm

Acknowledgements

The work has been supported by the Czech Science Foundation project GA21-00871S "Active non-collocated vibration absorption for robots and mechanical structures".

References

[1] Kraus, K., Šika, Z., Beneš, P., Krivošej, J., Vyhlídal, T., Mechatronic robot arm with active vibration absorbers, Journal of Vibration and Control 26 (13-14) (2020) 1145-1156.

[2] Olgac, N., Elmali, H., Hosek, M., Renzulli, M., Active vibration control of distributed systems using delayed resonator with acceleration feedback, Journal of dyn. systems, measurement, and control 119 (3) (1997) 380-389.

[3] Olsson, T., Haage, M., Kihlman, H., et al., Cost-efficient drilling using industrial robots with high-bandwidth force feedback, Robotics and Computer-Integrating Manufacturing 26 (1) (2010) 24-38.

[4] Šika, Z., Kraus, K., Beneš, P., Vyhlídal, T., Valášek, M., Active multidimensional vibration absorbers for light robots, Proceedings of the 5th Joint International Conference on Multibody System Dynamics, Lisbon, 2018, pp. 1-12.

COMPUTATIONAL MECHANICS 2022
37th conference with international participation
Srní
November 7 - 9, 2022

Pre-stress states and controllability of spatial cable-driven mechanisms

J. Krivošej, V. Halamka, Z. Šika

Faculty of Mechanical Engineering, Czech Technical University in Prague, Technická 4, 166 07 Praha, Czech Republic

The paper analyses several cable-driven mechanisms (manipulators) whose topology is based on the concept of deployable tensegrities. The term tensegrity was coined by shortening the phrase tensional integrity and the main feature of these structures is the presence of only compression (rods) and tension (cables) loaded members [3]. Deployable tensegrities are then a good choice for the creation of a manipulator, because they are divided into individual stages that form a tensegrity beam and allow a change of length in the axis of this beam [4]. Examples of the analysed structures are shown in Fig. 1.

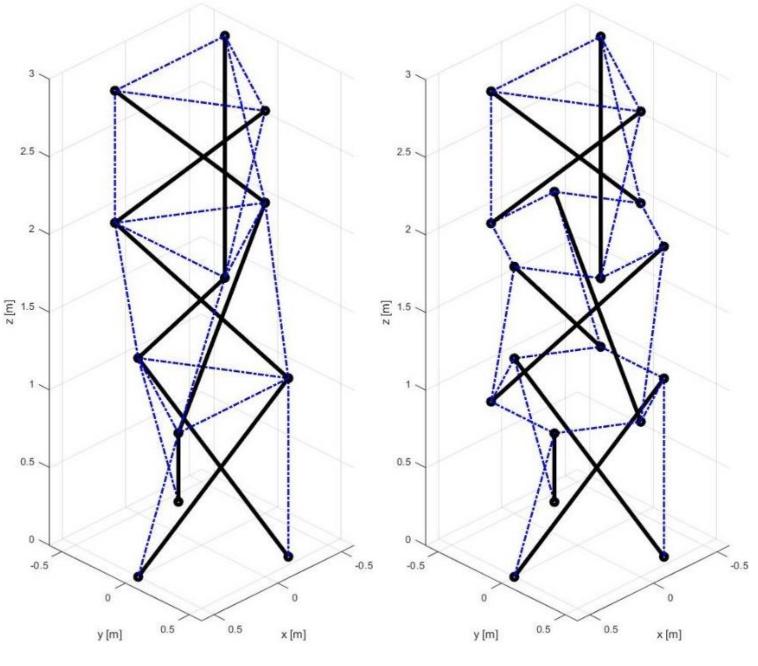

Fig. 1. Examples of analysed structure: structures with tensegrity features (left), pure tensegrity (right)

The analysis itself is then based on the definition of tensegrity described in [1], [2]. This definition classifies tensegrity structures into two groups based on the following features:

- T – the structure is truss,
- S – there is a self-stress state,
- C – tensile elements (cables) have no rigidity in compression,
- M – there is an infinitesimal mechanism stiffened by self-stress state,
- I – the set of struts is contained within the continuous net of tensile elements,
- D – compressed elements extremities do not touch each other.

The structures that have all features (T+S+C+M+I+D) are classified in the "pure tensegrity" group. "Structures with tensegrity features" fulfil three obligatory criteria (T+S+C) and have at least one of the features: M, I, or D. The main difference between pure tensegrity and structures with tensegrity properties is that only pure tensegrity has all the essential engineering properties such as the ability to tune the stiffness and natural frequency of structure based on the choice of prestress.

Thus, the key features for determining the group are M and S. Only the presence of self-stress states (S) is necessary for the possibility of controlling the tensegrity structure. The presence of self-stress states and infinitesimal mechanisms in the structure can be verified by analyzing the eigenvalues of matrices BB^T and B^TB, where B is the compatibility matrix. A least squares method was used to determine the prestressing of the entire structure, which optimizes the distribution of forces by combining the individual self-stress states so that the distribution is as close to homogeneous as possible.

Analysis of the examples shows that the structure on the left in Fig. 1 is a structure with tensegrity features and is controllable because it satisfies all features except D (there are 3 self-stress states and 3 infinitesimal mechanisms). To increase the range of motion, additional cables were added (Fig. 2), and in this configuration the structure has 9 self-stress states and no infinitesimal mechanisms. However, the use of the least squares method to choose prestress of structure determined the distribution of forces in the additional cables to be zero, thus they can be described as redundant.

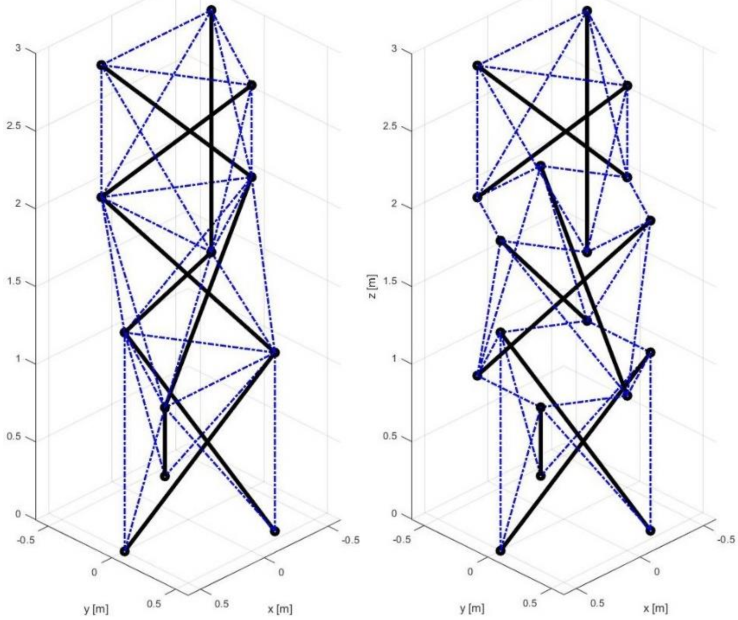

Fig. 2. Examples of analysed structure with additional cables

The structure on the right in Fig. 1, on the other hand, satisfies all features, i.e., it is a pure tensegrity and is controllable. In this configuration it has 1 self-stress state and 13 infinitesimal mechanisms. Adding cables (Fig. 2). changes the number of self-stress states to 3 and the number of mechanisms to 6. Like the structure with tensegrity properties, the added cables are zeroed using the least squares method. The controllability of this structure with the added cables is conditioned by the in-plane placement of the nodes between the stages. Thus, if the stages interpenetrate each other, the self-stress states are extinguished.

Based on the analysis, concepts were selected for which a dynamic model was built. The models were built using the SimScape environment. This tool allows the direct application of physical blocks and the definition of links between them, thus eliminating the compilation of dynamic behavior equations. The final step is then to design and build the demonstrator and control application.

Acknowledgements

The work has been supported by the Czech Science Foundation project 20-21893S "Mechatronic tensegrities for energy efficient light robots" and partly by the project SGS22/150/OHK2/3T/12 “Mechatronics and adaptronics 2022” of the Czech Technical University in Prague.

References

[1] Obara, P., Kłosowska, J., Gilewski, W., Truth and myths about 2D tensegrity trusses, Applied Sciences 9 (1) (2019) 179.
[2] Obara, P., Tomasik, J., Parametric analysis of tensegrity plate-like structures: Part 1 – Qualitative analysis, Applied Sciences 10 (20) 7042.
[3] Skelton, R. E., Oliveira, M. C., Tensegrity systems, Springer, 2009.
[4] Sultan, C., Skelton, R. E., Deployment of tensegrity structures, International Journal of Solids and Structures 40 (18) 4637-4657.

COMPUTATIONAL MECHANICS 2022
37th conference with international participation
Srní
November 7 - 9, 2022

Eigenmotion concept of cable driven mechanism with absorbing elements

J. Krivošej, Z. Šika

Faculty Faculty of Mechanical Engineering, CTU in Prague, Technická 4, 166 07 Praha 6, Czech Republic

The paper deals with the principle of eigenmotion, which is based on the idea of keeping the total energy constant during the motion of the mechanism. The idea of applying the eigenmotion principle is mainly linked to single-purpose mechanisms where there is a requirement to move along a periodically repeating trajectory [2]. Therefore, the paper deals with the extension of the eigenmotion principle to cable-driven mechanisms which potentially has a larger number of members giving the possibility of generating more complex trajectories or easier reconfiguration of the manipulator for switching from one eigenmotion trajectory to another.

The concept of eigenmotion is examined on two basic cable-driven manipulators. The first one is an inverse pendulum controlled by two cables (Fig. 1) and the second one is a body in planar space controlled by four cables (Fig. 2). Both concepts have two types of additional springs – the soft springs which directly connect the moving body and frame and the tension springs which prestress the cables and keep the level of prestress at certain level.

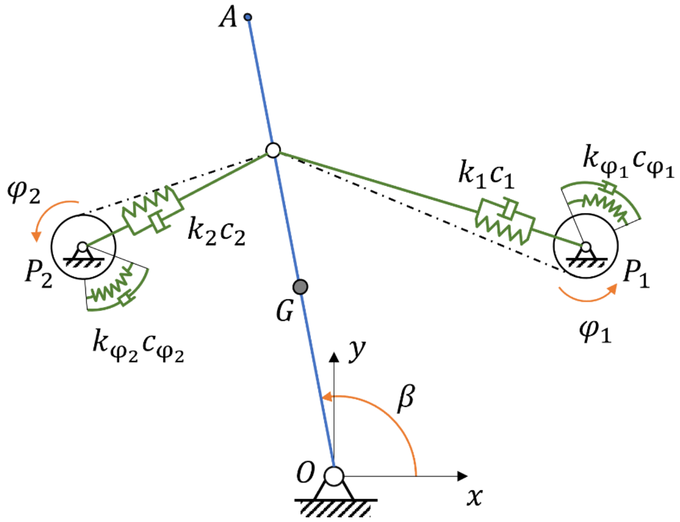

Fig. 1. A scheme of the inverse pendulum cable-driven manipulator designed for eigenmotion: k_{1-2} – soft springs with damping c_{1-2}, $k_{\varphi_{1-2}}$ – tension torsional springs with damping $c_{\varphi_{1-2}}$, G – centre of gravity, A – end-effector, O – rotational joint

The eigenmotion trajectory generation is based on the undamped scheme of the dynamic model, where repetitive point-to-point trajectories are considered. The dynamic model is assembled considering non-rigid cable model with variable stiffness depended on the actual cable length $k_{cable}(l_{cable})$. The i-th pulley is modelled as

$$I_{1Pi}\ddot{\varphi}_i = M_{c_i} - S_{cable_i} r_{Pi} - M_{k_{\varphi_i}} - M_{c_{\varphi_i}}, \tag{1}$$

where I_{1Pi} is the moment of inertia, M_{c_i} is moment generated by the motor, r_{Pi} is the radius of the pulley, S_{cable_i} is the force in the i-th cable, $M_{k_{\varphi_i}} = k_{\varphi_i}(\varphi_i - \varphi_{0_i})$ is the moment generated by the torsional spring and $M_{c_{\varphi_i}} = c_{\varphi_i}(\dot{\varphi}_i - \dot{\varphi}_{0_i})$ is the damping moment.

The control scheme is based on the computed torque method (CTM), which uses the inverse dynamics, and the cable force distribution, which defines the input M_{c_i}, is solved by the singular value decomposition (SVD) [1]. The final values of the control input M_{c_i} are optimized so that the control inputs M_{c_i} are minimized. This approach leads to the minimum energy costs, which are needed to stay on the eigenmotion trajectory and overcome the damping, model imperfections (parameters in the regulator are chosen a little differently than in the dynamic model), disturbances etc.

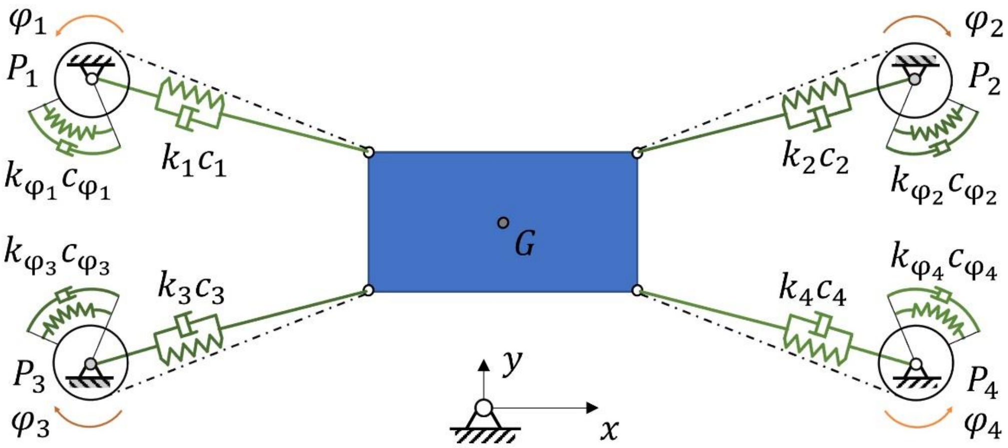

Fig. 2. A scheme of the body in planar space designed for eigenmotion: k_{1-4} – soft springs with damping c_{1-4}, $k_{\varphi_{1-4}}$ – tension torsional springs with damping $c_{\varphi_{1-4}}$, G – centre of gravity

In conclusion, the brief investigation to the eigenmotion idea of cable driven mechanism with absorbing elements is shown. Two planar models are presented and described. The control algorithm uses CTM with control inputs M_{c_i} using SVD with optimization algorithm which keeps the input moments at minimum level as close as possible to the passive prestress in cables during the eigenmotion motion. The simulation results show that the control algorithm keeps the motion of the mechanism on the chosen eigenmotion trajectory.

The future work considers the extension to more complex structures and mechanisms where additional soft springs can be rearranged so that the eigenmotion trajectory can be more complex and reconfigurable.

Acknowledgements

The work has been supported by the Czech Science Foundation project 20-21893S "Mechatronic tensegrities for energy efficient light robots" and partly by the project SGS22/150/OHK2/3T/12 “Mechatronics and adaptronics 2022” of the Czech Technical University in Prague.

References

[1] Krivošej, J., Šika, Z., Optimization and control of a planar three degrees of freedom manipulator with cable actuation, Machines 9 (12) (2021) 338.

[2] Schwarzfischer, F., Hüsing, M., Corves, B., The dynamic synthesis of an energy-efficient slider-crank-mechanism, In Proceedings of the Second International Symposium of Mechanism and Machine Science, Baku, 2017, pp. 156-163.

COMPUTATIONAL MECHANICS 2022
37th conference with international participation
Srní
November 7 - 9, 2022

Inverse dynamics approximation for controlling mechanisms with flexible elements

J. Lieskovský[a], P. Beneš[a], Z. Šika[a]

[a]*Faculty of Mechanical Engineering, CTU in Prague, Technická 4,160 00 Praha 6, Czech Republic*

Cable-driven mechanisms are usually a typical example of over-actuated systems, at least when the cables are considered rigid. If we include cable compliance, the systems generally become under-actuated. Although such a system remains controllable if kept under tension the end-effector's acceleration is not directly dependent on the input torques on cable winches which means that the inverse dynamics problem is unsolvable. It is usually desirable to make the cables as stiff as possible, which allows us to approximate the cables as rigid at each individual step of calculating the input torques, invalidating the equations of motion. We can restore equality by introducing fictitious cable tension (in the form of internal joint torques) that corresponds to the expected deformation. This expected deformation is used to maintain a certain degree of pre-tension within the cables and therefore controllability of the entire system.

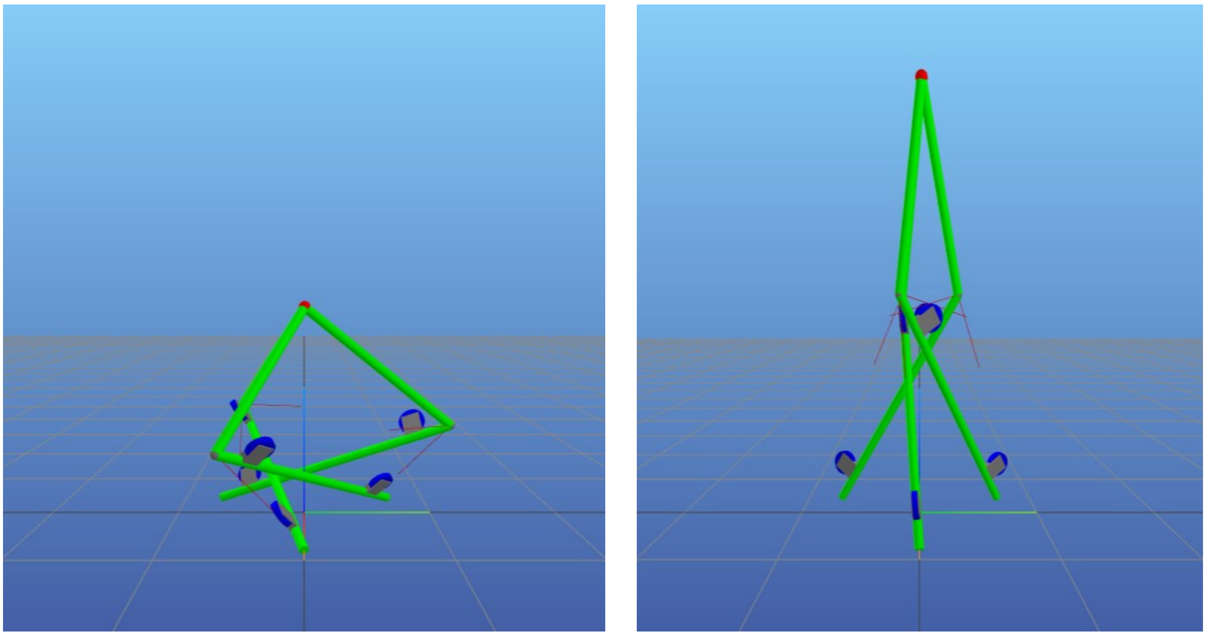

Fig. 1. Control of the tensegrity structure along the vertical axis – position in $t = 5\ s$ (left) and $t = 15\ s$ (right), [1]

The modified equations of motion can be written as

$$\boldsymbol{M}_d\ddot{\boldsymbol{y}}_d + \underbrace{\boldsymbol{M}_s\ddot{\boldsymbol{y}}_s}_{\boldsymbol{0}} + \boldsymbol{c} = \boldsymbol{W}\boldsymbol{f} + \boldsymbol{p} + \boldsymbol{A}_s\Delta\boldsymbol{y}_s + \boldsymbol{B}\boldsymbol{u}, \tag{1}$$

where $\ddot{\boldsymbol{y}}_{\boldsymbol{d}}, \ddot{\boldsymbol{y}}_{\boldsymbol{s}}$ are desired and superfluous accelerations, $\boldsymbol{M}_d$ and $\boldsymbol{M}_s$ are corresponding mass matrices, $\boldsymbol{c}$ is the vector of bias terms, $\boldsymbol{f}$ is the vector of external forces with wrench Jacobian matrix $\boldsymbol{W}$, $\boldsymbol{p}$ represents passive joint torques, $\boldsymbol{u}$ is the vector of inputs with matrix $\boldsymbol{B}$ and finally $\boldsymbol{A}_S \Delta \boldsymbol{y}_S$ represents the vector of elasticity torques, where $\Delta \boldsymbol{y}_S$ are expected changes in deformation. The solution was formulated as a quadratic programming problem [3] with maintaining tension within cables as optimizing parameters.

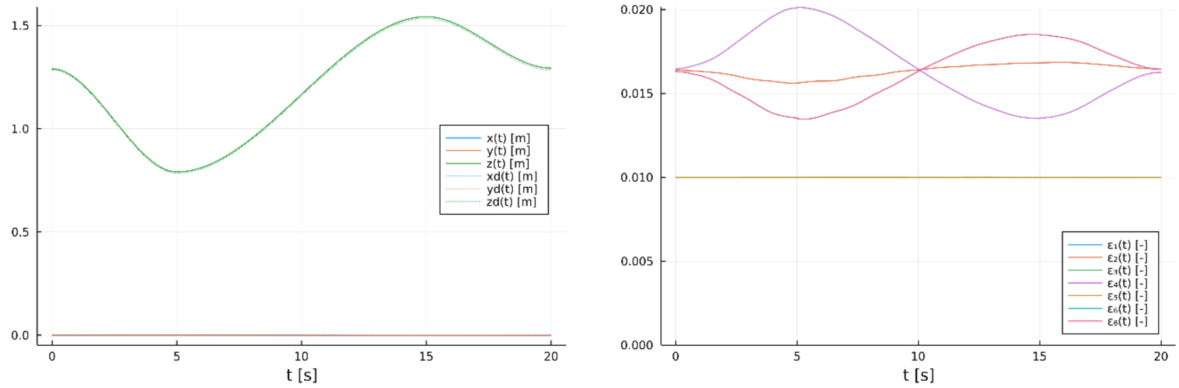

Fig. 2. Control of the tensegrity structure along the vertical axis – position of the end-effector (left), strain in cables (right), [1]

Figs. 1 and 2 show one of the verification experiments, which was the control of the tensegrity manipulator [2] along the vertical axis. The cable-pulley interaction is modelled using compliant involute joint with internal torque model, accounting for elasticity, damping and general uni-directionality of the cable Hermite C^1 continuous splines were used as desired trajectories. Fig 1 shows the manipulator in two different positions along the trajectory. The left part of the Fig. 2 shows that the position of the end-effector corresponds to the desired trajectory. The right part shows the strain in the cables during the manoeuvre.

The described approach can be used, for example, in conjunction with computed torques controllers. For this type of control, a precise inverse dynamics model is the key to proper functioning.

Acknowledgements

The work has been supported by the Czech Science Foundation project GA20-21893S - Mechatronic Tensegrities for energy efficient light robots.

References

[1] Lieskovský, J., Reconfiguration of tensegrity structures, Master thesis, CTU in Prague, 2022.
[2] Skelton, R. E., de Oliveira, M. C., Tensegrity systems, Springer-Verlag, 2009.
[3] Stellato, B., Banjac, G., Goulart, P., Bemporad, A., Boyd. S., OSQP: An operator splitting solver for quadratic programs, Mathematical Programming Computation 12 (4) (2020) 637–672.

COMPUTATIONAL MECHANICS 2022
37th conference with international participation
Srní
November 7 - 9, 2022

Two-scale numerical simulation of acoustic transmission in interaction with flow

V. Lukeš, E. Rohan

Faculty of Applied Sciences, University of West Bohemia, Univerzitní 8, 301 00 Plzeň, Czech Republic

Our previously developed two-scale models of the acoustic transmission on perforated plates, e.g., [1–3] or [4], consider acoustic wave propagation in a stationary acoustic medium. In this contribution, we present the computational algorithm for solving the extended problem of acoustic transmission on a rigid perforated plate interacting with an incompressible flow. The numerical solution consists of two separate problems involving two-scale computations. In the first problem, the potential flow through the rigid perforated interface is computed and the results are employed in the second problem, where the homogenized acoustic coefficients are calculated and the distribution of the global acoustic pressure is found. Both problems require solving the local (microscopic) subproblems defined in a reference cell Y, which represents the periodic structure of the perforated interface, and solving the macroscopic subproblems in order to get the global responses in a macroscopic domain, see Fig. 1.

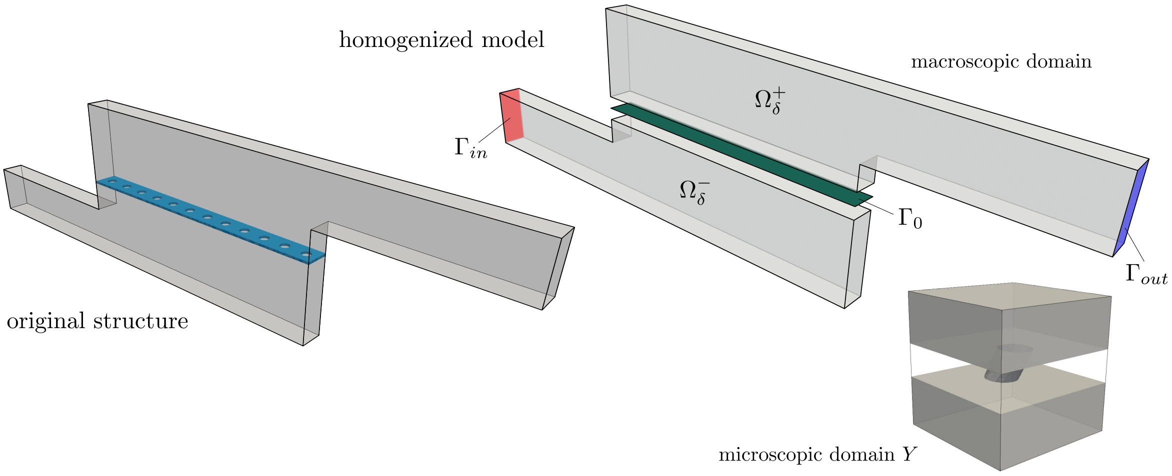

Fig. 1. *Left:* original structure. *Right:* homogenized macroscopic model and reference cell

Homogenization of the potential flow model leads to a set of subproblems defined in Y and to a macroscopic model of the homogenized layer Γ_0, which replaces the original perforated structure. This homogenized model constitutes the transmission condition coupling the separated domains Ω_δ^+, Ω_δ^-. The solution of the local subproblems in the reference cell Y gives the so called corrector functions that are used to evaluate homogenized flow coefficients appearing in the transmission condition. The global macroscopic solution provides the flow velocity field in the homogenized layer Γ_0 and in Ω_δ^+, Ω_δ^-. The reconstruction based on the corrector func-

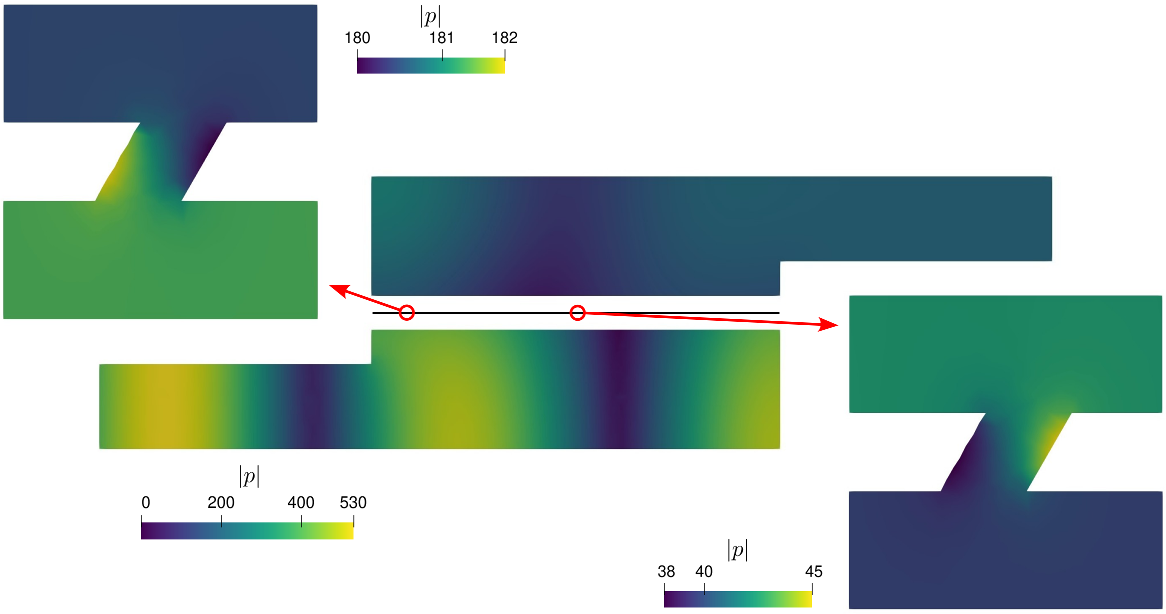

Fig. 2. Computed acoustic pressure in the waveguide and reconstructed pressure fields in two distinct macroscopic points

tions and the macroscopic solution must be performed to get the flow velocities in Y for given macroscopic locations, which will be required in the following calculations.

The extended Helmholz equation describing the acoustic waves interacting with an inviscid fluid is treated similarly to the flow problem above. It again leads to the local subproblems in Y and the homogenized transmission condition related to the acoustic problem. Because the local subproblems, and also the homogenized acoustic coefficients, now depend on the flow velocities that vary in space across the perforations, they must be solved for all given macroscopic points, usually corresponding to element centers or integration points of the finite element discretization of Γ_0. The space dependent homogenized coefficients enter the macroscopic simulation, which results in the global acoustic pressure fields in Γ_0, Ω_δ^+, and Ω_δ^-.

Fig. 2 shows the distribution of the macroscopic pressure in the waveguide and the reconstructed pressures in two distinct perforations. As stated above, the fluid flow influences the homogenized acoustic coefficients that affect the global acoustic pressure distribution. This is

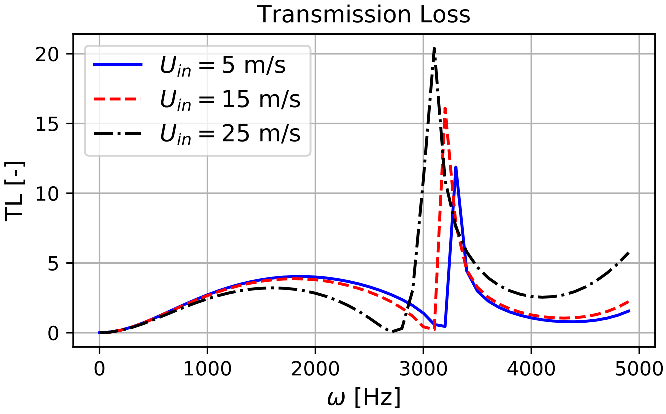

Fig. 3. Transmission loss curves calculated for different velocities $U_{in} = -U_{out} = 5,\ 15,\ 25$ m/s

illustrated in Fig. 3, where the transmission loss curves are calculated for different inlet and outlet velocities applied to the waveguide boundaries Γ_{in} and Γ_{out}, see Fig. 1.

Acknowledgement

The research has been supported by the grant project GA 2116406S of the Czech Science Foundation.

References

[1] Cimrman, R., Lukeš, V., Rohan, E., Multiscale finite element calculations in Python using SfePy, Advances in Computational Mathematics 45 (2019) 1897-1921.

[2] Rohan, E., Lukeš, V., Homogenization of the acoustic transmission through perforated layer, Journal of Computational and Applied Mathematics 234 (2010) 1876-1885.

[3] Rohan, E., Lukeš, V., Homogenization of the vibro-acoustic transmission on perforated plates, Applied Mathematics and Computation 361 (2019) 821-845.

[4] Rohan, E., Lukeš, V., Homogenization of the vibro-acoustic transmission on periodically perforated elastic plates with arrays of resonators, Elsevier Applied Mathematical Modelling 111 (2022) 201-227.

COMPUTATIONAL MECHANICS 2022
37th conference with international participation
Srní
November 7 - 9, 2022

Tensile testing of polymer composites reinforced with continuous fibers produced by CFF method

J. Majko, M. Vaško, M. Handrik, M. Sága

Faculty of Mechanical Engineering, University of Žilina, Univerzitní 8215/1, 301 00 Žilina, Slovak Republic

1. Introduction

3D printing is a manufacturing technology based on the gradual deposition of material layer upon layer. The development of additive manufacturing in recent years has led to the possibility of printing not solely pure plastics but also other materials. For example, thermoplastics reinforced with long or chopped fibres. Generally, the presence of fibre limits the portfolio of applicable 3D printing methods. The most suitable are methods based on the extrusion of material (e.g. Fused Filament Fabrication - FFF). In the case of these methods, the nylon with chopped fibre passes through the printer nozzle without substantial modifications to the printer. The deposition of the long filament into the structure was allowed by the augmentation of the FFF printer by adding the second nozzle intended for continuous fibre (Continuous Filament Fabrication - CFF). Fibre-reinforced plastic composites printing came on the market a few years ago. Therefore, research into the mechanical properties of these materials is currently ongoing. In the case of tensile testing, several studies have been published evaluating the results of experimental measurements performed on variously shaped specimens. The reason is that there are currently no standards focused on mechanical testing methodology for additively manufactured composites. In general, the authors used standards ASTM D3039 or ASTM D638-14. The former is dedicated to tensile testing of long fibre reinforced composites, and the latter specifies tensile testing of pure plastics. Both shapes lead to the creation of stress concentrators, which results in premature failure of specimens at inappropriate locations. Therefore, the authors proposed a new specimen shape using finite element analysis. The primary aim is to verify the specimen shape suitability by the experimental measurements. In addition, the comparison of obtained tensile strength with results published in peer-reviewed journals by other authors will be performed.

2. Experiment preparations

2.1. Manufacturing process

The production of the specimens was performed using a Markforged MarkTwo printer. This printer works on the principles of FFF and CFF methods, which we classify as extrusion technologies. The FFF method comprises the following procedures:

1) The material wound on a spool is fed into the printer head.
2) The material is heated to a melting temperature.
3) The molten material is extruded and deposited at precisely specified locations.
4) Upon deposition, the material cools and solidifies. In addition, deposited material forms bonding with adjacent filaments.

2.2. Material

The experimental measurement was carried out on laminates made of polymer reinforced with long fibres. The matrix function was fulfilled by nylon reinforced with chopped carbon fibre (trademark onyx). The long carbon fibres fulfilled the reinforcement function.

Table 1. Mechanical properties of essential materials specified by printer manufacturer

	Young Modulus [GPa]	Tensile strength [MPa]	Strain at fracture [%]
Onyx	1.4	30	58
Carbon fiber	60	800	1.5

2.3. Specimens

The tensile test was realized on the specimens with modified dog bone shapes (Fig. 1). Based on the FE analysis published in [6], this shape type appears to be the most suitable for tensile testing purposes. The shapes according to standards ASTM D3039 and ASTM D638-14 are inappropriate. The reason is the premature breakage caused by the formation of stress concentrators.

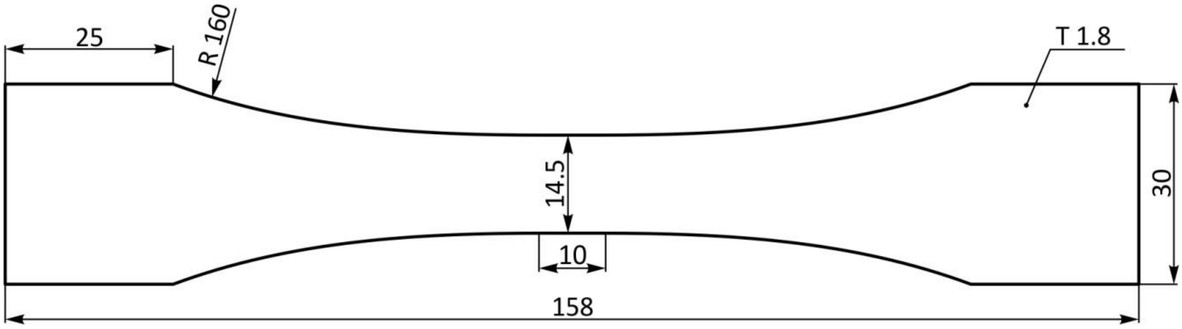

Fig. 1. Proposed specimen shape

2.4. Printing parameters

In the slicing software, the printer user can modify some parameters. Table 2 gives an overview of the print settings applied in this study.

Table 2. Printing parameters

Parameter	Value
Lamina thickness [mm]	0.125
Base plane	XY
Orientation of matrix filaments [degrees]	45/-45
Infill density [%]	100
Infill pattern	Solid infill
Number of roof and floor layers	4
Total number of laminas	14
Reinforcement type	Carbon
Reinforcement orientation	Unidirectional (0°)
Number of reinforced layers	6

The infill pattern was solid with 100% density and 45/-45 orientation. Also, the number of walls and roof/floor layers was 2 and 4, respectively. A previous study focused on nylon with chopped carbon fibres showed that all these parameters affect the strength of the laminates [8].

In the case of laminates reinforced with continuous fibre, there is no expectation of a significant effect of the matrix on the strength of the specimens since the strength of the fibres significantly exceeds the matrix strength.

3. Results

The results of the tensile test of the continuous fibre-reinforced thermoplastic composites performed using INSTRON 5985 are shown in Table 3.

Table 3. Tensile test results

Fibre type	**Fibre orientation**	**Number of rings**	**Maximum force [N]**	**Ultimate strength [MPa]**
Carbon	0°	0	8311.2	318.42

Subsequently, it was necessary to perform the comparison of the achieved tensile strength with results published by other research institutes. The comparison is in tabular form (Table 4) and also plotted using program Matlab (Fig. 2). The fibre volume fracture (FVF) was determined as the ratio between the number of reinforcing layers to the total number of laminas in the narrowest part of the specimens.

Table 4. Overview of the results of carbon fibre reinforced thermoplastic composite specimens published in scientific journals

Authors	**Specimen shape**	**FVF [%]**	**Ultimate strength [MPa]**	**Fiber deposition**
Majko	custom	42	318.42	0
Goh [5]	638-14	92	600	0
Lozada [9]	638-14	69	304.3	concentric
Al-Abadi [1]	3039	50	320	concentric
Dickson [3]	3039	30.7	216	concentric
Ghebretinse [4]	3039	71	560	0
		6.25	96.6	
Chacon [2]	3039	50	239.8	0
		87.5	436.7	
Iragi [7]	3039	88.8	779	0

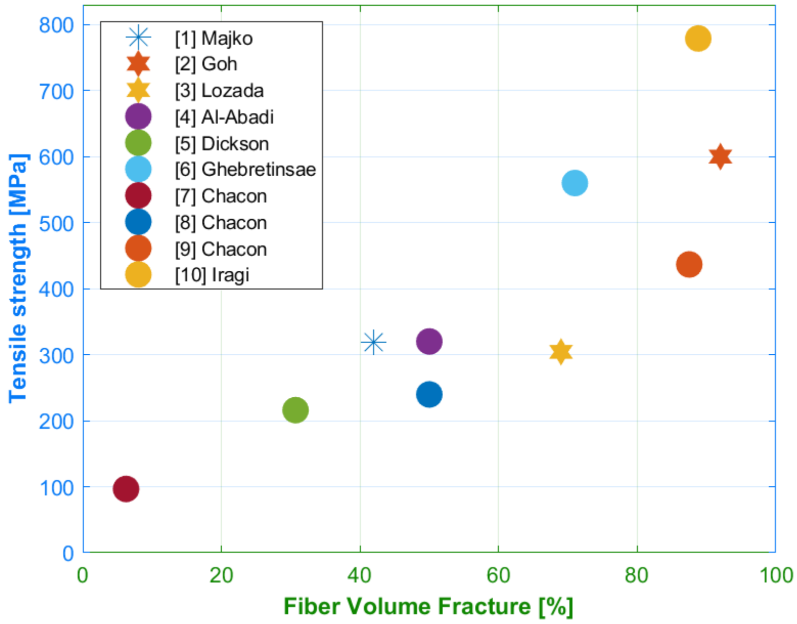

Fig. 2. Plot of results comparison

The specimen proposed by the authors achieved a tensile strength of 318.42 MPa at FVF of 42%. Comparable results obtained only specimens with shape according to ASTM D3039 in a study published by Al-Abadi et al. [1]. The tensile strength was 320 MPa at 50% FVF. Chacon et al. [2] realized the tensile test on identical specimens and achieved significantly lower tensile strength. The difference could lie in various fibre deposition arrangements. According to the results, the fibres deposited in rings around specimen circumference lead to higher tensile strength than unidirectionally deposited fibres.

For the ASTM D638-14 specimens, even a significantly higher FVF did not lead to tensile strength higher than 300 MPa.

4. Conclusion

The assessment of the results confirmed the suitability of the proposed shape for tensile testing of additively manufactured composite specimens. Therefore, in the future, the authors will follow up these results with further measurements to determine:

- the effect of FVF on the tensile strength,
- the influence of the reinforcement type and its arrangement on the tensile strength.

Acknowledgements

The work has been supported by the grant project KEGA 054ŽU-4/2021.

References

[1] Al Abadi, H., Thai, H., Paton-Cole, V., Patel, V.I., Elastic properties of 3D printed fibre-reinforced structures, Composite Structures 193 (2018) 8-18.

[2] Chacón, J.M., Caminero, M.A., Núñez, P.J., García-Plaza, E., García-Moreno, I., Reverte, J.M., Additive manufacturing of continuous fibre reinforced thermoplastic composites using fused deposition modelling: Effect of process parameters on mechanical properties, Composites Science and Technology 181 (2019) 107688.

[3] Dickson, A.N., Barry, J., McDonnell, K.A., Dowling, D.P., Fabrication of continuous carbon, glass and kevlar fibre reinforced polymer composites using additive manufacturing, Additive Manufacturing 16 (2017) 146-152.

[4] Ghebretinsae, F., Mikkelsen, O., Akessa, A.D., Strength analysis of 3D printed carbon fibre reinforced thermoplastic using experimental and numerical methods, IOP Conference Series: Materials Science and Engineering, 2019, 700, 012024.

[5] Goh, G.D., Dikshit, V., Nagalingam, A.P., Goh, G.L., Agarwala, S., Sing, S.L., Wei, J., Yeong, W.Y., Characterization of mechanical properties and fracture mode of additively manufactured carbon fiber and glass fiber reinforced thermoplastics, Materials and Design 137 (2018) 79–89.

[6] Handrik, M., Vaško, M., Majko, J., Sága, M., Dorčiak, F., Influence of the shape of the test specimen produced by 3D printing on the stress distribution in the matrix and in long reinforcing fibers, Strojnícky časopis – Journal of Mechanical Engineering 63 (3) (2019) 61-68.

[7] Iragi, M., Pascual-Gonzalez, C., Esnaola, A., Aurrekoetxea, J., Lopes, C.S., Aretxabaleta, L., Characterization of elastic and resistance behaviours of 3D printed continuous carbon fibre reinforced thermoplastics, In Proceedings of the ECCM 2018—18th European Conference on Composite Materials, Athens, Greece, 2018, pp. 24–28.

[8] Majko, J., Vaško, M., Handrik, M., Sága, M., Tensile properties of additively manufactured thermoplastic composites reinforced with chopped carbon fibre, Materials 15 (12) (2022) 4224.

[9] Naranjo-Lozada, J., Ahuett-Garza, H., Orta-Castaňon, P., Verbeeten, W.M.H., Sáiz-González, D., Tensile properties and failure behavior of chopped and continuous carbon fiber composites produced by additive manufacturing, Additive Manufacturing 26 (2019) 227-241.

COMPUTATIONAL MECHANICS 2022
37th conference with international participation
Srní
November 7 - 9, 2022

Assessment of the fatigue life of a city bus

R. Minich, M. Kepka jr., M. Kepka

Regional Technological Institute, research centre of Faculuty of Mechanical EngineeringUniversity of West Bohemia in Pilsen,
Univerzitní 8, 301 00 Plzeň, Czech Republic

The laboratory of service strength and fatigue life testing of the Regional Technological Institute has been cooperating with bus and trolleybus manufacturers SOR and SOALRIS for a long time. In order to assess the service life of city buses and trolleybuses, there is very often an insufficient amount of information from service loads available. One of the options for proceeding in such a case is to use so-called design load spectra. The paper aims to use a case study to calculation of the service life of a specific welded node using the service spectrum, which was evaluated for an empty and full car based on strain gauge measurements in urban traffic. Last but not least, the evaluation of thin-walled welded structures will also be discussed, especially with regard to the applied stress, as it is often problematic to place the strain gauge in such a way as to determine the commonly used nominal or hot-spot structural stress.

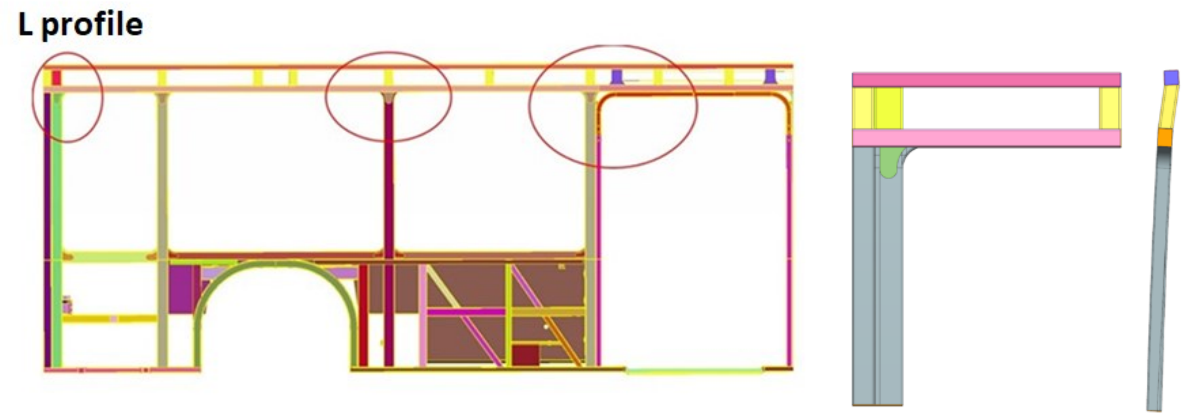

Fig. 1. CAD model of bus bodywork (left), CAD detail for testing (right)

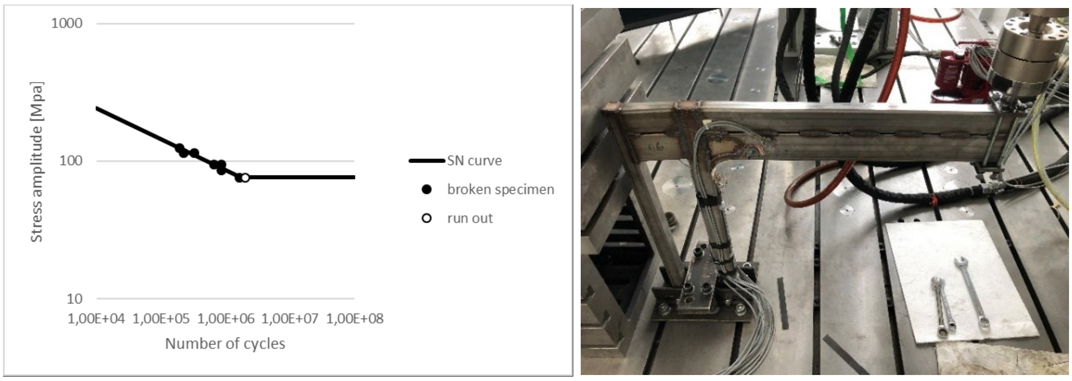

Fig. 2. S-N curve of bodywork detail (left), labor test (right)

The methodology will be demonstrated on the welded L profile, which is located in the rear part of the body. This welded detail has been tested in the laboratory, the test results are modified but realistic, the test was controlled by force and the failure criterion was the formation of a microcrack. The deformation was measured using strain gauges. Its values were used to transform force into stress.

The stress was measured on the real track, with the strain gauges placed in the same place during the ride and as during the test in the laboratory. Variable amplitude loading from real service representing approximately 13 km long track is shown below.

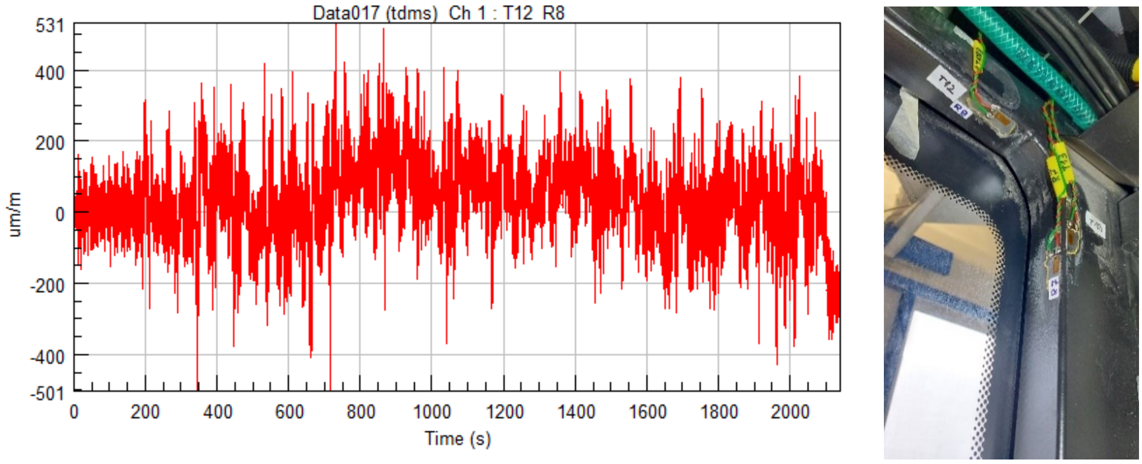

Fig. 3. The strain gauge signal, strain gauge on the bus

Software nCode and the fatigue damage accumulation hypothesis was used to calculate the service life. The methodology used for the calculation was described by authors mode deeply previously in [1].

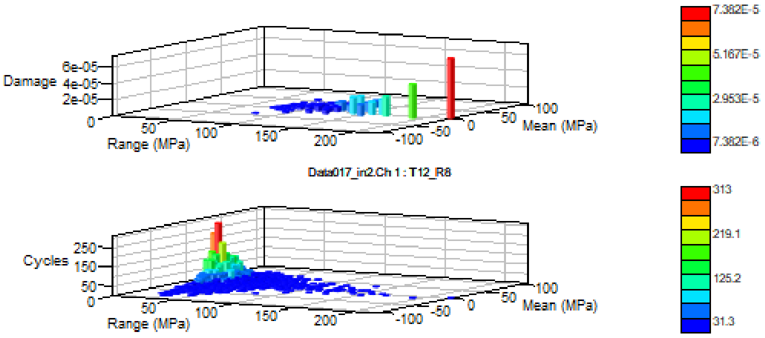

Fig. 4. nCode program results

Acknowledgement

The work has been supported by the Technology Agency of the Czech Republic, research project Nr. FW01010386 “Research and development of articulated electric bus”.

References

[1] Kepka, M. Consideration of random loading processes and scatter of fatigue properties for assessing the service life of welded bus bodyworks, International Journal of Fatigue (151) (2021) 106324.

COMPUTATIONAL MECHANICS 2022
37th conference with international participation
Srní
November 7 - 9, 2022

Kinematic and constitutive equations in warping torsion of FGMs beams with spatially varying material properties

J. Murín[a], S. Kugler[b], M. Aminbaghai[c], J. Paulech[a], J. Hrabovský[a],
V. Goga[a], V. Kutiš[a]

[a] *Department of Applied Mechanics and Mechatronics, IAMM FEI STUIlkovičova 3, 812 19 Bratislava, Slovakia*
[b] *University of Applied Sciences Wiener Neustadt, Department of Applied and Numerical Mechanics, Wiener Neustadt, Austria*
[c] *Vienna University of Technology, Institute for Mechanics of Materials and Structures, Karlsplatz 13, A-1040 Vienna, Austria*

1. Introduction

The most well-known theories of warping torsion beams with constant stiffness, (TTT), were elaborated by Vlasov [6], and Benscoter [1]. As is known, their difference lies in the determination of a new unknown quantity, which characterizes the axial deformation of the cross-section caused by its twisting $u_x(x,y,z)$. For Vlasov, this quantity is the relative torsion angle $\psi^{'}(x)$, which is a dependent quantity. In this case, $u_x(x,y,z)=\omega(y,z)\psi^{'}(x)$, This dependence, considered as a lack of this theory, was addressed by Benscoter by introducing an independent function $F(x)$: $u_x(x,y,z)=\omega(y,z)F(x)$. The warping ordinate function $\omega(y,z)$ depends only on the cross-sectional geometry of the beam. Significant contribution to the theory of warping torsion of thin-walled beams of constant stiffness are articles published by Rubin, e.g. [5], where the analogy between the II. order bending theory of beams and the warping torsion was used. The calculation of maximum normal and shear stresses is performed using known formulas based on TTT. However, the above procedures may not be used for FGM beams with spatial variability of material properties, because not only the primary quantities but also the normal and shear stresses and warping ordinates function depend on the variability. This dependence influences maximum stresses not only in their size but also in their place of action [2-4]. In proposed contribution, the new kinematic and constitutive equations for calculation of warping torsion deformation and stresses in the FGM beams with spatial variability of material properties will be formulated. These equations will include both the effects of material properties variability and the material-dependent warping ordinate function and its gradients. These equations can be used for warping torsion analysis of FGM beams with both open and closed cross sections. The significant influence of spatial variability of material properties on normal and shear stresses by warping torsion will be documented by numerical simulations of FGM thin-walled beams.

2. Kinematic and constitutive equations in warping torsion of FGM beams

Kinematics of a warping free cross-section of FGM beam with spatially varying material properties is shown in Fig. 1. In the cross-section, following quantities have to be known: the bimoment $M_\omega(x)$, the primary $M_{Tp}(x)$ and secondary $M_{Ts}(x)$ torsion moments, the relative twist angle $\psi^{'}(x)$, the part of the bicurvature $\psi^{'}_M(x)$ caused by the bimoment, the effective bimoment stiffness $EI_\omega(x)$ and the primary tosional stiffness $GI_T(x)$ and the effective secondary stiffness $GI_{Ts}(x)$. Further, $E(x,y,z)$ is the spatial distribution of the elasticity modulus and $G(x,y,z\ )$ is the spatial distribution of the shear modulus in the real FGM beam.

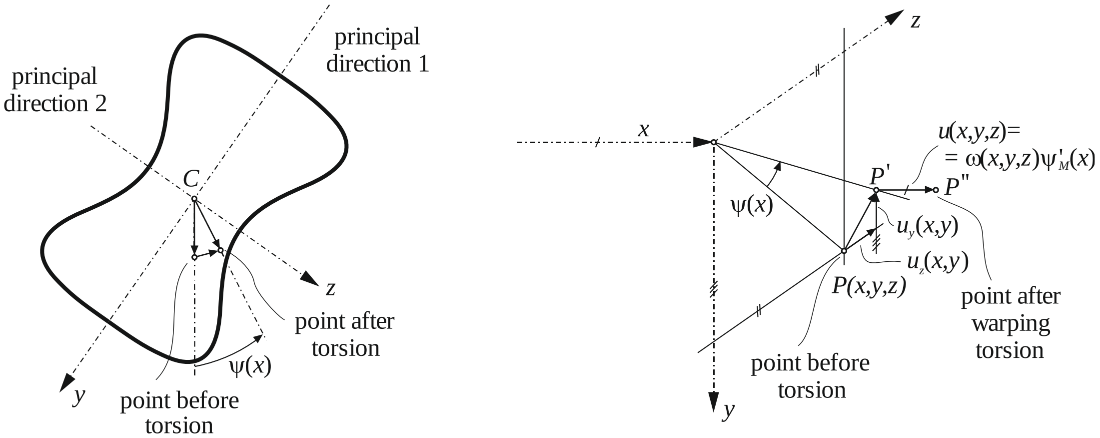

Fig. 1. Kinematics of arbitrary point in the warping free cross-section

After expressing the components of the displacement vector of the selected cross-section, the components of the normal stresses, $\sigma(x,y,z)$, and the shear stresses, $\tau(x,y,z)$, using Hooke's law, we get the resulting relations for their calculation of normal and shear stresses:

$$\sigma(x,y,z) = E(x,y,z)\left[\frac{\partial\omega(x,y,z)}{\partial x}\left(\frac{M_{Tp}(x)}{GI_T(x)} - \frac{M_{Ts}(x)}{GI_{Ts}(x)}\right) - \omega(x,y,z)\frac{M_\omega(x)}{EI_\omega(x)}\right], \qquad (1)$$

$$\begin{aligned}\tau_{xy}(x,y,z) &= G(x,y,z)\gamma_{xy}(x,y,z)\\ &= G(x,y,z)\left(\left(\frac{\partial\omega(x,y,z)}{\partial y} - z\right)\frac{M_{Tp}(x)}{GI_T(x)} - \frac{\partial\omega(x,y,z)}{\partial y}\frac{M_{Ts}(x)}{GI_{Ts}(x)}\right),\end{aligned} \qquad (2)$$

$$\begin{aligned}\tau_{xz}(x,y,z) &= G(x,y,z)\gamma_{xy}(x,y,z)\\ &= G(x,y,z\ )\left(\left(\frac{\partial\omega(x,y,z)}{\partial z} + y\right)\frac{M_{Tp}(x)}{GI_T(x)} - \frac{\partial\omega(x,y,z)}{\partial z}\frac{M_{Ts}(x)}{GI_{Ts}(x)}\right).\end{aligned} \qquad (3)$$

The warping ordinate function is denoted by $\omega(x,y,z)$. The displacements of the point $P(x,y.z)$ are:

$$u_x(x,y,z) = \omega(x,y,z)\psi_M'(x) \quad \text{and} \quad u_y(x,z) = -z\psi(x), \quad u_z(x,y) = y\psi(x)\ ,$$

from which the normal and shear strains can be obtained. Finally, by use of the Hooke's law the expressions for the normal and shear stresses (1-3) have been established.

3. Conclusions

In the author's contribution, by using the proposed warping torsion FGM WT beam finite element [3, 4], the results from the non-uniform torsional analysis of thin-walled cross-section FGM beams with spatially varying material properties are presented. These results agree very well with the ones obtained by a very fine mesh of the 3D solid FE. New equations for calculation of the normal and shear stresses caused by warping torsion of the FGM beams with spatially varying stiffness are presented. The deformation effect of the secondary torsion moment and the part of the bicurvature caused by the bimoment is accounted. The warping ordinates function and its gradients, which may depend on the spatially varying material properties, are established and implemented in the calculation of normal and shear stresses. Results of numerical experiments and their verification by very fine mesh of the solid finite elements will be presented in the conference presentation It is originally shown that a strong continuous change in material properties causes significant bimoment normal stresses not only at clamped cross-section but also in the field of the beam, and also in the internal points of the cross-section. The variability of material properties in the cross-section of a twisted beam can cause the rise of the maximum stresses at other points of the cross-section than is assumed by the classical theory of warping torsion of thin-walled shafts. For this reason, its use in such cases is inappropriate. Proposed warping torsion beam finite element is very effective - the FGM beam with a longitudinal polynomial variation of the effective material properties can be modelled with only one FGM WT beam finite element. The presented equations (1-3) allow calculation of the normal and shear stress at any point of the cross-section of the beam loaded by warping torsion.

Acknowledgements

The authors gratefully acknowledge financial support by the Slovak Grant Agency of the project VEGA No. 1/0416/21 and by the Slovak Research and Development Agency under Contract no. APVV-19-0406.

References

[1] Benscoter, S., A theory of torsion bending for multicel beams, Journal of Applied Mechanics (1954) 25-34.
[2] Kugler, S., Fotiu, P.A., Murin, J., A novel GBT-formulation for thin-walled FGM-beams-structures on reference beam problem, Composite Structures 257 (2021) 113-158.
[3] Murin, J., Kugler, S., Hrabovský, J., Kutis, V., Paulech, J., Aminbaghai, M., Influence of spatially varying material properties on the bimoment normal and shear stresses by warping torsion of FGM beams, Composite Structures 256 (2021) 113043.
[4] Murin, J., Kugler, S., Hrabovský, J., Kutiš, V., Paulech, J., Aminbaghai, M., Warping torsion of FGM beams with spatially varying material properties, Composite Structures 291 (2022) 115592.
[5] Rubin, H., Torsional warping theory including the secondary torsion-moment deformation-effect for beams with constant cross-section, *Stahlbau* 74 (2005) 826-842.
[6] Vlasov, V., Thin-walled elastic beams, Israel program for scientific translations, 1961.

COMPUTATIONAL MECHANICS 2022
37th conference with international participation
Srní
November 7 - 9, 2022

On the development of Cahn-Hilliard Navier-Stokes numerical solver within OpenFOAM framework

J. Musil

Faculty of Mechanical Engineering, Czech Technical University in Prague, Karlovo nám. 13, 121 35 Praha, Czech Republic

1. Introduction

One of the most common approach used in engineering applications dealing with two-phase fluid flows is Volume-of-Fluid (VoF) method. The VoF method consists of the Navier-Stokes equations equipped with transport equation for phase interface capturing indicator function. Although the VoF method experienced considerable improvements of numerical algorithms over the years, still it relies on artificially introduced features like interface compression term or algorithmically complex geometric interface reconstruction numerical schemes.

An alternative, less common approach refers to diffuse interface models, often labeled as Cahn-Hilliard models. Those models track the interface of two phases using a smooth phase-field function allowing a diffuse transition between the physical properties from one phase to the other and circumvents modeling the jump discontinuities at the interface. The Cahn-Hilliard equations exhibit many advantages, including mass conservation, thermodynamic consistency, and a free-energy based description of surface tension with a well-established theory from non-equilibrium thermodynamics.

Moreover, Cahn-Hilliard model combined with Navier-Stokes equations can be in fact regarded as a VoF model augmented by non-linear, fourth-order diffusive term which naturally incorporates surface tension and possibly allows under-resolving of flow field in regions of less importance, thus reduction of computational time. On the other hand, the system of equations is even more strongly coupled which pose challenging issue to design efficient, provably energy-stable and ideally decoupled numerical algorithms.

The contribution presents Cahn-Hilliard Navier-Stokes (CHNS) solver being developed within the OpenFOAM framework [4]. The aim of this endeavor is to provide efficient and robust solver of two-phase fluid flows integrated in popular OpenFOAM package already equipped with adaptive-mesh-refinemet and parallelization tools. The attention is paid to the description of two possible versions of numerical algorithms utilizing block-coupling framework introduced in OpenFOAM-extend. The performance of new solvers is compared with OpenFOAM native VoF solver on a simple test case. Some possible phase-field model adjustments and modifications are outlined and future development directions are discussed.

2. Mathematical models

The VoF model is described as follows. It consists of Eq. (1)–(3), where $0 \leq \alpha \leq 1$ is the indicator function (liquid fraction in the mixture) and the property of the mixture is calculated as $\chi = \alpha\chi_1 + (1-\alpha)\chi_2$ with χ here being substituted density ρ and dynamic viscosity η and χ_1, χ_2 representing values of unmixed phases. The deviatoric stress tensor $\boldsymbol{\tau} = \eta(\alpha)[\boldsymbol{\nabla u} + (\boldsymbol{\nabla u})^T]$

expresses tangential stresses, $\boldsymbol{g}$ is the acceleration due to gravity, σ is the surface tension and $\kappa = -\boldsymbol{\nabla} \cdot (\boldsymbol{\nabla}\alpha/|\boldsymbol{\nabla}\alpha|)$ is the surface curvature. The dynamic pressure and volume-averaged velocity of the mixture are denoted by p_d and $\boldsymbol{u}$, respectively.

$$\partial_t(\rho\boldsymbol{u}) + \boldsymbol{\nabla} \cdot (\rho\boldsymbol{u} \otimes \boldsymbol{u}) + \boldsymbol{\nabla} p_d - \boldsymbol{\nabla} \cdot \boldsymbol{\tau} + (\boldsymbol{g} \cdot \boldsymbol{x})\boldsymbol{\nabla}\rho - \sigma\kappa\boldsymbol{\nabla}\alpha = \boldsymbol{0}, \tag{1}$$

$$\boldsymbol{\nabla} \cdot \boldsymbol{u} = 0, \tag{2}$$

$$\partial_t\alpha + \boldsymbol{\nabla} \cdot (\alpha\boldsymbol{u}) = 0. \tag{3}$$

The second considered model, the phase-field formulation, is represented by the system of Cahn-Hilliard Navier-Stokes equations which reads (for detailed derivation of the model, see e.g. [1])

$$\partial_t(\rho\boldsymbol{u}) + \boldsymbol{\nabla} \cdot (\rho\boldsymbol{u} \otimes \boldsymbol{u}) + \nabla \cdot (\boldsymbol{u} \otimes \boldsymbol{J}) + \boldsymbol{\nabla} p_d - \boldsymbol{\nabla} \cdot \boldsymbol{\tau} + (\boldsymbol{g} \cdot \boldsymbol{x})\boldsymbol{\nabla}\rho + \varphi\boldsymbol{\nabla}\mu = \boldsymbol{0}, \tag{4}$$

$$\boldsymbol{J} = \frac{\rho_2 - \rho_1}{2} M(\varphi)\boldsymbol{\nabla}\mu, \tag{5}$$

$$\boldsymbol{\nabla} \cdot \boldsymbol{u} = 0, \tag{6}$$

$$\partial_t\varphi + \boldsymbol{\nabla} \cdot (\varphi\boldsymbol{u}) - \boldsymbol{\nabla} \cdot (M(\varphi)\boldsymbol{\nabla}\mu) = 0, \tag{7}$$

$$\left.\begin{aligned} \mu &= \frac{\sigma}{\epsilon}F'(\varphi) - \sigma\epsilon\Delta\varphi \\ F(\varphi) &= \frac{1}{4}(\varphi^2 - 1)^2 \end{aligned}\right\} \longrightarrow \ \mu = \frac{\sigma}{\epsilon}(\varphi^3 - \varphi) - \sigma\epsilon\Delta\varphi. \tag{8}$$

Here $-1 \leq \varphi \leq 1$ is the phase-field function and the density of the mixture is calculated as $\rho = \frac{\rho_1 - \rho_2}{2}\varphi + \frac{\rho_1 + \rho_2}{2}$. The dynamic viscosity is calculated similarly. The deviatoric stress tensor, dynamic pressure and volume-averaged velocity of the mixture are $\boldsymbol{\tau}$, p_d and $\boldsymbol{u}$, respectively. The $\boldsymbol{J}$ represents mass diffusion due to the concentration differences at the phase interface, μ is chemical potential function, $F(\varphi)$ is the bulk free energy potential function, σ is the surface tension, ϵ is parameter proportional to the interface thickness, $M(\varphi)$ is the mobility parameter.

3. Numerical algorithms

3.1 interFoam

As the reference for newly developing phase-field based algorithm, the OpenFOAM solver *interFoam* based on VoF model is chosen. The solver relies on a pressure-velocity coupling PISO algorithm when solving Eq. (2)–(3) in addition with solving the Eq. (1) which is achieved by means of the MULES explicit solver based on the FCT technique. The detailed description can be found in e.g. [3].

3.2 chnsCoupledFiMuFoam

In the first variant of presented phase-field algorithm Eq. (9)–(10) are substituted in the Eq. (3) in the original *interFoam* solver. The Eq. (9)–(10) are solved by means of block-matrix coupling framework available in foam-extend fork. The variables in $[\cdot]^{n+1}$ are solved implicitly, while the ones in $(\cdot)^{n+1}$ are updated by iterative loop. Then PISO algorithm for updating pressure and velocity follows.

$$\frac{[\varphi]^{n+1} - \varphi^n}{\delta t} + \boldsymbol{\nabla} \cdot ([\varphi]^{n+1}\boldsymbol{u}^n) - \boldsymbol{\nabla} \cdot (M(\varphi^{n+1})\boldsymbol{\nabla}[\mu]^{n+1}) = 0, \tag{9}$$

$$[\mu]^{n+1} = \frac{\sigma}{\epsilon}\Big((\varphi^{n+1})^2 - 1\Big)[\varphi]^{n+1} - \sigma\epsilon\Delta[\varphi]^{n+1}. \tag{10}$$

3.3 *chnsCoupledFiMuPdFoam*

The second variant of the phase field algorithm uses slightly modified pressure-velocity decoupled approach proposed in [2]. The system of Eq. (11)–(14) is solved by block-matrix coupling till congvergence is reached. Then, with use of updated mass flux of Eq. (15) the momentum equation (16) is solved only once.

$$\frac{[\varphi]^{n+1}-\varphi^{n}}{\delta t}+\boldsymbol{\nabla}\cdot([\varphi]^{n+1}\boldsymbol{u}_*)-\boldsymbol{\nabla}\cdot(M(\varphi^{n+1})\boldsymbol{\nabla}[\mu]^{n+1})=0, \tag{11}$$

$$\boldsymbol{u}_*=\frac{\rho^{n}\boldsymbol{u}^{n}}{\rho^{n+1}}-\frac{\delta t}{\rho^{n+1}}\Big(\varphi^{n+1}\boldsymbol{\nabla}[\mu]^{n+1}+\boldsymbol{\nabla}[p_d]^{n+1}+(\boldsymbol{g}\cdot\boldsymbol{x})\boldsymbol{\nabla}[\varphi]^{n+1}\Big), \tag{12}$$

$$\boldsymbol{\nabla}\cdot\boldsymbol{u}_*=0, \tag{13}$$

$$[\mu]^{n+1}=\frac{\sigma}{\epsilon}((\varphi^{n+1})^2-1)[\varphi]^{n+1}-\sigma\epsilon\Delta[\varphi]^{n+1}, \tag{14}$$

$$\boldsymbol{J}^{n+1}=\frac{\rho_2-\rho_1}{2}M(\varphi^{n+1})\boldsymbol{\nabla}\mu^{n+1}, \tag{15}$$

$$\frac{\rho^{n+1}[\boldsymbol{u}]^{n+1}-\rho^{n+1}\boldsymbol{u}_*}{\delta t}+\boldsymbol{\nabla}\cdot(\rho^{n+1}\boldsymbol{u}_*\otimes[\boldsymbol{u}]^{n+1})+\boldsymbol{\nabla}\cdot(\boldsymbol{u}_*\otimes\boldsymbol{J}^{n+1})-\boldsymbol{\nabla}\cdot[\boldsymbol{\tau}]^{n+1}=0. \tag{16}$$

4. Numerical results

Both two above mentioned versions of CHNS algorithms were tested on the simple 2D case of two collapsing water droplets. The computational domain is a square $\Omega=[0,0.1]^2$. The droplets of radii $r=0.01$ m are each distanced from the domain center horizontally by 0.025 m. The droplets are collapsed together by opposite horizontal velocities of magnitude $|\boldsymbol{u}|=0.05$ m/s. The boundary conditions were set as: $\boldsymbol{u}=\boldsymbol{0}$, $\boldsymbol{\nabla}p_d\cdot\boldsymbol{n}=0$, $\boldsymbol{\nabla}\varphi\cdot\boldsymbol{n}=0$, $\boldsymbol{\nabla}\mu\cdot\boldsymbol{n}=0$. The parameters in the model are chosen as $\rho_1=1\,\mathrm{kg/m^3}$, $\rho_2=10^3\,\mathrm{kg/m^3}$, $\eta_1=10^{-3}\,\mathrm{Pa\cdot s}$, $\eta_2=1.8\times10^{-5}\,\mathrm{Pa\cdot s}$. The surface tension is set as $\sigma=0.07\,\mathrm{kg/s^2}$ and interface thickness $\epsilon=10^{-3}$ m. The mobility parameter was considered constant: $M(\varphi)=M=10^{-6}\,\mathrm{kg^{-1}m^3s^{-1}}$. The gravity was not taken into account and the fluid flow was considered laminar. As a reference, the case was also computed with *interFoam* solver with the same corresponding physical parameters and boundary conditions ($\boldsymbol{\nabla}\alpha\cdot\boldsymbol{n}=0$).

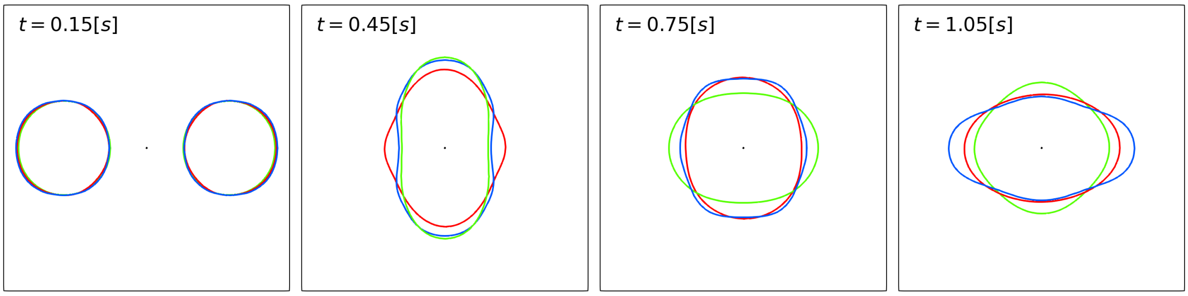

Fig. 1. Time evolution of collapsing droplets. The detail of (0.06×0.06) m centered square region of the original domain shows the contours of $\rho=500\,\mathrm{kg/m^3}$ (phase interface) for the solutions obtained by: • *interFoam* , • *chnsCoupledFiMuFoam*, • *chnsCoupledFiMuPdFoam*

In Fig. 1, one can see amplifying difference in the oscillating droplet shapes during the time. It has been found out that values of the mobility parameter M and the length parameter ϵ can have strong influence on the stability and speed of computations as well as the dynamics of the system.

In Fig. 2, there are plotted graphs of the relative total energy $\mathcal{E}_r(t) = \mathcal{E}(t)/\mathcal{E}(0)$, where $\mathcal{E}(t)$ being sum of total kinetic energy, gravitational potential energy and total free energy. The graphs suggest that *chnsCoupledFiMuPdFoam* performs better in the energy dissipation rate than *chnsCoupledFiMuFoam* while *interFoam* exhibits large oscillations in the total energy. This is probably caused by incompletely defined total free energy used for VoF formulation:

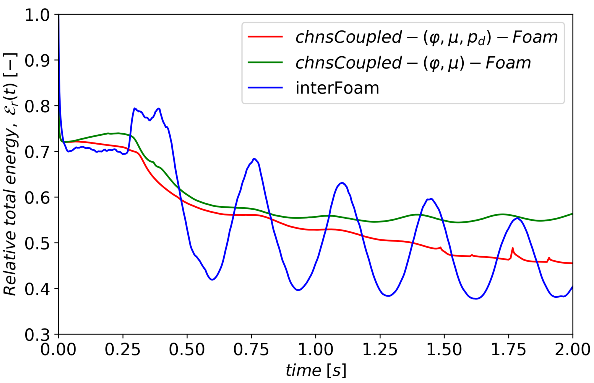

Fig. 2. Energy dissipation curves

$$\mathcal{F}_{CHNS} = \int_\Omega \left(\frac{\sigma}{\epsilon}F(\varphi) + \tfrac{1}{2}\sigma\epsilon|\nabla\varphi|^2\right)dx \qquad vs. \qquad \mathcal{F}_{VoF} = \int_\Omega \left(\tfrac{1}{2}\sigma\epsilon|\nabla\alpha|^2\right)dx \tag{17}$$

From the point of CPU efficiency, the best results were obtained by *interFoam*, up to 2 times faster than phase-field codes. But on the other hand the presented phase-field codes are sensitive to solver setting and need to be further examined and adjusted. The error of mass conservation was within 1% at the phase-field models, while at *interFoam* almost down to computer precision. The poor mass conservation of phase-field model can be caused by possibly ill posed boundary conditions.

5. Discussion

During the phase-field algorithm testing procedure it turned out that further investigation of the solver parameters setting playing crucial role in computational efficiency is needed. Future work will be focused on design of variable mobility parameter, based on grid resolution handled by adaptive-mesh-refinement and/or under-resolving flow conditions in order to fully utilize and improve the promising features of phase-field model which have not been met quite met at this stage. Other variants of coupled/segregated procedures will be considered with the aim to prove energy stability of such algorithms.

Acknowledgement

This work was supported by the Grant Agency of the Czech Technical University in Prague, grant No. SGS22/148/OHK2/3T/12.

References

[1] Abels, H., Garcke, H., Grün, G., Thermodynamically consistent, frame indifferent diffuse interface models for incompressible two-phase flows with different densities, Mathematical Models and Methods in Applied Sciences 22 (3) (2012) No. 1150013.

[2] Kou, J., Wang, X., Zeng, M., Cai, J., Energy stable and mass conservative numerical method for a generalized hydrodynamic phase-field model with different densities, Physics of Fluids 32 (11) (2020) No. 117103.

[3] Márquez Damián, S., An extended mixture model for the simultaneous treatment of short and long scale interfaces, Ph.D. thesis, National University of the Littoral, Santa Fe, 2013.

[4] Weller, H. G., Tabor, G., Jasak, H., Fureby, C., A tensorial approach to computational continuum mechanics using object-oriented techniques, Computers in Physics 12 (1998) 620-631.

COMPUTATIONAL MECHANICS 2022
37th conference with international participation
Srní
November 7 - 9, 2022

The numerical analysis of cantilever beam structures filled using aluminium foam

M. Naď, L. Rolník, P. Bucha

Faculty of Materials Science and Technology in Trnava, Slovak University of Technology in Bratislava,
Ul. Jána Bottu 25, 917 24 Trnava, Slovak Republic

The design trends in the field of civil engineering, mechanical engineering, but especially the automotive industry increasingly apply thin-walled structural components filled with foam structures mainly due to relatively low weight, possibility of achievement of the required stiffness, and also their excellent ability to absorb energy. Structural components have different shapes and are subject to different loads depending on their shape.

The beam constructions are generally classified as the most used and the most important constructions in the field of mechanical engineering. For these reasons, the specific beam structures with improved properties in terms of weight, stiffness and damping are currently being developed, which will also meet economic requirements. One of the design approaches that could meet the mentioned requirements is the creation of a beam structure with a closed cross-section, while its inner space is filled with a material with a specific structure created as aluminium foam.

The Al-foam and its material properties depend on the conditions and parameters of technological process. The global as well as the microstructural material properties of aluminium foam depend on the conditions and parameters of the technological process by which the creation of aluminium foam is achieved. From a global point of view, the properties as mass and stiffness of aluminium foam, which are crucial for the design of constructions from components filled using aluminium foam, are dominantly dependent on the size and distribution of cavities in structure of aluminium foam. On the basis of knowledge, it can be concluded that when using existing technological procedures, it is not possible to achieve either the same size of cavities or a deterministically arranged distribution of cavities in the volume of aluminium foam. However, this fact significantly complicates the possibilities for creating computational models and performing numerical simulations on virtual models of structures made of components with an aluminium foam structure. In principle, it is not possible to practically carry out computational simulations with the fact that the computational models of the foam structure would contain cavities created in detail in the volume of aluminium foam [1], [2]. This is due to the stochastic nature of the shape and also the distribution of cavities, but mainly due to the size of the computational model of the given structure. One of the possibilities to overcome these complications is the homogenization of the properties of the foam structure [3], i.e. determine the necessary equivalent mechanical properties of the homogenized volume without cavities, which replace the volume of the foam structure with cavities. The method of determining the equivalent mechanical properties of the homogenized aluminum foam structure is presented in the article. Due to the stochasticity of the aluminum foam structure (Fig. 1), the homogenization of these mechanical properties will be performed for the deterministic structural arrangement of the cavities. The basis for performing the homogenization of mechanical properties is the assumption of elastic behavior of aluminum foam.

a b

Fig. 1. Aluminium foam; a - structure of aluminium foam; b - profile filled using aluminum foam

The homogenization of the mechanical properties of the foam structure with a deterministic distribution of cavities and with a specified dimension of the cavities is based on the creation of a basic cell with a cavity inside the cell (Fig. 2). By using these cells representing part of the foam structure, the internal space of the beam structure is filled.

The mutual dimensional parameters of the cell and the cavity are specified, considering what part of the cell volume is occupied by the cavity, which is expressed by the ratio κ of the dimensions of the cell and the cavity

$$\kappa = \frac{d_1}{a_{c1}} = \frac{r_1}{a_1}, \tag{1}$$

where d_1 is cavity diameter and a_{c1} is length of the cell edge (cube shape).

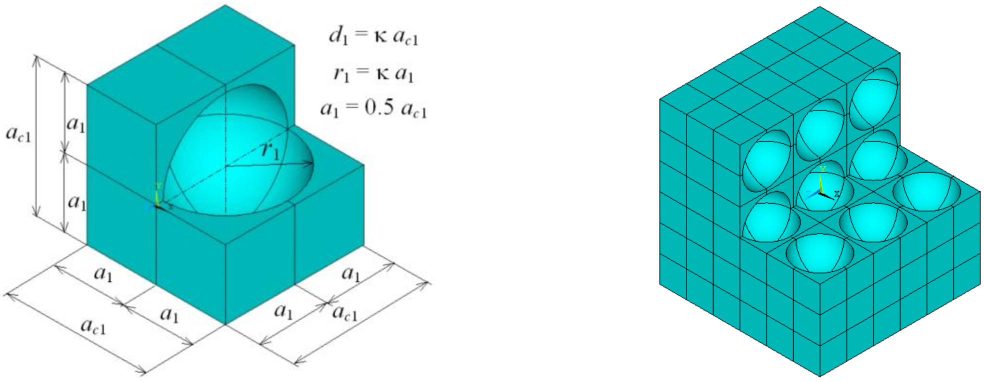

a b

Fig. 2. Computational models for homogenization of mechanical properties; a- fundamental geometry of cell with cavity; b-structural model of deterministic foam structure

The basic mechanical properties that need to be determined for the homogenized structure are Young modulus and Poisson's number. It is obvious that the homogenized mechanical properties of porous structures (Fig. 2b), which are created using deterministically arranged cells with a cavity (Fig. 2a), are dependent on the ratio κ and the number of cells in the porous structure. Therefore, computational models porous structure with the same global geometric dimensions and with different numbers of cells with cavities were created (Table 1).

Table 1. Models of porous structures

Type of structure		
T1	T2	T3
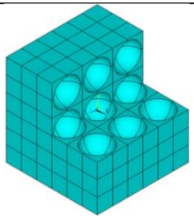	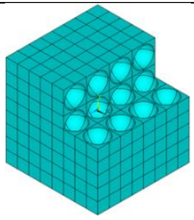	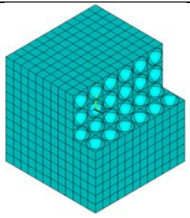

Uniaxial loading was applied to these porous sample models. Subsequently, a change in the global dimensions of the porous sample, i.e. elongation in the load direction and contraction perpendicular to the load direction. The calculation of the homogenized mechanical properties of porous structures is performed using well-known standard expressions from the theory of elasticity, so they can be expressed in the following form

- homogenized Young modulus $$E_h = \frac{F}{S}\frac{1}{\varepsilon_{x,p}}, \quad (2)$$

- homogenized Poisson´s number $$\mu_h = \frac{\varepsilon_{y,p}}{\varepsilon_{x,p}} = \frac{\varepsilon_{z,p}}{\varepsilon_{x,p}}, \quad (3)$$

where F - loading force,
S - surface on which the loading force acts,
L_x - length of the porous sample in the x-axis direction,
$\Delta L_{x,p}$ - elongation of the porous sample in the x-axis direction,
$\varepsilon_{i,p} = \Delta L_{i,p} / L_i$ - strain of the porous sample in the „i" axis direction ($i \approx x, y, z$).

The dependences of the homogenized Young modulus E_h and the homogenized Poisson's number μ_h of aluminium on volume ratio κ_V for different types of cavities arrangement are shown on Fig. 4 and Fig. 5.

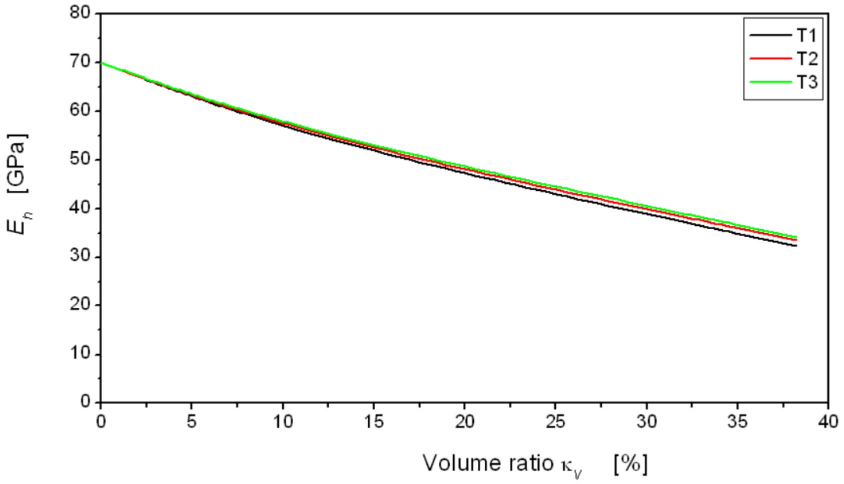

Fig. 3. Dependence of the homogenized Young modulus E_h of aluminum on the volume ratio κ_V for different types of cavity arrangement

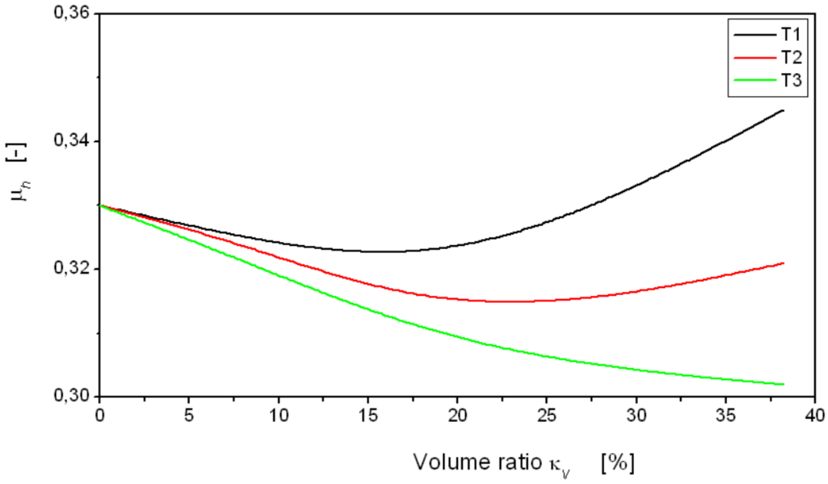

Fig. 4. Dependence of the homogenized Young modulus E_h of aluminum on the volume ratio κ_V for different types of cavity arrangement

To investigate the effect of the cavities size on the mechanical properties, the coefficient κ_V is defined, which represents the ratio of cavities volume V_c to the full material volume V_{full}

$$\kappa_V = \frac{V_c}{V_{full}}\,. \tag{4}$$

Comparison of the deformations of the cantilever beam structure filled with aluminum foam (porous material), which in the first case was modeled as a porous structure with deterministically arranged cavities and in the second case the beam filling was modeled from a non-porous material with homogenized mechanical properties, are shown in Fig. 5.

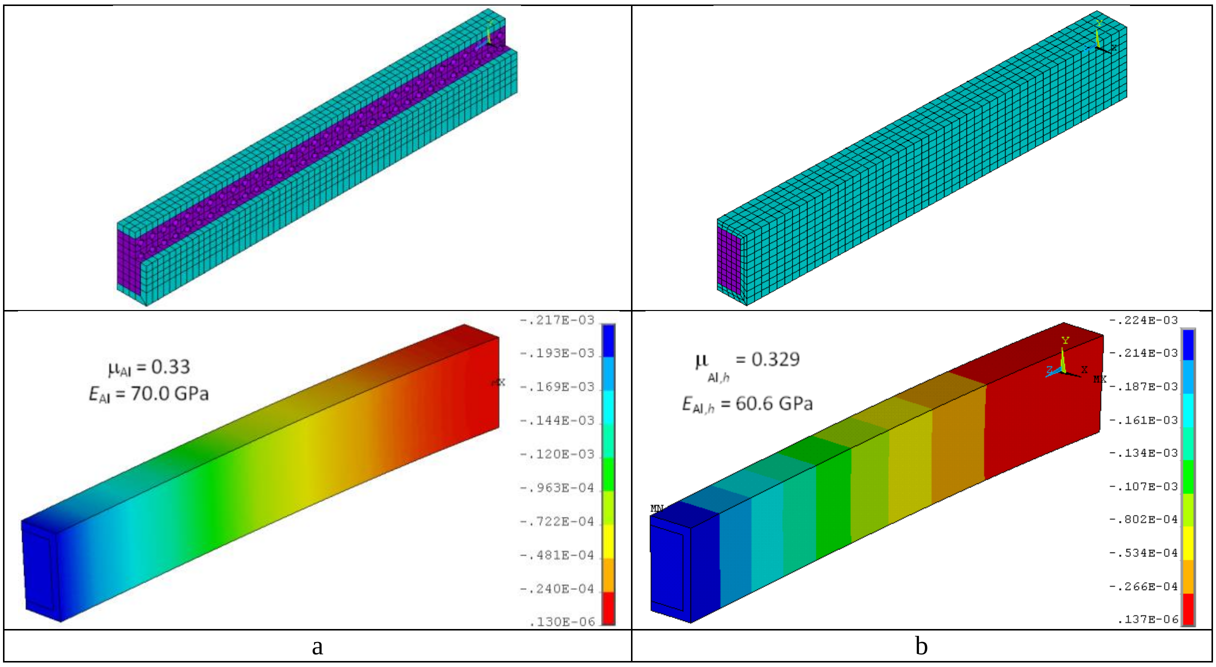

a

b

Fig. 5. Deflection of cantilever beam filled aluminium foam; a-porous model; b-homogenized model

Based on the obtained results, it can be concluded that a good agreement was obtained for the bending of the beam filled with aluminum foam, which was modeled in the first case as a porous material and in the second case as a model with homogenized mechanical properties. The above-mentioned methodology for modeling mechanical structures filled with porous material by homogenizing the filling and replacing it with homogenized mechanical properties provides, in addition to good agreement of results, a significant reduction in the size of the simulation models and the resulting reduction in calculation times.

Acknowledgements

The work has been supported by the research project KEGA 009STU-4/2021.

References

[1] Bırsan, M., Sadowski, T., Marsavina, L., Linul, E., Pietras, D., Mechanical behavior of sandwich composite beams made of foams and functionally graded materials, Journal of Solids and Structures 50 (2013) 519–530.

[2] Harte, A.M., Fleck, N.A, Ashby, M.F., Sandwich panel design using aluminum alloy foam, Advanced Engineering Materials 2 (4) (2000) 2019-2022.

[3] Zarei, H.R., Kröger, M., Bending behavior of empty and foam-filled beams: Structural optimization, International Journal of Impact Engineering 35 (2008) 521–529.

COMPUTATIONAL MECHANICS 2022
37th conference with international participation
Srní
November 7 - 9, 2022

Analysis of van der Pol equation on slow time scale for combined random and harmonic excitation

J. Náprstek, C. Fischer

Institute of Theoretical and Applied Mechanics of the Czech Academy of Sciences, Prosecká 76, 190 00 Prague, Czech Republic

1. Introduction

Vortex shedding represents one of the most important processes that constantly attract the attention of experimental and theoretical research. A number of non-linear effects arise from the fluid-structure interaction. The non-stationary response in the vicinity of the lock-in region has a quasi-periodic character, beating frequency of which varies considerably with the distance from the lock-in frequency. This property is significantly affected by the assumption of combined random and harmonic excitation. This paper describes several details that contribute to the probabilistic characteristics of the system on a time-slow scale using partial response amplitudes.

2. Mathematical model

The problem is defined by a strongly nonlinear SDOF oscillator with additive excitation combining deterministic and random components, see Fig. 1.

The nonlinear response properties can be captured by means of the van der Pol equation. The assumed configuration makes the trivial solution unstable and the limit cycle stable. Thus it can represent the beating effects and stabilization due to a stable limit cycle. The corresponding Stochastic Differential Equation (SDE) can be written in the normal form

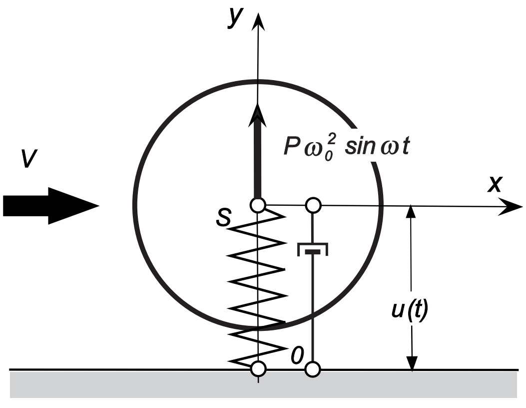

Fig. 1. SDOF system outline

$$\begin{aligned} \dot{u} &= v, \\ \dot{v} &= (\eta - \nu u^2)v - \omega_0^2 u + P\omega^2 \cos\omega t + h\xi(t), \end{aligned} \tag{1}$$

where

$u, v -$ the displacement, [m], and velocity, [m s^{-1}];
$\eta, \nu -$ parameters of the damping, [s^{-1}], [s^{-1}m^{-2}];
$\omega_0, \omega -$ the eigen-frequency of the linear SDOF system and frequency of the vortex shedding, [s^{-1}];
$P\omega^2, \xi(t) -$ the amplitude of the harmonic excitation force, [ms^{-2}], and the broadband Gaussian random process, [1];
$h -$ the multiplicative constant, [m s^{-2}].

3. Slow-time system

In order to apply the stochastic averaging method [1, 3], displacement and velocity $u(t), v(t)$ can be written in the form of the first harmonic approximate

$$u(t) = a_c \cos \omega t + a_s \sin \omega t \,, \qquad v(t) = -a_c \omega \sin \omega t + a_s \omega \cos \omega t \tag{2}$$

together with an auxiliary condition, which reflects the fact that an additional variable was introduced

$$\dot{a}_c \cos \omega t + \dot{a}_s \sin \omega t = 0 \,. \tag{3}$$

Such an approximation leads to an SDE system for amplitudes $a_c(\tau), a_s(\tau)$ slowly variable in time

$$\begin{aligned}\dot{a}_c = & \frac{\omega_0^2 - \omega^2}{\omega} \sin \omega t (a_c \cos \omega t + a_s \sin \omega t) - P\omega \sin \omega t \cos \omega t - \frac{h}{\omega} \sin \omega t \cdot \xi(t) \\ & - \sin \omega t [\eta - \nu (a_c \cos \omega t + a_s \sin \omega t)^2](-a_c \sin \omega t + a_s \cos \omega t),\end{aligned} \tag{4a}$$

$$\begin{aligned}\dot{a}_s = & - \frac{\omega_0^2 - \omega^2}{\omega} \cos \omega t (a_c \cos \omega t + a_s \sin \omega t) + P\omega \cos^2 \omega t + \frac{h}{\omega} \cos \omega t \cdot \xi(t) \\ & + \cos \omega t [\eta - \nu (a_c \cos \omega t + a_s \sin \omega t)^2](-a_c \sin \omega t + a_s \cos \omega t) \,,\end{aligned} \tag{4b}$$

which gives rise to the Itô averaged system

$$\mathrm{d}a_c = \frac{\pi}{\omega} \left[\ \eta a_c + 2\Delta a_s - \frac{1}{4} \nu \cdot a_c (a_c^2 + a_s^2) \right] \mathrm{d}t + \left(\frac{\pi}{\omega^2} \Phi_{\xi\xi}(\omega) \right)^{1/2} \mathrm{d}B_c(t), \tag{5a}$$

$$\mathrm{d}a_s = \frac{\pi}{\omega} \left[-2\Delta a_c + \eta a_s - \frac{1}{4} \nu \cdot a_s (a_c^2 + a_s^2) \right] \mathrm{d}t + \frac{\pi}{\omega} P\omega \ \mathrm{d}t + \left(\frac{\pi}{\omega^2} \Phi_{\xi\xi}(\omega) \right)^{1/2} \mathrm{d}B_c(t), \tag{5b}$$

where $B_c(t)$ is the Wiener process related with input excitation $\xi(t)$.

The closed form solution to Eq. (5) is available for vanishing detuning, $\Delta = 0$, see [2].

4. Fokker-Planck equation

The reduced FPE for the stationary cross PDF $p(a_c, a_s)$ (left side of the FPE is put to zero) can be written in the form

$$\begin{aligned} & \frac{\partial}{\partial a_c} \left(\Big[\quad \eta a_c + \Delta a_s - \frac{1}{4} \nu \cdot a_c (a_c^2 + a_s^2) \Big] p \right) & - \frac{1}{2\omega^2} \Phi_{\xi\xi}(\omega) \frac{\partial^2 p}{\partial a_c^2} \\ + & \frac{\partial}{\partial a_s} \left(\Big[- \Delta a_c + \eta a_s - \frac{1}{4} \nu \cdot a_s (a_c^2 + a_s^2) + P\omega \Big] p \right) & - \frac{1}{2\omega^2} \Phi_{\xi\xi}(\omega) \frac{\partial^2 p}{\partial a_s^2} = 0 \end{aligned} \tag{6}$$

with zero boundary conditions at the infinity. The unknown PDF is assumed to have the form

$$p(a_c, a_s) = p_0(a_c, a_s) \sum_{k,l=0}^{M,k} q_{kl} \cdot a_c^{k-l} \cdot a_s^l \,. \tag{7}$$

In this expression, $p_0(a_c, a_s)$ represents the weight function and is selected in the form of the FPE solution for zero detuning, see [2],

$$p_0(a_c, a_s) \ = \ C \cdot \exp \left(\frac{\eta}{2S} \left[\left(a_s + \frac{P\omega}{\eta} \right)^2 + a_c^2 - \frac{\nu}{8\eta} \left(a_c^2 + a_s^2 \right)^2 \right] \right) \,. \tag{8}$$

The normalizing factor C is to be determined numerically for a particular setting of parameters, it can be considered $C = 1$. The powers of a_c, a_s are assembled to form stochastic moments of k-th order sequentially up to the M-th level; they function as correction terms.

In order to deretmine coefficients $q_{k,l}$ using the Galerkin-Petrov orthogonalization, the approximate solution Eq. (7) is introduced into the FPE, Eq. (6), multiplied by the factor $\varphi_{rs} = a_c^{r-s} \cdot a_s^s$ and integrated in the whole plane $\mathbb{R}$

$$\begin{aligned}
&\iint\limits_{-\infty}^{\infty} a_c^{r-s} a_s^s \frac{\partial}{\partial a_c}\left(\left(\eta a_c + \Delta a_s - \frac{1}{4}\nu a_c(a_c^2 + a_s^2)\right) p_0(a_c, a_s)\sum_{k,l=0}^{M,k} q_{kl} a_c^{k-l} a_s^l\right) \mathrm{d}a_c \mathrm{d}a_s \\
+&\iint\limits_{-\infty}^{\infty} a_c^{r-s} a_s^s \frac{\partial}{\partial a_s}\left(\left(-\Delta a_c + \eta a_s - \frac{1}{4}\nu a_s(a_c^2 + a_s^2) + P\omega\right) p_0(a_c, a_s)\sum_{k,l=0}^{M,k} q_{kl} a_c^{k-l} a_s^l\right) \mathrm{d}a_c \mathrm{d}a_s \qquad (9) \\
-&\iint\limits_{-\infty}^{\infty} a_c^{r-s} a_s^s S\left[\frac{\partial^2}{\partial a_c^2} + \frac{\partial^2}{\partial a_s^2}\right]\left(p_0(a_c, a_s)\sum_{k,l=0}^{M,k} q_{kl} a_c^{k-l} a_s^l\right) \mathrm{d}a_c \mathrm{d}a_s \;=\; 0, \quad S \;=\; \frac{1}{2\omega^2}\Phi_{\xi\xi}(\omega)\,.
\end{aligned}$$

Here, M is the upper limit of stochastic moments we want to include into the analysis.

Several steps of the per-partes procedure and usage of homogeneous boundary conditions and particular forms of the $p_o(a_c, a_s)$ partial derivatives lead to a formula, which is applicable for the combined analytical-numerical integration

$$\begin{aligned}
0 = &\iint\limits_{-\infty}^{\infty} \Bigg\{ \left[a_c^{\varrho-2} a_s^{s-2} \left(\varrho(\varrho-1) a_s^2 - s(s-1) a_c^2\right) S + \Delta a_c a_s \left(\varrho a_s^2 - s a_c^2\right)\right] \sum_{k,l=0}^{M,k} q_{kl} a_c^{k-l} a_s^l \\
&- S\left[s\frac{\mathrm{d}}{\mathrm{d}a_s}\left(a_c^{\varrho} a_s^{s-1} \sum_{k,l=0}^{M,k} q_{kl} a_c^{k-l} a_s^l\right) - \varrho\frac{\mathrm{d}}{\mathrm{d}a_c}\left(a_c^{\varrho-1} a_s^{s} \sum_{k,l=0}^{M,k} q_{kl} a_c^{k-l} a_s^l\right)\right]\Bigg\} p_0(a_c, a_s) \mathrm{d}a_c \mathrm{d}a_s\,, \qquad (10) \\
&s = 0, .., r\,, \quad r = 0, .., M\,, \quad \varrho = (r - s)\,.
\end{aligned}$$

Further simplification of the expression (10) follows from the symmetry of the problem, so that the terms involving even powers of a_c vanish during integration. Eq. (10) represents a linear homogeneous algebraic system for $1/2 \cdot (M + 1)(M + 2)$ unknown coefficients $q_{kl}, k, l = 0, .., M; k + l \leq M$.

Eq. (10) degenerates for $s = 0, r = 0$. This missing condition can be replaced by Eq. (7), where setting $M = 0$ implies $q_{00} = 1$. This is equivalent to the condition of normalization of the resulting PDF.

Performance of the proposed procedure is shown in Fig. 2. Both partial amplitudes a_c, a_s are shown for six values $M = 0, \ldots, 5$. In each plot, the estimated PDF $p(a_c, a_s)$ is shown on the left and the value of the correction Galerkin term on the right. It can be seen that the value of the correction term within the selected domain of (a_c, a_s) increases for increasing M from approx. $\pm 5\%$ to approx. $\pm 10\%$ for $M = 5$.

5. Conclusions

The proposed procedure for estimation of PDF based on the partial amplitudes was shown on the example of the van der Pol equation, which was used for description of the vibrational effects based on the flow-structure interaction and vortex shedding. Sinmilar procedure is applicable to a variety of similar problems, namely those connected to traffic induced almost-resonant vibrations, identification problems and other system which work in a regime close to resonance.

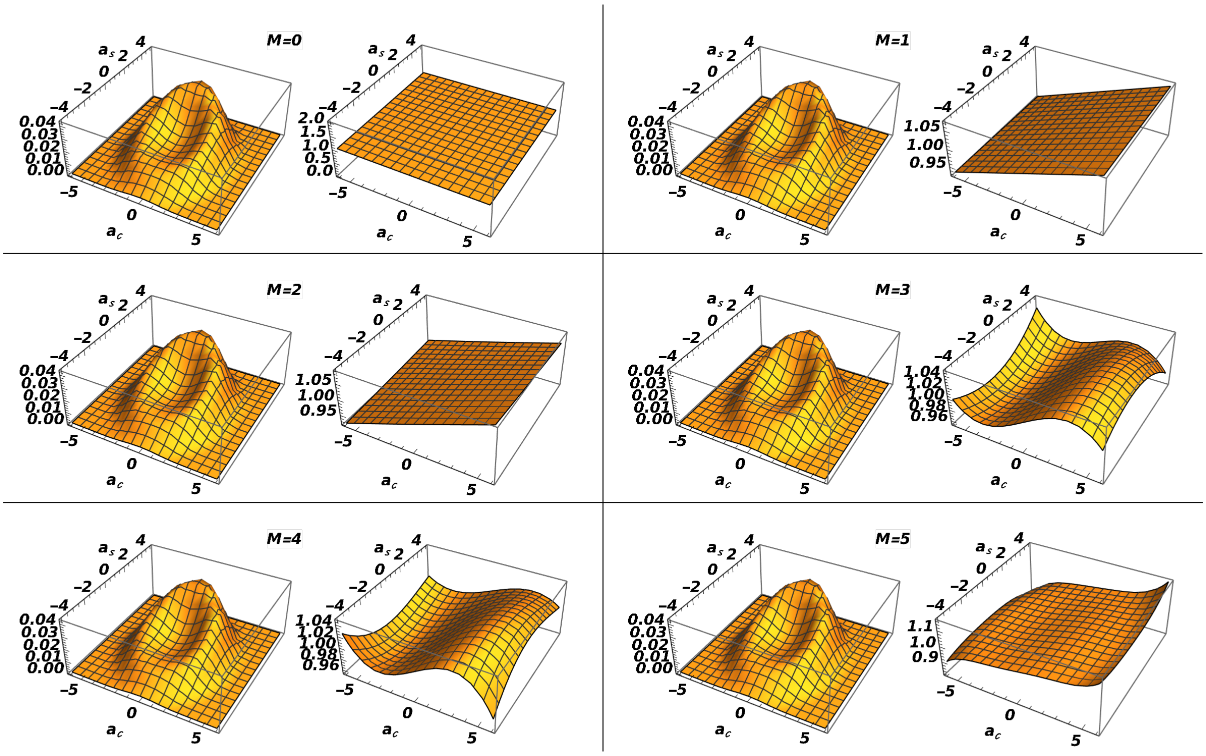

Fig. 2. Values of probability density function Eq. (7) for increasing value of M. Each pair of plots shows the Galerkin solution $p(a_c, a_s)$ on the left and the correction term value $\sum_{k,l=0}^{M,k} q_{kl} a_c^{k-l} a_s^l$ on the right. Values used: $\Delta = 0.05, \eta = 1.6, \nu = 1, P = 1, S = 4$

The approach based on the partial amplitudes, however, is based on a knowledge of the stationary solution of the corresponding FPE. For a really general approach, the dependence on the original time coordinate must be respected. For this purpose, the correction terms used for the Galerkin approximation has to encompass the time dependency. This topic is going to be further elaborated in the future.

Acknowledgements

The kind support of Czech Science Foundation project No. 21-32122J and of the RVO 68378297 institutional support are gratefully acknowledged.

References

[1] Lin, Y. K., Cai, G. Q., Probabilistic structural dynamics, New York, McGraw-Hill, 1995.

[2] Náprstek, J., Fischer, C., Pospíšil, S., Trush, A., Modeling of the quasi-periodic galloping response type under combined harmonic and random excitation, Computers & Structures 247 (2021) No. 106 478.

[3] Pugachev, V. S., Sinitsyn, I. N., Stochastic differential systems – Analysis and filtering, Chichester, John Willey, 1987.

COMPUTATIONAL MECHANICS 2022
37th conference with international participation
Srní
November 7 - 9, 2022

Construction of the Lyapunov function reflecting the physical properties of the model

J. Náprstek, C. Fischer

Institute of Theoretical and Applied Mechanics of the Czech Academy of Sciences, Prosecká 76, 190 00 Prague, Czech Republic

1. Introduction

Practical experience shows that the random excitation component can affect the system response and its dynamic stability not only negatively but also positively. For example, the presence of a certain artificially generated turbulence component can have a positive effect against the occurrence of resonance. Such mechanisms are usually developed heuristically and are often not sufficiently justified theoretically. On the other hand, the presence of random excitation can lead to dangerous interactions with deterministic processes and thus cause a reduction in the level of dynamic stability in conditions that do not seem serious at first sight (icing on cables or power lines, road roughness, etc.).

In the sense presented by Bolotin [1], the deterministic LF (as the total time derivative of a positive definite function), is replaced in the stochastic domain by the adjoint Fokker-Planck (FP) operator

$$\mathbf{L}\{\lambda(t,\mathbf{u})\} \;=\; \frac{\partial\lambda(t,\mathbf{u})}{\partial t} + \sum_{i=1}^{n}\frac{\partial\lambda(t,\mathbf{u})}{\partial u_i}\kappa_i + \frac{1}{2}\sum_{i,j=1}^{n}\frac{\partial^2\lambda(t,\mathbf{u})}{\partial u_i\partial u_j}\kappa_{ij}, \tag{1}$$

where κ_i, κ_{ij} are the drift and diffusion coefficients of the n-dimensional Markov process and m depends on the system structure

$$\kappa_i = \sum_{k=1}^{m} A_{ik}(t) f_{ik}(\mathbf{u}) + \frac{1}{2}\sum_{k,l=1}^{m}\sum_{p=1}^{n}\frac{\partial f_{ik}(\mathbf{u})}{\partial u_p} f_{ip}(\mathbf{u})\cdot s_{iklp}\,, \quad \kappa_{ij} = \sum_{k,l=1}^{m} f_{ik}(\mathbf{u}) f_{jl}(\mathbf{u})\cdot s_{ikjl}\,. \tag{2}$$

Eqs. (1) and (2) relate to the original stochastic system, the stochastic stability of which is being assessed

$$\dot{u}_i \;=\; \sum_{k-1}^{m}(A_{ik}(t) + w_{ik}(t)) f_{ik}(\mathbf{u}); \quad \mathbf{u}(t_0) \;=\; \mathbf{u}_0, \tag{3}$$

where $\lambda(t,\mathbf{u})$ is the LF candidate, $A_{ik}(t)$ are the nominal values of the system coefficients, $w_{ik}(t)$ is the Gaussian white noise of cross-intensity s_{ikjl}, and $f_{ik}(\mathbf{u})$ are the continuous non-decreasing functions.

Function $\lambda(t,\mathbf{u})$ should be a continuous positive definite. Its derivatives $\partial_t\lambda(t,\mathbf{u})$ and $\partial_{\mathbf{u},\mathbf{u}}\lambda(t,\mathbf{u})$ should be continuous as well. Let $\psi(t,\mathbf{u}) = \mathbf{L}\{\lambda(t,\mathbf{u})\} < 0$ in $\mathbf{u} \in \mathbf{\Omega}$ and $\psi(t,0) = 0$ or $\psi(t,0)$ is not defined, $\lambda(t,\mathbf{u})$ can be considered a Lyapunov function. Thus, for any $||\mathbf{u}_0|| \neq 0$ function $\lambda(t,\mathbf{u})$ decreases for $t \to \infty$ and, consequently, the trivial solution of Eq. (3) is stable in terms of probability.

It should be emphasized that an inappropriate choice of the form of the Lyapunov function can lead to inconsistent results. Therefore, it should be designed very carefully. However, it is well known that there is no universal method for constructing the Lyapunov function in either the deterministic or the stochastic case.

2. Construction of the Lyapunov function

Let us assume that the following first integrals $J_1, \dots J_s$ satisfy the equations of motion

$$J_1(\mathbf{u}) = C_1, ..., J_s(\mathbf{u}) = C_s\,. \tag{4}$$

The Lyapunov function can be selected as a linear combination of the first integrals and their functions. The most convenient selection for practical purposes will obviously be

$$\lambda(\mathbf{u}) = \sum_{i=1}^{s} a_i[J_i(\mathbf{u}) - J_i(0)] + b_i[J_i^2(\mathbf{u}) - J_i^2(0)], \tag{5}$$

where a_i, b_i are unknown constants that must be selected so that the function (5) satisfies the conditions of the positive definiteness.

The first integrals of the type (4) are most often found in the context of cyclic coordinates. In such cases, the corresponding Lagrange equation simplifies considerably

$$\frac{d}{dt}\frac{\partial T}{\partial \dot{u}_k} \;=\; D_k + \Gamma_k, \tag{6}$$

where D_k and Γ_k are dissipative and gyroscopic forces, respectively, and T is the kinetic energy.

If the system is subjected to Gaussian parametric random white noises, the system has a form

$$\mathbf{L}\{T\} = -\sum m \cdot \Theta_m, \tag{7}$$

where $\mathbf{L}\{\cdot\}$ is the adjoined FP operator and Θ_m are the homogeneous functions of phase coordinates and white noise intensities active in the system. The stability assessment procedure is then similar to the deterministic case.

3. Stability of a spherical pendulum

A spherical pendulum moves at a constant velocity around a vertical axis in the coordinates φ (angle around the vertical axis) and ξ (angle between the vertical axis and the pendulum suspension) in a horizontal circle, see, e.g., [2]. Small random perturbations of this movement can be denoted as u_1, u_3, see Fig. 1,

$$\xi = \alpha + u_1\;; \quad \dot{\xi} = u_2\;; \quad \dot{\varphi} = \omega + u_3, \tag{8}$$

where α is the angle between the suspension and the vertical in deterministic state $\omega^2 l \cdot \cos\alpha = g$, ω is the angular velocity of a circular motion and l denotes the length of the suspension. The perturbations u_1, u_2, u_3 are assumed to be small.

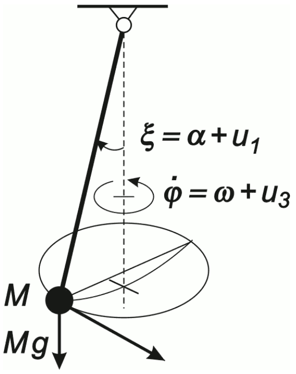

Fig. 1. Outline of a pendulum with coordinates

Two first integrals can be obtained from the general principles of dynamics—total energy $T + \Pi$ and the total momentum

$$T + \Pi = \frac{1}{2}Ml^2(\dot{\xi}^2 + \dot{\varphi}^2 \cdot \sin^2\xi) - Mgl \cdot \cos\xi\,, \tag{9a}$$

$$\frac{\partial T}{\partial \dot{\varphi}} = Ml^2\dot{\varphi} \cdot \sin^2\xi\,. \tag{9b}$$

Using Eqs. (9), it is possible to construct the Lyapunov function in the form of Eq. (5) and examine the stability of the pendulum movement. In the given case, it is sufficient to use the first part of Eq. (5), i.e., $b_i = 0\ (i = 1, 2)$, which means

$$\lambda(u_1, u_2, u_3) = a_1\left(J_1(\mathbf{u}) - J_1(0)\right) + a_2\left(J_2(\mathbf{u}) - J_2(0)\right)\,, \tag{10}$$

where J_1, J_2 are written in the form originating from the substitution of Eqs. (8) into Eqs. (9)

$$\begin{aligned} J_1(\mathbf{u}) &= \frac{1}{2}Ml^2\left(u_2^2 + (\omega + u_3)^2\sin^2(\alpha + u_1) - \frac{2g}{l}\cos(\alpha + u_1)\right)\,, \\ J_2(\mathbf{u}) &= \quad Ml^2\left(\,(\omega + u_3)\sin^2(\alpha + u_1)\,\right)\,. \end{aligned} \tag{11}$$

We shall select the parameters a_1, a_2 in the form of

$$a_1 = 2\left(Ml^2\right)^{-1}\,, \quad a_2 = a\left(Ml^2\right)^{-1}\,.$$

where a should be determined from the constraint of positive definiteness of the function λ. Substitution of Eqs. (9) and (11) into (10), and the assumption that $u_i, i = 1, 2, 3$ are small, yield

$$\begin{aligned} \lambda(u_1, u_2, u_3) =& u_1^2\omega\left((a + \omega)\cos 2\alpha + \omega\cos^2\alpha\right) + u_2^2 + u_3^2\sin^2\alpha + \\ & u_1\omega(a + 2\omega)\sin 2\alpha + u_3(a + 2\omega)\sin^2\alpha + u_1u_3(a + 2\omega)\sin 2\alpha + \dots \end{aligned} \tag{12}$$

To make function $\lambda(u_1, u_2, u_3)$ positive definite, it is necessary to eliminate perturbations u_i in the first power. This occurs if $a = -2\omega$. Function λ as a Lyapunov function, thus, takes the form

$$\lambda(u_1, u_2, u_3) = (u_1^2\cdot\omega^2 + u_3^2)\sin^2\alpha + u_2^2 + \mathcal{O}(u_i^3)\,. \tag{13}$$

The Lagrange equations of motion can be determined using the expressions for T, Π

$$\begin{gathered} \ddot{\xi} - \dot{\varphi}^2\sin\xi\cos\xi + \frac{g}{l}\sin\xi = \mu l(\xi - \alpha)w(t)\,, \\ \ddot{\varphi} + 2\dot{\varphi}\dot{\xi}\cdot\cot\xi = 0\,, \end{gathered} \tag{14}$$

where parametric (white) noise $w(t)$ has been introduced into the first equation. Its effect is proportional to the deviation from the basic inclination α. In Eqs. (14) we shall substitute for $\xi, \dot{\xi}, \dot{\varphi}$ according to Eqs. (8) and modify this system into the normal form for u_1, u_2, u_3

$$\begin{aligned} \dot{u}_1 &= u_2\,, \\ \dot{u}_2 &= (\omega + u_3)^2\sin(\alpha + u_1)\cos(\alpha + u_1) - \omega^2\cos\alpha\,\sin(\alpha + u_1) + \mu l u_1 w(t)\,, \\ \dot{u}_3 &= -2u_2(\omega + u_3)\,\cot(\alpha + u_1)\,. \end{aligned} \tag{15}$$

In a linearized form

$$\begin{aligned} \dot{u}_1 &= u_2\,, \\ \dot{u}_2 &= (\omega^2\cos 2\alpha - \frac{g}{l}\cos\alpha)u_1 + \omega\sin 2\alpha\cdot u_3 + \mu l u_1 w(t)\,, \\ \dot{u}_3 &= -2u_2\cdot\omega\,\mathrm{cotg}\alpha\,. \end{aligned} \tag{16}$$

The general stochastic system is assumed to have a form

$$\dot{u}_i = f_i(\mathbf{u}) + \sum_{k=1}^{m} h_{ik}(\mathbf{u})\cdot w_k(t) \quad ; \quad \mathbf{u}(t_0) = \mathbf{u}_0\,, \tag{17}$$

where the diffusion coefficients κ_i, κ_{ij} are as follows:

$$\kappa_i = f_i(\mathbf{u}) \; ; \; \kappa_{ij} = \sum_{k,l=1}^{m} h_{ik}(\mathbf{u}) h_{jl}(\mathbf{u}) \cdot s_{kl} \, . \tag{18}$$

In this particular case, the respective coefficients (with $m = 1$) are

$$h_{1,1} = h_{3,1} = 0 \, , \; h_{2,1} = \mu l u_1 \, ; \qquad f_1 = \dot{u}_1 \, , \; f_2 = \dot{u}_2 - h_{2,1} w(t) \, , \; f_3 = \dot{u}_3 \, . \tag{19}$$

The first two parts of the adjoined FP operator (1) are equivalent to the total time derivative of the Lyapunov function in the deterministic domain and only the third term with the coefficients κ_{ij} represents a supplement introducing the influence of random parametric noises. Their influence on the stability of the system Eqs. (17) is determined, consequently, exclusively by the character of matrix $\mathbf{h}(\mathbf{u})$ and joint links of white noises $w_i(t)$. If, for instance, $w_i(t)$ are independent white noises $(s_{ij} = 0, i \neq j)$, the parametric noises are of destabilizing character only. However, it is also possible to construct such $\mathbf{h}(\mathbf{u})$ matrices where the random noises contribute to improve the stability of the system.

In the case of the spherical pendulum described by Eqs. (15) and LF (13), we obtain

$$\begin{aligned} \psi(\mathbf{u}) =& \, \mathbf{L}\{\lambda(t, \mathbf{u})\} \\ =& \, 2u_1 u_2 \omega^2 \sin^2\alpha + 2u_2 \left(\frac{1}{2}(\omega + u_3)^2 \sin 2(\alpha + u_1) - \omega^2 \cos\alpha \, \sin(\alpha + u_1) \right) - \\ & - 4u_2 u_3 (\omega + u_3) \sin^2\alpha \, \cot(\alpha + u_1) + u_1^2 \cdot (\mu l)^2 s_{11} \, . \end{aligned} \tag{20}$$

The destabilizing effect of the noise $w(t)$ is obvious. The stability of the system, therefore, depends on the character of other right-hand side terms of Eq. (20). If we construct the function $\psi(\mathbf{u})$ on the basis of the linearized version of the normal system Eqs. (16), the right-hand side of Eq. (20) will disappear except for the last term as a result of the character of the first integrals. This means that in the linearized state the system is not stable. It can be stabilized by inserting dissipative forces or by an adequate selection of the matrix $\mathbf{h}(\mathbf{u})$ and the characteristics of $w_i(t)$ which, naturally, are determined by the physical character of the actual system.

4. Conclusion

The Lyapunov function constructed on the basis of first integrals provides a possibility to work with the stochastic part of the problem with a much greater overview and to construct mathematical models with regard to the stabilizing or destabilizing effects of parametric random noises. Such properties are due to the fact that the structure of the actual system is fully applied to the very construction of the basic form of the function. This type of analysis is applicable to a variety of dynamic stability problems, including naturally the problem of signal and noise separation in structural health monitoring and various indirect measuring methods.

Acknowledgements

The kind support of Czech Science Foundation project No. 21-32122J and of the RVO 68378297 institutional support are gratefully acknowledged.

References

[1] Bolotin, V. V., Random vibrations of elastic systems, Springer, Netherlands, 1984.
[2] Eiserman, M. A., Classical mechanics, Nauka, Moscow, 1980. (in Russian)

COMPUTATIONAL MECHANICS 2022
37^{th} conference with international participation
Srní
November 7 - 9, 2022

EMA-driven model updating based on material homogenization

J. Otta[a], M. Šudoma[b]

[a] ZF Friedrichshafen AG, 88038 Friedrichshafen, Germany
[b] ZF Engineering Plzeň s.r.o., Macháčkova 24, 318 00 Plzeň, Czech Republic

1. Introduction

The printed circuit boards (PCB) are complex geometrical and functional systems connecting electronic components for communication between them. PCBs also play an important role in protecting these components from their damage. It takes the form of a laminated sandwich structure of conductive copper layers and base material which is acting as an insulator. The base material FR-4 is made from a flame retardant epoxy resin and glass fabric, cf. Fig. 1.

The printed circuit boards used in automotive industry are exposed to vibration-, static- and thermal-loadings. Field failures in electronic equipment hardware over a period of 20 years show that these failures are related to connectors, to interconnects, and to component parts. Around 20% of field failures related to operating environments are related to vibration- and shock- loading, [8]. During testing on shakers, the components must survive the load conditions according to the LV 124 / LV148 Automotive Test Standard, [3].

To avoid failure in operation environment, virtual testing of PCBs based on the dynamic models of the printed circuit boards is performed. For that reason, it is important to use in the simulation validated dynamic models of the PCBs whose system responses correlate with the hardware experiment.

To achieve this, modal updating based on global optimization of surrogate model is performed. As a reference are used eigenshapes and eigenfrequencies from the experimental modal analysis (EMA).

2. Experimental modal analysis

The experimental modal analysis was performed with free-free boundary conditions by placing the PCB on the foam, see Fig. 1. The specimen was excited using an automatic impulse hammer (type: PCB 086E80), vibrations were measured by 1D doppler laser vibrometer (type: Polytec PSV 400-H4) in 175 sampling measurement points, see Fig. 1.

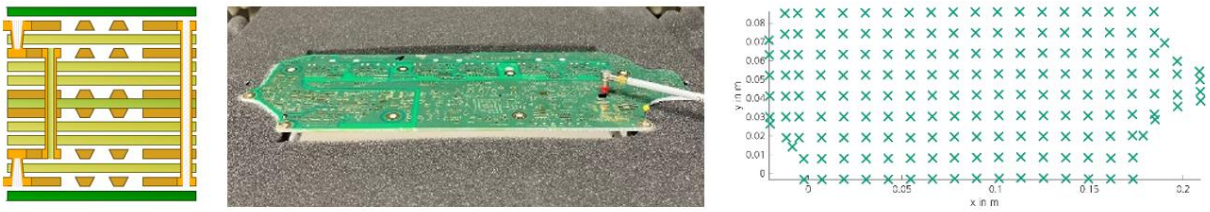

Fig. 1. PCB cross section (solder mask, copper foil, FR4 prepreg, FR4 core), measurement set-up and measurement points [4]

Table 1. Results from EMA – summary of eigenfrequencies, [4]

Mode [-]	Frequency [Hz]	Mode [-]	Frequency [Hz]	Mode [-]	Frequency [Hz]
1	140	7	827	13	1577
2	207	8	927	14	1796
3	350	9	1089	15	2007
4	446	10	1153	16	2209
5	652	11	1311	17	2313
6	777	12	1527	18	2366

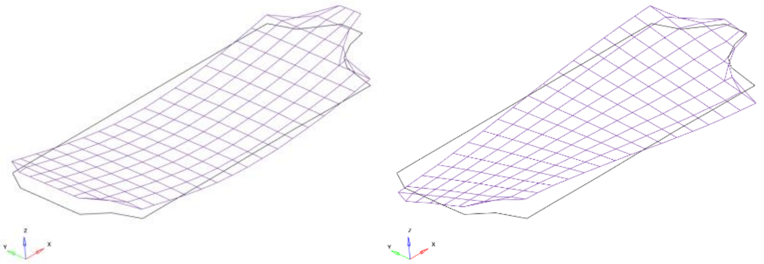

Fig. 2 Example of measured eigenshapes (mode#01, mode#02)

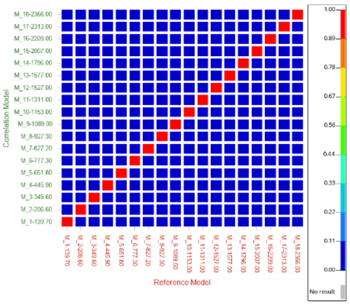

Fig. 3. AutoMAC matrix with proper choice of evaluation points

In total, 18 eigenshapes have been extracted in the frequency range 20-2500Hz, see Table 1. Example of the eigenshapes can be found on Fig. 2 together with AutoMAC matrix showing proper choice of the evaluation points (off-diagonal terms evince very low values).

AutoMAC is a special case of the modal assurance criterion (MAC) that is used to correlate simulation data with experimental data. The MAC is calculated as the normalized L$_2$-scalar product of the two sets of vectors $\{\varphi_r\}$ and $\{\varphi_s\}$. The resulting scalars are arranged into the MAC matrix as follows

$$MAC(\{\varphi_r\},\{\varphi_s\}) = \frac{\left|\{\varphi_r\}^T\{\varphi_s\}\right|^2}{(\{\varphi_r\}^T\{\varphi_r\})(\{\varphi_s\}^T\{\varphi_s\})}\,. \tag{1}$$

If the MAC value is 1 (red color), then eigenshapes $\{\varphi_r\}$ and $\{\varphi_s\}$ are identical, if MAC is equal to 0, eigenshapes are not correlating. MAC values above 0.8 are considered as indicator of high correlation, [6].

3. Model updating

3.1. Method description

The model updating approach is based on the idea of tuning unknown parameters of the FE-model such as material parameters, damping, stiffness variation. The choice of these uncertain parameters is based on the performing parametric space sampling in some optimal manner. Afterwards relevant parameters having highest influence on the change of eigenshapes and eigenfrequencies are identified. Change of the eigenshapes is evaluated using MAC whereas set of the selected reference eigenshapes is taken from the experiment.

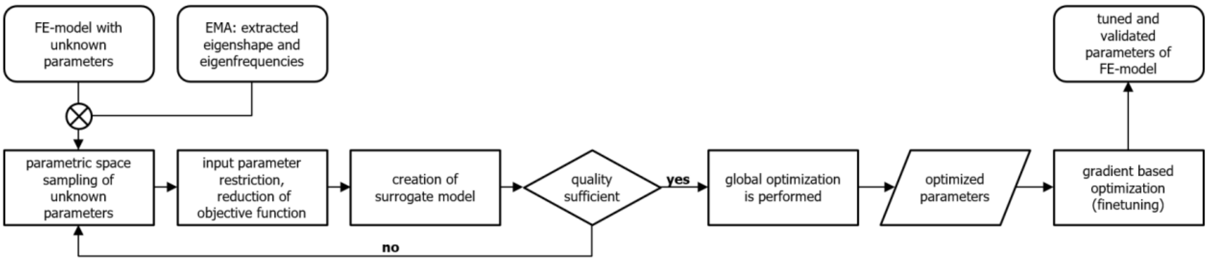

Fig. 4. Model updating workflow

This is followed by the creation of a surrogate model, and if its quality is high in some mathematical or physical sense, global optimization can be performed to maximize correlation of eigenshapes and eigenfrequencies.

Since the optimum is found on surrogate model which could deviate from the results of the real FE-models, authors propose to perform gradient based optimization in the FE-solver with initial conditions given by the global minimum from surrogate model. The output from this last step are tuned and validated parameters of FE-model.

3.2. Method Application and Results

As an input were used all 18 measured eigenshapes and eigenfrequencies extracted from experimental modal analysis, cf. Tab 1. Finite element model of the PCB was created using hexahedral 1st order elements (28523 elements, 58144 nodes) and one element across the thickness with orthotropic material (MAT90RT) defined by parameters E_X, E_Y, E_Z, G_{XY}, G_{YZ}, G_{ZX}, ν_{XY}, ν_{YZ}, ν_{ZX}.

The normal modal analysis was performed for first 30 eigenshapes evaluated in normal direction (Z-axis) in same points as in the measurement, cf. Fig. 1.

For the space filling scheme in DoE study was used Modified Extensible Lattice Sequence (MELS), that equally spreads out points in a space by minimizing clumps and empty spaces, [1]. A total of 250 FE-model variants were simulated for input parameters constrained by material stability conditions, [5]:

$$E_i > \nu_{ij}^2 E_j \ , \tag{2}$$

$$1 - \nu_{12}\nu_{21} - \nu_{23}\nu_{32} - \nu_{31}\nu_{13} - 2\nu_{21}\nu_{32}\nu_{13} > 0 \ . \tag{3}$$

Since the simulation tasks are independent from each other, parallel execution of the tasks was performed. During these simulations responses such as eigenfrequency and MAC were monitored. Eigenshapes between EMA and FE-model were paired by mode tracking tool.

Using a pareto plot, it was identified that the Youngs modulus in planar directions E_X and E_Y and the planar shear modulus G_{XY} of the FR-4 material have the highest influence on MAC and eigenfrequencies.

Relative dense sampling of parameter space allows to derive surrogate model for relevant input parameters by automatic selection of the approximation methods as least squares, moving least squares, radial basis function (depends on the best approximation). During this phase, the R^2 parameter was monitored. Fitting functions with R^2 less than 0,95 were neglected due to credibility [1]. For this reason, 14 eigenshapes (eigenfrequencies and MAC values) were used as an input for subsequent global optimization method instead of 18 measured from EMA.

For searching global minimum on the surrogate model the genetic algorithm was chosen. Objective function was selected as weighted sum of squares of relative differences:

$$\min \sum_{i=1}^{n} w_i \left(\frac{f_i - \tilde{f}_i}{\tilde{f}_i} \right)^2 , \tag{4}$$

where f_i stands for i-th eigenfrequency of optimized model and $\tilde{f}_i$ are reference of i-th eigenfrequency from EMA, weighting factor w_i takes values from 0 to 1. As a constraint was used MAC with threshold value of 0.8.

In the last step, gradient-based optimization of the FE-model was performed with same objective as in the global optimization.

Comparison of the baseline material properties known from literature [4] with EMA is showing relative good correlation of the eigenshapes but evinces large deviations of the eigenfrequencies. The results of updated FE-model show low differences of the corresponding eigenfrequencies but with several degraded MAC values, see Table 2 and Fig. 5.

Table 2. Results from EMA – summary of eigenfrequencies, [4]

	Frequency [Hz]			**Freq. diff. [%]**		**MAC [-]**	
pair #	EMA (target)	Before opti..	After opti.	Before opti.	After opti.	Before opti.	After opti.
1	**140**	100	**129**	28.6	**7.6**	0.96	**0.96**
2	**207**	179	**213**	13.5	**2.9**	0.99	**0.99**
3	**350**	265	**341**	24.3	**2.6**	0.93	**0.93**
4	**446**	384	**466**	13.9	**4.6**	0.97	**0.97**
5	**652**	486	**620**	25.5	**5.0**	0.96	**0.96**
6	**777**	624	**778**	19.7	**0.1**	0.85	**0.96**
7	**827**	643	**865**	22.2	**4.6**	0.87	**0.97**
8	**927**	722	**922**	22.1	**0.5**	0.91	**0.90**
9	**1089**	827	**1097**	24.1	**0.7**	0.91	**0.86**
10	**1152**	918	**1160**	20.3	**0.6**	0.92	**0.90**
11	**1311**	1034	**1329**	21.1	**1.4**	0.92	**0.90**
12	**1527**	1159	**1518**	24.1	**0.6**	0.83	**0.77**
13	**1576**	1250	**1573**	20.7	**0.2**	0.85	**0.80**
14	**1796**	1411	**1816**	21.4	**1.1**	0.89	**0.86**

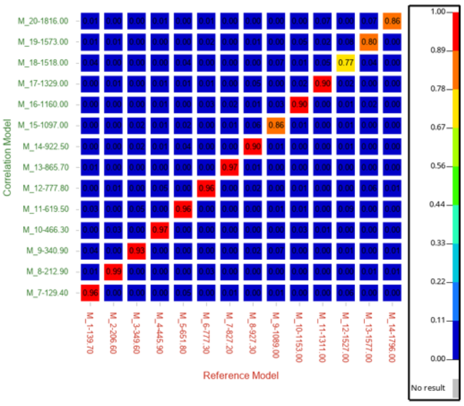

	M_1-139.70	M_2-206.60	M_3-349.60	M_4-445.90	M_5-651.80	M_6-777.30	M_7-827.20	M_8-927.30	M_9-1089.00	M_10-1153.00	M_11-1311.00	M_12-1527.00	M_13-1577.00	M_14-1796.00
M_20-1816.00	0.01	0.00	0.00	0.01	0.00	0.01	0.00	0.00	0.00	0.00	0.07	0.00	0.07	0.86
M_19-1573.00	0.01	0.01	0.00	0.00	0.00	0.02	0.00	0.01	0.00	0.05	0.02	0.08	0.80	0.00
M_18-1518.00	0.04	0.00	0.00	0.00	0.04	0.00	0.00	0.00	0.07	0.01	0.05	0.77	0.04	0.00
M_17-1329.00	0.00	0.01	0.00	0.01	0.01	0.01	0.00	0.05	0.00	0.02	0.90	0.02	0.00	0.00
M_16-1160.00	0.00	0.00	0.00	0.01	0.00	0.03	0.02	0.01	0.03	0.90	0.00	0.01	0.02	0.00
M_15-1097.00	0.00	0.00	0.02	0.01	0.02	0.00	0.01	0.06	0.86	0.01	0.00	0.01	0.00	0.00
M_14-922.50	0.00	0.00	0.02	0.01	0.04	0.00	0.00	0.90	0.01	0.00	0.00	0.01	0.00	0.00
M_13-865.70	0.01	0.00	0.00	0.00	0.00	0.00	0.97	0.01	0.00	0.00	0.00	0.00	0.00	0.00
M_12-777.80	0.00	0.01	0.00	0.05	0.00	0.96	0.00	0.02	0.00	0.01	0.00	0.00	0.06	0.01
M_11-619.50	0.03	0.00	0.05	0.00	0.96	0.00	0.00	0.00	0.01	0.01	0.00	0.09	0.00	0.00
M_10-466.30	0.00	0.03	0.00	0.97	0.00	0.00	0.00	0.00	0.00	0.03	0.01	0.00	0.00	0.00
M_9-340.90	0.04	0.00	0.93	0.00	0.00	0.00	0.00	0.02	0.07	0.00	0.00	0.01	0.00	0.01
M_8-212.90	0.01	0.99	0.00	0.00	0.00	0.03	0.00	0.00	0.00	0.00	0.00	0.00	0.01	0.01
M_7-129.40	0.96	0.00	0.00	0.00	0.05	0.00	0.01	0.00	0.01	0.00	0.00	0.06	0.00	0.00

Fig. 5. MAC matrix correlation between EMA (reference model) and FE-model (correlation model) valideted material properties

4. Summary

Proposed automated workflow allows to perform model updating of relative complex structures as PCBs without consideration of detailed and time demanding models of the PCBs. Homogenized orthotropic material models simplifying complex PCB structure evince relative good correlation of the eigenshapes and eigenfrequencies which can be used in further studies as dynamic or vibration fatigue investigations.

Presented method offers robust alternative to more complex and time demanding model updating of FE-models based on locally homogenized PCBs models, cf. [4], or offers an alternative to very detailed FE-models modeling copper traces in the FR4 material, [2, 7].

Acknowledgements

The authors thank to ZF management for supporting their participation in the conference and in preparing this paper.

References

[1] Altair Engineering, Introduction into FIT approximations with Altair HyperStudy.
[2] Ansys Sherlock, https://www.ansys.com/products/structures/ansys-sherlock.
[3] Getto, R., Electric and electronic components in motor vehicles up to 3,5t – general requirements, Test Conditions and Tests, 2013, Mercedez-Benz Company Standard 2013.
[4] Hülsebrock, M., Modelling and characterization of printed circuit boards, Fraunhofer LBF 2022.
[5] Lekhnitskii, S., G., Theory of elasticity of an anisotropic elastic body, Holden-Day Inc., 1963.
[6] Randal, J., The modal assurance criterion – twenty years of use and abuse, University of Cincinnati.
[7] SimLab, https://support.altair.com/csm?id=community_blog&sys_id=2d16e3121b83c950c4dfdbd9dc4bcb11.
[8] Steinberg, D.S., Vibration Analysis for electronic equipment, John Wiley Sons, 2000.

COMPUTATIONAL MECHANICS 2022
37th conference with international participation
Srní
November 7 - 9, 2022

Stress analysis in filament wounded composite pressure vessels

Z. Padovec, D. Vondráček, T. Mareš

Czech Technical University in Prague, Faculty of Mechanical Engineering, Technická 4, 160 00, Prague, Czech Republic

Main goal of presented work is comparison of the results for cylindrical and spherical pressure vessel (manufactured by filament winding technology) obtained by analytical solution with results from finite element method (FEM). Classic lamination theory for shells is used in combination with netting theory (see [1] for an example) for determination of stresses in axial and circumferential direction. The assumptions for the solution comprise:

- an elastic material model of the composite,
- a wall thickness h that is significantly lower than the smallest radius of the shell,
- an inner pressure that leads to membrane loading in the walls of the shell,
- a composite wall that is a balanced laminate consisting of two layers with fiber orientations of $\pm\omega$ of the same thickness and volumetric fiber contents.

Cylindrical pressure vessel is manufactured with integrated domes (dome analysis is not presented in this study) with ($90/\pm\omega_0/90$) lay-up. Balanced laminated $\pm\omega_0$ creates dome, hoop winding reinforces cylindrical part of the vessel (See Fig. 1).

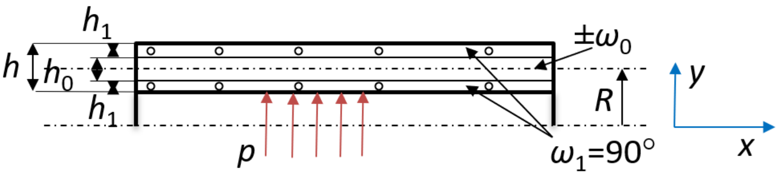

Fig. 1. Cylindrical part of pressure vessel

Thickness of layers is given by the isotensoidal condition of the construction (same stress/strain in all layers), $\pm\omega_0$ is given by the geodesic condition of the winding (ratio of polar opening r_0 and radius R of the cylindrical part of the shell – see Fig. 2).

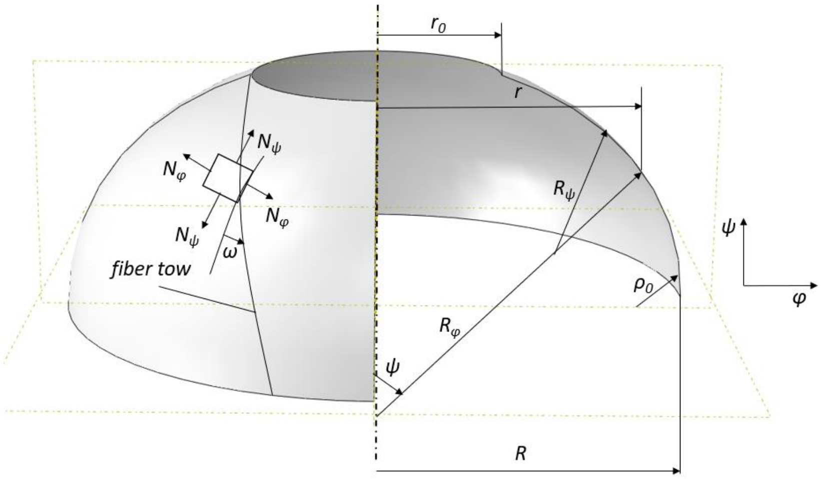

Fig. 2. The geometry and forces on the shell of the revolution of double curvature manufactured by means of helical winding

Spherical pressure vessel is manufactured with ±ω lay-up and it has maximum volume with minimum surface area [2]. Spherical shell is not isotensoid construction and compared to isotropic sphere, which is symmetrical to the centre, filament wounded sphere is symmetrical just to the axis of the rotating mandrel. For each filament wounded shell of the revolution of double curvature is typical change of thickness and winding angle along the meridian curve. Minimum thickness is on the equator, maximum thickness is near polar opening. Winding angle has its minimum on the biggest radius (equator) and its maximum (90°) near polar opening – stiffness/compliance/strength vary along meridian curve.

For computational example a cylinder/sphere manufactured from glass/epoxy system with volumetric fiber content 60 %, loaded with inner pressure 1 MPa was chosen. Polar opening radius is r_0 = 20 mm and radius R = 50 mm of the cylindrical part of the shell (or radius on sphere equator respectively). Last input parameters were thickness of hoop layers h_1 = 1 mm for case of cylindrical vessel and thickness on equator h_0 = 1 mm in case of spherical vessel. FE model was prepared in Abaqus software with the use of shell elements in spherical case and shell and continuum shell elements in cylindrical case. Comparison of calculated stress can be seen in Fig. 3 – 5 for cylindrical case and in Fig. 6 for spherical case.

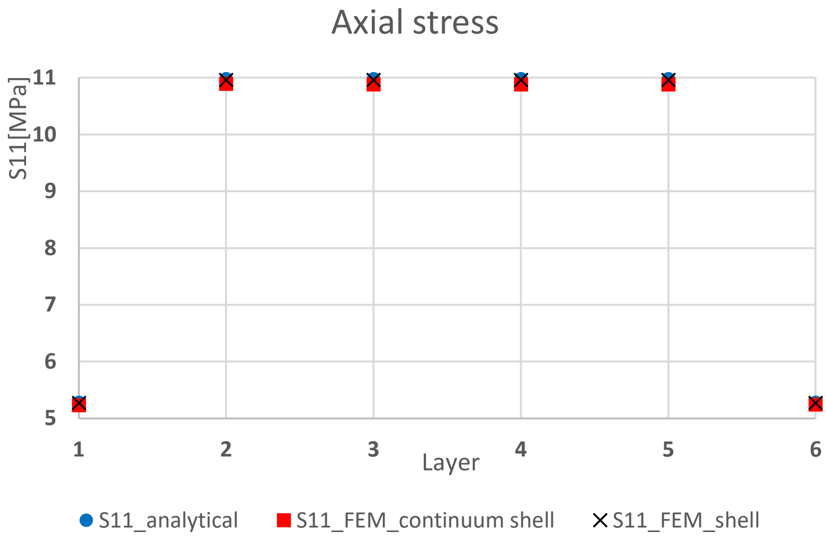

Fig. 3. Comparison of axial stress values for cylindrical case

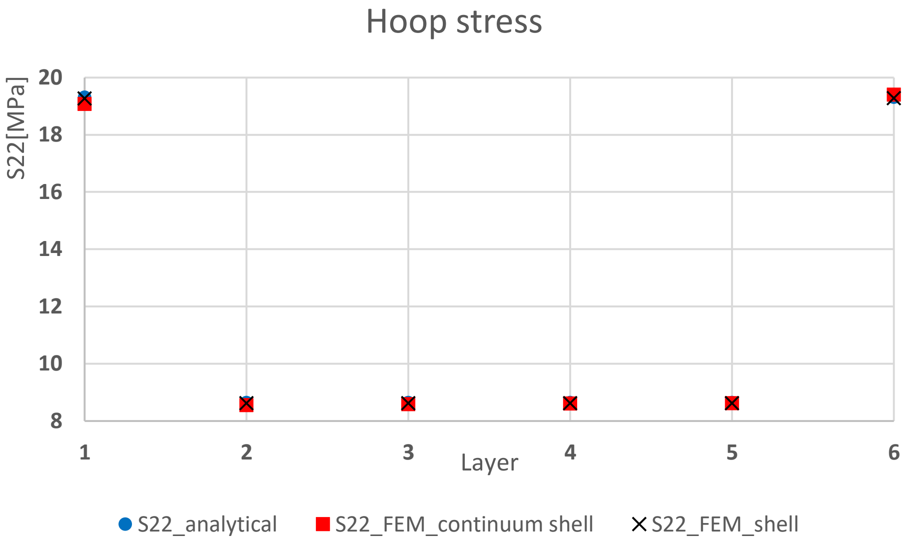

Fig. 4. Comparison of hoop stress values for cylindrical case

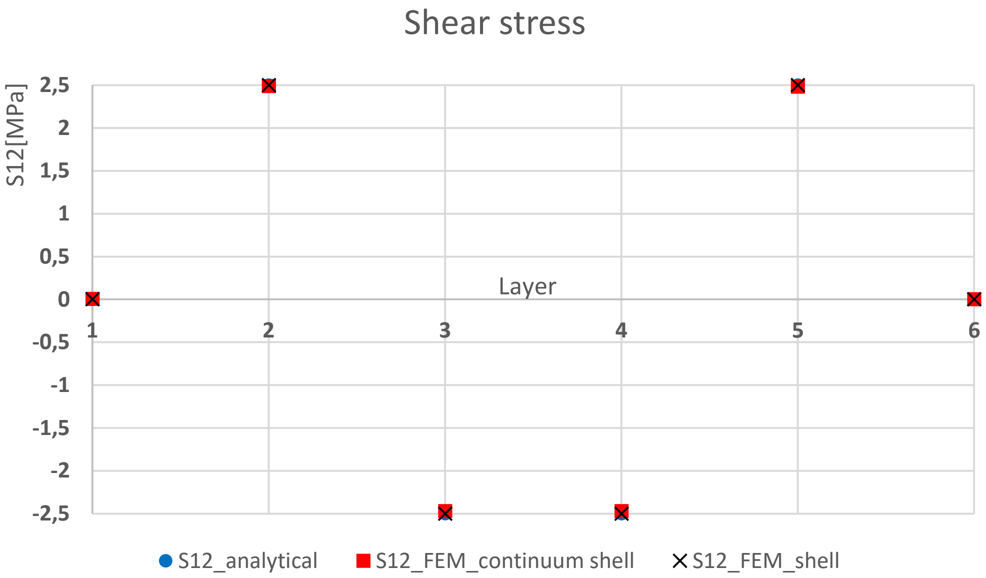

Fig. 5. Comparison of shear stress values for cylindrical case

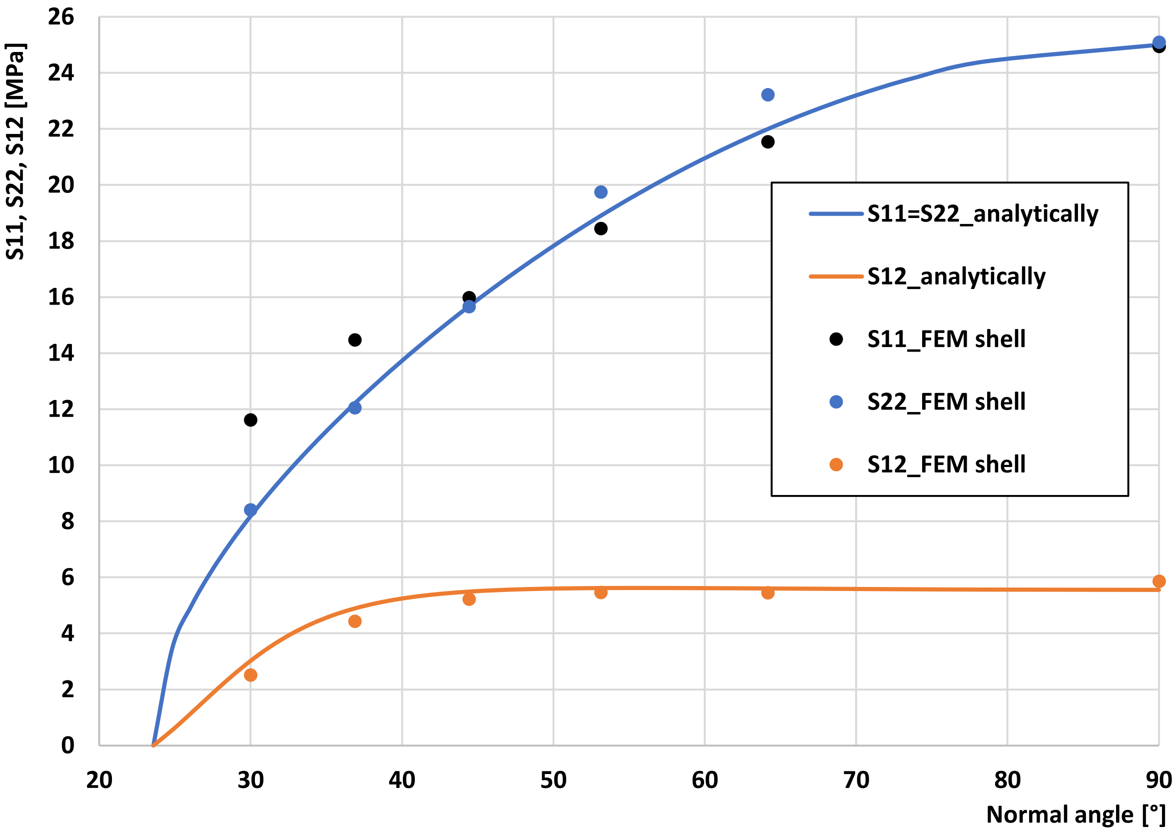

Fig. 6. Comparison of computed stress values for spherical case

The analytical computations were prepared in the MATLAB code, which allows both for the rapid determination of the results and the simple changing of the input parameters (the material, the polar hole and the equator radius, the thickness, and the inner pressure). The FEA provided comparable results to those of the analytical solution for cylindrical case, for spherical case particularly for a normal angle of ψ of 90° to 40° (the difference amounted to 10%). The areas defined with a lower normal angle of ψ were affected by the closure of the polar hole and by the discretization of areas with the same thickness.

Acknowledgements

This work has been supported by the Grant Agency of the Czech Technical University in Prague, under grant No. SGS21/151/OHK2/3T/12.

References

[1] Young, R., E., History and potential of filament winding, Proceedings of 13th Annual Technical Conference SPI – RP, Chicago, sect. 15 – C 1958.

[2] Vasiliev, V., V., Composite pressure vessels: Design, analysis and manufacturing, Bull Ridge Publishing, Blacksburg, 2009.

COMPUTATIONAL MECHANICS 2022
37th conference with international participation
Srní
November 7 - 9, 2022

On a class of biped underactuated robot models with upper body: Sensitivity analysis of the walking performance

Š. Papáček[a], P. Polach[b], R. Prokýšek[c], M. Anderle[a]

[a] *Czech Academy of Sciences, Institute of Information Theory and Automation, Pod vodárenskou věží 4, 182 08 Prague, Czech Republic*
[b] *Research and Testing Institute Plzeň Ltd., Tylova 1581/46, Plzeň, Czech Republic*
[c] *Department of Mechanics, Biomechanics and Mechatronics, CTU, 160 00 Prague, Czech Republic*

1. Introduction

Biped underactuated robots with an upper body (being a torso) form a subclass of legged robots. This study deals with the walking performance of such class of legged robot models and has been motivated by the need to implement of the previously developed sensor and control algorithms for the real-time movement of the laboratory walking robot, designed and built at the Department of Control Theory of the Institute of Information Theory and Automation (ÚTIA) of the Czech Academy of Sciences, see Fig. 1 (left). A detailed description of this underactuated walking-like mechanical system (called further UTIA Walking Robot – UWR) is provided in [2] and [5]. The simplest underactuated walking robot hypothetically able to walk is the so-called Compass gait biped walker, alternatively called the Acrobot, see Fig. 1 (right). For a review of underactuated mechanical systems, i.e. systems with fewer actuators than degrees of freedom, which encounter many applications in different fields (e.g., in robotics, in aeronautical and spatial systems, in marine and underwater systems, and in-flexible and mobile systems), see [3].

As follows, we examine the walking performance of parametrized models for different walking regimes and different values of model parameters. More specifically, the sensitivity analysis (i.e., parameter study) of the walking performance with respect to certain design variables (model parameters) is carried out using the software package *alaska/MultibodyDynamics*. The main attention is attracted to the role of the upper body mass m_3 and position l_{c3}, see Fig. 1 (right).

Last but not least, having surveyed the mechanics of planar biped robots, our subsequent goal is the analysis of a 3D biped model where lateral balance is either controlled, suppressed or compensated.

2. Model formulation

The robot model, see Fig. 1 (right), is planar, with two rigid massless legs of length l_l, i.e., with pointmasses (scaled masses $m_1 = m_2 = m_f = 0.1$) as feet (where scaled lengths $l_{c1} = l_{c2} = l_l = 1$), a finite pointmass (scaled mass $m_3 = 0.3$) at the hip joint (pelvis). Moreover, the upper body (a scaled pointmass $m_b = 0.7$) is connected via a rigid, massless stick (of scaled length $l_{c3} = 0.4$) to the hip joint, see Fig. 1 (right). There are two degrees of freedom mechanism for one pair of legs without knees, ankles and feet actuated only in the hips. Moreover, an additional

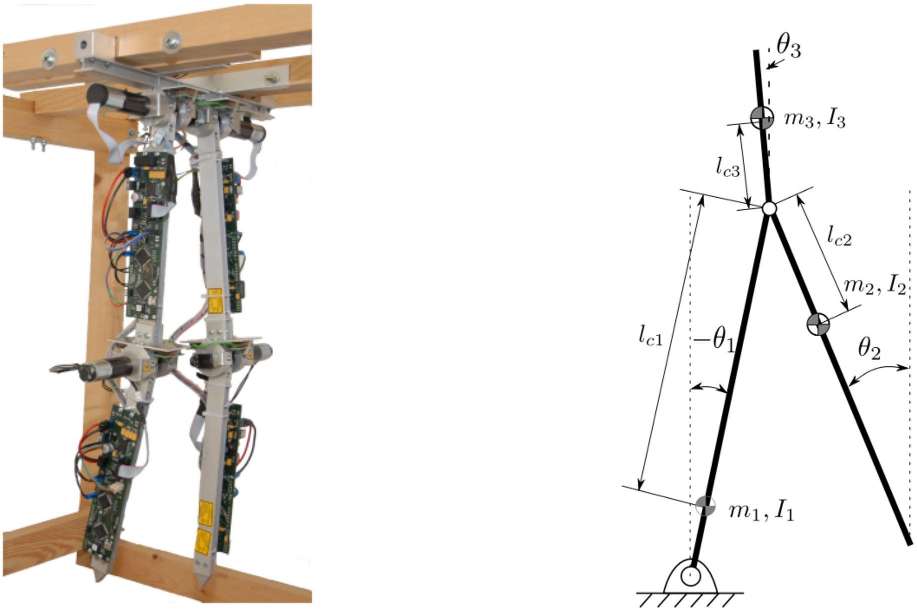

Fig. 1. (*Left*) UTIA Walking Robot: laboratory mechatronic walking robot-like system – immobile until now; (*right*) Compass gait biped walker with upper body: parameters and coordinates

(third) link is representing a torso (within the pelvis) in the human body description. Thus, there are 3 planar links in form of rigid sticks with pointmasses at the end and one degenerated point-like link of scaled mass $(1-m_b)$ which connects all 3 stick-like links together. As it was already mentioned, the mass and length parameters are dimensionless. The mass scaling is done using the total mass (pelvis + upper body), for the length scaling is used the leg length l_l.

Furthermore, it is convenient to introduce two actuated hip joints, i.e., the upper body (the torso) is not actuated. For instance, for sake of simplicity, the upper body position described by the angle θ_3 undergoes the kinematic coupling, modelled as simple as possible, i.e., the third link with upper body mass dwells in midway between the two legs

$$\theta_3 = \frac{\theta_1 + \theta_2}{2}\,. \tag{1}$$

The above restriction (1) makes the Compass gait system fully actuated and represents a starting point to more complex ones.

3. Walking performance

As it was stated in the Introduction, we aim to study the walking performance of our model for different walking regimes and different values of upper body length. This sensitivity analysis is carried out using the software package *alaska/MultibodyDynamics* [1]. The energy consumption of the model is usually represented in the non-dimensional form of specific resistance, which is defined as the energy consumption per distance traveled per kilogram mass per gravity, see [4] and references within there.

For the previously computed trajectories, we perform numerical simulations on a robot model derived from the software package *alaska/MultibodyDynamics*. Afterwards, we solve the corresponding torques at both hip joints (based on the D'Alembert principle). Finally, for this relatively simple case of a bipedal robot walking in two dimensions, we calculate how the cost functional, being the specific resistance, depends on the upper body length.

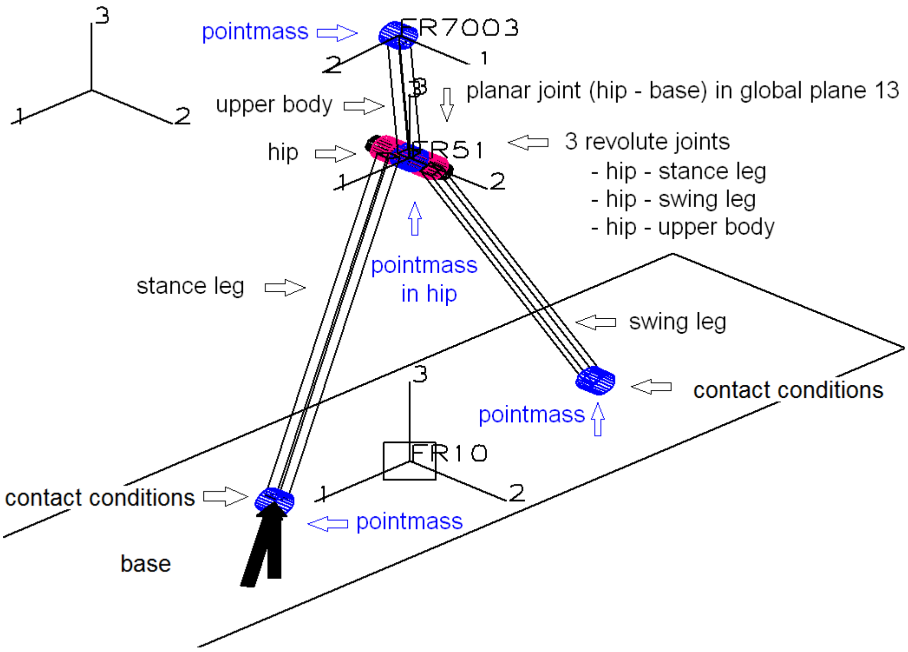

Fig. 2. Visualization of the Compass gait biped walker (with the description of kinematic joints) by Alaska 2.3 simulation tool

4. Conclusions

In this work, using the Alaska simulation tool, we studied the sensitivity of the walking performance of a class of biped robot models with respect to the upper body length. Encouraged by the successful implementation of the model kinematics, the analysis of system dynamics is conceived for the near future. In this way, we are open to the possibility of running a similar study concerning the robot model stability, or more precisely, to describe the stability of the walking for different upper body lengths. Here, the expected result is to find in some sense optimal realisation of the robot geometry for a specific walking regime. The optimization of both the robot geometry and walking regime (distribution of the torque to be applied into actuators at the hip) are left for a future publication.

Acknowledgments

The work of Milan Anderle and Štěpán Papáček was supported by the Czech Science Foundation through the research grant No. 21-03689S. The work of Pavel Polach was originated in the framework of institutional support for the long-time conception development of the research institution provided by the Ministry of Industry and Trade of the Czech Republic to Research and Testing Institute Plzeň. The work of Roman Prokýšek was supported by himself.

References

[1] Alaska 2021, alaska Reference Manual Release 2021.1, Institut fűr Mechatronik e. V., Chemnitz, 2021.

[2] Anderle, M., Čelikovský, S., On the controller implementation in the real underactuated walking robot model, Proceedings of the 12th Asian Control Conference (ASCC), Kitakyushu, Fukuoka, Japan, June 2019, pp. 91-99.

[3] Krafes, S., Chalh, Z., Saka, A., A review on the control of second order underactuated mechanical systems, Complexity 2018 (2018) No. 9573514.

[4] McGeer, T., Passive dynamic walking, International Journal of Robotics Research 9 (2) (1990) 62-82.

[5] Polach, P., Anderle, M., Papáček, Š., On the design and modeling of a trainer for the underactuated walking robot without ankles, Proceedings of 27/28th International Conference Engineering Mechanics 2022, Milovy, Czech Republic, Institute of Theoretical and Applied Mechanics of the CAS, v. v. i., 2022, pp. 309-312.

COMPUTATIONAL MECHANICS 2022
37th conference with international participation
Srní
November 7 - 9, 2022

Sensitivity analysis of thermodynamical parameters on the thermal bowed rotor using 2D finite element model

J. Pařez[a], P. Kovář[b], T. Vampola[a]

[a] Department of Mechanics, Biomechanics and Mechatronics, Faculty of Mechanical Engineering, Center of Aviation and Space Research, Czech Technical University in Prague; Technicka 4; 160 00, Prague 6; Czech Republic, Jan.Parez@fs.cvut.cz
[b] Department of Technical Mathematics, Faculty of Mechanical Engineering, Center of Aviation and Space Research, Czech Technical University in Prague; Technicka 4; 160 00, Prague 6; Czech Republic, Patrik.Kovar@fs.cvut.cz

Numerical modelling of mechanical systems is a helpful tool for system behaviour analyses. There are several well-known commercial softwares that deal with different solution areas. When interdisciplinary tasks are solved, the possibility of using software is more limited. It is due to many differences in the specific field of solutions as structural analyses, temperature distribution, heat transfer, etc. Therefore, solvers based on finite element method (FEM) are limited to a narrow group of solvable problems for the most part or they are generalized to universal problems. For specific analyses of aircraft engine rotors, a FEM solver consisted of MATLAB scripts was developed where different types and scopes of the task are implemented. Optional choice of boundary and initial conditions are possible as well. This contribution deals with a sensitivity analysis of the basic thermodynamic parameters during the operation of the aircraft engine rotor and their influence on the structural analysis and, above all, the deformation of the system.

The problem of the thermal bow has been known and solved in the field of energy for a long time. Zhuo [7] introduced a new computational method for thermal bow predicting on heavy gas turbines. The subsequent vibrations affecting the safe operation during restart of the rotor system caused by the temperature bowed rotor were presented in several works, for example in Chatterton [1], Pennacchi [4], or Marinescu [2]. In the field of aircraft engines, the rotor thermal

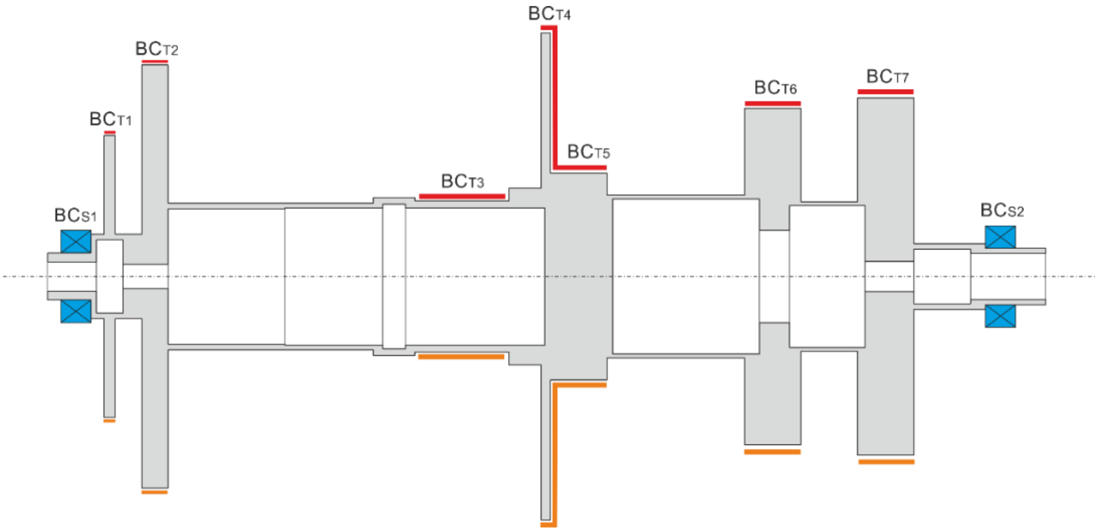

Fig. 1. Sketch of the turbine engine rotor system computational domain

deformation is very significant due to high temperature exposures and the radial clearance limitation which influences the efficiency. A significant contribution to research in this area was made by E.O. Smith in [5]. Last but not least contribution in thermal bow research, supplemented with experimental measurements by research at the Harbin Institute of Technology [6, 8].

Fig. 1 shows a sketch of simplified turbine aircraft engine rotor system computational domain including the location of prescribed boundary conditions. The two axial compressor discs on the right side are followed by a simplified model of the centrifugal compressor impeller in the centre of the rotor system. The generator turbine disc is located on the left side of the rotor system and ends with a disc of labyrinth seals.

According to the following table Table 1., initial and boundary conditions for temperature field distribution are prescribed. All listed values are given in degrees Celsius. Dirichlet boundary conditions are considered for surfaces with heat transfer and oil cooling. As mentioned above, locations of the boundary conditions are shown in the figure Fig. 1.

Table 1. Prescribed boundary condition for the turbine engine analysis

	BC_{T1}	BC_{T2}	BC_{T3}	BC_{T4}	BC_{T5}	BC_{T6}	BC_{T7}	BC_{S1}	BC_{S2}
Case 1	448	548	424	371	338	277	260	Pinned	Roller
	412	502	410	348	327	252	247		
Case 2	465	787	553	432	385	282	268	Pinned	Roller
	449	742	536	408	372	264	251		
Case 3	494	926	674	493	421	287	272	Pinned	Roller
	473	875	647	462	401	269	254		
Case 4	448	548	424	371	338	277	260	Pinned	Pinned
	412	502	410	348	327	252	247		
Case 5	465	787	553	432	385	282	268	Pinned	Pinned
	449	742	536	408	372	264	251		
Case 6	494	926	674	493	421	287	272	Pinned	Pinned
	473	875	647	462	401	269	254		

The rotor system is supported by two bearings BC_{S1} and BC_{S2}. In the analysis, variants when bearing displacement is possible are considered for Cases marked as 1 – 3 and the variant of a stuck bearing with a restriction to displacement for dilation for Cases denoted as 4 – 6. Furthermore, BC_{T1} – BC_{T7} represent the temperatures in significant areas divided into the upper and lower side when considering the inhomogeneous distribution of the temperature field due to the developed natural convection published in [3]. BC_{T7} and BC_{T6} represent the first two stages of the axial compressor. BC_{T4} to BC_{T5} represents the centrifugal compressor impeller. BC_{T3} is the area of the combustion chamber cooled by flowing fuel. BC_{T2} is the generator turbine wheel area and BC_{T1} stands for the temperature in the labyrinth seals.

Temperatures are considered for the turbine engine cooling when it is shut down after 5 minutes in three stable flight modes, i.e., idle mode, cruise mode and maximum take-off mode.

In the figure Fig. 2., there is a visualization of the calculated temperature field for the Case 6 representing the maximum take-off mode under the influence of the boundary conditions listed in the table Table 2. The deformation of the rotor without the possibility of axial dilation of the rotor system for the same case is shown in figure Fig. 3.

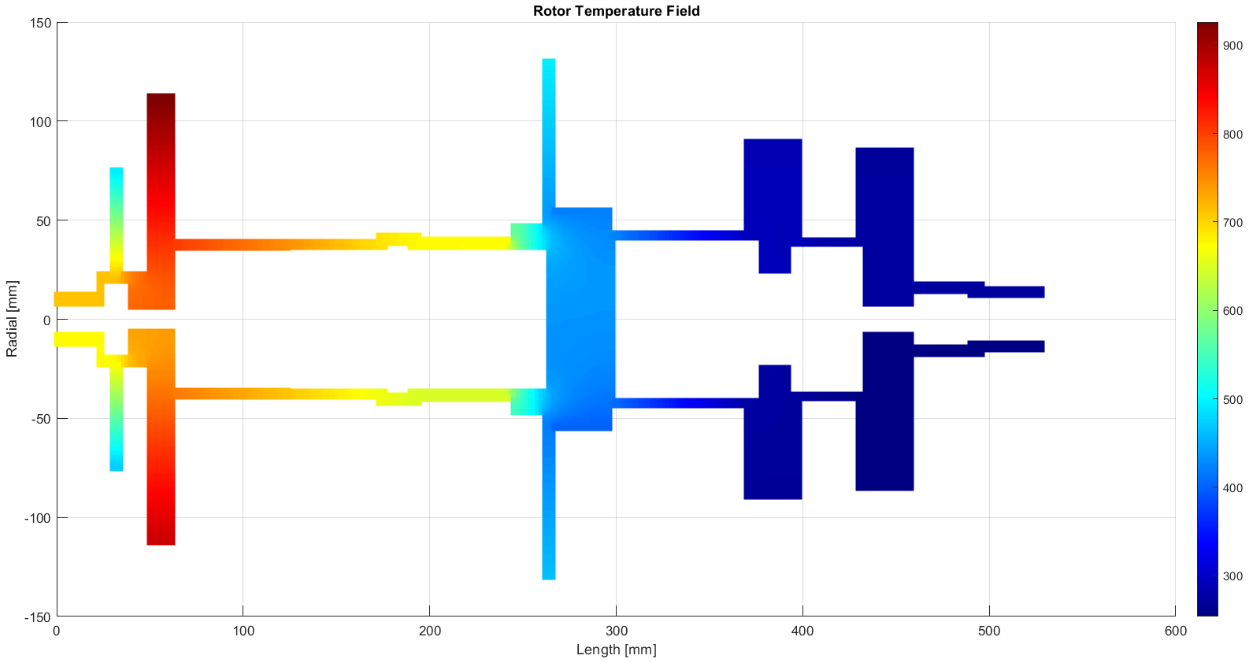

Fig. 2. Temperature field distribution on the turbine engine rotor system

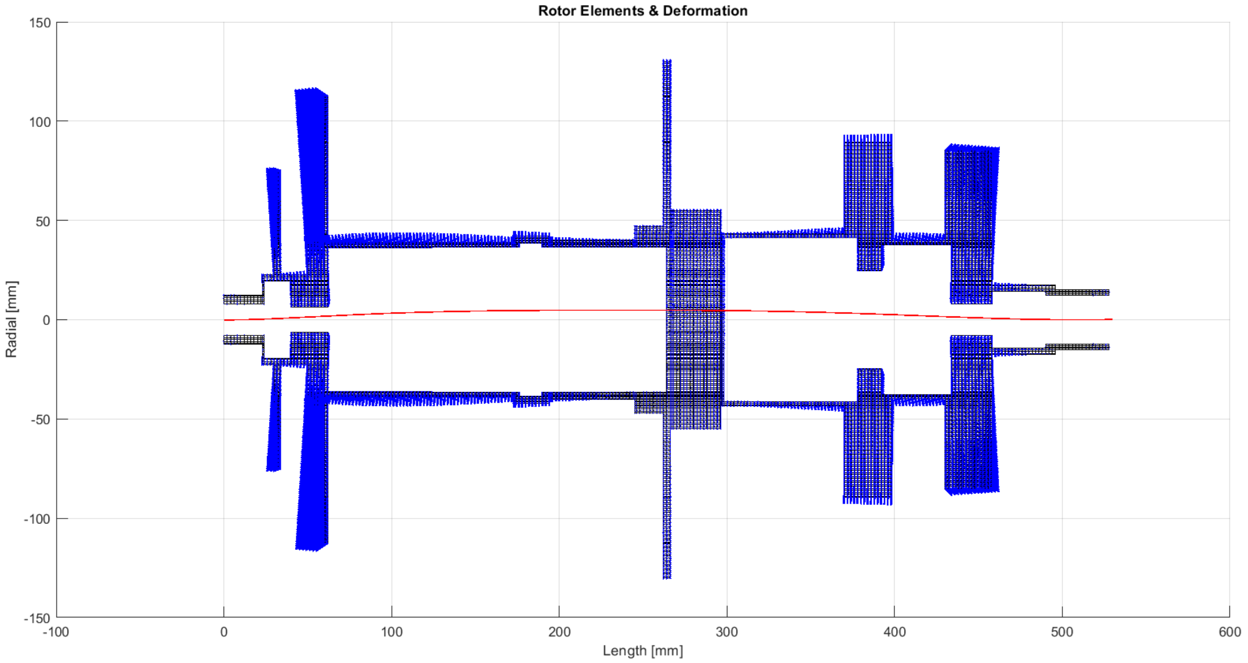

Fig. 3. Deformation and deflection distribution on the turbine engine rotor system

Fig. 2 shows the variable distribution of the temperature field due to heating from the flowing gases on the generator turbine as well as other structural nodes of the turbine engine. The asymmetric temperature field distribution between the upper and lower sides of the rotor is considered due to cooling by natural convection.

The asymmetry and inhomogeneous temperature field results in the rotor deformation shown in Fig. 3. Axial and radial components of the deformation are indicated by blue vector lines for each node of the computational mesh. Total deflection of the rotor centreline is plotted as a red curve, for clearer visibility this deflection is plotted as tenfold of this deformation.

The maximum rotor deflection, together with its position, are listed in Table 2 for all specified cases.

Table 2. Maximum deflection for specified cases

	Max. deflection [mm]	Max. deflection distance [mm]	BC_{S1}	BC_{S2}
Case 1	0.235	162	Pinned	Roller
Case 2	0.224	165	Pinned	Roller
Case 3	0.305	167.5	Pinned	Roller
Case 4	0.498	240	Pinned	Pinned
Case 5	0.483	238	Pinned	Pinned
Case 6	0.613	232.5	Pinned	Pinned

The resulting deflections of the rotor axis due to the temperature field distribution after shutting off the engine in the defined modes can be seen from Table 2. There is an increase in deflection with the increasing temperature difference of the asymmetric temperature field at higher speed mode. There is also a requirement for the functionality of the axial displacement of bearing which is also of key importance for the dynamic behaviour of the rotor system. The results show a dependence on the position of the maximum deflection, which is not much dependent on the selected mode respectively temperatures but dependent on the possibility of axial displacement of the bearing.

Acknowledgements

Authors acknowledge support from the ESIF, EU Operational Programme Research, Development and Education, and from the Center of Advanced Aerospace Technology (CZ.02.1.01/0.0/0.0/16_019/0000826), Faculty of Mechanical Engineering, Czech Technical University in Prague.

This work was supported by the Grant Agency of the Czech Technical University in Prague, grant No. SGS19/157/OHK2/3T/12.

References

[1] Chatterton, S., et al., An unconventional method for the diagnosis and study of generator rotor thermal bows, Journal of Engineering for Gas Turbines and Power 144(1) (2022) 011024.

[2] Marinescu, G., Ehrsam, A., Experimental investigation into thermal behavior of steam turbine components. Part 2 – Natural cooling of steam turbines and the impact on LCF life, ASME Turbo Expo Copenhagen, Denmark, 2012.

[3] Pařez, J., et al., Experimental and numerical study of natural convection in 3D double horizontal annulus, EPJ Web of Conferences, 2022, 264(1), ISSN 2100-014X.

[4] Pennacchi, P., Vania, A., Accuracy in the identification of a generator thermal bow, Journal of Sound and Vibration 274 (2004) 273-295.

[5] Smith, E., Neely, A., A study of cranking effectiveness as a treatment for rotor thermal bow in gas turbines, International Society of Airbreathing Engines (2019) 24025.

[6] Yuan, H.Q., et al. Dynamic characteristics of transient thermal starting up of a rotor system, Journal of Vibration and Shock 28 (2009) 33-37.

[7] Zhuo, M., et al. A new computational method for predicting the thermal bow of a rotor, Proceedings of the Institution of Mechanical Engineers, Part C: Journal of Mechanical Engineering Science (2019) 4372-4380.

[8] Zhu, X.Z., et al., Effects of steady temperature field on vibrational characteristics of a rotor system, Journal of Northeastern University 29 (2008) 113-116.

COMPUTATIONAL MECHANICS 2022
37th conference with international participation
Srní
November 7 - 9, 2022

Effects of hardenability on mechanical properties of tool steel 56NiCrMoV7 for forging die

M. Paulec, P. Kopas, M. Sága

Faculty of Mechanical Engineering, University of Žilina, Univerzitná 8215/1, 010 26 Žilina, Slovak Republic

1. Introduction

Hot forging is a way to preform metal parts quickly and at low cost. It belongs to the methods of mass forming of metals. The high strength of components produced by this method has drawn special attention to this method in various industries such as aerospace, marine, railway and automotive. Forging processes normally involve two dies that press the hot billet into the desired shape. Hot forging enables complicated geometry with a reduced amount of mechanical energy. Hot forging has two main disadvantages. The first disadvantage is a deformed billet, which due to the impossibility of surface quality and geometric tolerance (surface oxidation, thermal contraction, the possibility of phase transformation in some alloys, etc.). The second is the cost of heat forging dies. The cost of hot forging dies is generally estimated at 8 to 15% of all manufacturing costs. For small production runs, it can reach 30% or even 50% if unexpected damage is considered. [2]

Most unexpected failures of hot forging dies are caused by inappropriate die materials, die design, die manufacturing, or forging operations. In addition, there are insufficient forging ratio, insufficient cleanliness and heat treatment of the dies, small radius of corners, insufficient width and thickness of the die, insufficient surface treatment, repair of the weld surface of the die, insufficient preheating, insufficient surface of the die and lubrication. The main factors that lead to unexpected failure of hot forging dies. [3, 1]

Fig. 1. Broken part of forging die

2. Experimental materials and method

The frequently used tool steel 56NiCrMoV7 was used as the experimental material. A chemical analysis was conducted, and the outcomes are displayed in Table 1.

Table 1. Chemical composition of a fractured die made of 56NiCrMoV7 steel

Element	**C**	**Si**	**Mn**	**Cr**	**Mo**	**Ni**	**V**	**P**	**S**
Ratio in %	0.56	0.38	0.68	0.79	0.50	1.69	0.06	0.006	0.0015

The die material was supplied in the form of a forged and heat-treated steel block with dimensions of 670x480x320 mm, which was heat treated - hardened and tempered to a surface hardness of 44 HRC.

A static tensile test was used to detect the decrease in mechanical properties. In Fig. 2 is geometry and dimension of specimen for static tensile test.

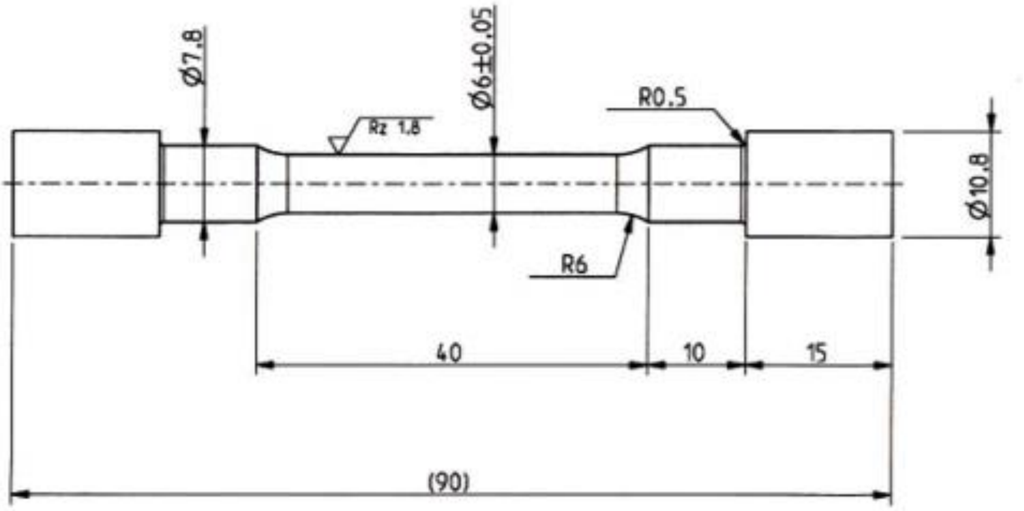

Fig. 2. Geometry and dimensions of specimen for static tensile test

A fatigue test was used to detect the decrease in mechanical properties. In Fig. 3 is geometry and dimension of specimen for static tensile test.

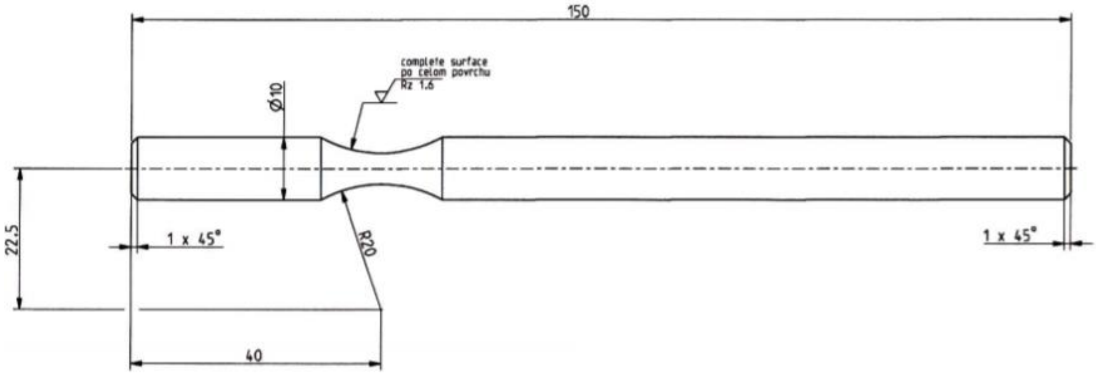

Fig. 3. Geometry and dimensions of specimen for fatigue test.

3. Results

The results of the static tensile test for a set of material 56NiCrMoV7 hardened and tempered to a hardness of 44 HRC are in Table 2. The average value of upper yield point is 1196 MPa. The average value of tensile strength is 1377 MPa. The average value of elongation is 10,4 % MPa.

Table 2. Mechanical properties of steel 56NiCrMoV7 hardened and tempered to the hardness of 44 HRC

Name	**Upper yield point**	**Tensile strength**	**Elongation**
Units	**R_{eH}** [MPa]	**R_m** [MPa]	**A** [%]
Measurement 1	1208	1394	10.8
Measurement 2	1185	1369	9.9
Measurement 3	1197	1375	10.3
Measurement 4	1177	1336	9.7
Measurement 5	1213	1411	11.3
Average	**1196**	**1377**	**10.4**

The results of the static tensile test for a set of material 56NiCrMoV7 hardened and tempered to a hardness of 34 HRC are in the Table 3. The average value of upper yield point is 789 MPa. The average value of tensile strength is 994 MPa. The average value of elongation is 12,6 % MPa.

Table 3. Mechanical properties of steel 56NiCrMoV7 hardened and tempered to the hardness of 34 HRC

Name	**Upper yield point**	**Tensile strength**	**Elongation**
Units	**R_{eH}** [MPa]	**R_m** [MPa]	**A** [%]
Measurement 1	775	971	11.5
Measurement 2	809	1027	13.7
Measurement 3	798	1013	13.1
Measurement 4	785	982	12.5
Measurement 5	778	977	12.2
Average	**789**	**994**	**12.6**

The hardness test results showed a decrease from 44 HRC to 34 HRC. The maximum drop of hardness was at a height of 160 mm from surface. The hardness drop graph can be seen in Fig. 4.

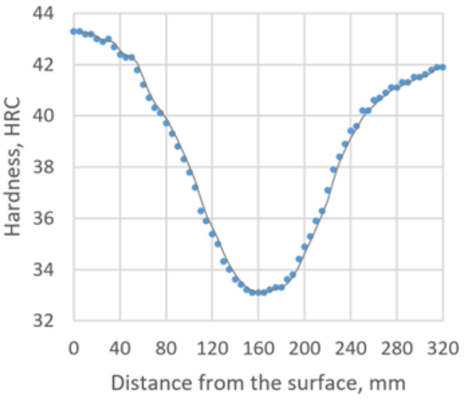

Fig. 4. Graph of drop hardness

The results of the fatigue test for a set of material 56NiCrMoV7 hardened and tempered to a hardness of 44 HRC and 34 HRC are in the Fig. 5. Based on the results, a decrease in fatigue can be seen.

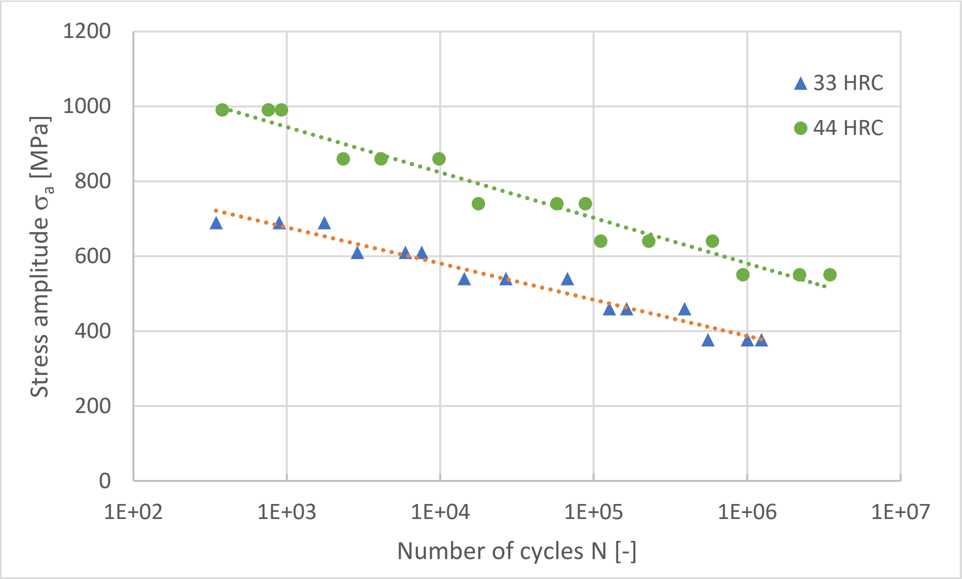

Fig. 5. Graph of decrease fatigue life

4. Conclusions

Based on research devoted to the issue of the decline of mechanical properties, the following can be said:

- the upper yield point drop is 33%,
- the tensile strength drop is 29%,
- the decrease in hardness due to hardenability is 25%.

Acknowledgements

This research was funded by the KEGA project Implementing of additive technologies into the education process of engineers study programs, grant number 001ŽU-4/2020.

References

[1] Bayramoglu, M., Polat, H., Geren, N., Cost and performance evaluation of different surface treated dies for hot forging process, Journal of Materials Processing Technology 205 (2008) 394-403.

[2] Guido, B., Monti, M., Thermo-mechanical fatigue life assessment of hot forging die steel, Fatigue & Fracture of Engineering Materials & Structures 28 (11) (2005) 1025-1034.

[3] Widomski, P., Kaszuba, M., Dobras, D., Zindulka, O., Development of a method of increasing the wear resistance of forging dies in the aspect of tool material, thermo-chemical treatment and PVD coatings applied in a selected hot forging process, Wear 477 (2021) 9.

COMPUTATIONAL MECHANICS 2022
37th conference with international participation
Srní
November 7 - 9, 2022

Online identification using linear neural unit with guaranteed weights convergence

V. Pawlik, P. Steinbauer, I. Bukovský

Faculty of Mechanical Engineering, CTU in Prague, Technická 4, 160 00 Praha 6, Czech Republic

For many modern control strategies, a model of the controlled plant must be known. This model does not need to be known a priori and can be found online using an adaptive process. Online identification is very useful, especially if the plant's properties change during the run, for example, in context of vibration testing. This model can be a high order neural unit (HONU), such as a linear neural unit (LNU) with structure

$$y_m = \sum_{i=0}^{n} w_i x_i = \mathbf{w}^T \mathbf{x}, \tag{1}$$

where $\mathbf{x}$ is the input vector and $\mathbf{w}$ is the neural weights vector [1].

The general HONU output formula is

$$y_m = \mathbf{w}^T \mathrm{col}\mathbf{x}, \tag{2}$$

where $\mathbf{w}$ and $\mathrm{col}\mathbf{x}$ are both column vectors. The neural weights $\mathbf{w}$ can be adapted using a gradient descent algorithm, for example, normalised least mean squares (NLMS), which is derived by optimising a criterion

$$J = \frac{1}{2} e(k)^2, \tag{3}$$

where the error e is the difference between the desired and the current output

$$e(k) = y(k) - y_m(k). \tag{4}$$

The gradient of the criterion J with respect to $\mathbf{w}$, which is the steepest direction, is

$$\frac{\partial J}{\partial \mathbf{w}} = e(k) \left(\frac{\partial J}{\partial \mathbf{w}} y(k) - \frac{\partial J}{\partial \mathbf{w}} y_m(k) \right) = e(k) \left(0 - \mathrm{col}\mathbf{x} \right) = -e(k) \mathrm{col}\mathbf{x}. \tag{5}$$

The weights are then adjusted toward the minimum of the criterion

$$w(k+1) = w(k) - \mu_k \frac{\partial J}{\partial \mathbf{w}} = w(k) + \mu_n e(k) \mathrm{col}\mathbf{x}(k), \tag{6}$$

using a learning rate $\mu_n = \mu \frac{1}{\varepsilon + ||\mathrm{col}\mathbf{x}(k)||}$, where $\varepsilon \approx 1e^{-5}$ and the normalisation improves convergence and $\mu \in (0, 2)$.

To assess the performance of HONU, the sum of squared errors (SSE) over a certain horizon N_e might be used

$$\mathrm{SSE} = \sum_{i=k-N_e}^{k} e(i)^2. \tag{7}$$

To ensure convergence of the weights [2], the learning rate μ might be chosen iteratively such that

$$||\mathbb{A}(k)|| = ||\mathbb{I} - \mu_n \mathrm{col}\mathbf{x}(k)\mathrm{col}\mathbf{x}(k)^T|| \leq 1, \tag{8}$$

where $\mathbb{I}$ is the identity matrix and $\mathbb{A}(k)$ is the matrix of update dynamics

$$\mathbf{w}(k+1) = \mathbb{A}(k)\mathbf{w}(k) + \mathbb{B}(k)\sqcap(k) = \left(\mathbb{I} - \mu_n \mathrm{col}\mathbf{x}(k)\mathrm{col}\mathbf{x}(k)^T\right)\mathbf{w}(k) + \mu_n y(k)\mathrm{col}\mathbf{x}(k). \tag{9}$$

At the start of the adaptation process the value $\mu = 2$ is chosen and the decreased $\mu(k+1) = 0.9\mu(k)$, until the condition (8) is satisfied. Then the weights are updated using the update rule (6). If the condition is violated during the run, then the learning rate μ is lowered until a value that satisfies the condition is reached again.

A plant with a transfer function

$$Y(s) = \frac{30530s + 3.765e06}{s^4 + 204.2s^3 + 15278s^2 + 415450s + 588660}U(s) \tag{10}$$

was used as a test system with square wave input signal. The input signal and the system output are shown in Fig. 1 with time step $\Delta T = 0.01$ s.

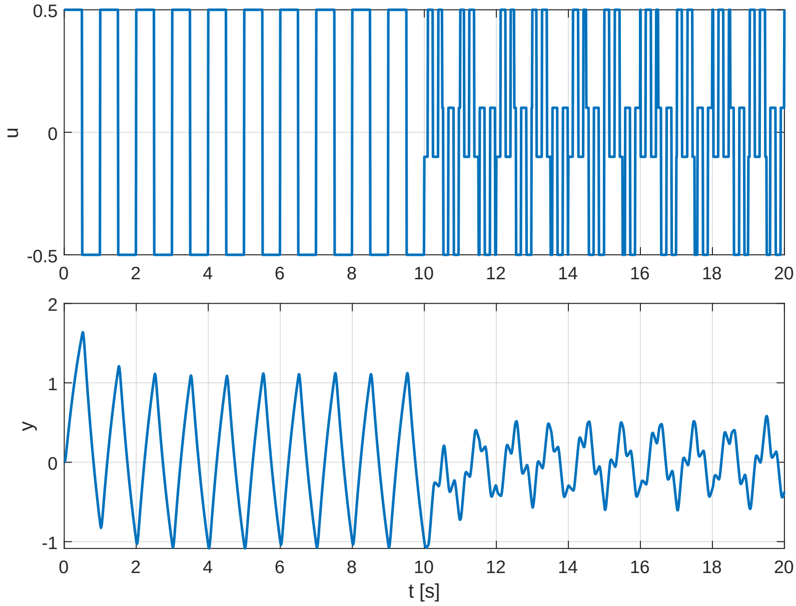

Fig. 1. The input and output of the testing plant

The input vector $\mathbf{x}$ consist of bias and a number of samples of the input and output of the plant

$$\mathbf{x}(k+1) = \begin{bmatrix} 1 \\ u(k+1) \\ \vdots \\ u(k-n_u+1) \\ y(k) \\ \vdots \\ y(k-n_y) \end{bmatrix}, \tag{11}$$

where n_u and n_y are chosen such that the best performance is achieved. The performance of various choices is shown in Fig. 2. Performance is measured with $N_e = 100$.

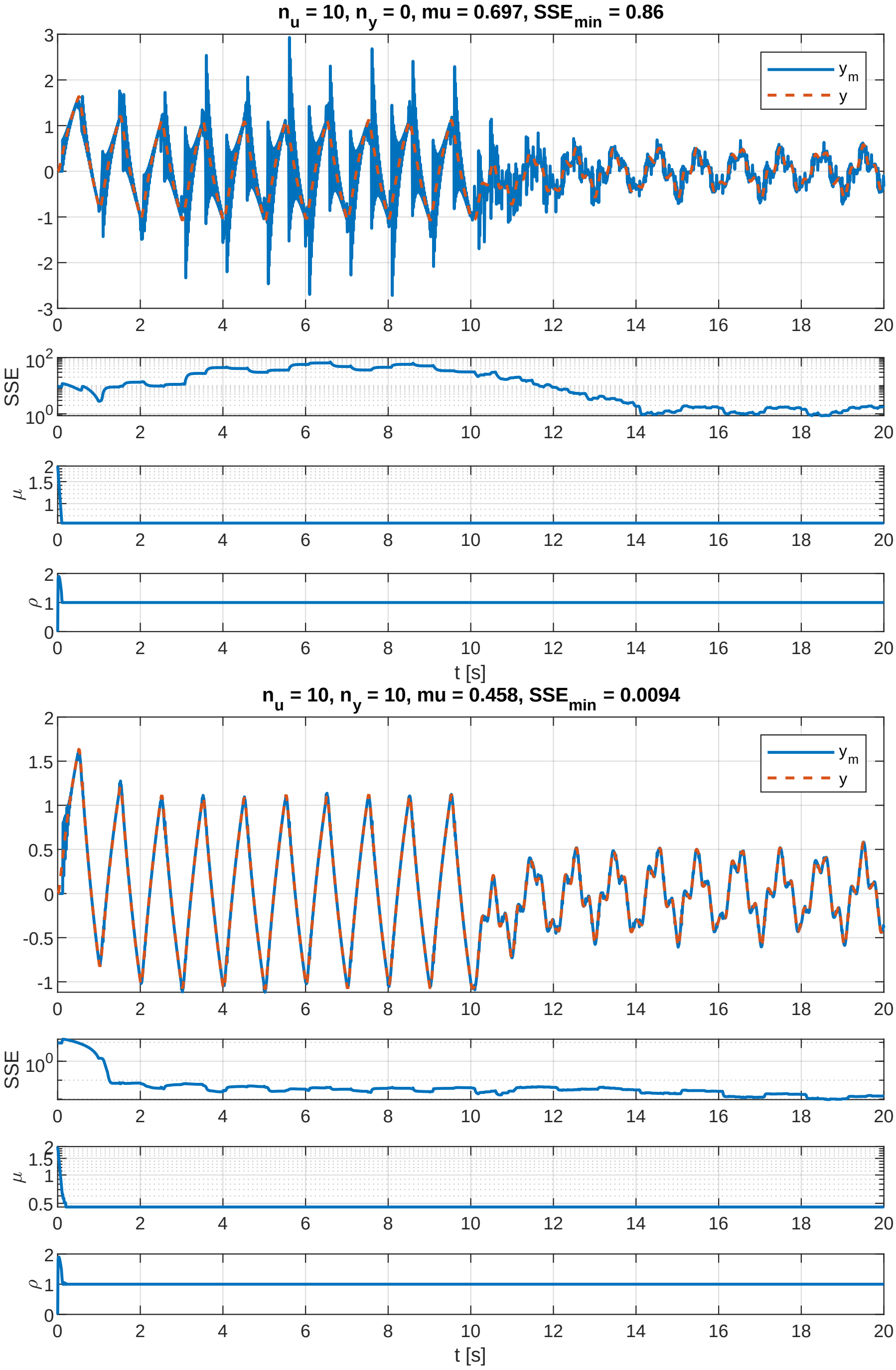

Fig. 2. Performance of the LNU for identification with various choices of n_u and n_u. The best performance is achieved with $n_u = 10$ and $n_y = 2$

The linear neural unit shows great performance in the identification of the plant. The plant is sufficiently approximated for a wide selection of n_u and n_y, which is enabled by the selection of μ_k that guarantees the convergence of the weights. In future work, this approach will be used to automatically identify a model for an adaptive controller.

Acknowledgement

The work has been supported by the project SGS22/150/OHK2/3T/12 “Mechatronics and adaptronics 2022” of Czech Technical University in Prague.

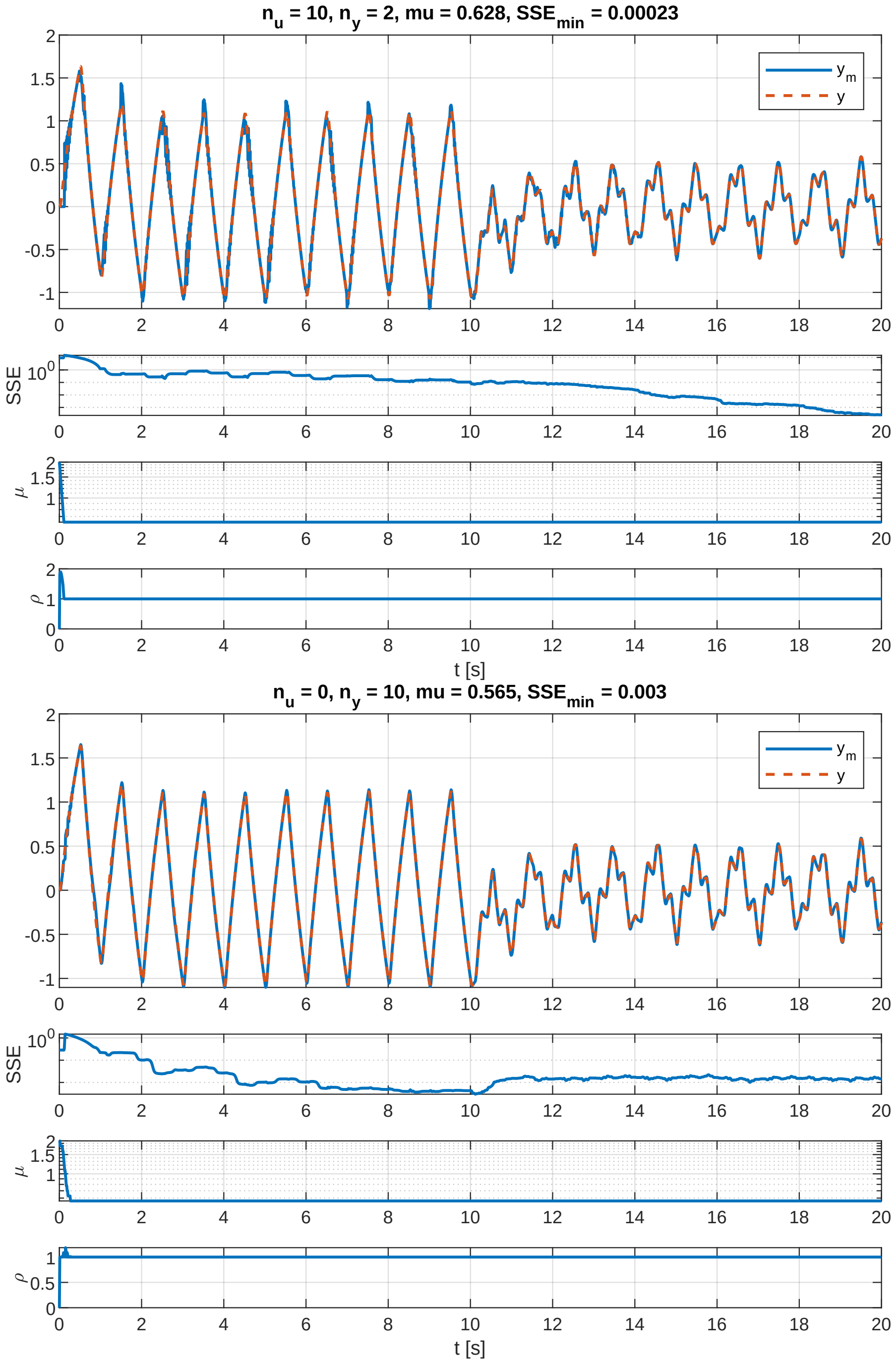

Fig. 2. (*Continued*)

References

[1] Bukovsky, I., Voracek, J., Ichiji, K., Noriyasu, H., Higher order neural units for efficient adaptive control of weakly nonlinear systems, Proceedings of the 9th International Joint Conference on Computational Intelligence, Funchal, Madeira, Portugal, 2017, pp. 149-157.

[2] Bukovsky, I., Dohnal, G., Benes, P. M., Ichiji, K., Homma, N., Letter on convergence of in-parameter-linear nonlinear neural architectures with gradient learnings, IEEE Transactions on Neural Networks and Learning Systems, 2021, doi: 10.1109/TNNLS.2021.3123533. (in press)

COMPUTATIONAL MECHANICS 2022
37th conference with international participation
Srní
November 7 - 9, 2022

Numerical simulations of aeroelastic instabilities in turbine blade cascade by modified Van der Pol model at running excitation

L. Pešek, P. Šnábl, C. S. Prasad, Y. Delanney

Institute of Thermomechanics, Czech Academy of Sciences, Dolejškova 5, 182 00 Prague, Czech Republic

Apart from rotary test rig for evaluation of structural dynamics of the bladed wheels, the control flutter experiments have been performed on the linear cascade model in the subsonic wind tunnel in the Institute of Thermomechanics, of CAS, in Prague. These experiments are aimed at stability evaluation of the cascade at running waves or at stability limit testing by flow speed changes or by force impulses of blades. The onset of flutter and its spreading in the cascade are observed, too. The linear cascade model consists of five NACA010 blades. All the blades can be separately excited with electromagnetic torque excitation mechanism and all of them are instrumented to measure the aerodynamic moments which can be used to calculate the aerodynamic work. A more details about the linear blade cascade experimental set up can be found in [3, 8]. To predict a dynamic behaviour in the blade cascade, we have been dealing with simplified theoretical modelling of the aeroelastic instability in turbine blade cascade [2, 4, 5]. Due to the application of the reduced cascade model consisting of simple elements – springs, rigid bodies, linear dampers – and aeroelastic forces introduced by analytical Van der Pol model, it facilitates to study the dangerous states of vibration of such complicated turbine parts [1, 6, 7, 9]. This study is aimed at examination of aeroelastic instabilities of 10-blade cascade at running excitation that arises due to the wakes flowing from stator the blades to the rotating blades. They cause forced excitation in the narrow frequency range.

The computing model of turbine wheel with ten blades with the simplest type of linear connections between neighbouring blades. The sector of blade cascade is shown in Fig. 1.

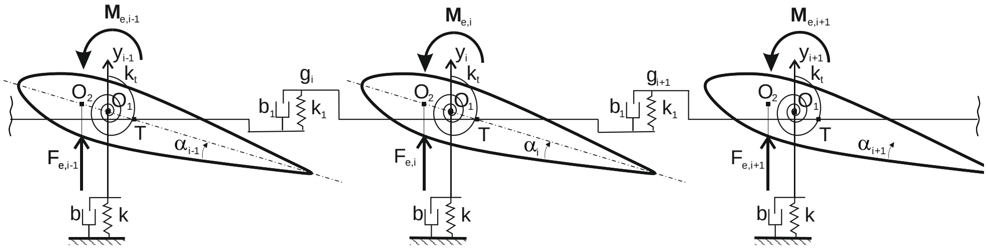

Fig. 1. Section of blade cascade

The blades' interconnections g_i are defined by stiffness k_1 and viscous damping b_1 constants. These viscous-elastic connections between neighbouring blades can express dynamic properties of connections in turbine disk, blade-shroud or damping wires. The 2 DOF profile has the centre of mass in point *T*. Corresponding moment of inertia is *I*. Flexural axis of this profile is labelled by O_1 and the transitional stiffness in vertical direction *y* is *k*. Parallel to the elastic force acts also viscous damping force with coefficient *b*. Pitch spring stiffness around this flexural axis is k_t.. This stiffness is again parallel connected by a damping moment with torsional damping coefficient b_t. The vertical aerodynamic force F acting on the blade in direction y is shifted in distance e_2 into point O_2. There is also an aero-elastic moment $M_e = F\,(e_1 + e_2)$ acting around the flexural axis O_1 and oriented to increase of pitch angle α .

The aerodynamic forces F act on the blades in points O_2 in distance of e_2=0.005m from the elastic axes O_1. The flowing steam through the rotating blade cascade produces besides periodic forced vibration also vertical and torsional aero-elastic self-exciting forces $F_{eV,i}$ and $M_{e,i}$, respectively. Steam flowing through the rotating blade-cascade can cause decrease of damping and aero-elastic flutter instability. Exact mathematical model of this aero-elastic phenomenon is very complicated; therefore we will proposed Van der Pol model [4] which can describe two aerodynamic effects: the first one acting on individual blades controlled by only one blade's motion and the other one, considered here, interacting blades controlled by relative motions of neighbouring blades

$$\begin{aligned} F_{eV,i} &= -\mu_1(1-((y_i - y_{i-1})/r_1)^2)(\dot{y}_i - \dot{y}_{i-1}) + \mu_1(1-((y_{i+1} - y_i)/r_1)^2)(\dot{y}_{i+1} - \dot{y}_i)\ , \\ M_{e,i} &= -\mu_2(1-((\alpha_i - \alpha_{i-1})/r_2)^2)(\dot{\alpha}_i - \dot{\alpha}_{i-1}) + \mu_2(1-((\alpha_{i+1} - \alpha_i)/r_2)^2)(\dot{\alpha}_{i+1} - \dot{\alpha}_i)\ , \end{aligned} \tag{1}$$

where $y_i,\ \dot{y}_i, \alpha_i,\ \dot{\alpha}_i$ are vertical and angular displacements of blade i and their velocities, $r_{1,2}$ are displacement limits of blades at which the aerodynamic forces change their sign, $\mu_{1,2}$ give intensities of the considered models.

When the periodic excitation forces and the modified type of Van der Pol forces (1) are applied, differential equations of blade cascade are

$$\begin{aligned} m\ddot{y}_i + \frac{k_t m e_1}{I}\alpha_i + (k + \frac{k m e_1^{\,2}}{I})y_i + b\dot{y}_i + F_{eV,i} + g_i - g_{i+1} &= F_{0i}\cos(\omega t - (i-1)\Delta\varphi), \\ I\ddot{\alpha}_i + k_t\alpha_i + b_t\dot{\alpha}_i - (e_1+e_2)F_{eV,i} + M_{e,i} + k e_1 y_i &= (e_1+e_2)F_{0i}\cos(\omega t - (i-1)\Delta\varphi), \end{aligned} \quad i = 1,.....,10, \tag{2}$$

where $g_i = k_1(y_i - y_{i-1}) + b_1(\dot{y}_i - \dot{y}_{i-1})$ are viscous-elastic connections among blades. Conditions $g_{11} = g_1,\ F_{eV,11} = F_{eV,1}, M_{e,11} = M_{e,1}$ preserve circular periodicity of the system.

Response curves are computed in the following example for backward running force excitation when $\Delta\varphi = -2\pi/5$ at noozle excitation frequency $\omega = 62.8\,rad/s$. It corresponds to 12 stator blades and revolution frequency 1.25 Hz. The structural profiles parameters

$$\begin{aligned} &m = 0.18 \text{ kg},\ k = 50000 \text{ kg s}^{-2},\ b = 2 \text{ kg s}^{-1},\ I = 0.000025 \text{ kg m}^2,\ k_t = 1 \text{ kg m}^2\text{ s}^{-2}, \\ &e_1 = e_2 = 0.005 \text{ m},\ b_t = 0.00005 \text{ kg m}^2\text{ s}^{-2}/\text{rad} \end{aligned} \tag{3}$$

and amplitude of external wake force F_0 = 0.01 N were applied, too.

As to the intensity factor of Van der Pol model (1) we considered its linear growth over time given by coefficient c_μ . Therefore, we extend the system of differential equations (2) by equation of the first order $\dot{\mu} = c_\mu$ with initial condition $\mu(0) = 5e-4\,kgs^{-1}$ and constant $r = 0.1745 rad$. The linear growth of intensity factor simulates the increase of instability in flow due to gradually increasing flow speed.

As a simulation case, we choose herein no inter-blades viscous-elastic Kelvin-Voigt connections and only damping connections are via modified van der Pol model of flow aero-elastic forces which corresponds to the tested linear cascade. The time characteristics of the first blade displacements and its aerodynamic moment (Fig. 2) show that flutter arises at time cca 1 s when intensity coefficient achieves a value 5.5e-3. Due to arising self-excited vibrations on the first torsional eigen-frequency the dominant vibration are observed at torsional mode but it causes also increase on vertical displacements. Even after stabilization of vibrations at time 1.5 s the amplitude of vibrations are not constant and course of vibration is non-stationary.

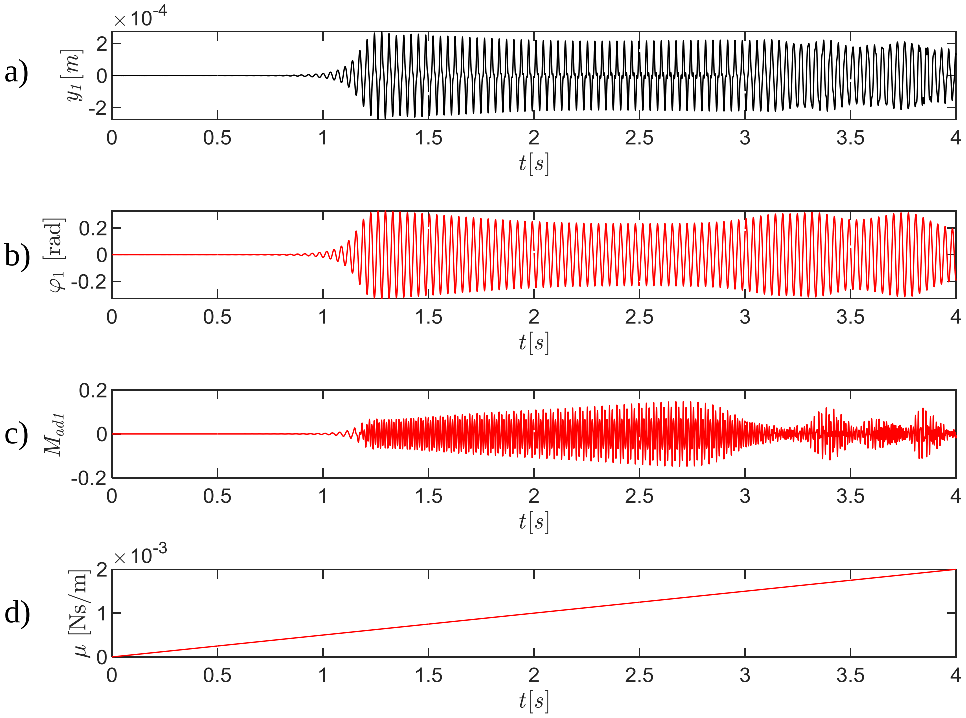

Fig. 2. Time characteristics of amplitudes of vertical and angle displacements (a,b) of 1st blade, of aerodynamic moment of 1st blade (c) and of intensity coefficient (d) at excitation frequency 10 Hz and $\Delta\varphi = -2\pi/5$

In Fig. 3 we can see mode of vibration across the cascade at certain times: a) at the onset of flutter; b) at the flutter state. It is clear that till the onset of the flutter the mode of vibration has shape of eigenmode with 2 ND and this mode is travelling. However in the state of flutter the vibration mode becomes more complex with higher number of ND. Both these modes are still travelling. However, in longer times (above 3.7 s) when the flutter is more developed, a mode of 4ND prevails at the vibration and this travelling mode becomes standing.

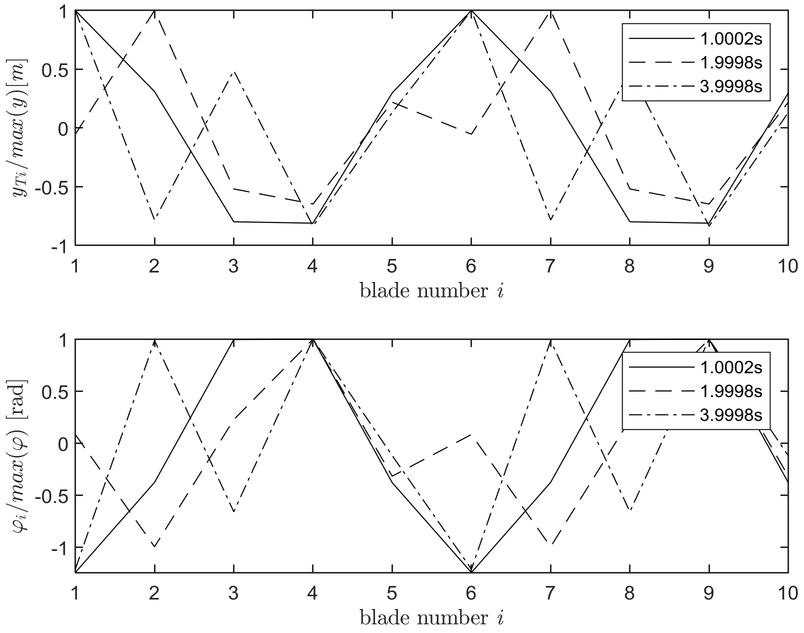

Fig. 3. Modes of vibration of the cascade at times at the beginning (1s) and at at two flutter states (at 2 s and 4 s)

The results of numerical simulations bring valuable findings about dynamic behaviour of the blade cascade of turbine wheels under running nozzle excitation and arising travelling waves at onset and development of the flutter state. The numerical simulations can be further exploited for testing a new algorithm for prediction of the flutter onset detection.

Acknowledgements

This work was supported by the research project of the Czech Science Foundation Study of dynamic stall flutter instabilities and their consequences in turbomachinery application by mathematical, numerical and experimental methods [No. 20-26779S].

References

[1] Kielb, R.E., Barter, J., Chernysheva, O., Fransson, T., Flutter of low pressure turbine blades with cyclic symmetric modes: A preliminary design method, Journal of Turbomachinery-transactions of the ASME 126 (2004) 306-309.

[2] Pešek, L., Půst, L., Šnábl, P., Study of dry-friction damping effect on two simplified models of flutter oscillations. In: Advances in Mechanism and Machine Science, Springer Nature Switzerland, Krakow, 2019, pp. 3419-3428.

[3] Prasad, C.S., Šnábl, P., Procházka, P., Chindada, S., Effect of geometrical and flow parameters on subsonic stall flutter in blade cascade, IFASD 2022: international forum on aeroelasticity and structural dynamics 2022, Madrid, Spain, 2022.

[4] Půst, L., Pešek, L., Blades forced vibration under aero-elastic excitation modelled by Van der Pol., International Journal of Bifurcation and Chaos 27 (11) (2017) 1750166.

[5] Půst, L., Pešek, L., Byrtus, M., Modelling of flutter running waves in turbine blades cascade, Journal of Sound and Vibration 436 (2018) 286-294.

[6] Rao, J.S., Turbomachine blade vibration, Wiley Eastern Limited, New Delhi, 1991.

[7] Schlaefli, D., Experiments on unsteady flow effects in vibrating annular cascades, Ph.D. Thesis, Lausanne: EPFL, 1989. (in German)

[8] Šnábl, P., Pešek, L., Prasad, C.S., Bula, V., Cibulka, J., Experimental setup and measurement for evaluation of blade cascade stall flutter instability, In: Advances in Acoustics, Noise and Vibration 2021. (https://www.icsv27.org/)

[9] Vogt, D.M., Fransson, T.H., A new turbine cascade for aeromechanical testing, Proc. 16th Symp. Measuring Techniques in Transonic and Supersonic Flows in Cascades and Turbomachines, Cambridge, 2002.

COMPUTATIONAL MECHANICS 2022
37th conference with international participation
Srní
November 7 - 9, 2022

Treatise on dynamic behaviour modelling of tilting pad journal bearing under operating conditions: From the real world to numerical simulations

J. Rendl[a], L. Smolík[a], Š. Dyk[a], R. Bulín[a], Z. Kubín[b]

[a]NTIS, Faculty of Applied Sciences, University of West Bohemia, Technická 8, 301 00 Plzeň, Czech Republic
[b]Výzkumný a zkušební ústav Plzeň, Tylova 1581/46, 301 00 Plzeň, Czech Republic

Tilting pad journal bearings, see Fig. 1a, are used to support machinery with journals of high circumferential speed. A unique design of these bearings prevents the formation of oil-induced instability and causes low sensitivity to load direction, reducing the shaft axial misalignment and is known for relatively low oil consumption [2]. The pads can tilt around the pivots with respect to the journal and the housing, see Fig. 1b.

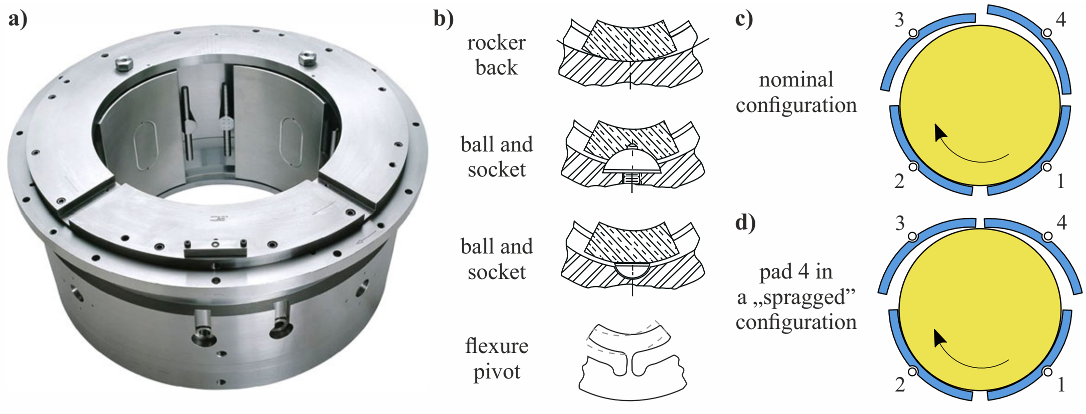

Fig. 1. (a) Tilting pad journal bearing with four pads, (b) various pivot designs, (c, d) comparison of common and abnormal operating configurations of the bearing

The pads are supplied with lubricant oil which fills the bearing gap during the operation. In the ideal case, the bearing gap has a wedge form, see Fig. 1c. Lower pads are loaded mainly by rotor mass and tend to tilt to achieve a convergent bearing gap from the leading edge. However, upper pads are loaded only by their mass and can move freely in the bearing gap [1,2]. In this case of the unloaded pad, the leading edge can come close to the journal and form the divergent bearing gap, see Fig. 1d, due to operating conditions dependent on the preload, pad moment of inertia, volume of supplied oil, circumferential journal speed and pivot position. Furthermore, the pressure gradient disappears, and solid contact between the journal and the pad can occur. This state can be distinguished into two phenomena [1,4]:

- Spragging – the journal and/or pad positions jump into the new positions due to rapid changes in the pressure field.

- Fluttering – repeated formation and reformation of the pressure field cause fluctuation and/or solid contact between the bearing parts, and vibrations at subsynchronous frequency occur.

Computational modelling of tilting pad journal bearing is a complex problem involving the modelling of hydrodynamic lubrication and sufficient description of the pads' motion [4]. The planar lateral motion of the pad without axial misalignment is supposed. Hence, the pad motion is described by one degree of freedom (tilting around the pivot necessary for proper tilting pad journal bearing operation). The additional degree of freedom (radial) can be added to consider the radial pivot flexibility under the loading transferred through the oil film.

A load of the individual pad is mainly given by pad preload and can be considered different for separate pads. The spragging or fluttering phenomena can occur in case of improperly chosen preload, mainly for upper pads. Then, the bearing clearance can disappear and the modelling of solid contact between the part based on Hertz contact theory must be taken into account.

The pressure distribution in the bearing gap is given by the Reynolds equation. The laminar or turbulent flow is distinguished based on the Reynolds number, which involves the bearing dimensions and operating conditions. Developed hydrodynamic pressure acts on the bearing parts by the hydrodynamic force determined by pressure integration over the pad surface. It is a nonlinear force coupling. A slight change of resultant force sets the pad into motion. Pressure distribution is influenced by the relative position of the pads and the journal. Another aspect of the bearing modelling is the thermodynamics in the lubricant flow, which affects the dynamic viscosity of the lubricant and cavitation.

The friction in the pivots, mainly in the ball-and-socket coupling, can be considered, and the stick and slip phases of the pad can further occur. The friction has a negative role on the pad tilting behaviour, and the global bearing behaviour can be close to the bearing with fixed geometry. The most used friction models are the Bengisu-Akay model and the Lugre model [3]. Both models are susceptible to the control parameters, and it is necessary to focus more on their establishment during the modelling.

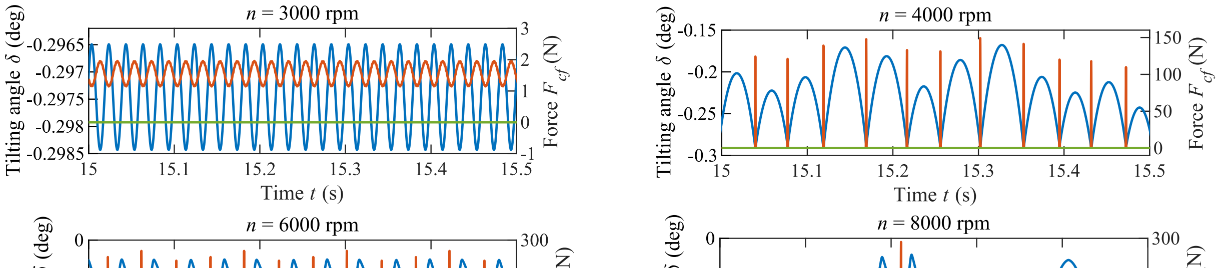

Fig. 2. Obtained waveforms for tilting angle of pad 4 and contact forces at the leading and trailing edges

Obtained waveforms from the steady-state simulations [4] of the unbalanced rotor supported by the four-pad tilting pad journal bearing in the configuration load-between-pads are depicted in Fig. 2. The figure contains the tilting angle of a lightly loaded upper pad 4 (Fig. 1) and contact force at the leading and trailing edges for various rotor speeds. The pad lies on the rotor for a speed of 3000 rpm, and the contact force fluctuates due to journal vibrations. For higher rotor speeds, the pad tilts out of the journal and repeatedly hits the journal, see the force impulses at the leading edge. The tilting angle becomes irregular or chaotic due to pad hits and changing operating conditions. The contact at the trailing edge is secured by hydrodynamic force from the newly reformated pressure gradient during the pad tilting. The solid contact at this edge does not occur.

Long-lasting operation with undesirable phenomena has a negative impact on the durability of the affected pad. The main problem is the damage at the place of contact between the pad and the journal [1]. It is the leading edge of pad 4 along the whole axial length. This damage is apparent in illustrative Fig. 3. This failure progress to 1/3 of the pad surface in the journal rotation direction. Repeated impacts negatively affect durability due to the development of cracks and the cover layer can disappear [1], see Fig. 3. Operating diagnostics of undesirable phenomena is quite tricky. Distinguishing of the phenomena during the operation is dependent only on sensors capturing the relative and absolute bearing pedestal vibrations. The sensors measuring the tilting angle are not usually installed, and the pad's spragging and fluttering are not directly detectable.

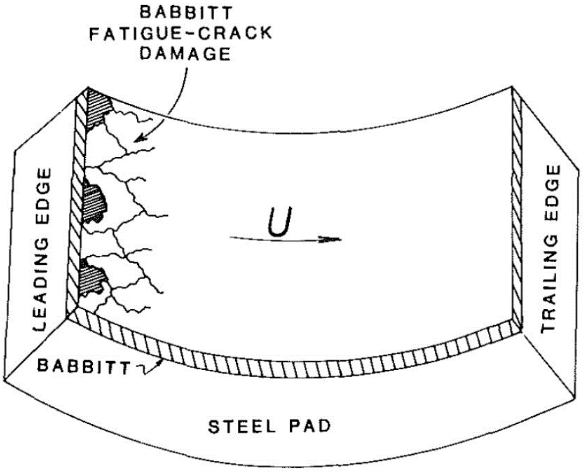

Fig. 3. Illustrative scheme of Crack failure development at the leading edge of the pad [1]

Acknowledgement

This paper was supported by the Technology Agency of the Czech Republic under the THETA Programme within the TK04020057 project.

References

[1] Adams, M. L., Payandeh, S., Self-excited vibration of statically unloaded pads in tilting-pad journal bearings, Journal of Lubrication Technology 105 (3) (1983) 377-383.

[2] Dmochowski, W. M., Dadouche, A., Fillon, M., DeCamillo, S. M., Hydrodynamic tilting-pad journal bearings, In: Encyclopedia of tribology, Q. J. Wang, Y.-W. Chung (eds), Springer, New York, 2013, pp. 1749-1757.

[3] Marques, F., Flores, P., Claro, J. C. P., Lankarani, H. M., A survey and comparison of several friction force models for dynamic analysis of multibody mechanical systems, Nonlinear Dynamics 86 (3) (2016) 1407-1433.

[4] Rendl, J., Dyk, Š., Smolík, L., Nonlinear dynamic analysis of a tilting pad journal bearing subjected to pad fluttering, Nonlinear Dynamics 105 (2021) 2133-2156.

COMPUTATIONAL MECHANICS 2022
37th conference with international participation
Srní
November 7 - 9, 2022

Homogenization based two-scale modelling of unilateral contact in micropores of fluid saturated porous media

E. Rohan, J. Heczko

Faculty of Applied Sciences, University of West Bohemia, Univerzitní 8, 301 00 Plzeň, Czech Republic

1. Introduction

We consider fluid-saturated poroelastic structures characterized by unilateral self-contact at the pore level of the periodic microstructure. The unilateral frictionless contact interaction is considered on matching pore surfaces of the elastic skeleton. Depending on the deformation due to applied macroscopic loads, the self-contact interaction alters the one between the solid and fluid phases. Both the disconnected and connected porosities are treated; in the latter case, quasistatic fluid flow is described by the Stokes model. We derive two-scale models of the homogenized porous media for the two types of porosities using the framework of the periodic unfolding homogenization [2, 4], *cf.* our previous paper [5] where only empty pores were considered. For the closed pore microstructures, a nonlinear elastic model is obtained at the macroscopic scale. For the connected porosity, a regularization is introduced, assuming the contact interaction never close perfectly the pores, which prevents the pore connectivity. The macroscopic model attains the form of a nonlinear Biot continuum, whereby the Darcy flow model governs the fluid redistribution. To respect that the permeability and other poroelastic coefficients depend on the deformation, an approximation based on the sensitivity analysis is employed [6].

We propose and test new modifications of the original two-scale computational algorithm reported [5] which is based alternating micro- and macro-level steps. As a novelty, a dual formulation of the pore-level contact problems in the local representative cells provides actual active contact sets which enables to compute consistent effective elastic coefficients at particular macroscopic points. At the macroscopic level, a sequential linearization leads to an incremental equilibrium problem which is constrained by a projection arising from the homogenized contact constraint, such that the Uzawa algorithm can be used. At the local level, the finite element discretized contact problem attains the form of a nonsmooth equation which which is solved using the semi-smooth Newton method [3] without any regularization, or a problem relaxation. Numerical examples of 2D deforming structures are presented.

2. Problem formulation

In the framework of the unfolding method of homogenization, using the asymptotic analysis with respect to heterogeneity scale parameter $\varepsilon \to 0$, we derived limit two-scale models of the unilateral contact in porous structures with disconnected and connected porosity. Below we present the variational formulations of the contact problems for heterogeneous structures with disconnected, or connected pores. An open bounded domain $\Omega \subset \mathbb{R}^d$, with the dimension $d = 2, 3$, is constituted by the solid elastic skeleton Ω_s^ε and by the fractures (fissures) Ω_f^ε which

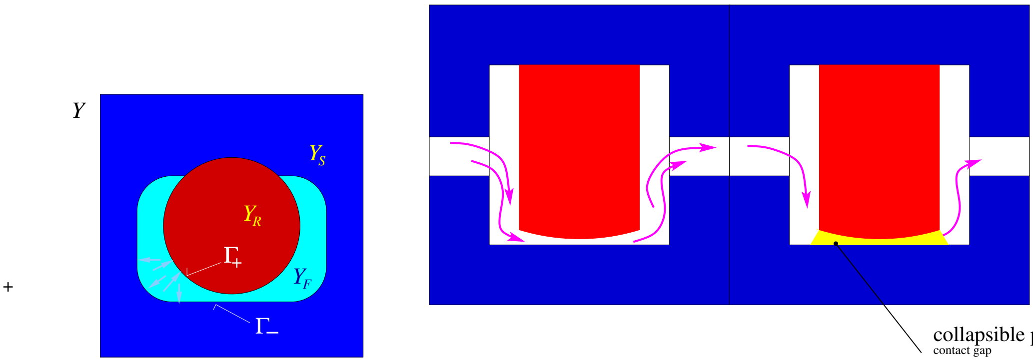

Fig. 1. Representative cells Y for the two types of porous structures. Closed pores (left), connected pores allowing for flow (right). Contact surfaces $\Gamma_c^{+/-}$, subparts on the pore surface Γ_{fs}

are saturated by a viscous fluid, so that

$$\Omega = \Omega_s^\varepsilon \cup \Omega_f^\varepsilon \cup \Gamma^\varepsilon \ , \quad \Omega_s^\varepsilon \cap \Omega_f^\varepsilon = \emptyset \ , \quad \overline{\Omega_f^\varepsilon} \subset \Omega \ , \tag{1}$$

where $\Gamma^\varepsilon = \overline{\Omega_s^\varepsilon} \cap \overline{\Omega_f^\varepsilon}$ is the interface; the contact is possible on $\Gamma_c^\varepsilon \subset \Gamma^\varepsilon$. The pores Ω_f^ε and the skeleton are constituted as periodic lattices using domains Y_f and Y_s, respectively, where $Y = Y_s \cup Y_f \cup \Gamma$ is the representative unit cell.

2.1 Disconnected pores – static problems

The problem is described by a variational inequality governing the displacements $\boldsymbol{u}^\varepsilon$ and pore pressure p^ε which is defined by constants in each closed pore $\Omega^{k,\varepsilon} \subset \Omega_f^\varepsilon$. The following sets are employed:

$$\begin{aligned} \textit{kinematic constraint:} \quad & \mathcal{K}^\varepsilon = \{\boldsymbol{v} \in \mathbf{H}^1(\Omega_s^\varepsilon) |\ \boldsymbol{v} = 0 \text{ on } \partial_u \Omega_s^\varepsilon \ , \ g_c^\varepsilon(\boldsymbol{v}) \le 0 \ \text{ on } \Gamma_c^\varepsilon\} \ , \\ \textit{admissible pressure field:} \quad & \mathcal{Q}^\varepsilon = \{q \in L^2(\Omega) |\ q \text{ is constant in each } \Omega^{k,\varepsilon} \ , \ k \in I_f^\varepsilon\} \ , \end{aligned}$$

where g_c^ε is the contact gap function. The variational formulation reads: Find $\boldsymbol{u}^\varepsilon \in \mathcal{K}^\varepsilon$ and the pressure $p^\varepsilon \in \mathcal{Q}^\varepsilon$ such that (given volume forces $\boldsymbol{f}^\varepsilon$)

$$\begin{aligned} \int_{\Omega_s^\varepsilon} \mathbb{D}\boldsymbol{e}(\boldsymbol{u}^\varepsilon) : \boldsymbol{e}(\boldsymbol{v}^\varepsilon - \boldsymbol{u}^\varepsilon) + \int_{\partial\Omega_f^\varepsilon} p^\varepsilon \boldsymbol{n}^{[\mathrm{s}]} \cdot (\boldsymbol{v}^\varepsilon - \boldsymbol{u}^\varepsilon) \ge \int_{\Omega_s^\varepsilon} \boldsymbol{f}^\varepsilon \cdot (\boldsymbol{v}^\varepsilon - \boldsymbol{u}^\varepsilon) \ , \quad \forall \boldsymbol{v}^\varepsilon \in \mathcal{K}^\varepsilon \ , \\ \int_{\partial\Omega_f^\varepsilon} q^\varepsilon \boldsymbol{u}^\varepsilon \cdot \boldsymbol{n}^{[\mathrm{s}]} - \gamma \int_{\Omega_f^\varepsilon} p^\varepsilon q^\varepsilon = 0 \quad \forall q^\varepsilon \in \mathcal{Q}^\varepsilon \ , \end{aligned} \tag{2}$$

where $\boldsymbol{e}(\boldsymbol{v}) = (e_{ij}(\boldsymbol{v}))$ is the small strain tensor, γ is the fluid compressibility, and $\mathbb{D} = (D_{ijkl})$ is the elasticity. $\boldsymbol{n}^{[\mathrm{s}]}$ designates the unit normal vector outward to Ω_s^ε.

2.2 Quasistatic flow in collapsible connected pores

We consider the Stokes slow flow of an incompressible fluid in collapsible pores $\tilde{\Omega}_f^\varepsilon$ of a deformable porous structure. While the solid skeleton small deformations are described in the fixed (initial) configuration Ω_s^ε, the flow in the deformed pores $\tilde{\Omega}_f^\varepsilon(\boldsymbol{u}^\varepsilon)$,

$$\tilde{\Omega}_f^\varepsilon(\boldsymbol{u}^\varepsilon) = \{\boldsymbol{z} \in \mathbb{R}^3 | \boldsymbol{z} = \boldsymbol{x} + \boldsymbol{u}^\varepsilon(\boldsymbol{x}), \ \boldsymbol{x} \in \Omega_f^\varepsilon\} \ , \tag{3}$$

must be respected to comply with the unilateral contact on Γ_c^ε. The variational formulation reads, as follows: Find $(\boldsymbol{u}^\varepsilon, p^\varepsilon, \boldsymbol{w}^\varepsilon) \in \mathcal{K}^\varepsilon \times L^2(\tilde{\Omega}_f^\varepsilon) \times W(\tilde{\Omega}_f^\varepsilon)$ satisfying

$$\begin{aligned} a_\Omega^\varepsilon(\boldsymbol{u}^\varepsilon, \boldsymbol{v}^\varepsilon - \boldsymbol{u}^\varepsilon) + \mathcal{I}^\varepsilon(\boldsymbol{\sigma}_f^\varepsilon, \boldsymbol{v}^\varepsilon - \boldsymbol{u}^\varepsilon) \geq \int_{\Omega_s^\varepsilon} \boldsymbol{f}^\varepsilon \cdot (\boldsymbol{v}^\varepsilon - \boldsymbol{u}^\varepsilon) \;, \quad \forall \boldsymbol{v}^\varepsilon \in \mathcal{K}^\varepsilon \;, \\ \varepsilon^2 \int_{\tilde{\Omega}_f^\varepsilon} \bar{\mu} \nabla \boldsymbol{w}^\varepsilon \cdot \nabla \boldsymbol{\vartheta}^\varepsilon - \int_{\tilde{\Omega}_f^\varepsilon} (\nabla p^\varepsilon - \boldsymbol{f}^\varepsilon) \cdot \boldsymbol{\vartheta}^\varepsilon = 0 \;, \quad \forall \boldsymbol{\vartheta}^\varepsilon \in W(\tilde{\Omega}_f^\varepsilon) \;, \\ \nabla \cdot \boldsymbol{w}^\varepsilon = 0 \quad \text{a. e. in } \tilde{\Omega}_f^\varepsilon \;, \end{aligned} \tag{4}$$

where $a_\Omega^\varepsilon(,)$ is the elastic bilinear form and the interaction integral is established using the stress in fluid $\boldsymbol{\sigma}_f^\varepsilon = -p^\varepsilon \boldsymbol{I} + \varepsilon^2 2 \bar{\mu} \boldsymbol{e}(\boldsymbol{w}^\varepsilon)$,

$$a_\Omega^\varepsilon(\boldsymbol{u}, \boldsymbol{v}) = \int_{\Omega_s^\varepsilon} \mathbb{D}^\varepsilon \boldsymbol{e}(\boldsymbol{u}) : \boldsymbol{e}(\boldsymbol{v}) \;, \quad \mathcal{I}^\varepsilon(\boldsymbol{\sigma}_f^\varepsilon, \boldsymbol{v}^\varepsilon) = \int_{\Gamma_{fs}^\varepsilon} \boldsymbol{n}^{[\mathrm{s}]} \cdot \boldsymbol{\sigma}_f^\varepsilon \cdot \boldsymbol{v}^\varepsilon \;. \tag{5}$$

3. Homogenized porous medium with self-contact at pore level

For the structures with fluid saturated disconnected pores, the homogenized limit problem attains the same form as the one derived for the structures without fluid (empty pores), although the effective tangent stiffness modulus involved in the incremental formulation reflects the fluid action. Henceforth, we focus on the model describing the quasistatic response of the homogenized medium with connected pores. We denote by $\boldsymbol{u}^0$ and p^0 the macroscopic displacement and pressure fields, respectively, and by $\boldsymbol{u}^1$ and p^1 the two scale counterparts of these fields, being Y-periodic functions in the micro-variable $y \in Y$. These constitute the truncated asymptotic expansions introduced using the unfolding operator $\mathcal{T}_\varepsilon()$, see [1], for $x \in \Omega$ and $y \in Y$,

$$\begin{aligned} \mathcal{T}_\varepsilon(\boldsymbol{u}^\varepsilon(x)) &= \boldsymbol{u}^0(x) + \varepsilon \boldsymbol{u}^1(x,y) + \varepsilon^2(\dots \;, \\ \mathcal{T}_\varepsilon(p^\varepsilon(x)) &= p^0(x) + \varepsilon p^1(x,y) + \varepsilon^2(\dots \;, \\ \mathcal{T}_\varepsilon(\boldsymbol{w}^\varepsilon(x)) &= \hat{\boldsymbol{w}}(x,y) + \varepsilon(\dots \;, \qquad \text{where } \hat{\boldsymbol{w}}(x,\cdot) = 0 \text{ in } \overline{Y_s} \;. \end{aligned}$$

Admissible two-scale displacements must satisfy $\boldsymbol{u}^1 \in \mathcal{K}_Y(\nabla \tilde{\boldsymbol{u}}^0)$ where the set $\mathcal{K}_Y$ is defined using the gap function $g_c^Y(\boldsymbol{u}^1, \nabla \boldsymbol{u}^0) = [\nabla \boldsymbol{u}^0 \widehat{y} + \boldsymbol{u}^1 - \widehat{y}]_n^Y \leq 0$ with $\widehat{y} \in \Gamma_c$, where $\Gamma_c \subset \Gamma_{fs}$ is the contact surface, a part of the pore wall Γ_{fs}. The limit two-scale problem with quasistatic flow is derived from Problem (3)-(4). It involves Local problems defined in Y for a.a. $x \in \Omega$, and the Global problem defined in Ω.

The Local problem describes the FSI problem with the unilateral contact and with the Stokes flow in deformed pores $\tilde{Y}_f$,

$$\begin{aligned} \fint_{Y_s} a_{Y_S}\left(\boldsymbol{u}^1 + \boldsymbol{\Pi}^{ij} e_{ij}^x(\boldsymbol{u}^0),\, \boldsymbol{v} - \boldsymbol{u}^1\right) + p^0 \fint_{Y_s} \nabla_y \cdot (\boldsymbol{v} - \boldsymbol{u}^1) \geq 0 \;, \quad \forall \boldsymbol{v} \in \mathcal{K}_Y(\nabla \boldsymbol{u}^0) \;, \\ \bar{\mu} \fint_{\tilde{Y}_f} \nabla_y \hat{\boldsymbol{w}} \cdot \nabla_y \hat{\boldsymbol{v}} + \fint_{\tilde{Y}} (\nabla_y p^1 + \nabla_x p^0 - \boldsymbol{f}^f) \cdot \hat{\boldsymbol{v}} = 0 \;, \forall \hat{\boldsymbol{v}} \in \mathbf{H}_{\#0}^1(\tilde{Y}_f) \;, \\ \fint_{\tilde{Y}_f} q \nabla_y \cdot \hat{\boldsymbol{w}} = 0 \;, \forall q \in L^2(\tilde{Y}_f) \;, \end{aligned} \tag{6}$$

where $\bar{\boldsymbol{u}} = \boldsymbol{\Pi}^{ij} e_{ij}^x(\boldsymbol{u}^0)$ is the displacement field in Y_s produced by the homogeneous strain $\boldsymbol{e}_x(()\boldsymbol{u}^0)$ with $\Pi_k^{ij} = \delta_{ik} y_j$ and the Sobolev space $\mathbf{H}_{\#0}^1$ contains Y-periodic functions with zero traces on the pore wall Γ_{fs}. The elastic bilinear form $a_{Y_S}(,)$ is defined in analogy with the one introduced in (5), but using strains $\boldsymbol{e}_y(\,)$ and domain Y_s in the periodic cell Y. The Global problem is constituted by the static equilibrium and by the Darcy flow involving the permeability $\tilde{\boldsymbol{K}}$, thus,

$$
\begin{aligned}
\int_\Omega \tilde{\boldsymbol{K}}(\nabla_x p^0 - \boldsymbol{f}^f) \cdot \nabla q = 0 \;, \forall q \in Q_0(\Omega) \;, \\
\int_\Omega a_{Y_S} \left(\boldsymbol{u}^1 + \boldsymbol{\Pi}^{ij} e^x_{ij}(\boldsymbol{u}^0),\, \tilde{\boldsymbol{v}}(\boldsymbol{v}^0) + \boldsymbol{\Pi}^{ij} e^x_{ij}(\boldsymbol{v}^0)\right) \\
- \int_\Omega p^0 \left(\phi_f \nabla_x \cdot \boldsymbol{v}^0 - \fint_s \nabla_y \cdot \tilde{\boldsymbol{v}}(\boldsymbol{v}^0)\right) = \int_\Omega \bar{\boldsymbol{f}} \cdot \boldsymbol{v}^0 \;, \forall \boldsymbol{v}^0 \in U_0(\Omega) \;,
\end{aligned}
\tag{7}
$$

whereby the test displacement field $\tilde{\boldsymbol{v}}(\boldsymbol{v}^0)$ must satisfy $g_c^Y(\tilde{\boldsymbol{v}}, \nabla \boldsymbol{v}^0) = 0$ on the actual contact set Γ^* defined a.e. in Ω.

The permeability tensor $\tilde{\boldsymbol{K}}$ depends on the deformation by virtue of the deformed pores $\tilde{Y}_f$ in the local reference cell $Y(x)$. A regularization is considered to prevent a complete closing of the pore at the vicinity of the active contact, *i.e.* where $g_c^Y = 0$. This enables to preserve the well posedness of the local flow problem $(6)_{2,3}$ and, by the consequence, to rely on a strict posive definiteness of $\tilde{\boldsymbol{K}}$, though possibly very small. The permeability dependence on the deformation of Y_f is treated approximately using the sensitivity analysis approach [6], thus $\tilde{\boldsymbol{K}} \approx \boldsymbol{K}^0 + \delta \boldsymbol{K} = \partial_p \boldsymbol{K} \delta p^0 + \partial_{\boldsymbol{e}} \boldsymbol{K} : \boldsymbol{e}_x(\delta \boldsymbol{u}^0)$ at $x \in \Omega$. The two-scale algorithm proposed in [5] can be adapted. The macroscopic increments $(\delta \boldsymbol{u}^0, \delta p^0)$ driven by the out of balance are computed with the "fixed sliding contact" due to active contact sets (local true contact surfaces identified), which modifies the effective macroscopic tangent stiffness.

Acknowledgement

The research has been supported by the grant project GA 22-00863K of the Czech Science Foundation.

References

[1] Cioranescu, D., Damlamian, A., Griso, G., The periodic unfolding method in homogenization, SIAM Journal on Mathematical Analysis 40 (4) (2008) 1585-1620.

[2] Cioranescu, D., Damlamian, A., Orlik, J., Homogenization via unfolding in periodic elasticity with contact on closed and open cracks, Asymptotic Analysis 82 (3-4) (2013) 201-232.

[3] De Luca, T., Facchinei, F., Kanzow, C., A semismooth equation approach to the solution of nonlinear complementarity problems, Mathematical Programming 75 (3) (1996) 407-439.

[4] Griso, G., Migunova, A., Orlik, J., Homogenization via unfolding in periodic layer with contact, Asymptotic Analysis 99 (1-2) (2016) 23-52.

[5] Rohan, E., Heczko, J., Homogenization and numerical modelling of poroelastic materials with self-contact in the microstructure, Computers & Structures 230 (2020) No. 106086.

[6] Rohan, E., Lukeš, V., Modeling nonlinear phenomena in deforming fluid-saturated porous media using homogenization and sensitivity analysis concepts, Applied Mathematics and Computation 267 (2015) 583-595.

COMPUTATIONAL MECHANICS 2022
37th conference with international participation
Srní
November 7 - 9, 2022

Analytical and numerical methods for modelling of acoustic streaming in homogenized rigid porous structures

E. Rohan, F. Moravcová

Faculty of Applied Sciences, University of West Bohemia, Univerzitní 8, 301 00 Plzeň, Czech Republic

1. Introduction

In the paper, we recall the classical perturbation approach which enables to linearize the Navier-Stokes (N-S) equations governing the barotropic viscous fluid dynamics in pores in a rigid periodic structure. The obtained first and second order sub-problems are treated by the asymptotic homogenization to derive the macroscopic model of the porous medium describing the acoustic streaming (AS) phenomenon.

2. Successive approximations of the Navier-Stokes equations

The Acoustic Streaming (AS) appears due to inhomogeneities in viscous flow due to non-zero divergence of the Reynolds stress (due to the kinetic energy of the velocity fluctuations), or due to vibrating fluid-solid interface. It is observed at fluid boundary layers as the Rayleigh streaming due thermal and viscous phenomena, or in the bulk fluid as the high-frequency Eckart streaming.

To distinguish the phenomenon of the AS, pursuing the standard approach of the perturbation analysis, see [4], *cf.* [3], we consider the following approximation of the flow field expressed in terms of different order with respect to the small parameter $\alpha \approx v_0/c_0$, where c_0 is the reference sound speed and v_0 is a characteristic flow velocity, $v_0 \ll c_0$. The fluid velocity, pressure, and density denoted by $\boldsymbol{v}^f, p^f$ and ρ^f are represented by expansions

$$\begin{aligned} \boldsymbol{v}^f &= \alpha \boldsymbol{v}_1 + \alpha^2 \boldsymbol{v}_2 + \dots \ , \\ p^f &= p_0 + \alpha p_1 + \alpha^2 p_2 + \dots \ , \\ \rho^f &= \rho_0 + \alpha \rho_1 + \alpha^2 \rho_2 + \dots \ , \end{aligned} \tag{1}$$

where p_0, ρ_0 are positive constants and a_k denotes k-th order in α approximation of the quantity a. Moreover, we assume that a_k quantity is T-periodic in time, such that the time average of the time derivative vanishes, $\overline{\partial_t a} = 0$. Using (1) substituted in the N-S equations, the 1st and 2nd order problems with respect to α can be distinguished. At the first order, $o(\alpha^1)$,

$$\begin{aligned} \frac{\partial}{\partial t}\rho_1 + \rho_0 \nabla \cdot \boldsymbol{v}_1 &= 0 \ , \\ \rho_0 \frac{\partial}{\partial t}\boldsymbol{v}_1 + \nabla p_1 &= \mu \nabla^2 \boldsymbol{v}_1 + (\mu/3 + \eta)\nabla(\nabla \cdot \boldsymbol{v}_1) \ , \\ p_1 &= c_0^2 \rho_1 \ , \end{aligned} \tag{2}$$

Using the time average over period T of the second order terms, $o(\alpha^2)$, we get

$$\begin{aligned}\frac{\partial}{\partial t}\bar{\rho}_2 + \rho_0 \nabla \cdot \bar{\boldsymbol{v}}_2 &= -\nabla \cdot \overline{(\rho_1 \boldsymbol{v}_1)}\;,\\ \rho_0 \frac{\partial}{\partial t}\bar{\boldsymbol{v}}_2 + \nabla \bar{p}_2 - \mu \nabla^2 \bar{\boldsymbol{v}}_2 + (\mu/3 + \eta)\nabla(\nabla \cdot \bar{\boldsymbol{v}}_2) &= -\rho_0 \left(\overline{(\boldsymbol{v}_1 \cdot \nabla)\boldsymbol{v}_1} + \overline{\boldsymbol{v}_1 (\nabla \cdot \boldsymbol{v}_1)} \right)\;,\\ \bar{p}_2 &= c_0^2 \bar{\rho}_2 + c_0 c_0' \overline{(\rho_1)^2}\;.\end{aligned} \tag{3}$$

The right hand side terms in (3) defined by the time average of the acoustic T-periodic fluctuations $\boldsymbol{v}_1$, *i.e.* the divergence of the Reynolds stress, present the driving force for the AS phenomenon described by $\bar{\boldsymbol{v}}_2$, the time average of the 2nd order velocity field. Different treatment allowing for the acoustic modulation due to multiple time scales, thus, respecting the fast and slow dynamics, was considered in [1].

3. AS in the homogenized medium

We consider the system (2) governing the acoustic waves in the fluid saturating periodic scaffolds represented by the fluid part Y_f of the periodic unit cell, $Y_f \subset]0,1[^2$. The asymptotic homogenization yields the macroscopic model which presents the Darcy flow. In the frequency domain, amplitudes of the acoustic pressure waves $\underset{\sim}{p}_1^0$ satisfying

$$\mathrm{i}\omega \frac{\phi_f}{c_0^2} \underset{\sim}{p}_1^0 - \nabla_x \cdot (\underset{\sim}{\boldsymbol{\mathcal{K}}} \nabla_x \underset{\sim}{p}_1^0) = 0\;, \tag{4}$$

where $\underset{\sim}{\boldsymbol{\mathcal{K}}}(\mathrm{i}\omega)$ is the dynamic permeability and ϕ_f is the porosity. Since the associated velocity $\boldsymbol{v}_1(x,y)$ appears to be incompressible at the microscale, *i.e.* $\nabla_y \cdot \boldsymbol{v}_1 = 0$, the acoustic streaming force involved in the 2nd order system (3) is given by $\overline{\boldsymbol{v}_1(\nabla \cdot \boldsymbol{v}_1)}$. Homogenization of (3) leads to a flow model describing the acoustic streaming phenomenon. The macroscopic flow is described by solutions of

$$-\overline{\boldsymbol{\mathcal{K}}} : \nabla_x \otimes \nabla_x p_2^0 = \nabla_x \cdot \underline{S}(p_1^0, \omega)\;, \quad \mathbf{W}_2 = -\overline{\boldsymbol{\mathcal{K}}} \nabla_x p_2^0 - \underline{S}(p_1^0, \omega)\;, \tag{5}$$

where the "steady" permeability $\overline{\boldsymbol{\mathcal{K}}} = \underset{\sim}{\boldsymbol{\mathcal{K}}}(\mathrm{i}\omega = 0)$ is given by $\underset{\sim}{\boldsymbol{\mathcal{K}}}$ obtained in the 1st order system homogenization, and $\underline{S}(p_1^0(x), \omega)$ depends on the streaming force $\overline{\boldsymbol{v}_1(\nabla \cdot \boldsymbol{v}_1)}$ expressed using p_1^0.

4. Example

To illustrate the acoustic streaming effect, we consider harmonic pressure waves in a 1D macroscopic domain $\Omega =]0,1[$. The microstructure is generated as a periodic lattice by representative cell $Y = Y_f \cup \overline{Y}_s$ whereby the solid obstacle is non-symmetric, see Fig. 3For boundary conditions $\underset{\sim}{p}_1^0(x=0) = 0$ and $(\underset{\sim}{p}_1^0)'(x=1) = 0$, in Fig. 1 we display the analytic solution of (4) which is expressed in terms of Fourier series, such that

$$\underset{\sim}{p}_1^0 = \bar{p} \left(1 + \sum_k A_k \sin\left(\frac{(2k+1)\pi}{2} \frac{x}{L} \right) \right)\;, p_1^0(x,t) = \Re\{\underset{\sim}{p}_1^0(x) \exp(\mathrm{i}\omega t)\}\;, \tag{6}$$

where A_k are the Fourier coefficients. The real response p_1^0 is needed to define the acoustic streaming vector $\underline{S}$ involved in (5). The second order macroscopic pressure distribution $\bar{p}_2^0$ is shown in Fig.2. Since no outflow condition at $x = 1$ is considered, the macro-streaming vanishes $\mathbf{W}_2 = 0$ in the whole of Ω, see (5). Nevertheless, the micro-streaming $\mathbf{v}_2^0(x, \mathbf{y})$ is not zero; the permanent microscopic flow in the fluid domain Y_f is shown in Fig. 3. Different boundary conditions enable for the macroscopic acoustic jet, in general.

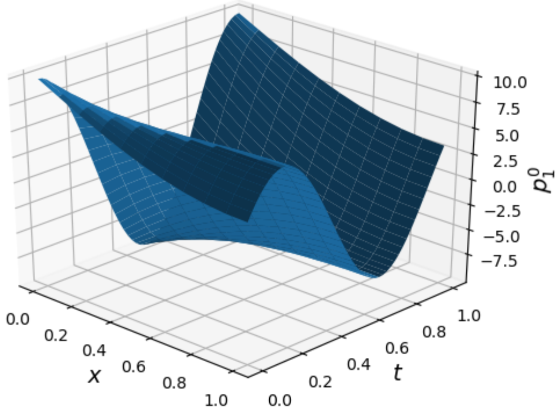

Fig. 1. The space-time distribution of the first order acoustic pressure wave $p_1^0(x,t)$

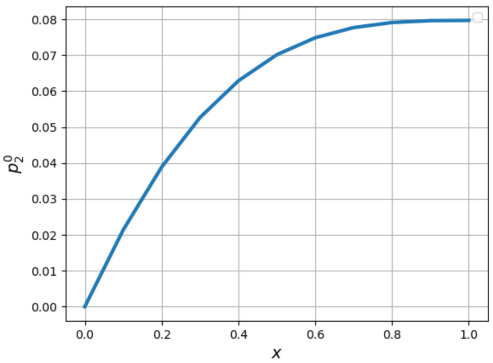

Fig. 2. The distribution of $p_2^0(x)$

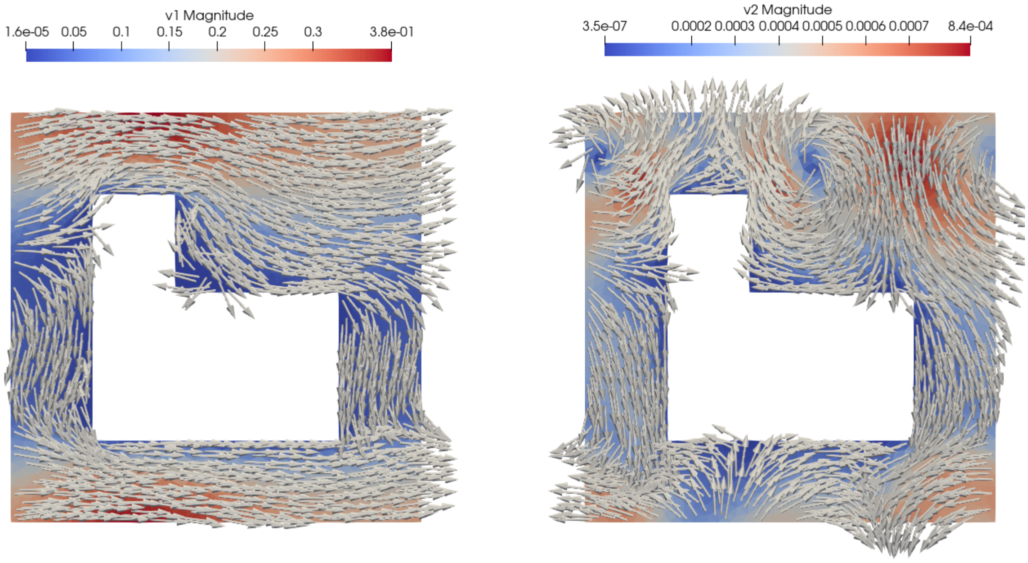

Fig. 3. Reconstruction of the harmonic velocity $\mathbf{v}_1$ at time $t = 0$ (*left*) and permanent $\mathbf{v}_2$ (*right*) in the representative volume Y_f located at the macroscopic position $x = 0$ of the periodic scaffolds

Acknowledgement

The research has been supported by the grant project GA 2116406S of the Czech Science Foundation.

References

[1] Chini, G. P., Malecha, Z., Dreeben, T. D., Large-amplitude acoustic streaming, Journal of Fluid Mechanics 744 (2014) 329-351.

[2] Cioranescu, D., Damlamian, A., Griso, G., The periodic unfolding method in homogenization, SIAM Journal on Mathematical Analysis 40 (4) (2008) 1585-1620.

[3] Lighthill, S. J., Acoustic streaming, Journal of Sound and Vibration 61 (3) (1978) 391-418.

[4] Nyborg, W. L., Acoustic streaming due to attenuated plane waves, Journal of the Acoustical Society of America 25 (1) (1953) 68-75.

COMPUTATIONAL MECHANICS 2022
37th conference with international participation
Srní
November 7 - 9, 2022

Analysis of production parameters of automotive components by injection moulding technology

A. Sapietová, V. Dekýš, R., Z. Šavrnoch

Faculty of Mechanical Engineering, University of Zilina, Univerzitná 8215/1, 010 26 Žilina, Slovakia

The article will present selected requirements necessary for the manufacturability of a plastic component by injection molding technology. With the help of simulation tools, manufacturability will be assessed on the selected plastic component of the car seat. The simulation of the injection molding process will be analyzed using Autodesk Moldflow software. The analysis will take into account the conditions of production of the polymer part by injection with regard to the requirements for its functionality defined by the production drawing.

If we take a closer look at the technology of plastic injection molding, we will discover significant advantages such as automation, reproducibility, precision and low production costs. This technology also has its limitations and specifics, which should be paid attention to. Today, we have simulation tools available that help either directly in product development or tool design [1]. By simulating flow, we can predict the properties of the behavior of the hot-melt in the mold and assume the influence of important parameters such as the choice of the location of the injection point or the deformation .

The component in Fig. 1 (Lockshift) is part of the locking mechanism, which, after pressing the button, allows the movement of the headrest in the vertical direction.

When choosing the material, the strength limit and its impact strength are taken into account. A disproportionate increase in wall thickness is not recommended, as it leads to increased weight, material usage and lengthening of the production cycle due to the extension of the cooling time.

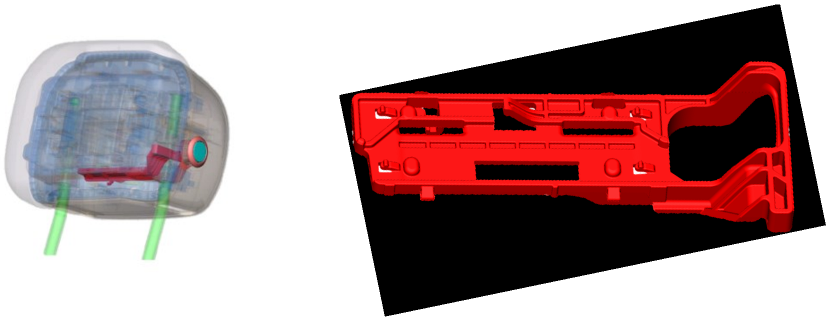

Fig. 1. Headrest (left) and Lockshift (right)

Polymers have become popular due to their properties. They are relatively cheap, have a low specific density and often good electrical insulating properties. They can be combined with other materials to create composites [4]. POM (polyoxymethylene) material was chosen for Lockshift. Emissions of volatile substances are a disadvantage of this material, as it is produced by polymerization of formaldehyde and this is excreted in small quantities during the life cycle. Thanks to its other positive properties (very good sliding and abrasion properties, it is stable in shape and size and has a relatively high strength), it is difficult to replace it.

The injection point is the connection between the inlet system and the molding. Its cross-section should be as small as possible, as it is visible on the molding, but it must also be large enough so that the values of shear stress and pressure loss are not exceeded. The cross-section and position of the injection point have a significant effect on the injection process and are a very common cause of injection problems. Editing it already in its finished form is often difficult and expensive. Therefore, every designer must choose the concept of the inlet system very carefully when designing the part and the mold.

The designer of the molding should already think about the chosen concept of the mold and, therefore, in which direction the molding will be unmolded. The strength of the machine's closing unit depends on the projection of the molding surface in the main direction and the material used, as the injection pressure is projected onto the molding surface. Injection pressures depend on the material and the nature of the product [5]. The simulation program can predict the required closing force based on the viscosity, flow index and shape of the model. When the necessary closing force is estimated, the parts manufacturer can calculate how strong an aggregate will be needed for production. Subsequently, it is necessary to design the part with regard to the release angles. The Lockshift part does not have any elements with negative angles.

The material and its parameters are defined in the simulation program libraries. The simulation program Autodesk Moldflow perform the analysis by using the finite element method (FEM). The simulation results presented in Fig. 2 show that the injection point is not optimally positioned, as the injection time is too long (5.6 s) and the melt junction point is in the weak point of the component. The pressure during switching is 1190 bar (119.2 MPa).

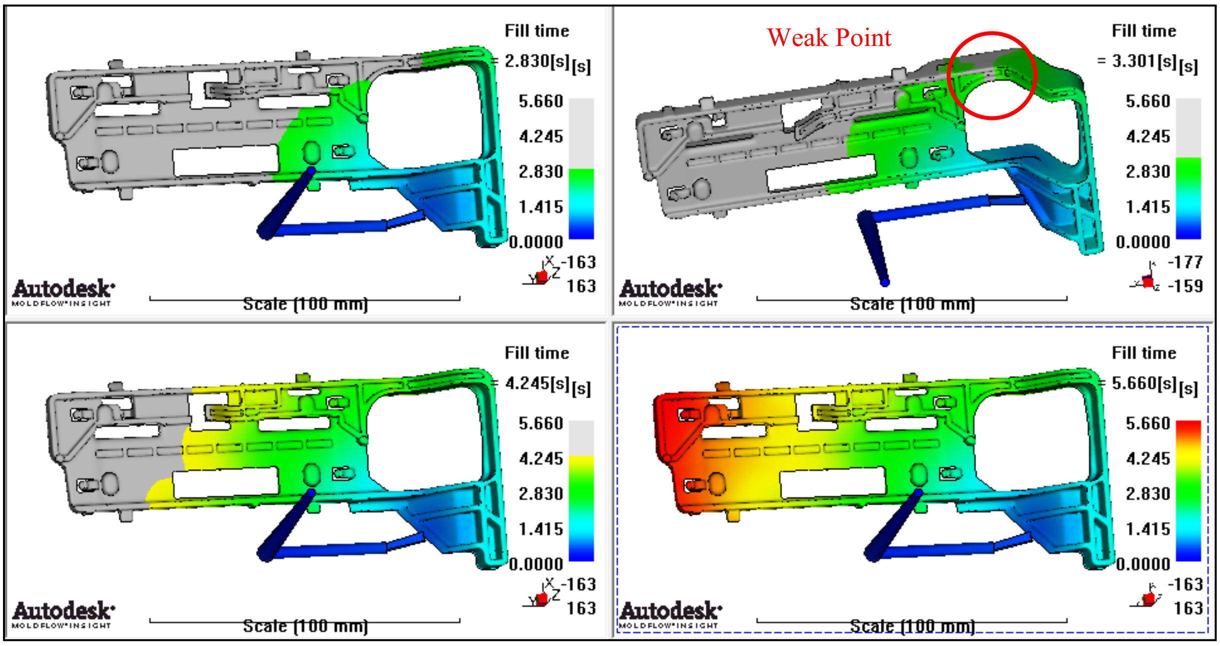

Fig. 2. Flow rate with the originally positioned injection point

From the filling simulation in Fig. 2 and Fig. 3, it takes 5.66 s to fill the part and the switching pressure is approximately 1120 bar. It can be seen from the simulation that the melt flow is not optimal (Fig. 2). The melt has to unnecessarily pass narrow places in order to subsequently reach the open space and also joins in the narrow place. Here it creates a joint line that has lower strength and may break during dynamic tests. Our effort is to make the connection line as long as possible. For a part that weights 21 g, the filling time is relatively long, which is due to how the part is complicated to fill. The filling pressure for POM material should be in the range of

1000 to 1500 bar [2, 3]. The currently predicted injection pressure is within this range, but if the filling point were better chosen, the pressure could be lower. Higher injection pressures mean higher shear stress for the material.

For the reasons discussed above, we changed the location of the injection point and subjected the component to a new analysis in Moldflow software.

From the visualization of filling the cavity with the new injection point in Fig. 4, it is clearly seen that the filling time has been reduced to about 2.8 s. The fusion joint has moved to a more robust part of the part and thus the risk of cracking under dynamic stress has been reduced.

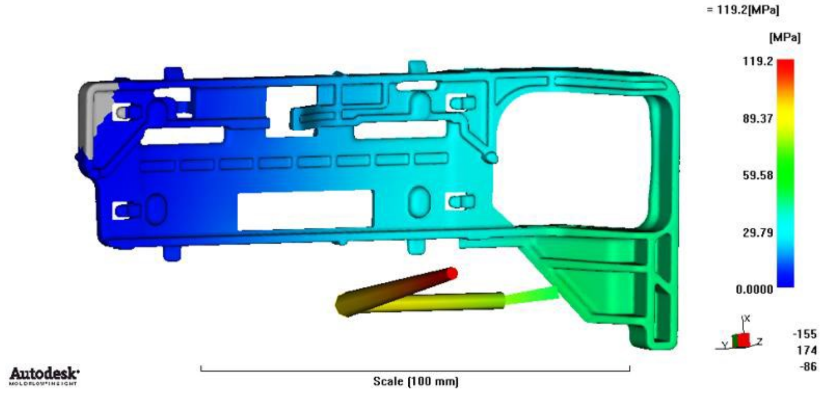

Fig. 3. Mold pressure

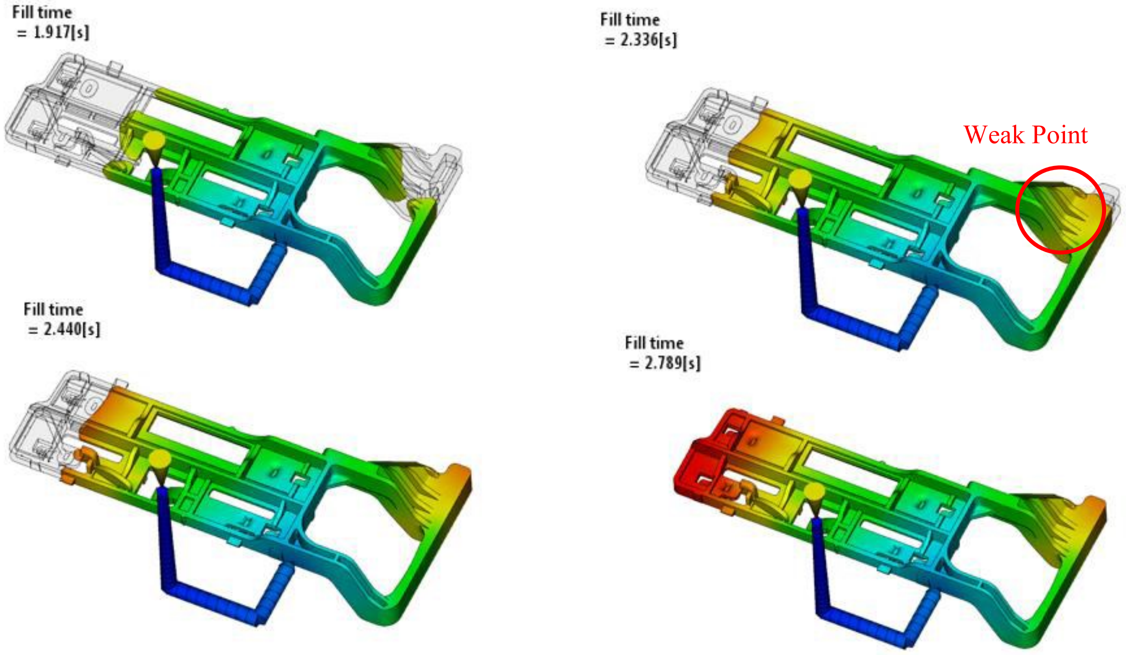

Fig. 4. Flow rate with repositioned injection point

Another improvement is the injection pressure dropped significantly, down to a value of 573 bar. This represents a significantly reduced stress on the material and the reduction in injection time will represent a shortening of the injection cycle by almost 3 seconds. If we further compare the visualization of the deformation from Fig. 5 before and Fig. 6 after adjusting the location of the injection point, we can see that here too we have achieved a significant improvement.

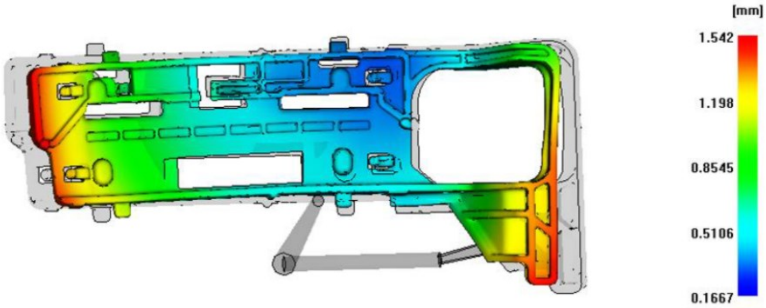

Fig. 5. Deformation with originally positioned injection point

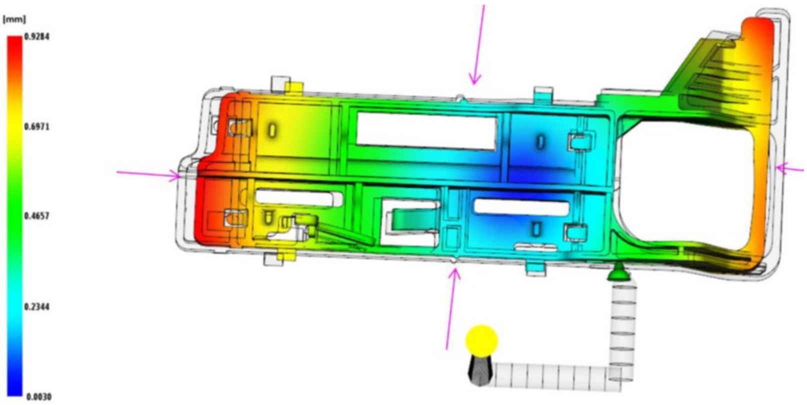

Fig. 6. Deformation after the reposition of injection point

Acknowledgements

This article has been possible with the support of the VEGA 1/0510/20 and VEGA 1/0141/20 projects.

References

[1] Bikas, A., Pantelelis, N., Kanarachos, A., Computational tools for the optimal design of the injection moulding process, Journal of Materials Processing Technology 122 (1) (2002) 112-126.
[2] Kerkstra, R. Brammer, S., Injection molding advanced troubleshooting guide, Hanser Publications, Ohio, 2021.
[3] Lucyshyn, T., D'avernas L.V.D., Holzer, C., Influence of the mold material on the injection molding cycle time and warpage depending on the polymer processed, Polymers 13 (18) (2021) 3196.
[4] Majko, J., Vasko, M., Handrik, M., Saga, M., Tensile properties of additively manufactured thermoplastic composites reinforced with chopped carbon fibre, Materials 15 (12) (2022) 4224-4224.
[5] Yang, W. Zhiwei, J., Injection moulding of polymers, Advances in Polymer Processing: From Macro to Nano Scales, 2009, pp. 175-203.

COMPUTATIONAL MECHANICS 2022
37th conference with international participation
Srní
November 7 - 9, 2022

Spatial active absorber for non-collocated vibration suppression

Z. Šika, J. Gregor, J. Krivošej, T. Vyhlídal

Faculty of Mechanical Engineering, Czech Technical University in Prague, Technická 4, 160 00 Praha 6, Czech Republic

Vibration plays an important role in many engineering applications and often needs to be eliminated. These problems occur with robots, machine tools, with turbine rotors for different applications, in precise instruments such as electron microscopes, deep space telescopes, particle detectors, etc. A novel methodology for vibration absorption of mechanical structures is proposed utilizing tuneable active absorbers as key elements. The absorber(s) are considered to be located in a certain distance from the point on the structure, where vibrations are to be suppressed. This original concept, referred to as the “non-collocated vibration absorption” has a high potential towards applications, where the absorber cannot be placed in the conventional “collocated” manner due to various technological constraints.

The idea of passive vibration absorber connected to the primary mechanical structure to suppress its vibrations is known and patented many decades. The active versions of vibration absorption concept however significantly improve its efficiency. There is a lot of ways of control algorithm design. One specific alternative is a Delayed Resonator (DR) approach [1], which has recently been generalized for simple unidirectional flexible mechanical structures also to non-collocated absorption of vibrations [2].

Realization of non-collocated absorption for a general spatial structures is neither straightforward nor simple. Reduced modal description with consideration of the static residues [3] for neglected higher eigenfrequencies/eigenmodes seems to be suitable form of model. The original state space model is described by matrices in form (1), part of the states corresponding to low frequencies “1” is preserved, whereas part “2” is reduced and replaced by residues. Using modal state variables, the whole state matrix is simplified (2), and residues affect only the feedthrough matrix (3). The matrix $\boldsymbol{A}_{22}$ is tridiagonal and consequently inversion $\boldsymbol{A}_{22}^{-1}$ is also tridiagonal [3]

$$SS_{orig} = \begin{bmatrix} \mathbf{A}_{11} & \mathbf{A}_{12} & \mathbf{B}_1 \\ \mathbf{A}_{21} & \mathbf{A}_{22} & \mathbf{B}_2 \\ \mathbf{C}_1 & \mathbf{C}_2 & \mathbf{D} \end{bmatrix}, \tag{1}$$

$$\mathbf{A} = \begin{bmatrix} \mathbf{A}_{11} & \mathbf{A}_{12} \\ \mathbf{A}_{21} & \mathbf{A}_{22} \end{bmatrix} = diag(\mathbf{A}_{mi}), \mathbf{A}_{mi} = \begin{bmatrix} 0 & \Omega_i \\ -\Omega_i & -2b_{di}\Omega_i \end{bmatrix}, \tag{2}$$

$$SS_{\mathrm{mod}\,spa} = \begin{bmatrix} \mathbf{A}_{11} & \mathbf{B}_1 \\ \mathbf{C}_1 & \mathbf{D} - \mathbf{C}_2\mathbf{A}_{22}^{-1}\mathbf{B}_2 \end{bmatrix}. \tag{3}$$

As the significant extension of previous 2D-DR research [4], [5] the aim of the current investigation is 6 DOF spatial absorber on the flexible spatial multi-DOF structure. The absorber is proposed as compact three-dimensional active device with six identical eigenfrequencies, which could be based e.g. on Stewart platform equipped with springs and voice-coil actuators in each leg (Fig. 1a). The cubic architecture is close to the uni-frequency ideal. Subsequently, applying delayed position feedbacks from voice-coil length encoder sensors, the 3D-6 DOF absorber is turned to the ideal absorber at the given frequency similarly to planar case in [4] and [5]. Basic configuration, with elastically mounted rigid 6 DOF primary platform (Fig. 1b), is farther extended to the above mentioned general flexible spatial multi-DOF primary structure. The example of spatial uni-frequency absorber functionality in *x*, *y*, *z* directions on multi-DOF flexible structure is shown in Fig. 2.

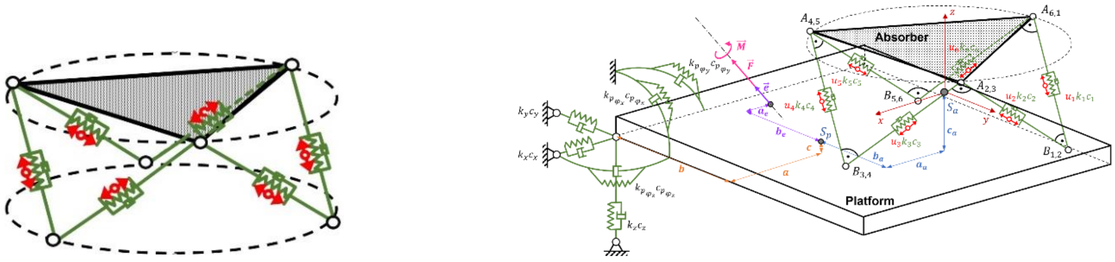

a) absorber mechanical scheme b) absorber mounted on primary platform

Fig. 1. Spatial 6 DOF active absorber

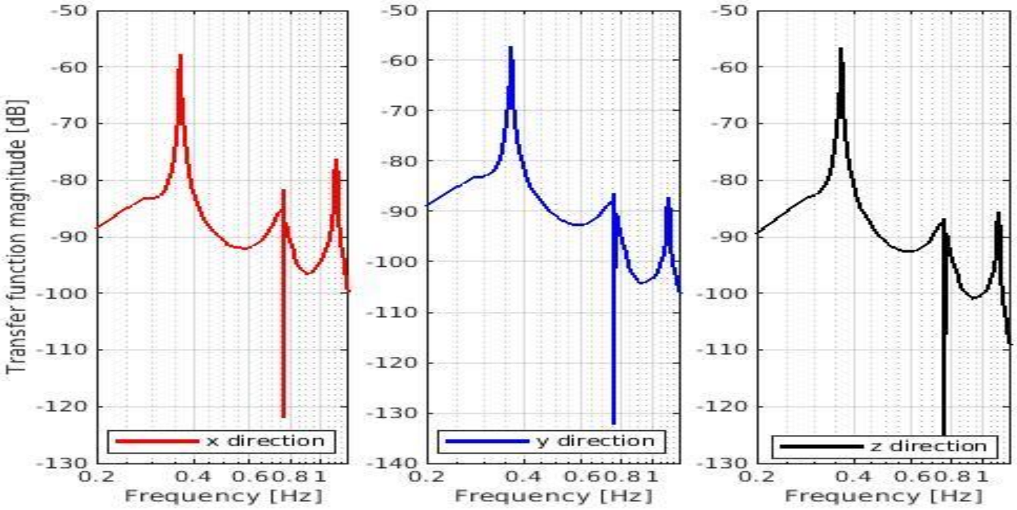

Fig. 2. Example of absorber functionality in *x*, *y*, *z* directions on flexible structure

Acknowledgements

The work has been supported by the Czech Science Foundation project GA21-00871S “Active non-collocated vibration absorption for robots and mechanical structures”. The third author was partly supported by the project SGS22/150/OHK2/3T/12 „Mechatronics and adaptronics 2022” of the Czech Technical University in Prague.

References

[1] Olgac, N., Holm-Hansen, B., A novel active vibration absorption technique: Delayed resonator, Journal of Sound and Vibration, 176 (1994) 93-104.

[2] Olgac, N., Jenkins, R., Time-delayed tuning of vibration absorbers for non-collocated suppression, American Control Conference (ACC), 2020, pp. 1381-1386.

[3] Šika, Z., Zavřel, J., Valášek, M., Residual modes for structure reduction and efficient coupling of substructures, Bulletin of Applied Mechanics 5 (19) (2009) 54-59.

[4] Šika, Z., Vyhlídal, T., Neusser, Z., Two-dimensional delayed resonator for entire vibration absorption, Journal of Sound and Vibration 500 (2021) 116010.

[5] Vyhlídal, T., Michiels, W., Neusser, Z., Bušek, J., Šika, Z., Analysis and optimized design of an actively controlled two-dimensional delayed resonator, Mechanical Systems and Signal Processing 178 (2022) 109195.

COMPUTATIONAL MECHANICS 2022
37th conference with international participation
Srní
November 7 - 9, 2022

Active vibration suppression synthesis of mechanisms with tensegrity properties

T. Šindel, Z. Šika, J. Zavřel

Faculty of Mechanical Engineering, The Czech Technical University in Prague, Technická 4, 160 00 Praha, Czech Republic

1. Introduction

Only a relatively small number of projects is focused on tensegrity structures undergoing large structural deformations. The reason is a highly nonlinear dynamic behaviour complicating the analysis in many ways. In robotic locomotion, for example, the main task of the robot is to transport oneself relative to a global reference frame in terms of an untethered movement. The main advantage of using the tensegrity structures for locomotion is their robustness to the outside environment in terms of damage tolerance and the diffusive force distribution, which allows the structure to be less susceptible to failure when subjected to an unpredictable external disturbance, especially during highly dynamic motion [1]. During this highly dynamic movement, vibrations occur, and they must be eliminated in order to achieve precise movement. This aim applies for robotic manipulation as well.

There are three main types of vibration control: passive, semi-active and active. The passive type, still being the most conventional of the three, is based on inherent properties of the structure itself [3]. The dampers have inherent force-velocity characteristics, imprinted in them during the manufacturing process, and these stay the same if we neglect the temperature changes and the mechanical wear over time. Active and semi-active methods have shown themselves to be more universal, for they can be deliberately adjusted in real time to produce a desired response. Semi-active devices can only absorb energy from the interacting system, hence cannot destabilize it. The passive and semi-active methods essentially rely on their composing material and precision components. Active damping, on the other hand, offers an increased performance in a given control bandwidth while reducing the application cost and is a promising candidate for applications in tensegrity robotics [2].

2. Optimal placement of high-authority actuators

The optimal placement of actuators plays the key role especially for large spatial movements of the structure. The optimization objective is to find a suitable actuation vector c for a given set of contraction responses. Due to the nature of cables, the translational DOFs can be actuated only in one direction – the pulling direction. Thus, it is necessary to ensure the motion of the end-effector (task-space) DOFs in both directions. For this purpose, we rectify the response vectors in positive x^+ and negative x^- senses, respectively. The objective is to maximize the balanced sensitivity function S, which is a weighted sum of sensitivity magnitudes for all task-space DOFs (1)

$$S = 4\sum_{i=1}^{n_t} w_i S_i = \boldsymbol{c^T Q c}; \quad \boldsymbol{Q} = \sum_{\boldsymbol{i=1}}^{\boldsymbol{n_t}} \boldsymbol{w\_i}\left(\left|\boldsymbol{x_i x_i^T}\right| - \boldsymbol{x_i x_i^T}\right). \tag{1}$$

The optimal actuator placement vector for a given number of actuators n_a is then

$$c_{opt} = \arg\max(\boldsymbol{c^T Q c})\,; \quad ||\boldsymbol{c}||_1 = n_a\,. \tag{2}$$

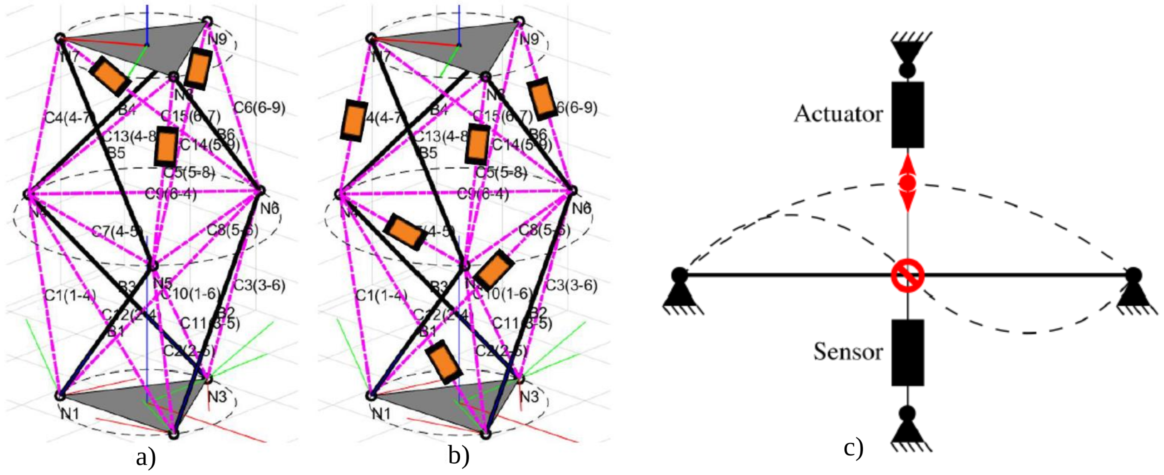

a) b) c)

Fig. 1. Sensor placement for: a) 3 sensors, b) 6 sensors, c) modal shapes

3. Optimal placement of low-authority sensors and actuators

In active vibration suppression, a mere focus on the control algorithm with neglected consideration of a suitable sensor and actuator placement results in a sub-optimal solution. As illustrated on the example (Figs. 1a, b) of a simply supported beam in Fig. 1c, the collocated actuator/sensor pair is placed optimally for the first mode. However, the second mode, and all even modes for that matter, are uncontrollable and unobservable by the actuator, resulting in poorly damped vibrations of these modes. For this reason, it is of a substantial importance to address this issue early in the design process, so that the desired control performance is achieved. An optimal placement of sensors and actuators for a generic tensegrity structure is proposed. The optimization algorithm is based on the derived finite-element dynamic model.

For the actuator placement, a suitable objective is the minimization of control energy required to bring the system eigenmodes to the desired states after a certain time t. This can be expressed by the quadratic form

$$J_c = \int_0^t \boldsymbol{u}^{\boldsymbol{T}}(\tau)\boldsymbol{u}\,(\tau)dt\,. \tag{3}$$

For the placement of sensors, we seek an arrangement that maximizes the output energy of the system in the form

$$J_o = \int_0^\infty \boldsymbol{y}^{\boldsymbol{T}}(\tau)\boldsymbol{y}\,(\tau)dt \tag{4}$$

for the desired modes. To demonstrate this algorithm, a specific example of tensegrity structure was developed (Figs. 1a, b). It is a tensegrity tower with two stages of second order, which implies that two struts are connected at most within the structure. In our case the struts are connected in pairs with spherical joints between the stages. The nodes are fully connected with cables. We can divide the cables in three groups based on their orientation: vertical, horizontal, and diagonal.

Figs. 1a, b shows the geometrical model of the tower which was used in FEM modelling and the following optimization. The placement of sensors and actuators is considered in cables only. The model is has 18 DOF in total including the strut axial deformation and excluding the strut parasitic rotations. This consequently results in 18 modelled vibrational modes. The two objective functions used for optimization are the degrees of controllability and observability. Maximizing these scalar functions by genetic algorithm yields following results: quantitative and qualitative.

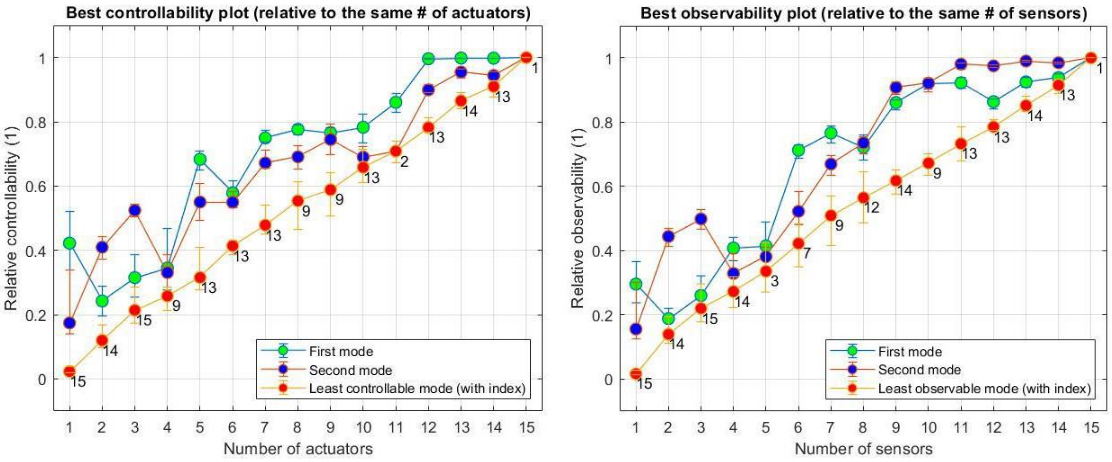

a) b)

Fig. 2. Best controllability/observability plot relative to a single actuator for each possible number of actuators. It is displayed for three different modes

In Fig. 2a a DEGC (degree of controllability) for varying number of actuators is shown. It is displayed for three modes: first, second and the least controllable. Because DEGC is computed relative to the maximum value of controllability across all placements, the maximum value will be unity. In Fig. 2b the controllability relative to a single actuator is displayed. This plot has a significance for the decision-making purposes, where it serves as a useful tool to determine the used number of actuators for the application.

Qualitative results correspond to the best possible placement of sensors (actuators) for every number n_s (n_a) of them starting with one and ending with the total number of cables (when there are sensors/actuators present in each cable). These results are visualized in Fig. 2a and Fig. 2b.

4. Active vibration control synthesis and simulation

A two-stage tensegrity manipulator of type 1, which means that no two struts are connected, was constructed as shown in Fig. 3a. This demonstrator consists of two S3 tensegrity simplexes stacked on top of each other while being surrounded by two platforms – a bottom and a top platform. The bottom platform is considered fixed to the world frame and the top platform supports the end-effector, which is not shown in the figure. The platforms are attached to the struts by universal joints, eliminating parasitic rotations, otherwise present in spherical joints.

For simulation, control law synthesis, and testing, a specific bending movement pattern was chosen as shown in Fig. 3b. The figure shows the task-space coordinates of the top platform along the chosen trajectory performed by the manipulator. The control of large displacements of the manipulator was produced using the computed torque control (CTC) on which the IFF active vibration control was later superimposed. Fig. 3b displays the deviation of the real trajectory from the desired trajectory for the case when only CTC control is used. For practical testing of active vibration suppression, the disturbance signals are injected into the nonlinear simulation model. These signals are modelled in two ways: band-limited white noise injected to both the top and the bottom platform reference frames; and force impulse applied only to the top frame. The vibrational response of the structure is shown in Fig. 3c. It is clear that the response on the disturbance excitations has been attenuated for both the translational and the rotational degrees of freedom.

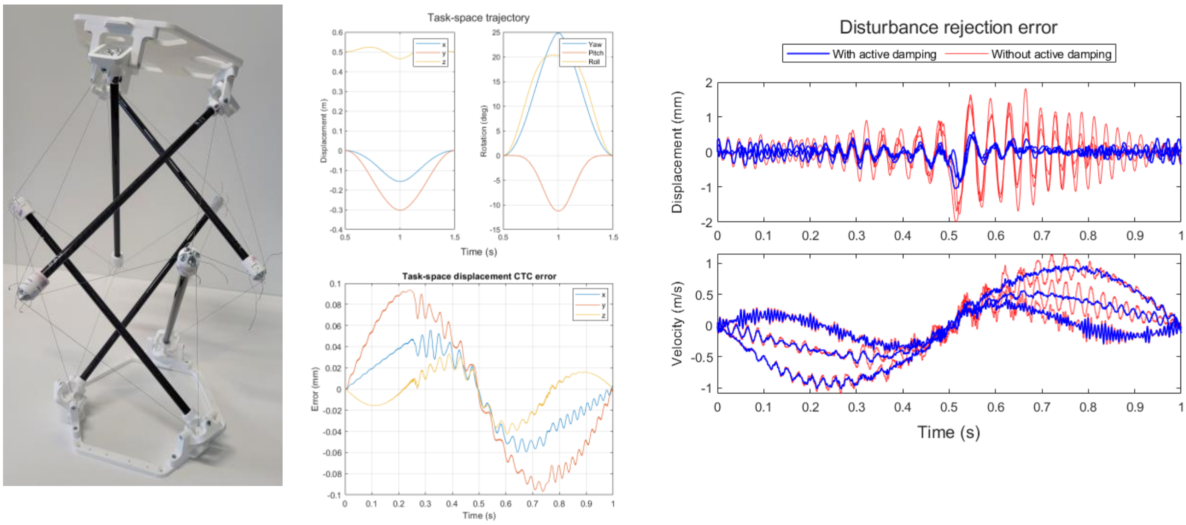

a) b) c)

Fig. 3. a) The physical demonstrator of tensegrity structure, b) displacement and rotation time plot of the top platform and a CTC task-space displacement error plot along the trajectory without disturbances, c) task-space displacement and velocity error with white noise disturbance

5. Conclusion

A complex simulation of the model is performed both in open-loop and closed-loop, both in presence and absence of external disturbances of distinct types. It is shown that the implemented method of active vibration suppression using collocated decentralized integral force feedback is highly effective for tensegrity structures. The suppression was successful for both cases of translational task-space vibrations, but to the lesser extent for the rotational vibrations, where the substantial damping is recorded for the former case only. This finding results in a realization that the pointing performance of controlled tensegrity manipulators needs to be addressed more deeply when kinematic excitations of the base frame are present [4].

Acknowledgements

The research is supported by the Czech Science Foundation project No GA20-21893S “Mechatronic Tensegrities for energy efficient light robots “.

References

[1] Iscen, A., Agogino, A., SunSpiral, V., Tumer, K., Learning to control complex tensegrity robots, in Proceedings of the 2013 international conference on Autonomous agents and multi-agent systems, 2013.
[2] Shah, D. S., Booth, J. W., Baines, R. L., et al., Tensegrity robotics, Soft robotics, 2021.
[3] Skelton, R. E., Adhikari, R., Pinaud, J.-P., et al., An introduction to the mechanics of tensegrity structures, in Proceedings of the 40th IEEE Conference on Decision and Control, Orlando, Florida, USA, 2001.
[4] Šindel, T., Tensegrity mechanisms with active vibration suppression, master thesis, CTU in Prague, 2022.

COMPUTATIONAL MECHANICS 2022
37th conference with international participation
Srní
November 7 - 9, 2022

Finite element model of interaction of human body and seat with variable stiffness

J. Škoda, D. Cirkl, A. Luciová

Faculty of Mechanical Engineering, Technical University of Liberec, Studenstká 2, 461 17 Liberec 1, Czech Republic

1. Introduction

Prolonged sitting is a source of discomfort. We consider the option of changing seat cushion stiffness as the next level of seat customization, which can potentially increase sitting comfort. Modification of the cushion stiffness results in the change of distribution of contact pressure between the human body and the seat. To assess the effects of various seat designs on the contact pressure distribution, we decided to build a finite element model.

2. FEM model

To create the FEM model of the seat (see Fig. 1), we used the 3D scanning of the real seat to get the geometric data of the cushion since we could not get the original CAD data. In order to create a volume finite element mesh of the seat cushion, we first generated the surface tria-quad shell mesh with the target element size of 5 mm. To generate volume mesh, we used the “HEXA POLY“ function of the ANSA pre-processor. Which creates hexahedral mesh inside the volume and polyhedral mesh closer to the surface – see Fig.3.We kept the surface shell mesh in the model for the latter definition of the cushion-human contact and surface pressure recovery. To simplify the model, we did not model the backrest. Thus, we applied a boundary condition to a human body model instead.

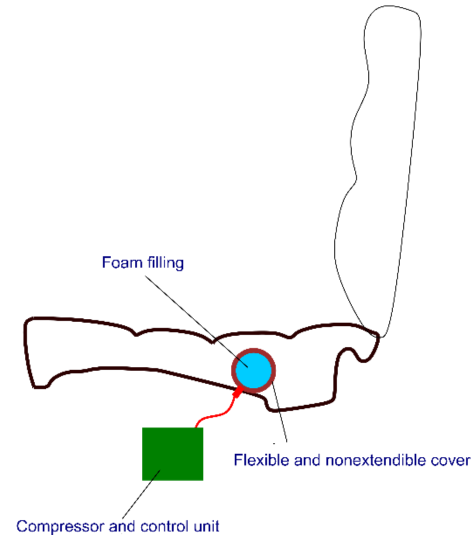

Fig. 1. automotive seat with variable stiffness

Fig. 2. TOYOTA AM50 5.03 occupant model

To identify the material model parameters of the cushion polyurethane foam, we provided laboratory measurements with the foam specimens sized 100x100x50 mm. We exposed the specimen to compressive loading up to relative deformation of 60%. We chose MSC.Marc built-in material model of type "foam," which is a modification of the Ogden model for compressible materials – for the details, see [1].

Next, we implemented the model of the pneumatic element according to the patent [2] (closely described in [3]) into the seat FEM model. The used model of the human body is based on the THUMS human body model AM50 by TOYOTA [4] (see Fig. 2). The THUMS model was initially intended for vehicle collision simulations, but its FEM mesh is coarse enough to keep the model simple and fine enough to maintain its fidelity. Moreover, it is modeled in the sitting position. To shorten the computational time, we used only part of the body, and the rest we replaced with boundary conditions.

3. Conclusion

We simulated the model without applying internal pressure to the pneumatic element – such a case we consider as it was the seat simulation without a pneumatic element. Although we collected experimental data on the pressure distributions of several volunteers seated in the real seat, a comparison of simulated human-seat contact pressure distribution to the experiments is yet to be done.

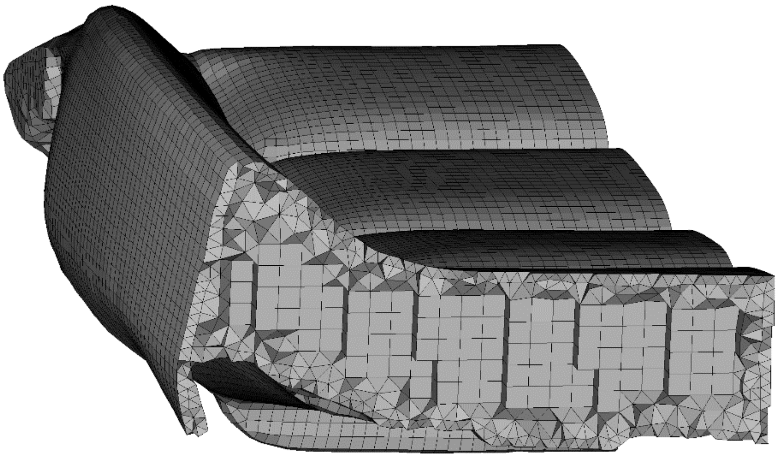

Fig. 3. volume mesh of the seat cushion with hexahedral elements insideand polyhedral close to the surface

Acknowledgements

This work was supported by project European Smarter Seats for Global Innovation in the Automotive Sector (ESSGIAS, no. LTE 120004). The project is co-funded by Czech Ministry of Education, Youth and Sports within the INTER-EUREKA (LTE) INTER-EXCELLENCE programme, supported by EURIPIDES^2 programme and monitored by AENEAS.

References

[1] Cirkl, D., Luciová, A., Škoda, J., Mendřický, R., Validation of FEM model of interaction of car seat chushion and rigid indenter, Engineering Mechanics 2022, 27/28th International Conference, Prague, Institute of Theoretical and Applied Mechanics of the Czech Academy of Sciences, 2022, pp. 77-80.

[2] Technická Univerzita V Liberci. Sedadlo. Patentový spis CZ 303163 B6. 24.9. 2010.

[3] Tran Xuan, T., Cirkl D., FEM model of pneumatic spring supported by a rigid plate, Computational mechanics 2017, 33rd Conference with International Participation, Špičák, University of West Bohemia, 2017, pp. 141-142.

[4] Toyota Central R&D Labs., Inc. total human model for safety (THUMS), AM50 Occupant Model Version 5.03. Technical report, Toyota Motor Corporation, 2021.

COMPUTATIONAL MECHANICS 2022
37th conference with international participation
Srní
November 7 - 9, 2022

Vibration analysis of a vertical rotor immersed in fluid at extreme operating temperatures

L. Smolík[b], R. Bulín[b], M. Hajžman[a], M. Byrtus[a], J. Rendl[b]

[a] *Department of Mechanics, University of West Bohemia, Univerzitní 8, 301 00, Pilsen, Czech Republic*
[b] *NTIS – New Technologies for the Information Society, University of West Bohemia, Technická 8, 301 00, Pilsen, Czech Republic*

Contemporary fusion reactors, such as the International Thermonuclear Experimental Reactor (ITER), require deuterium and tritium to fuel the fusion reaction. Whereas deuterium can be easily extracted from seawater, tritium is very rare. Fortunately, a tokamak can produce tritium when neutrons escaping the plasma collide with lithium in its inner wall. This procedure is called tritium breeding. The search for the superior tritium breeding material is still ongoing, although it started more than 40 years ago. One of the potential candidates evaluated during the ITER project is lead-lithium (PbLi) eutectic material [5], a homogenous mixture of Pb and Li that solidifies at a single temperature. The mixture is produced in a *saturator* that continuously mixes involved substances under laminar flow conditions.

The saturator can be constructed as a vertical rotor with several thin discs, which is placed in a pressure vessel. The clearance between the saturator and vessel is occupied by PbLi, which is mixed as it flows through the vessel thanks to the saturator rotation. The temperature of the PbLi mixture reaches 550 °C, rendering the usage of rolling element bearings or petroleum-based lubricants in journal bearings impossible. However, the dynamic viscosity of PbLi is only $1.28\,\mathrm{mPa\,s}$ at 550 °C [5], which is suitable for providing hydrodynamic lubrication at low specific loads. On the other hand, the density of PbLi at 550 °C is ca. $9300\ \mathrm{kg\,m^{-3}}$ resulting in significant buoyancy and inertia forces acting on the saturator.

This paper explores the potential of using PbLi as a lubricant in the journal bearings of the saturator. PbLi has similar lubricating properties to water due to its low dynamic viscosity, which raises concerns regarding possible whirl/whip instability [2]. Moreover, the high temperature and density of PbLi influence the mechanical properties of the rotor and can cause problems in a thrust bearing due to centrifugal forces. As noted by Nishimura et al. [2], the influence of the pressure vessel (*stator*) on the rotor dynamics is also critical because its first natural frequency is close to the nominal speed of the saturator.

Fig. 1 shows a saturator assembly consisting of three flexible bodies (main rotor, drive shaft and stator), a rigid drive and couplings including a radial journal bearing, a conical bearing supporting the main rotor radially and axially, three deep groove ball bearings and two torsional couplings. Since the assembly contains several flexible bodies and nonlinear couplings, its motion is described utilising the Newton-Euler equations for multi-body dynamics. The exact form of these equations for body B reads [3]

$$\boldsymbol{M}\,\dot{\boldsymbol{v}} - \boldsymbol{p}^{\mathrm{rb}}(\boldsymbol{s},\,\dot{\boldsymbol{s}}) = \boldsymbol{p}^{\mathrm{gyr}}(\boldsymbol{s}) + \boldsymbol{f}^{j}(\boldsymbol{s},\,\boldsymbol{w}) + \boldsymbol{f}^{e}(\boldsymbol{s}) - \boldsymbol{D}\,\dot{\boldsymbol{q}} - \boldsymbol{K}\,\boldsymbol{q}, \tag{1}$$

$$\dot{\boldsymbol{x}}_B = \boldsymbol{v}_B, \tag{2}$$

$$\dot{\boldsymbol{q}} = \boldsymbol{v}, \tag{3}$$

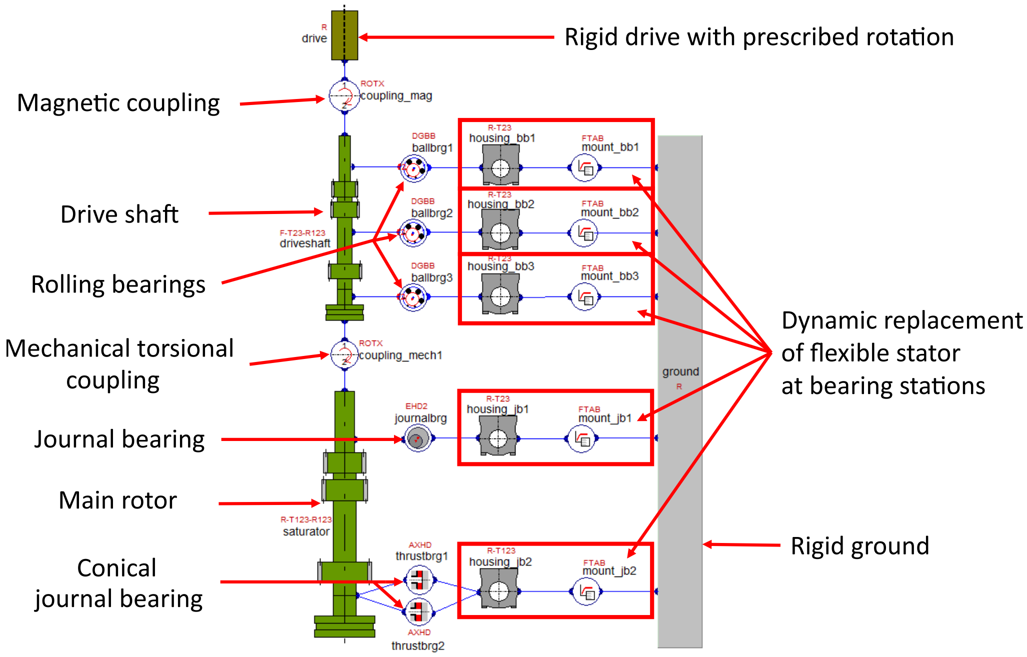

Fig. 1. Scheme of the computational model of the saturator

$$\boldsymbol{\theta}_B^{\mathsf{T}}\boldsymbol{\theta}_B = 1, \tag{4}$$

$$2\,\boldsymbol{S}\left(\boldsymbol{\theta}_B\right)\dot{\boldsymbol{\theta}}_B = \boldsymbol{\Omega}_B, \tag{5}$$

$$\boldsymbol{r}\left(\boldsymbol{q}\right) = \boldsymbol{0}, \tag{6}$$

where $\boldsymbol{x}_B \in \mathbb{R}^{3\times1}$ and $\boldsymbol{\theta}_B \in \mathbb{R}^{4\times1}$ hold the position of a body reference and its orientation given by four Euler parameters. $\boldsymbol{q} \in \mathbb{R}^{6N\times1}$ contains all elastic coordinates defined w.r.t. the body reference with N being a number of nodes that describe the body configuration. State vector $\boldsymbol{s} = \left(\boldsymbol{x}_B^{\mathsf{T}},\, \boldsymbol{\theta}_B^{\mathsf{T}},\, \dot{\boldsymbol{x}}_B^{\mathsf{T}},\, \boldsymbol{\Omega}_B^{\mathsf{T}},\, \boldsymbol{q}^{\mathsf{T}},\, \dot{\boldsymbol{q}}^{\mathsf{T}}\right)^{\mathsf{T}}$ contains both global and elastic coordinates and their respective time derivatives, and vector $\boldsymbol{w}$ consists of state vectors of all bodies coupled to B. $\boldsymbol{M}$, $\boldsymbol{D}$, $\boldsymbol{K} \in \mathbb{R}^{6N\times6N}$ are constant mass, damping and stiffness matrices, respectively. Vectors $\boldsymbol{p}^{\mathrm{rb}}$, $\boldsymbol{p}^{\mathrm{gyr}}$, $\boldsymbol{f}^{j}$, $\boldsymbol{f}^{e} \in \mathbb{R}^{6N\times1}$ incorporate forces resulting from inertia and gyroscopic effects, joint deformations and predefined external loading, respectively. An exact form of vectors $\boldsymbol{p}^{\mathrm{rb}}$, $\boldsymbol{p}^{\mathrm{gyr}}$ is derived in [3] and the form of vector $\boldsymbol{f}^{j}$ depends on governing equations of the coupling forces.

Eqs. (2) and (3) are substitutions required for a numerical integration. Eqs. (4) and (5) describe relations between the Euler parameters, body orientation and angular speed [3]. The system of Eqs. (1)–(5) does not necessarily have a unique solution. Therefore, Eq. (6), which ensures a unique separation of the global and flexible coordinates, has to be attached [3].

Hydrodynamic forces acting in the journal bearings are evaluated employing the modified Reynolds equation complemented with the JFO cavitation model. Governing equations and a method for their solution based on finite volume and multi-grid methods are introduced in [4], and boundary conditions are shown in Fig. 2. Elastic forces acting in the rolling element bearings are estimated using the Hertzian theory. The dynamic characteristics of the stator are computed using a detailed finite element model, which is capable of evaluating frequency response functions (FRFs) between individual bearing stations and the ground. The multi-body model incorporates the FRFs that contain the first two natural frequencies, which correspond to first-order bending mode shapes.

The influence of PbLi on flexural vibrations of the main rotor is implemented in accordance

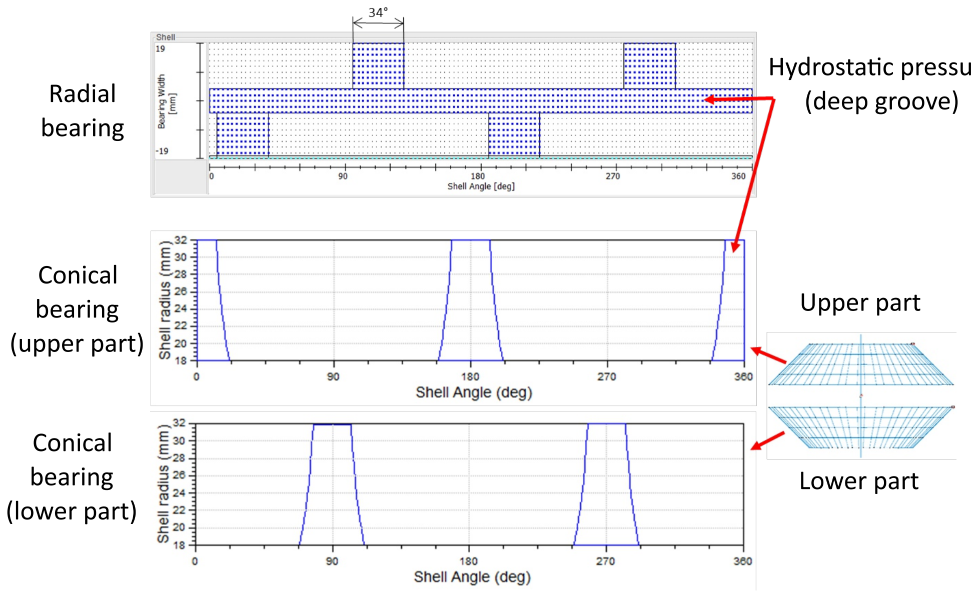

Fig. 2. Boundary conditions considered in the journal bearings of the main rotor

with [1]. Assuming that inertial terms dominate over viscosity terms, the resulting forcing is

$$F_{x,i} = -m_{\mathrm{eff},i}\left(\ddot{x}_i - 2\,\omega_{\mathrm{eff},i}\,\dot{z} + \omega^2_{\mathrm{eff},i}\,x_i\right), \tag{7}$$

$$F_{z,i} = -m_{\mathrm{eff},i}\left(\ddot{z}_i - 2\,\omega_{\mathrm{eff}}\,\dot{x}_i + \omega^2_{\mathrm{eff},i}\,z_i\right), \tag{8}$$

where x, z are horizontal displacements of the i-th node, $m_{\mathrm{eff},i}$ and $\omega_{\mathrm{eff},i}$ are the effective mass and angular speed of PbLi in the vicinity of the i-th node.

Due to the inherent nonlinearity, the system of Eqs. (1)–(6) is solved numerically employing a backward differentiation formula with the variable time step $\Delta t \in \langle 5\cdot 10^{-6},\, 5\cdot 10^{-4}\rangle$ s. The response is simulated in the interval $t \in \langle 0,\, 3\rangle$ s.

Fig. 3 shows hydrodynamic pressure fields in the conical bearing. Apparently, only the upper half of the bearing is active due to the buoyancy force. The hydrodynamic pressure in the lower half is determined only by the boundary conditions. Fig. 3 also reveals that the pressure field is asymmetric. The asymmetry generates a pressure gradient sufficient for hydrodynamic lubrication and is caused by the relative misalignment of the main rotor to the stator.

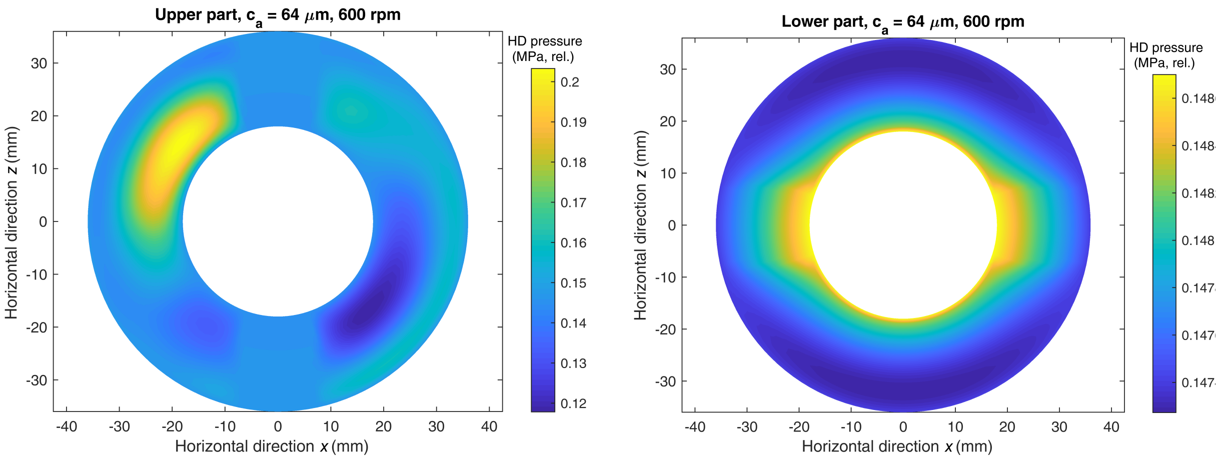

Fig. 3. Results – Hydrodynamic pressure fields in the conical bearing assuming axial (half) clearance $c_a = 64\ \mu\mathrm{m}$ and speed $n = 600$ rpm

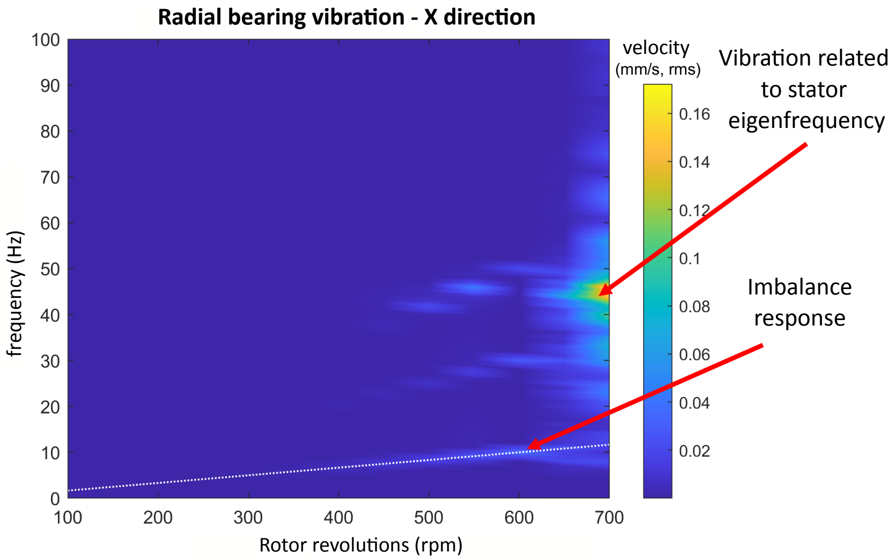

Fig. 4. Results – waterfall plot of absolute vibrations at the radial journal bearing

Fig. 4 depicts a waterfall plot of absolute vibrations of the stator at the radial journal bearing. The vibrations are dominated by the synchronous component caused by rotating unbalance up to 600 rpm. The stator experiences asynchronous vibration related to its natural frequency at speeds from 650 rpm. This asynchronous vibration is surprisingly associated with the conical bearing, which is very lightly loaded because the buoyancy force is almost equal to the gravitational force. The vibration can be attenuated by introducing an additional thrust load.

In conclusion, PbLi is suitable for journal-bearing lubrication, provided the sliding velocity is low to moderate. The low viscosity of PbLi guarantees acceptable power losses, but its high density can be problematic at higher sliding velocities due to innegligible inertial forces.

Acknowledgments

This publication was supported by the project 22-29874S of the Czech Science Foundation. The usage of the AVL Excite software in the framework of the University Partnership Program of AVL List GmbH is greatly acknowledged.

References

[1] Axisa, F., Antunes, J., Flexural vibrations of rotors immersed in dense fluids, Part I: Theory, Journal of Fluids and Structures, 6 (1992) 3-21.

[2] Nishimura, A., Inoue, T., Watanabe, Y., Nonlinear analysis and characteristic variation of self-excited vibration in the vertical rotor system due to the flexible support of the journal bearing, ASME Journal of Vibration and Acoustics 140 (1) (2018) No. 011016.

[3] Offner, G., Modelling of condensed flexible bodies considering non-linear inertia effects resulting from gross motions, Proceedings of the Institution of Mechanical Engineers, Part K: Journal of Multi-body Dynamics 225 (3) (2011) 204-219.

[4] Reichelt, M., Windisch, M., Offner, G., Santner, S., A multigrid method for elasto-hydrodynamic contact simulations of radial slider bearing, Electronic Transactions on Numerical Analysis 54 (2021) 355369.

[5] de les Valls, E. M., Sedano, L.A., Batet, L., Ricapito, I., Aiello, A., Gastaldi, O., Gabriel, F., Leadlithium eutectic material database for nuclear fusion technology, Journal of Nuclear Materials 376 (3) (2008) 353-357.

COMPUTATIONAL MECHANICS 2022
37th conference with international participation
Srní
November 7 - 9, 2022

Problematics of aerodynamic damping calculation from measured data of 5-blade cascade

P. Šnábl, L. Pešek, C. S. Prasad, S. Chindada

Institute of Thermomechanics of the CAS, v. v. i., Dolejškova 1402/5, 182 00 Praha 8, Czech Republic

Aerodynamic damping as a function of inter-blade phase angle (IBPA), so called S-curve, is crucial for assessment of aeroelastic stability of blade cascades, e.g. turbines, compressors, etc. For constructing the S-curve, the motion-induced controlled flutter is introduced to the blades of the cascade. As decribed in [2], two testing methods exist: aerodynamic influence coefficient (AIC) approach and travelling wave mode (TWM) approach. In TWM approach, all blades in a row oscillate with the same frequency and amplitude with various IBPAs. The response is measured only on the reference blade. With this approach, several measurements with different IPBAs are needed to construct the S-curve. On the other hand, AIC uses single oscillating blade and principle of linear superimposition of aerodynamic influence responses measured on all blades in a cascade. The result of one single measurement can be used for estimation of aerodynamic damping for any IBPA.

In the past year a new 5-blade cascade with rotating symmetrical NACA 0010 profiles was designed and built. The blades of the cascade were placed further apart and thus we are now able to reach stall flutter. Also, the suspension of the blades and sensors were significantly improved. Now, our goal is to evaluate S-curves using AIC approach for different flow conditions and oscillation frequencies.

In AIC approach only the middle blade oscillates. Motion of the oscillating blade is measured by laser vibrometer; its moment and moment of two adjacent blades is measured by strain gauges placed on the blade shafts. The aerodynamic moment generated by the flow and acting on the oscillating blade, however, cannot be easily measured as the measured signal also contains moment generated by inertia and damping of the blade. Two methods of extracting the aerodynamic moment from the measured signal, subtraction and identification methods, were used on the previous blade cascade and are described in [1].

Subtraction method subtracts the moment measured with oscillations without the flow from the moment measured with the flow. The disadvantage of this method is that each measurement must be repeated with and without the flow and its accuracy is limited to the cases where the motion of the blade is not affected by the flow.

Identification method is based on identification of the blade inertia and damping from measured data without the flow and using those identified parameters to calculate structural moment using measured motion and subtract it from the measured moment. The advantage over the subtraction method is that only one measurement without the flow is needed and also it is not sensitive to the disturbances in the motion caused by the flow.

Both of those methods, however, subtract a small aerodynamic moment caused by the damping of the air present around the blades in measurements without the flow. They would need to be performed in the vacuum to overcome this issue.

In the new cascade the blade attachment is made with as less damping as possible. With the forced excitation, the only structural damping is caused by deformation of the blade and its shaft and by friction in pin bearing. This structural damping is assumed to be lower then the damping by surrounding air mentioned above. And since the S-curve is calculated from the work per cycle and the inertia of the blade is not generating any work, it is reasonable to integrate the work per cycle directly from the measured moment. Moreover, this direct method is the upper boundary of the true result – no structural nor aerodynamic damping is subtracted, while the two previous methods are the lower boundary – both aerodynamic damping from steady air and the structural damping are subtracted.

Experiments were conducted on the cascade with angle of attack -10°, wind speed 25 m/s and various oscillation frequencies. S-curves were evaluated using all three mentioned methods and compared. Fig. 1 shows comparison of the methods for oscillation frequencies 10 and 40 Hz. In the case when the motion is not disturbed by the flow, subtraction and identification methods should give the same results, as they do for 40 Hz in Fig. 1b. However, this is not true for 10 Hz in Fig. 1a where the S-curve evaluated by subtraction method is shifted downwards and is not correct. As it was mentioned above, the identification (or subtraction) method should be a lower boundary of the true result and direct method the upper boundary. When we look both on Fig. 1a and Fig. 1b, the shift between those two curves is negligible.

This brings us to a conclusion that with the new cascade it is possible to evaluate aerodynamic damping by directly integrating the measured moment to obtain work per cycle. By doing so we can avoid errors caused by imprecise subtraction or identification.

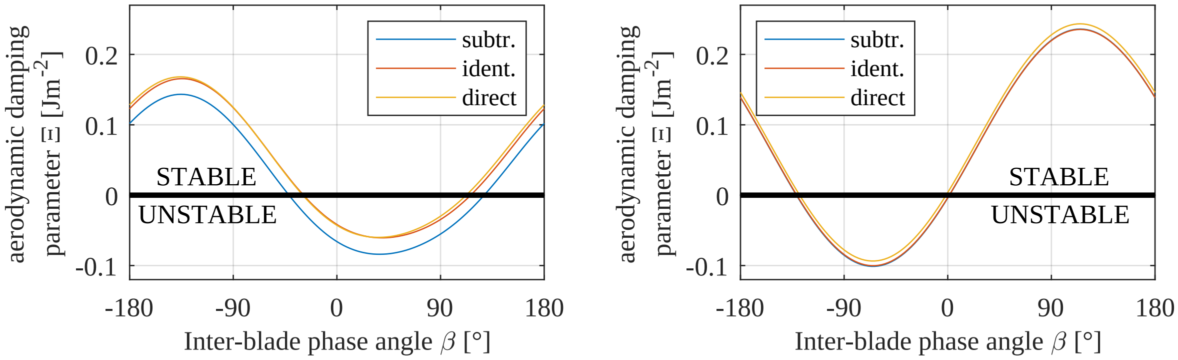

(a) Oscillation frequency 10 Hz

(b) Oscillation frequency 40 Hz

Fig. 1. Comparison of S-curves evaluated by three different methods

Acknowledgement

This research is supported by the research project of Czech science foundation No. 20-26779S "Study of dynamic stall flutter instabilities and their consequences in turbomachinery application by mathematical, numerical and experimental methods".

References

[1] Šnábl, P., Pešek, L., Prasad, C.S., Procházka, P., Experimental investigation of classical flutter in blade cascade, International Forum on Aeroelasticity and Structural Dynamics, Madrid, 2022.

[2] Vogt, D., Experimental investigation of three-dimensional mechanisms in low- pressure turbine flutter, Ph.D. thesis, KTH, School of Industrial Engineering and Management (ITM), Energy Technology, 2005.

COMPUTATIONAL MECHANICS 2022
37th conference with international participation
Srní
November 7 - 9, 2022

Vocal tract acoustic modelling using FEM with specific element

J. Štorkán, T. Vampola

Department of Mechanics, Biomechanics and Mechatronics, Faculty of Mechanical Engineering, Czech Technical University in Prague.
Technická 4 Praha 6 Czech Republic

1. Introduction

The acoustics of the vocal tract are involved in the creation of vowel and the timbre of the voice. Bioacoustics and the creation of the human voice is an intensively researched field. Acoustic analyses of vocal tracts investigate the influence of geometry on the character of the voice. This is based on work [1]. According to this work, the vocal cords generate pressure or velocity pulses (source voice) that are independent of the phonated voice. The vocal tract is a dynamic system that modulates the frequency spectrum of the source voice. The transmission function of the vocal tract between the vocal cords and the mouth determines the vowel and timbre of the voice.

Vocal tract analyses are most often performed using the finite element method (FEM) or experimentally. Other methods are less used. The vocal tract is geometrically complicated. Its shape is characteristic. It is a channel of variable cross-section. Frequencies below 4kHz are important for the human voice. At these frequencies, mainly longitudinal waveforms and the simplest transverse waveforms are existed. A conventional FEM model must have a fine mesh to describe complex geometry. Such a model is suitable for analyses in a wide spectrum of frequencies. It is unnecessarily complex for the frequencies of the human voice. A coarser model would not describe the geometry well. In this work, a new element for FEM is developed. This element is suitable for modelling vocal tracts. It has a minimum of degrees of freedom and yet it can describe the geometry of the vocal tract well. This will make it possible to build numerically more efficient models that are similarly accurate as classic FEM models.

2. Formulation acoustic for FEM

The propagation of acoustic waves in the environment is described by the wave equation. A wave equation of the form with losses in the medium is assumed

$$\frac{\partial^2 p'}{\partial t^2} + \frac{r}{\rho_0}\frac{\partial p'}{\partial t} = c_0^2 \Delta p'. \tag{1}$$

The FEM uses a weak formulation of the partial differential equation problem [2]. Multiply the equation by the test function and integrate over the solved volume

$$\int_V \left(\delta p' \frac{\partial^2 p'}{\partial t^2} + \delta p' \frac{r}{\rho_0}\frac{\partial p'}{\partial t}\right) dV = \int_V (\delta p' c_0^2 \Delta p')\, dV\,, \tag{2}$$

$$\int_V \left(\delta p' \frac{\partial^2 p'}{\partial t^2} + \delta p' \frac{r}{\rho_0}\frac{\partial p'}{\partial t} + c_0^2 (\nabla \delta p')^T (\nabla p')\right) dV = \int_{\partial V} (n^T c_0^2 \delta p' \nabla p')\, dS\,. \tag{3}$$

From the theory of potential flow, it is possible to determine the dependence between acoustic pressure and acoustic velocity

$$\rho_0 \frac{dv'}{dt} = -\nabla p' . \tag{4}$$

Then it applies

$$\int_V \left(\delta p' \frac{\partial^2 p'}{\partial t^2} + \delta p' \frac{r}{\rho_0} \frac{\partial p'}{\partial t} + c_0^2 (\nabla \delta p')^T (\nabla p') \right) dV = -\int_{\partial V} \left(n^T c_0^2 \delta p' \rho_0 \frac{dv'}{dt} \right) dS . \tag{5}$$

Acoustic velocity is eliminated by using acoustic impedance

$$n^T v' = \frac{p'}{Z} , \tag{6}$$

$$\int_V \left(\delta p' \frac{\partial^2 p'}{\partial t^2} + \delta p' \frac{r}{\rho_0} \frac{\partial p'}{\partial t} + c_0^2 (\nabla \delta p')^T (\nabla p') \right) dV = -\int_{\partial V} \left(c_0^2 \delta p' \frac{\rho_0}{Z} \frac{dp'}{dt} \right) dS . \tag{7}$$

The integration is over the entire volume (surface). Since integration is additive, it is possible to convert it to integration over individual elements and use shape functions

$$p'(t,x,y,z) = N_e(x,y,z) P_e(t) , \tag{8}$$

$$\delta p'(t,x,y,z) = \delta P_e^T(t) N_e^T(x,y,z) . \tag{9}$$

The equation will take the form

$$\delta \hat{P}_e^T \left(\int_{V_e} \left(-N_e^T N_e \ddot{P}_e + N_e^T \frac{r}{\rho_0} N_e \dot{P}_e + c_0^2 (\nabla N_e)^T (\nabla N_e) P_e \right) dV + \int_{\partial V_e} \left(N_e^T c_0^2 \rho_0 \frac{1}{Z} N_e \dot{P}_e \right) dS \right) = 0 . \tag{10}$$

After dividing the equation by the square of the sound speed, it is possible to introduce the matrices defining the element

$$M_e = \frac{1}{c_0^2} \int_{V_e} (N_e^T N_e) dV , \tag{11}$$

$$B_e = \frac{1}{c_0^2 \rho_0} \int_{V_e} (r N_e^T N_e) dV + \rho_0 \int_{\partial V_e} \left(N_e^T \frac{1}{Z} N_e \right) dS , \tag{12}$$

$$K_e = \int_{V_e} \left((\nabla N_e)^T (\nabla N_e) \right) dV . \tag{13}$$

The integral of one element turns into the form

$$\delta P_e^T \left(M_e \ddot{P}_e + B_e \dot{P}_e + K_e P_e \right) = 0 . \tag{14}$$

Since the integration is additive, the contributions of all elements must be added. This will create a global mass, stiffness and damping matrix

$$\delta P^T \left(M \ddot{P} + B \dot{P} + K P \right) = 0 . \tag{15}$$

The nodal sound pressure variation is any value satisfying the boundary conditions. Therefore, the form of the equilibrium equations is as follows

$$M \ddot{P} + B \dot{P} + K P = 0 . \tag{16}$$

3. New element

The purpose of the new element is to describe the complex shape of the cross-section of the geometry with a minimum of nodal points. Significant vibration shapes are longitudinal in nature. Transverse sound pressure gradients should be less significant. That is why we are looking for an element that ideally describes the entire cross-section. The elements are then stacked on top of each other, this makes it possible to change the cross-section along the length. Internal element nodes are not desirable. They increase the size of the model and the computational complexity.

A separate element that would have the described properties was not created. The created element must be used at least 3 times in each section. The element used is shown in Fig. 1. The element is based on a triangular element in the η-ξ plane. It is an isoparametric element in the reference coordinate system [3]. This element is of the sixth order of accuracy. It has 28 nodes, these nodes have been eliminated at the shape function level. Only corner nodes and nodes on coordinates satisfying the equation η+ξ-1=0 are left. Such a planar element is swept out into 3D space. In the third spatial direction, the element is linear. The resulting element is shown in Fig. 1. The nodes at coordinates (0,0,0) and (0,0,1) are located on the midline of the vocal tract. The other nodes form the surface of the vocal tract. In this work, 6 elements are used in one layer. There are 36 nodes in the section on the circuit.

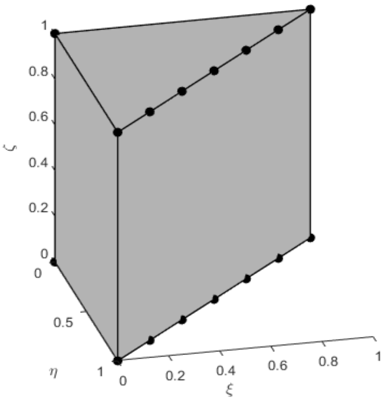

Fig. 1. Used element

Numerical tests showed excellent conditionality of the element even with complex geometric configurations. Fig. 2 shows that for a circular cross-section the worst-case condition is 2.5 and for a strongly non-convex geometry it is 5.5.

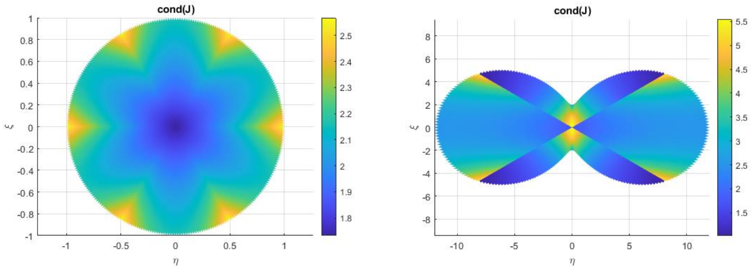

Fig. 2. Conditionality elements creating circle and nonconvex area

4. Vocal tract modelling

Vocal tract geometry was obtained using MRI. This is the geometry for the vowel /a:/.

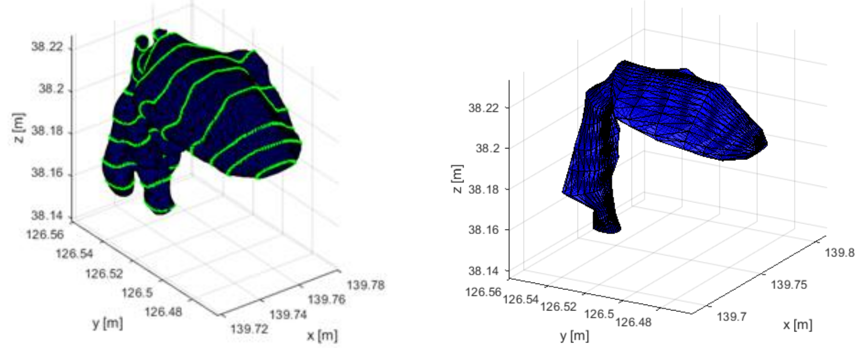

Fig. 3. MRI measurement with cross sections and FEM model

The geometry is shown in Fig. 3. The green lines are the positions of the sections, and the resulting FEM model is on the right. The model was subjected to a modal analysis with velocity boundary condition at the inlet and acoustic impedance at the outlet. The impedance was set according to [4].

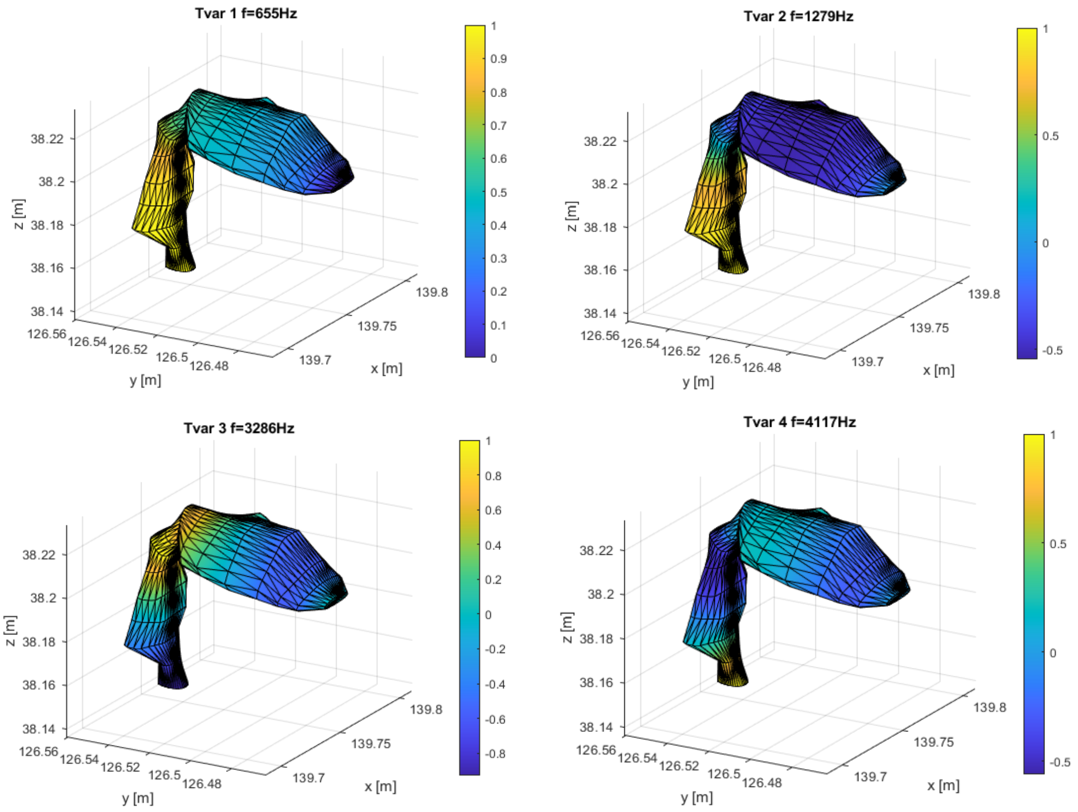

Fig. 4. First 4 eigenmodes

The results of the analyses from Fig. 4 show a good agreement with the generally accepted data, as well as with other better models.

5. Conclusion

The designed element has ideal properties for modelling the acoustics of vocal tracts. The model of the vocal tract composed of 15 layers with 6 elements has only 592dof and in the frequency band 0-6kHz shows a deviation from analytical models of less than 5%. The FEM model with new elements can accelerate the analysis and research of the biomechanics of the human voice.

Acknowledgements

The study was supported by the Czech Science Foundation, Grant No. 19-04477S: “Modelling and measurements of fluid-structure-acoustic interactions in biomechanics of human voice production.”

References

[1] Fant, G., Acoustic theory of speech production, 2nd edition, The Hague, Netherlands: Mouton, 1970.
[2] Johnson, C., Numerical solution of partial differential equations by the finite element method, Cambridge Universiry Press, Cambridge, 1987.
[3] Silvester, P., High-order polynomial triangular finite elements for potential problems, International Journal of Engineering Science 7 (8) (1969) 849-861.
[4] Vampola, T., Horáček, J., Švec, J.G., FE modelling of human vocal tract acoustics. Part I: Production of Czech Vowels, Acta Acustica united with Acustica 94 (2008) 433-447.

COMPUTATIONAL MECHANICS 2022
37^{th} conference with international participation
Srní
November 7 - 9, 2022

Identification of dispersion and attenuation curves of thin non-prismatic heterogeneous viscoelastic rods

J. Šulda[a], R. Kroft[b], V. Adámek[a]

[a] *Department of Mechanics, Faculty of Applied Sciences, University of West Bohemia, Univerzitní 8, 301 00 Plzeň, Czech Republic*
[b] *NTIS – New Technologies for the Information Society, Faculty of Applied Sciences, University of West Bohemia, Technická 8, 301 00 Plzeň, Czech Republic*

This work deals with the identification of the dispersion and attenuation properties of a thin heterogeneous viscoelastic non-prismatic rod. The first two parts of the text will discuss applications of these properties and the possible identification method. Next, the experiments are described, which are performed on several thin homogeneous prismatic rods but also on heterogeneous and non-prismatic rods. The experimental results are compared with analytically obtained results in the following section. At the end of this work, the results are discussed.

The reason for the identification of dispersion and attenuation properties of viscoelastic materials is mainly to solve the problems of passive vibration damping, and for the SHPB test, which consists of a thin input and output rod, between which a sample of similar impedance is placed (see [3]). Previously, typically elastic thin rods have been used in the SHPB test, which was based primarily on investigating the propagation of longitudinal elastic waves. Over time, during the development of plastic materials, it was also necessary to investigate wave phenomena in rods with significantly lower impedance, for which the theory of elastic wave propagation was no longer sufficient. For the description of wave phenomena in viscoelastic materials, discrete rheological models are advantageously used, which can be drawn schematically as a connection of elastic springs and viscous dashpots.

Each homogeneous part of the layered rod is described by a different dashpot viscosity and spring stiffness. Due to this and the variable cross-section of the rod, different attenuation and dispersion behaviour occurs in these parts. To determine the properties of the layered rod, measuring after the wave has passed through the entire rod under investigation is necessary. Several identification methods can be found that meet these requirements. A method described by Blanc (see [2]) will be used in this work. This method requires a Fourier transform of the acceleration measured at two different locations ($x_1 < x_2$) on the rod caused by the passage of the wave packet. According to Blanc, the relations for calculating the phase velocity $c(\omega)$ and the wave number $\kappa(\omega)$ or the attenuation $\alpha(\omega)$ can be written as [2]

$$\begin{aligned} c(\omega) &= \frac{\omega}{\kappa(\omega)} = -\omega \frac{x_2 - x_1}{\theta(x_2,\omega) - \theta(x_1,\omega)}, \\ \alpha(\omega) &= -\frac{1}{x_2 - x_1} \ln \frac{\vartheta(x_2,\omega)}{\vartheta(x_1,\omega)}, \end{aligned} \tag{1}$$

where ω is the angular frequency, $\theta(x,\omega)$ and $\vartheta(x,\omega)$ are the phase and the modulus of the Fourier transform of the acceleration, respectively.

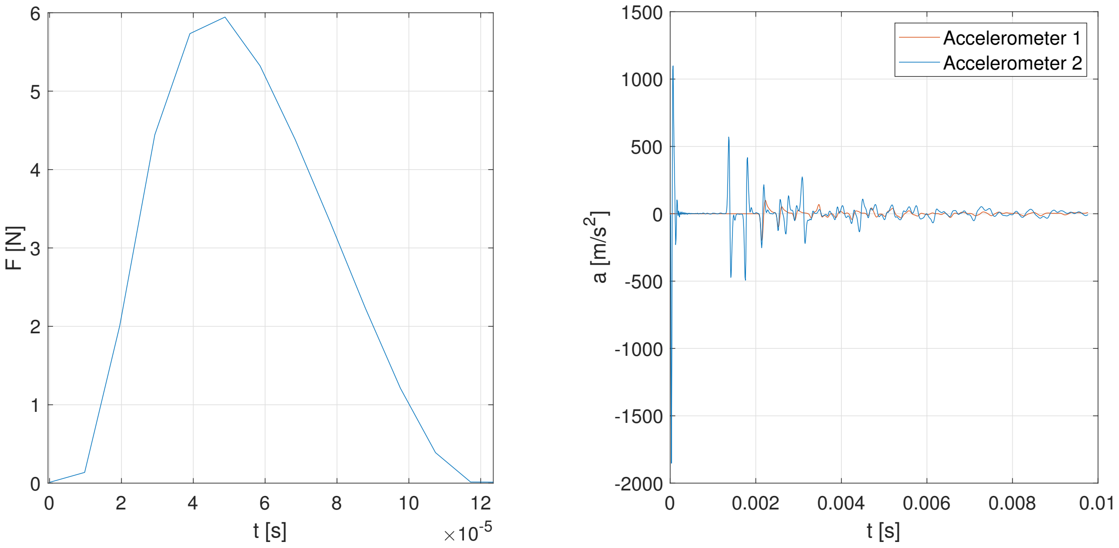

(a) Excited pulse (b) Acceleration response

Fig. 1. Experimental data for the heterogeneous non-prismatic rod

Acceleration was measured by two accelerometers of brand *Brüel & Kjær Miniature DeltaTron® Accelerometer – Type 4519* at the ends of the investigated rods. Rods were excited at one end by an impact hammer *Brüel & Kjær Miniature Impact Hammer – Type 8204*. The signals from the accelerometers and the hammer were processed by an eight-channel analyser *OROS OR35* with a sampling rate of $100\,\mathrm{kHz}$. The measurement was performed on four homogeneous prismatic rods of approximate length $1\,\mathrm{m}$ made of polypropylene (PP), polyvinyl chloride (PVC), polyethene terephthalate (PET), polylactic acid (PLA). Also on a homogeneous non-prismatic rod made of PLA of a length $1\,\mathrm{m}$ and on a heterogeneous non-prismatic rod, which was composed of 4 homogeneous prismatic parts of different cross-sections and made of acetal heteropolymer (POM-C), aluminium (AL), polycarbonate (PC1000) and PP in this order with a total length of $4\,\mathrm{m}$. A smooth cosine pulse of length $100 - 200\,\mu\mathrm{s}$ was generated for all rods using the mentioned impedance hammer. This pulse excited the heterogeneous rod at the end of the POM-C segment, and the acceleration response to this pulse can be seen in Fig. 1b. The amplitude of each excited pulse depends proportionally on the weight of the examined rod, so Fig. 1a shows the highest measured amplitude. From Fig. 1b, it is possible to observe a significant decrease in the acceleration amplitude, i.e., the energy dissipation due to the viscosity and various cross-sections of the rod segment.

The measured phases and modulus of the transformed acceleration were used in relation (1), and the frequency dependences of longitudinal wave phase velocity and attenuation were obtained for each rod. These curves were compared with analytically calculated curves for homogeneous prismatic rods whose material is characterised by Zener rheological model. Analytical relations for the evaluation of these curves are provided, for example, by Ahonsi in his work [1]. In his relations

$$\kappa^2(\omega) = \frac{\rho\omega^2}{2E_E}\left(H_1 + H_2\right), \quad \alpha^2(\omega) = \frac{\rho\omega^2}{2E_E}\left(H_1 - H_2\right), \tag{2}$$

the author considers transverse contractions during the propagation of the pulse, i.e., the nonzero Poisson ratio ν and the inertia of the rod elements in the radial direction characterised by the radius of gyration r. The density of the rod is denoted by ρ, and E_E is the modulus of

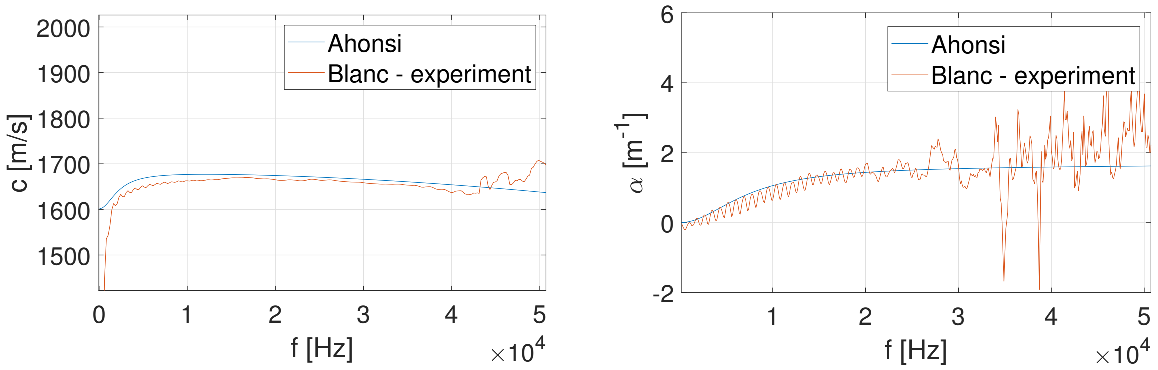

(a) Dispersion curve of the homogeneous PVC rod

(b) Attenuation curve of the homogeneous PLA rod

Fig. 2. Comparison of analytically obtained and experimentally measured dispersion and attenuation curves for rods made of homogeneous material

elasticity of the alone-standing spring in the Zener material model. Real functions H_1 and H_2 in (2) are given by

$$
\begin{aligned}
H_1 &= \sqrt{\frac{1+\omega^2 t_R^2}{\left[\left(1+\frac{E_1}{E_E}\right)-\frac{\rho\nu^2 r^2\omega^2}{E_E}\right]^2 \omega^2 t_R^2 + \left(\frac{\rho\nu^2 r^2\omega^2}{E_E}-1\right)^2}}, \\
H_2 &= \frac{\left[\left(1+\frac{E_1}{E_E}\right)-\frac{\rho\nu^2 r^2\omega^2}{E_E}\right] \omega^2 t_R^2 - \left(\frac{\rho\nu^2 r^2\omega^2}{E_E}-1\right)}{\left[\left(1+\frac{E_1}{E_E}\right)-\frac{\rho\nu^2 r^2\omega^2}{E_E}\right]^2 \omega^2 t_R^2 + \left(\frac{\rho\nu^2 r^2\omega^2}{E_E}-1\right)^2}.
\end{aligned}
\tag{3}
$$

Symbols E_1 and t_R denote the modulus of elasticity of the spring and the relaxation time characterising the Maxwell branch in the Zener model, respectively.

When comparing the analytically obtained dispersion curves for all homogeneous materials, it was possible to achieve agreement within 20 to $50\,\mathrm{kHz}$. For example, the comparison for a rod made of PVC material is shown in Fig. 2a. For the attenuation curves, it was possible to achieve a much smaller agreement with the analytics (curves marked as Ahonsi), i.e., from 8 up to $25\,\mathrm{kHz}$, see Fig. 2b showing the attenuation of the PLA rod. The accuracy of the results, especially the attenuation, was influenced by the relatively low sampling rate of the signal. The transverse contraction of the rod in the relation (2) positively influenced the agreement of the results. In the case of a non-prismatic and heterogeneous rod, the comparison of the curves identified from the excitation at both ends of the rod was used to verify the results. In this way, it was possible to verify the dispersion curve up to $40\,\mathrm{kHz}$ for the non-prismatic rod (see Fig. 3a), and the attenuation curve only up to $35\,\mathrm{kHz}$ (see Fig. 3b). For the heterogeneous rod, dispersion and attenuation have been verified up to $18\,\mathrm{kHz}$ as shown in Fig. 3c and 3d.

The identified dispersion and attenuation curves in Fig. 2 are similar to the curves presented in [1] and [2]. The phase velocity and the attenuation for a homogeneous viscoelastic rod increase with higher frequencies. For thicker rods, where the measured acceleration is more influenced by transverse contractions, it was shown that with increasing frequency, the wave speed decreases but the attenuation increases. The dispersion curve of homogeneous non-prismatic and heterogeneous non-prismatic rods is constant on the identified part, and the attenuation

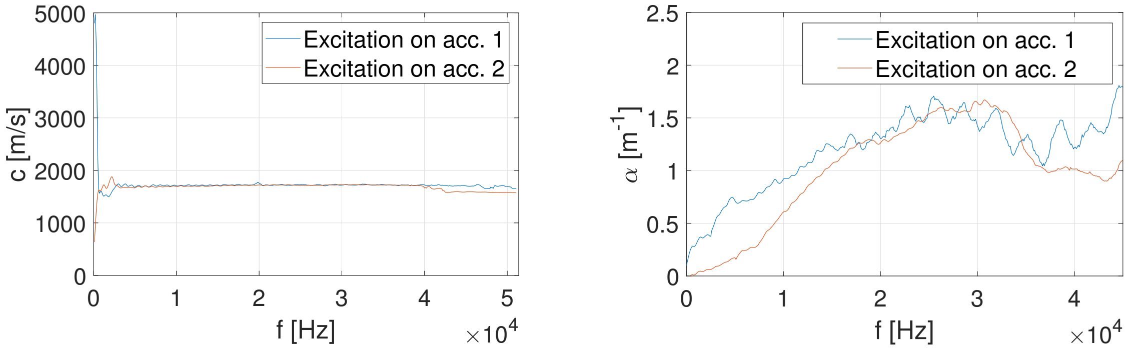

(a) Dispersion curve for non-prismatic rod (b) Attenuation curve for non-prismatic rod

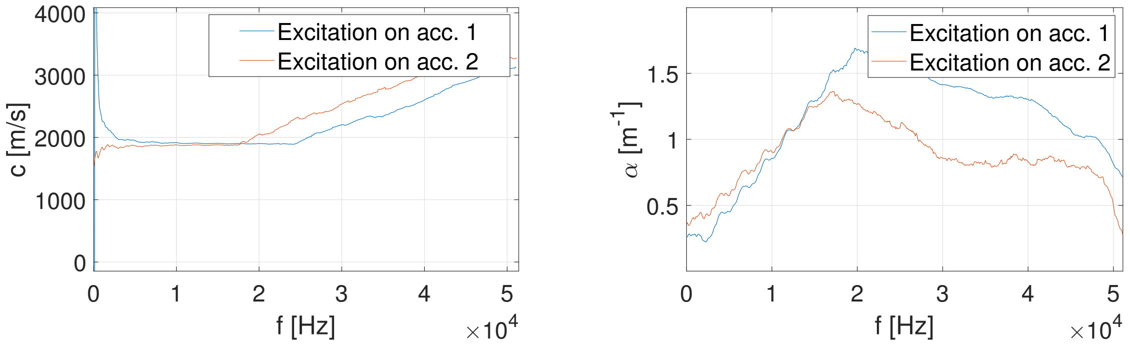

(c) Dispersion curve for heterogeneous rod (d) Attenuation curve for heterogeneous rod

Fig. 3. Experimentally measured dispersion and attenuation curves for homogeneous non-prismatic and heterogeneous non-prismatic rod

curve is increasing (see Fig. 3). The maximum frequency to which these properties can be determined is mainly influenced by the weight of the accelerometers, the low sampling frequency and the shape of the excited cosine pulse.

In this work, a method of identifying the dispersion and attenuation properties of homogeneous prismatic as well as heterogeneous non-prismatic thin viscoelastic rods was described. Using this method, it was possible to determine these properties from the measured acceleration and verify them up to tens of kHz.

Acknowledgements

The publication was supported by the project SGS-2022-008 and by the grant GA 22-00863K.

References

[1] Ahonsi, B., Harrigan, J. J., Aleyaasin, M., On the propagation coefficient of longitudinal stress waves in viscoelastic bars, International Journal of Impact Engineering 45 (2012) 39-51.

[2] Blanc, R. H., Transient wave propagation methods for determining the viscoelastic properties of solids, Journal of Applied Mechanics 60 (1993) 763-768.

[3] Hopkinson, B., A method of measuring the pressure produced in the detonation of high explosive or by the impact of bullets, Philosophical Transactions of the Royal Society A 213 (1914) 437-456.

COMPUTATIONAL MECHANICS 2022
37th conference with international participation
Srní
November 7 - 9, 2022

On algebraic flux corrections for finite element approximation of transport phenomena

P. Sváček

Czech Technical University in Prague, Faculty of Mechanical Engineering, Department of Technical Mathematics, Czech Republic

1. Introduction

In this paper we shall focus on numerical discretization of a general hyperbolic system written for the vector of conservative variables $u = u(x,t)$ in the form

$$\frac{\partial u}{\partial t} + \nabla \cdot \boldsymbol{f}(u) = 0 \qquad \text{in } \Omega \times I_T, \tag{1}$$

where $\boldsymbol{f} = \boldsymbol{f}(u)$ denotes the array of the inviscid fluxes. Eq. (1) is equipped with the initial condition $u(x,0) = u_0(x)$ for $x \in \Omega$.

For the hyperbolic system (1) the aspects of spatial discretization by the finite element method is discussed. For such a systems there are several physical constraints for the solution as boundedness of physical quantities (e.g., positive density) which needs to be guaranteed also for the numerical solution. Moreover, the solution of such system needs to satisfy the entropy inequality, see, e.g., [1, 6]. The numerical analysis of the approximate method usually focus on the consistency, stability and convergence. The mostly used techniques as finite volumes or discontinuous-Galerkin finite elements moreover satisfy the conservativity naturally by the construction of the scheme. However, for the higher-order finite element method the conservativity needs to be discussed, see, e.g., [2].

Moreover, the construction of the numerical scheme should also avoid the occurrence of nonphysical states. To this end many modern high-resolution schemes use limiters to ensure preservation of local bounds or at least positivity for scalar quantities of interest. In the context of finite element approximations, such schemes can be constructed using the framework of algebraic flux correction (AFC) and its extensions to hyperbolic systems, see, e.g., [2, 3]. However, the bound-preserving schemes for nonlinear hyperbolic problems are usually not entropy stable and vice versa, the entropy stable schemes are usually not bound-preserving. In [4], the AFC scheme is extended for continuous finite element discretization of a scalar conservation law using a bound-preserving flux limiter and a semi-discrete entropy fix based on Tadmor's condition.

In this paper the construction of the AFC for continuous linear finite element method is discussed, its application realized on a simple linear scalar problem. The attention is paid on the realization of the Dirichlet boundary conditions. Numerical results are shown.

2. FE discretization and its properties

We consider a scalar transport equation in the form

$$\frac{\partial u}{\partial t} + \nabla \cdot \boldsymbol{f}(u) = s \tag{2}$$

equipped with a suitable initial and boundary conditions. We consider the fluxes in the form $\boldsymbol{f} = \boldsymbol{v}u - \varepsilon \nabla u$, where $\boldsymbol{v}$ is the velocity and $\varepsilon \geq 0$ denotes the diffusion.

2.1 Linear FE method

For the purpose of the application of FE method, the weak formulation of (2) is derived in the form

$$\int_\Omega w\frac{\partial u}{\partial t} + w\nabla \cdot (\boldsymbol{v}u) + \nabla w \cdot (\varepsilon \nabla u) dx = \int_\Omega wsdx + \int_{\Gamma_N} w(\varepsilon \nabla u) \cdot \boldsymbol{n} dS. \tag{3}$$

Consider the FE space V_h with base ϕ_j and approximate the solution u and the velocity $\boldsymbol{v}$ by the FE approximations u_h and $\boldsymbol{v}_h$ as $u \approx u_h(x,t) = \sum_j u_j(t)\phi_j(x)$, $\boldsymbol{v} \approx \boldsymbol{v}_h = \sum_j \boldsymbol{v}_j \phi_j$. For the multiplication $u\boldsymbol{v}$ the approximation the *group FE formulation* is used $\boldsymbol{v}u \approx (\boldsymbol{v}u)_h = \sum_j (u_j \boldsymbol{v}_j)\phi_j$. This leads to system of ODE written as

$$\sum_j \left(m_{ij} \frac{du_i}{dt} \right) + \sum_j ((c_{ij} + d_{ij})u_j) = r_i \tag{4}$$

where $\mathbb{M} = (m_{ij})$ is the mass matrix, $\mathbb{C} = (c_{ij})$ represents the convective terms, $\mathbb{D} = (d_{ij})$ corresponds to the diffusion terms (proportional to ε) and (r_i) are the source terms. For the inviscid limit $\varepsilon \to 0_+$ with zero source terms we get the system in the form $\mathbb{M}\dot{\vec{u}} = \mathbb{K}\vec{u}$ with $\mathbb{K} = -\mathbb{C}$, or in the discrete form

$$\sum_j \left(m_{ij} \frac{du_j}{dt} \right) = \sum_j k_{ij} u_j. \tag{5}$$

2.2 Discrete operator properties

For the discrete operators the partition of unity(PU) valid for finite elements is important. Taking the partition of unity propery, i.e., $\sum_j \phi_j = 1$, we by differentiation get $\sum_j \nabla \phi_j = 0$. This has direct influence on the properties of the discrete (e.g., mass, Laplace) operators. The mass matrix is symmetric, positive definite and with the PU we have $\sum_i \sum_j m_{ij} = |\Omega|$. The diffusion matrix $\mathbb{D} = (d_{ij})$ is symmetric with zero row and column sums. The discrete gradient/divergence operator $\overline{\mathbb{C}} = (\overline{\boldsymbol{c}}_{ij})$ is nonsymmetric with zero row sums whereas the column sums does not have to be always zero as it is influenced by the mesh properties and boundary fluxes. For the interior nodes $\overline{\boldsymbol{c}}_{ii} = 0$ and $\overline{\boldsymbol{c}}_{ij} = -\overline{\boldsymbol{c}}_{ji}$.

2.3 Algebraic flux limiting technique

The description of the main idea is shown for the finite element approximation of the problem with zero viscosity and zero sources, which leads to the discrete equations in the form $\mathbb{M}\dot{\vec{u}} = \mathbb{K}\vec{u}$, where $\vec{u} = (u_i)$ is vector of the nodal values, $\mathbb{M}$ is the consistent mass matrix and $\mathbb{K}$ is the discrete transport operator. In order to obtain scheme both without undershoots/overshoots as well as not too diffusive, we need to switch between linear “upwind-like” approximations and the original scheme. In the finite element context the idea of algebraic flux corrections reads: replace the consistent mass matrix M_C by lumped mass matrix M_L, and add an artificial diffusion operator D to operator K to eliminate all negative off-diagonal coefficients of K. The linear local extremum diminishing scheme then reads $M_L\dot{\vec{u}} = L\vec{u}$, $L = K + D$. The artificial diffusion operator D can be rewritten as

$$(D\vec{u})_i = -\sum_{j\neq i} f^d_{ij}, f^d_{ij} = d_{ij}(u_i - u_j) = -f^d_{ji}.$$

The original scheme can be then recovered $M_L\dot{\vec{u}} = L\vec{u} - D\vec{u} + (M_L - M_C)\vec{u}$, or component by component

$$m_i\dot{u}_i = \sum_j l_{ij}U_j + \sum_{j\neq i} f_{ij}, \qquad f_{ij} = f^d_{ij} + m_{ij}(\dot{u}_i - \dot{u}_j) = -f_{ji}, \tag{6}$$

where m_i are coefficients of the lumped mass matrix. In order to prevent the oscillations of the solution, the fluxes f_{ij} are multiplied by suitable correction factors

$$f^*_{ij} = \alpha_{ij} f_{ij}, \text{ where } 0 \leq \alpha_{ij} \leq 1.$$

Inserting these fluxes into (6) we get the nonlinear combination of the low order scheme ($\alpha_{ij} = 0$) and the original higher order scheme ($\alpha_{ij} = 1$). Following the detailed description from [2] the positive and negative edge contribution to fluxes are accounted for separately

$$\begin{array}{ll} P_i = P^+_i + P^-_i, & P^{\pm}_i = \sum_{j\neq i} \min\{0, k_{ij}\}\, min_{max}\{0, u_j - u_i\}, \\ Q_i = Q^+_i + Q^-_i, & Q^{\pm}_i = \sum_{j\neq i} \min\{0, k_{ij}\}\, max_{min}\{0, u_j - u_i\} \end{array}$$

and use in order to limit positive or negative antidiffusive fluxes. The nodal corrections factors are computed by $R^{\pm}_i = \min\{1, Q^{\pm}_i/P^{\pm}_i\}$ which determine the percentage of $P^{\pm}_i$ that can be accepted to node i without violating the LED constraint for row i of the modified transport operator K_{mod}. The corrections α_{ij} are then computed using a suitable limiter, see [2], by

$$\alpha_{ij} = \left\{ \begin{array}{ll} R^+_i d_{ij}(u_i - u_j) & \text{if } u_i \geq u_j, \\ R^-_i d_{ij}(u_i - u_j) & \text{if } u_i < u_j. \end{array} \right. \tag{7}$$

3. Algebraic flux corrections for hyperbolic systems

As an example we can consider Euler equations in the conservative form $\frac{\partial W}{\partial t} + \nabla \cdot \mathbb{F}(W) = 0$ where $W = (\rho, \rho\boldsymbol{u}, E)^T$ and flux is given as $\mathbb{F}(W) = (\rho\boldsymbol{u}, \rho\boldsymbol{u} \otimes \boldsymbol{u} + p\mathbb{I}, E\boldsymbol{u} + p\boldsymbol{u})^T$ Here, the total energy E is given as sum of internal energy and kinetic energy, i.e. as $E = \rho e + \frac{1}{2}\rho|\boldsymbol{u}|^2$ and the pressure is then computed using additional equation of state, for ideal gas expressed as $p = (\gamma - 1)\rho e$. In this case the application of AFC needs to take into account the properties of the hyperbolic system, see [3].

4. Numerical results

First, the developed flux corrected transport scheme was tested for finite element implementation in 1d and 2d (see Figs. 1–2). The exact solution in this case is just transported with a constant velocity $\boldsymbol{v}$ and no diffusive fluxes are used, i.e., $\varepsilon = 0$. In Fig. 1 the convection of rectangle (left) and semiellipse (right) is shown, where the dashed line shows the initial condition, the dotted line shows the exact solution, and the solid line shows the numerical approximation. In this case the transport velocity for 1D case was chosen as $\boldsymbol{v} = 1$ (1D vector) and the computations was performed for time period of $T = 0.5$. For the two dimensional case, the convection of the block with the rotational flow velocity $\boldsymbol{v}(x, y) = (-(y - 1/2), (x - 1/2))$ around the origin is approximated. Here, the time period of $T = 2\pi$, so that the initial condition is the exact solution at time instant $t = T$. Fig. 2 shows the exact solution (left) and the numerical

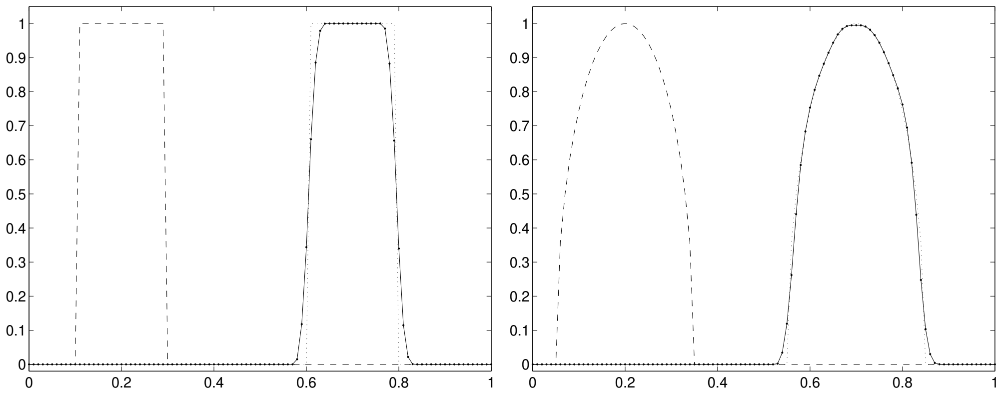

Fig. 1. Algebraic flux corrections (1d)

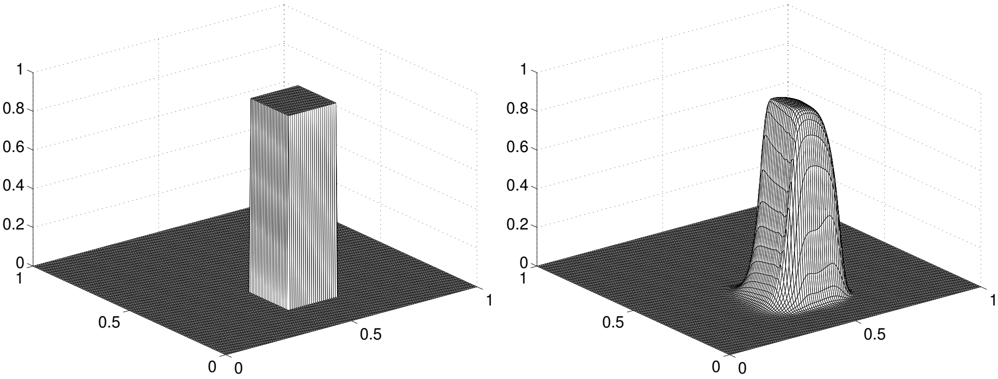

Fig. 2. Algebraic flux corrections (2d)

solution(right). Although the solution is slightly smeared, no undershoots or overshoots were detected.

Acknowledgements

Authors acknowledge support from CTU and computational time provided by the Center of Advanced Aerospace Technology (CZ.02.1.01/0.0/0.0/16_019/0000826), Faculty of Mechanical Engineering, Czech Technical University in Prague.

References

[1] Dafermos, C. M., Hyperbolic conservation laws in continuum physics, 1st edition, Springer, 2000.
[2] Kuzmin, D., Möller, M., Algebraic flux correction I. Scalar conservation laws, In: Flux-corrected transport, Kuzmin, D., Löhner, R., Turek, S. (eds), Scientific Computation, Springer, Berlin, 2005.
[3] Kuzmin, D., Möller, M., Algebraic flux correction II. Compressible Euler equations, In: Flux-corrected transport, Kuzmin, D., Löhner, R., Turek, S. (eds), Scientific Computation, Springer, Berlin, 2005.
[4] Kuzmin, D., Quezada de Luna, M., Algebraic entropy fixes and convex limiting for continuous finite element discretizations of scalar hyperbolic conservation laws, Computer Methods in Applied Mechanics and Engineering 372 (2020) No. 113370.
[5] Kuzmin, D., Turek, S., Flux correction tools for finite elements, Journal of Computational Physics 175 (2002) 525–558.
[6] LeVeque, R. J., Numerical methods for conservation laws, Birkhäuser, 1992.

COMPUTATIONAL MECHANICS 2022
37th conference with international participation
Srní
November 7 - 9, 2022

Dual frequency vibration absorber

S. Timorian, M. Valášek

Faculty of Mechanical Engineering, Czech Technical University in Prague, Technická 4, 166 00 Praha 6, Czech Republic

1. Introduction

One way of vibration suppression of mechanical systems is traditionally the usage of vibration absorber. It consists of one mass attached by spring, damper and also an actuator into the vibrating mechanical system. The actuator is usually used for precise tuning of tonal vibration suppression. Such vibration absorber can suppress one frequency in tonal way or some interval of frequencies in the vicinity of tuned frequency.

The paper describes the way how to achieve dual tonal frequency vibration suppression by one mass vibration absorber. Previous attempts [1-2] were using delayed feedback and they suffer from difficult tuning combined with stability analysis. This paper describes another approach with straightforward and simple tuning and stability analysis. The feedback law of force actuator is increasing the single mass dynamics in such way that two tonal frequencies can be placed into the vibration absorber. The paper then investigates the stability regions of dual frequency vibration absorber and the resulting vibration suppression of the overall mechanical system.

2. Formulation

The system of primary mass (mass mb, stiffness kb, damping bb) with active vibration absorber (mass ma, stiffness ka, damping ba) in Fig. 1 is described by the equation of motion

$$m_a\ddot{x}_a = b_a(\dot{x}_b - \dot{x}_a) + k_a(x_b - x_a) + u\,, \tag{1}$$

$$m_b\ddot{x}_b = -b_b(\dot{x}_b) - k_b(x_b) - b_a(\dot{x}_b - \dot{x}_a) - k_a(x_b - x_a) - u + F\,. \tag{2}$$

In order to achieve dual frequency vibration absorber it is needed to place two frequencies ω_1, ω_2 into absorber (1) by the control u. It can be achieved by the control law PDII^2 in bellow.

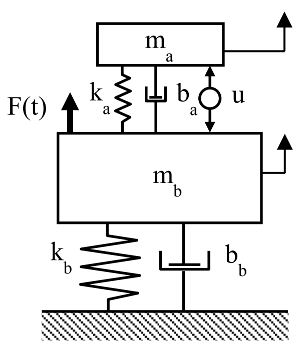

Fig. 1. Primary system m_b and vibration absorber m_a

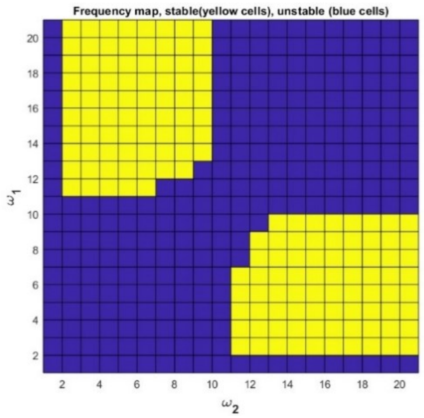

Fig. 2. Frequency map of (ω_1 and ω_2), each frequency is ten times the current grid

$$u = -k_p x_a - k_d \dot{x}_a - k_1 \int x_a dt - k_2 \iint x_a dt\, dt\,, \tag{3}$$

$$u = -k_p x_a - k_d \dot{x}_a - k_1 \int x_a dt - k_2 \iint x_a dt\, dt + \mathrm{e_b x_b} + \mathrm{d_b \dot{x}_b} + \\ + \mathrm{k_{1b}} \int \mathrm{x_b dt} + \mathrm{k_{2b}} \iint \mathrm{x_b dt\, dt}\,. \tag{4}$$

Then, the vibration absorber (1)-(3) with the primary system (3) are stable in some intervals of frequencies ω_1, ω_2 but not overall, so there is no guaranteed stability. This means that the combined system for some tuned frequencies ω_1, ω_2 is stable and for another ones unstable. The regions/islands of stability are in the plane ω_1, ω_2 . The ω_1, ω_2 are parameters of the stability of overall combined system. For some values stable, for another unstable.

3. Results

The proposed control law (3)-(4) has been used by two approaches. First case I was with tonal vibration absorber where $\alpha_{1a} = 0$ and $\alpha_{2a} = 0$, (absorber can be tuned to poles $-\alpha_{1a} \pm j\omega_{1a}, -\alpha_{2a} \pm j\omega_{2a}$) using partial feedback with gains (db=10 and eb=-1500, k1b=0, k2b=0). The map of stable/unstable frequencies is in Fig. 2 and resulting complete vibration suppression in Fig. 4 above. Second case II was with non-tonal vibration absorber where $\alpha_{1a} = -0.001$ and $\alpha_{2a} = -0.001$ are non-zero. But the partial feedback gains are zero (db=0 and eb=0, k1b=0, k2b=0). The map of stable/unstable frequencies is in Fig. 3 and resulting vibration suppression in Fig. 4 below.

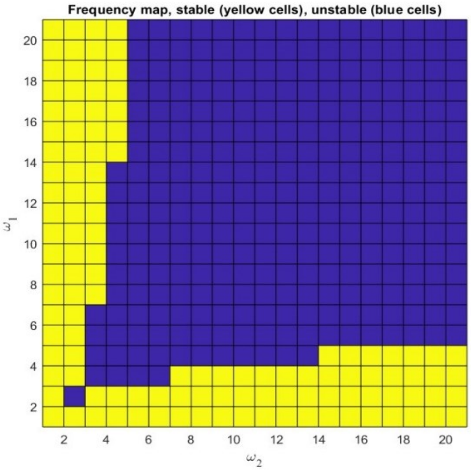

Fig. 3. Frequency map of (ω_1 and ω_2) case II, each frequency is ten times the current grid

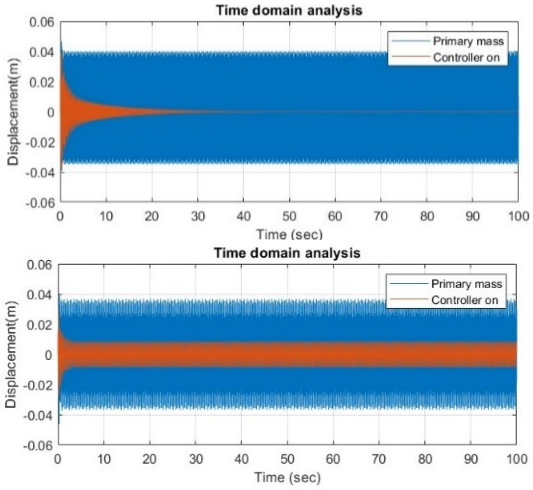

Fig. 4. Resulting vibration response

4. Conclusions

The dual frequency vibration suppression is acheived using two case studies. First case study with tonal damping shows good suppresion whereas in the seond case the degree of suppression is satisfactory. Apart from that, the number of stable and unstable frequencies are localised and plotted in the frequency map.

Acknowledgement

The work has been supported by the postdoc programme of Czech Technical University in Prague.

References

[1] Valášek, M., Olgac, N., New concept of active multiple-frequency vibration supression technique, In Smart Structures, Springer, Dordrecht, 1999, pp. 373-382.

[2] Valášek, M., Olgac, N., Neusser, Z., Real-time tunable single-degree of freedom, multiple-frequency vibration absorber, Mechanical Systems and Signal Processing 133 (2019) 1-14.

COMPUTATIONAL MECHANICS 2022
37th conference with international participation
Srní
November 7 - 9, 2022

On comparison of suitable interpolations for finite element meshes respecting physical laws

J. Valášek, P. Sváček

Faculty of Mechanical Engineering, Czech Technical University in Prague, Karlovo nám. 13, Praha 2, 121 35

1. Introduction

This paper is devoted to the interpolation between two computational finite element meshes. Such interpolation of FE solution onto a new mesh is needed in many applications like material cutting, casting, welding, etc., or in the numerical simulation of fluid-structure interaction with large displacements, where a computational flow mesh quality can significantly deteriorate. In this talk we are interested in the interpolation with restrictions as introduced by authors Pont & Codina [3]. They proposed to combine a computationally cheap interpolation method together with constraints in the form of Lagrange multipliers which enforce conservation of desired quantities, like e.g. total mass, kinetic energy or potential energy. This approach respects physical laws and it is efficient, on the other hand its disadvantage is only a global conservation of physical quantities not the local one. The numerical results consist of comparison of the Lagrange interpolation and the natural neighbour as representatives of cheap interpolation methods on a few test cases.

2. Interpolation with restrictions

Let us assume for sake of simplicity a two-dimensional Ω of $\mathbb{R}^2$ which is covered by triangulations $\mathcal{T}^o$ and $\mathcal{T}^n$ representing the old donor and the new target FE mesh, respectively. Further we suppose that boundary vertices of $\mathcal{T}^o$ and $\mathcal{T}^n$ are identical. Generalizations of these assumptions are quite straightforward, see e.g. [3].

Next, we denote a FE function from FE space $\mathcal{V}_h^o$ built over the FE mesh $\mathcal{T}^o$ by u^o and similarly FE function $u^n(x) \in \mathcal{V}_h^n$ connected with the given triangulation $\mathcal{T}^n$. Function u^o can be expressed as linear combination of FE basis functions $\psi_j^o(x)$, i.e., $u^o(x) = \sum_j U_j^o \, \psi_j^o(x)$; correspondingly for function u^n.

The interpolation with restrictions (IwR) as introduced in [3] consists of two steps. First, the solution from the old mesh is projected on the new mesh. There are many possibilities, the preferred one is Lagrange projection, see [3]. Our aim is to compare performance of the Lagrange projection and the Natural neighbour (NN) interpolation as two different ingredients of the IwR.

The second step consists of application of appropriate restrictions as a correction step. The idea of imposing additional restrictions is a key how to improve some bad behaviour of presented interpolations. One of the biggest interpolation problems is the violation of physical nature of interpolated variable. The advantage of using restrictions is a generality of the algorithm which can be potentially used in many different scenarios. The disadvantage is that restriction (i.e., conservation) is still valid only in global and not local sense.

Natural Neighbour. Natural neighbor (NN) interpolation, introduced in [4], is based on Voronoi tessellation of given points, i.e., vertices of a considered mesh. The interpolant is a continuously differentiable function everywhere except at locations of the donor vertices, nevertheless values of the interpolant coincides with the input data here, see [1]. The computation of interpolating function G at a query point X is following. Point X is added to the given Voronoi tessellation leading to the creation of a new containing polygon (also called neighboring polygons) and it's associated sample points x_i are the natural neighbors of the point X. Then $G(X)$ is evaluated as

$$G(X) = \sum_{i=1}^{N} w_i \, f(x_i), \tag{1}$$

where function f denotes known input data at N points x_i. The weights w_i are defined as $w_i = \sum_{i=1}^{N} \frac{S_i}{S}$, where S_i are area of intersection of i-th original polygon and the newly inserted polygon having total surface $S = \sum_{i=1}^{N} S_i$, see [4].

3. Application to fluid flow problem

The previous general concept is now applied on incompressible flow velocity $\mathbf{v}^o \in \mathbf{V}_h^o = \mathcal{V}_h^o \times \mathcal{V}_h^o$. By $\widetilde{\mathbf{v}}^n$ is denoted the result of projection $\mathcal{P}$ used in first step of IwR $\widetilde{\mathbf{v}}^n = \mathcal{P}(\mathbf{v}^o)$ and $\mathbf{v}^n$ is the final result of the IwR on the target mesh $\mathcal{T}^n$. We require the conservation of following quantities: 1) mass (more precisely only velocity divergence), 2) both linear momenta and 3) kinetic energy. This leads to following problem: Find

$$[\mathbf{v}^n, \boldsymbol{\lambda}] = \arg \inf_{\mathbf{u}^n \in \mathbf{V}_h^n} \sup_{\boldsymbol{\mu} \in \mathbb{R}^4} L(\mathbf{u}^n, \boldsymbol{\mu}), \tag{2}$$

where $\boldsymbol{\mu}$ are Lagrangian multipliers and $L(\mathbf{u}^n, \boldsymbol{\mu})$ is Lagrangian function defined as

$$\begin{aligned} L(\mathbf{u}^n, \boldsymbol{\mu}) = {} & \frac{1}{2} \int_\Omega \left(\sum_k (U_k^n - \widetilde{U}_k^n) \, \boldsymbol{\psi}_k^n \right)^2 \mathrm{d}x - \mu_1 \int_\Omega \nabla \cdot \left(\sum_k U_k^n \, \boldsymbol{\psi}_k^n - \sum_j U_j^o \, \boldsymbol{\psi}_j^o \right) \mathrm{d}x \\ & - \sum_{l=1}^{2} \mu_l \int_\Omega \left(\sum_k U_{k,l}^n \, \boldsymbol{\psi}_k^n - \sum_j U_{j,l}^o \, \boldsymbol{\psi}_j^o \right) \mathrm{d}x - \mu_4 \int_\Omega \left(\sum_k U_k^n \, \boldsymbol{\psi}_k^n \right)^2 - \left(\sum_j U_j^o \, \boldsymbol{\psi}_j^o \right)^2 \mathrm{d}x. \end{aligned} \tag{3}$$

The sought solution needs to have first derivatives with respect to all variables equal to zero. Equations obtained by this differentiating can be written in matrix form as

$$\begin{pmatrix} \mathbb{M}^n & -R_1^T & -R_{2:3}^T & -2\mathbb{M}^n \mathbf{U}^n \\ R_1 & 0 & 0 & 0 \\ R_{2:3} & 0 & 0 & 0 \\ (\mathbb{M}^n \mathbf{U}^n)^T & 0 & 0 & 0 \end{pmatrix} \begin{pmatrix} \mathbf{U}^n \\ \mu_1 \\ \mu_{2:3} \\ \mu_4 \end{pmatrix} = \begin{pmatrix} \mathbb{M}^n \widetilde{\mathbf{U}}^n \\ R_1^o \mathbf{U}^o \\ R_{2:3}^o \mathbf{U}^o \\ (\mathbf{U}^o)^T \mathbb{M}^o \mathbf{U}^o \end{pmatrix}, \tag{4}$$

where $\mathbb{M}^n$ denotes mass matrix with components $m_{ij}^n = \int_\Omega \boldsymbol{\psi}_j^n \boldsymbol{\psi}_i^n \, \mathrm{d}x$, $\mathbb{M}^o$ is the mass matrix defined on the old mesh $\mathcal{T}^o$ and vectors R_1, R_2, R_3 have components

$$(R_1)_i = \int_\Omega \nabla \cdot \boldsymbol{\psi}_i^n \, \mathrm{d}x, \qquad (R_2)_i = \int_\Omega \boldsymbol{\psi}_{i,x}^n \, \mathrm{d}x, \qquad (R_3)_i = \int_\Omega \boldsymbol{\psi}_{i,y}^n \, \mathrm{d}x. \tag{5}$$

Vectors $R_{1:3}^o$ are defined similarly on the old mesh. Nonlinear problem (4) is solved with the Newton-Rhapson method.

4. Numerical results

The Lagrange (Lag) and NN interpolations alone and also as part of the IwR are compared in two tests. Further, by IwR are denoted the results based on the Lagrange interpolation.

First, academic interpolation test. The interpolation test of [2, 3] consists of 20 pairs of interpolations between the donor and target triangular meshes covering domain $\langle 0, 1\rangle^2$. Both unstructured meshes has characteristic length $h = 0.025$ and the inner vertices of target mesh are shifted by $h/2$ to the right. The considered divergence-free velocity $\mathbf{F}(x, y)$ has given components $f_1(x, y) = 2x^2(x-1)^2y(y-1)(2y-1),\ f_2(x, y) = -2y^2(y-1)^2x(x-1)(2x-1)$.

Fig. 1 shows error distributions after all interpolations and Table 1 quantitatively summarizes the results. The NN interpolation alone is even more diffusive and produces bigger error than the Lagrange projection, e.g. compare kinetic energy E_{kin}. Nevertheless method IwR-NN substantially improves the NN results and it even provides slightly lower error than the IwR with approximately similar time of interpolation computations.

Table 1. Comparison of interpolation results of the first test

method	max $\|\mathbf{F}\|$	E$_{kin}$	L_2 error	L_∞ error	approx. time [s]
exact	1.200×10^{-2}	6.013×10^{-5}	–	–	–
Lag	1.142×10^{-2}	5.126×10^{-5}	5.760×10^{-7}	1.698×10^{-3}	2.5
IwR	1.237×10^{-2}	6.013×10^{-5}	2.405×10^{-7}	1.137×10^{-3}	215.8
NN	1.087×10^{-2}	4.748×10^{-5}	9.082×10^{-7}	1.869×10^{-3}	1.8
IwR-NN	1.223×10^{-2}	6.013×10^{-5}	1.823×10^{-7}	1.036×10^{-3}	247.2

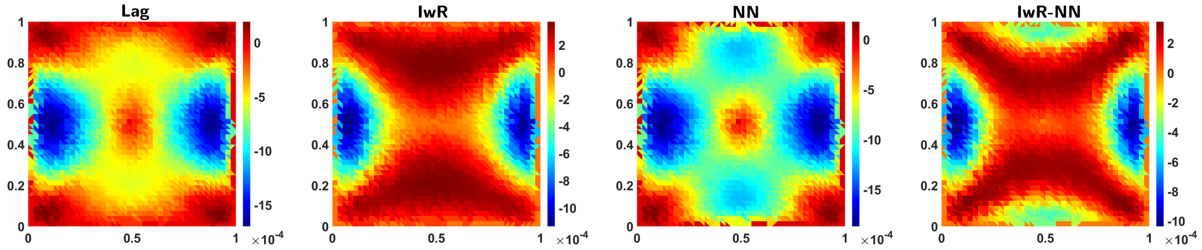

Fig. 1. Error magnitude of interpolated vector field on structured FE mesh after 20 runs. Mind the different scales of colorbars for each result

Second interpolation test – real data. The velocity field obtained during a simulation motivated by human phonation is used in the second test, see [5]. The second test performs one pair of interpolations from the donor to the target mesh and back where both meshes differ in the middle part representing a channel constriction.

Fig. 2 illustrates relative error distributions after one pair of interpolation runs. The NN results are again significantly worse than for Lag projection however in this case the application of IwR-NN does not improve results substantially. This is obvious from quantitatively viewpoint – see Table 2, as well as qualitatively from the extent of domain with relative maximal error bigger than 1% (Fig. 2). The IwR results surpasses the Lag one here only slightly with a considerable increase of computational time on the other hand the IwR conserves total kinetic energy (and linear momenta and divergence) and, thus, its application once per ten time step is still favourable.

Special attention should be paid also to the target mesh. A relative high interpolation error, particularly in the boundary layer, is caused by a coarseness of the target mesh. In the case with similarly dense target mesh the interpolation error would be significantly lower as in the first test.

Table 2. Comparison of interpolation results of the second test

method	max $\|\mathbf{F}\|$	E$_{kin}$	L_2 error	L_∞ error	approx. time [s]
exact	114.200	9.644×10^{-2}	–	–	–
Lag	114.081	9.580×10^{-2}	9.914×10^{-5}	35.115	1.643
IwR	114.459	9.644×10^{-2}	9.838×10^{-5}	34.985	81.092
NN	114.039	9.473×10^{-2}	2.617×10^{-4}	55.723	0.242
IwR-NN	115.062	9.644×10^{-2}	2.564×10^{-4}	55.426	78.537

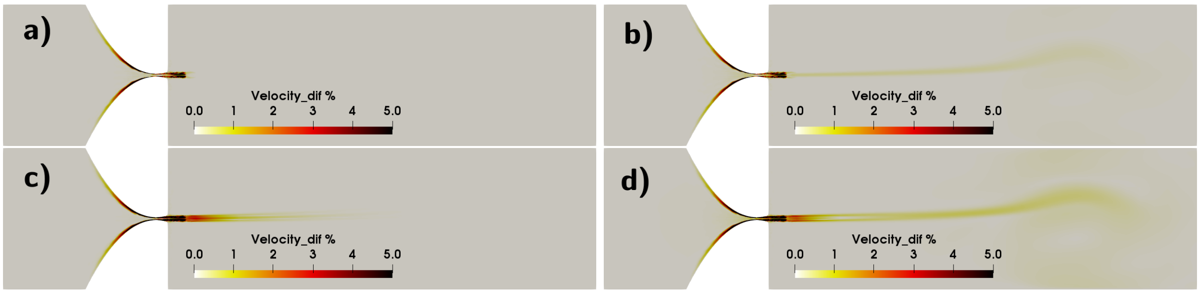

Fig. 2. Distributions of relative error magnitudes after one pair of interpolations. Results: a) Lag (top left) ($\max E_\infty = 31.1\%$), b) IwR (top right) ($\max E_\infty = 31\%$), c) NN (bottom left) ($\max E_\infty = 49\%$) and d) IwR-NN (bottom right) ($\max E_\infty = 48.8\%$). The maximal error (out of presented colorbar scale) is located for all methods similarly in a few elements of boundary layer inside constriction

5. Conclusion

The paper describes method called interpolation with restrictions (IwR) based on [3]. This general interpolation method between FE meshes improves performance of classical interpolation techniques by additional requirement of conservation of arbitrary chosen (physical) quantities. Such approach offers an interesting mix of a relatively computationally cheap method which moreover conserves (total) physical key quantities of the given problem.

Here, the natural neighbour (NN) interpolation is described and used as the first step of the IwR. The four different interpolations are compared in two tests. The NN interpolation provides surprisingly more diffusive results than the Lagrange interpolation though it theoretically provides smoother results. In connection with IwR it performs better on a relatively dense mesh.

References

[1] Amidror, I., Scattered data interpolation methods for electronic imaging systems: A survey, Journal of Electronic Imaging 11 (2) (2002), doi: 10.1117/1.1455013.

[2] Bussetta, P., Boman, R., Ponthot, J. P., Efficient 3d data transfer operators based on numerical integration, International Journal for Numerical Methods in Engineering 102 (3-4) (2015) 892-929.

[3] Pont, A., Codina, R., Baiges, J., Interpolation with restrictions between finite element meshes for flow problems in an ale setting, International Journal for Numerical Methods in Engineering 110 (13) (2017) 1203-1226.

[4] Sibson, R., A brief description of natural neighbour interpolation, Interpreting multivariate data In: Interpreting multivariate data, V. Barnett (ed), John Wiley & Sons, Chichester, 1981, pp. 21-36.

[5] Valášek, J., Sváček, P., Interpolation between finite element meshes respecting mass and energy conservation for flow problems, PANM 21 – Proceedings of Seminar (2022). (submitted)

COMPUTATIONAL MECHANICS 2022
37th conference with international participation
Srní
November 7 - 9, 2022

Notch and load direction influence on impact toughness of composites reinforced with long fibers produced by 3D printing

M. Vaško, J. Majko, M. Handrik, A. Vaško, M. Sága

Faculty of Mechanical Engineering, University of Žilina, Univerzitní 8215/1, 301 00 Žilina, Slovak Republic

1. Introduction

Composites are materials composed of two or more components. One of the components serves as a matrix, i.e. holds the object shape, transfers the load to the reinforcement and protects the reinforcement. The second component is the reinforcement, which has a strengthening function.

The progress FFF method by adding one additional nozzle opened the possibility to print continuous fibre-reinforced thermoplastic composites. Unlike conventional production methods, the user adjusts the location of the fibre in the structure of the composite and adapts the mechanical properties of the composite, see [1].

In the past, the authors published a scientific article [4] focused on the Charpy impact test and comparison of selected printing parameters (infill orientation, fibre type, fibre volume fraction) influence on impact toughness. All observed series of specimens were without a notch as allows the relevant standard. However, in similar studies [2, 3], the other authors selected notched specimens. Therefore the authors aimed to perform preliminary assessment of notch application possibility and identification of notch effect on the impact toughness.

2. Experiment preparations

The Charpy impact test was performed on a series of specimens with the shape and dimensions defined in Fig. 1. Each of series comprised five specimens.

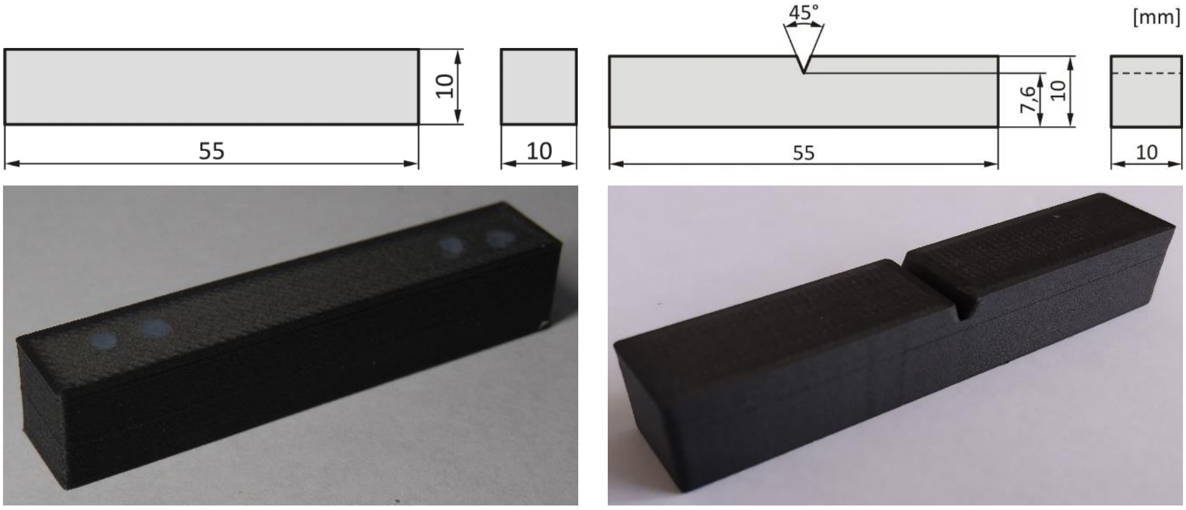

(a) (b)

Fig. 1. Shape and dimensions of specimens: (a) without notch; (b) V-notched

The function of the matrix was fulfilled by nylon reinforced with chopped carbon fibre (trademark Onyx). The selected laminas contained reinforcement in the form of HSHT glass fibre. The data provided by the printer manufacturer reveals the following mechanical properties.

Table 1. Mechanical properties of composite components (data provided by manufacturer)

	Young Modulus [GPa]	Tensile strength [MPa]	Flexural strength [%]
Onyx	1.4	30	50
HSHT Glass fiber	21	600	420

3. Nylon reinforced with chopped carbon fibre and continuous HSHT fibre

As part of the preparation process, the authors modified the printing parameters (Table 2). Each laminate comprised 100 layers, whereas the thickness of laminas was 0.1 mm. The infill type was a solid fill with an infill density of 100%.

Table 2. Printing parameters

Parameter	Value
Lamina thickness [mm]	0.1
Number of walls	2
Reinforcement	HSHT glass fibre
Reinforcement deposition strategy	Concentric rings (Fig. 2a and Fig. 2b)
Loading direction	Direct (Fig. 3a) or perpendicular (Fig. 3b)

The resulting laminate structure was a sandwich with a suitable fibre location concerning the presence of a notch and the need for comparability of results. The selected arrangement type of the reinforced fibres in the laminas was concentric rings.

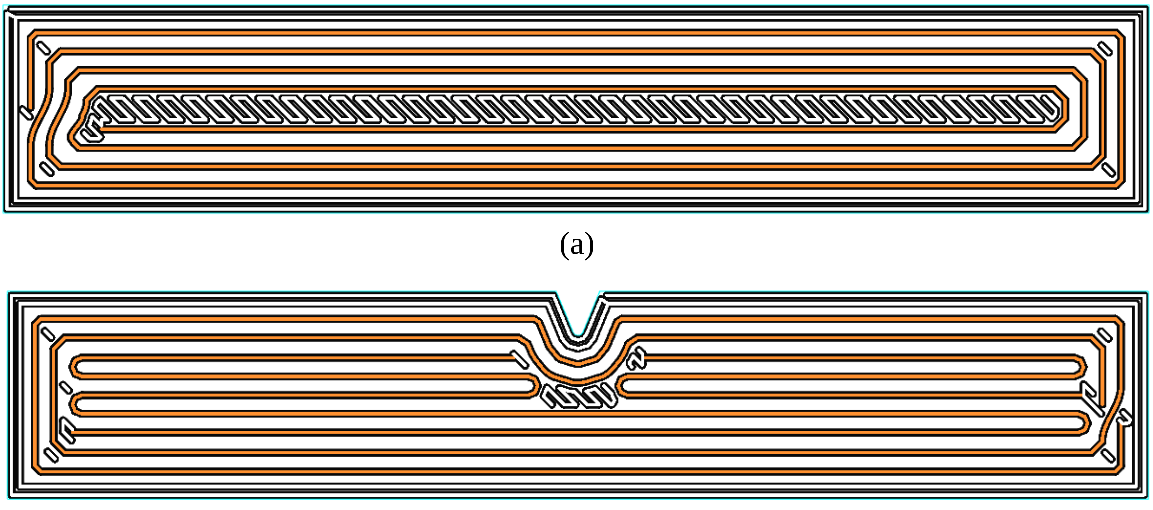

(a)

(b)

Fig. 2. Concentric rings: (a) specimen without notch; (b) specimen with notch

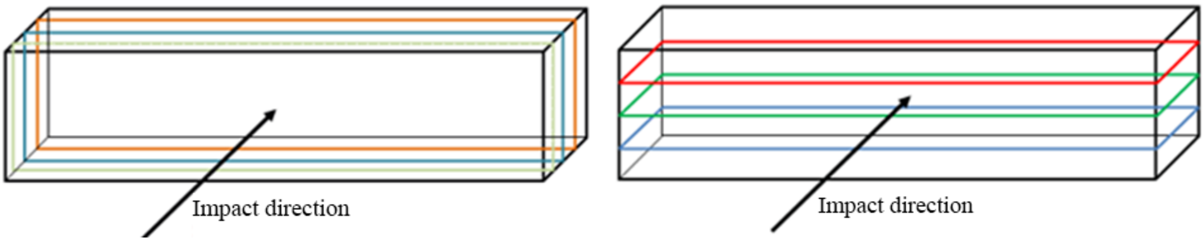

(a) (b)

Fig. 3. Loading direction: (a) direct to stacking of laminas; (b) perpendicular to stacking of laminas

The resulting laminate structure was a sandwich with a suitable fibre location concerning the presence of a notch and the need for comparability of results (Fig. 4).

Fig. 4. Stacking of the reinforced laminas in the structure: matrix laminas (purple); reinforced laminas (orange)

4. Results

The average results of the conducted Charpy impact test are provided in Table 3.

Table 3. Charpy impact test results

Series	**Notch presence**	**Direction of loading**	**Energy [kJ/m^2]**
Alpha	No	Perpendicular	440
Beta	Yes	Perpendicular	220
Gamma	No	Direct	480
Delta	Yes	Direct	475

The results showed the effect of loading orientation on the impact toughness of the specimens. In both cases, the specimens loaded directly had higher impact toughness. In the case of direct loading, the differences between the notched and unnotched specimens were negligible. On the other hand, in the case of perpendicular loading, the application of a notch resulted in a 50% decrease in impact toughness. Part of the obtained data was also processed and analyzed using algorithms programmed in the MATLAB software package.

5. Conclusion

The primary aim was to identify the effect of a notch on the impact toughness. In the case of specimens with laminas oriented perpendicular to the direction of the loading, the notch influence was observed. The value of impact toughness of specimens with notch was significantly reduced. On the contrary, no decrease in absorbed energy was observed for specimens loaded directly.

Acknowledgements

The work has been supported by the grant project KEGA 054ŽU-4/2021.

References

[1] Barbero, J.E., Introduction to composite materials design, 3rd edition, CRC Press: Boca Raton, FL, USA, 2017, pp. 366.

[2] Caminero, M.A., Chacón, J.M., García-Moreno, I., Rodríguez, G.P., Impact damage resistance of 3D printed continuous fibre reinforced thermoplastic composites using fused depositionmodelling, Composite Part B 148 (2018) 93–103.

[3] Scrocco, M., Chamberlain, T., Chow, C., Weinreber, L., Ellks, E., Halford, C., Cortes, P., Conner, B.P., Impact testing of 3D printed kevlar-reinforced Onyx material. Available online: http://sffsymposium.engr.utexas.edu/sites/default/files/2018/091%20ImpactTestingof3DPrintedKevlarReinforcedOny.pdf (accessed on 17 July 2020)

[4] Vaško, M., Sága, M., Majko, J., Handrik, M., Vaško, A., Impact toughness of FRTP composites produced by 3D printing, Materials 13 (24) (2020) 1-23.

COMPUTATIONAL MECHANICS 2022
37th conference with international participation
Srní
November 7 - 9, 2022

Cruciform biaxial tests of FRP: Influence of tabs thickness

V. Vomáčko, M. Šulc

Computations and Modeling Department, VÚTS, a.s., Svárovská 619, 46001, Liberec, Czech Republic

1. Introduction

Structural design of parts made of long-fiber composite materials is complicated due to their anisotropy. Data only from uniaxial mechanical tests are insufficient to perform reliable failure analysis for complex stress states [2]. Therefore, results of failure criteria provided by FEM simulations should be validated by multiaxial mechanical tests. Fiber reinforced composites are commonly characterized by small thickness (out-of-plane stresses are negligible) and simplified approach in form of plane stress is possible [1]. Consequently, biaxial mechanical tests can be performed to failure criteria validation.

Two types of biaxial tests for fiber reinforced composites are commonly used. Combination of axial (tensile/compression), torsional and pressure loading (internal/external) can induce biaxial stress state in tube specimens. Tube specimens were used World Wide Failure Exercise [4]. Second commonly used approach are planar cruciform specimens. Desired biaxial stress state is induced by combination of tension and compression in two independent axes. The advantage of using cruciform specimens is relatively easy and repeatable manufacturing compared to the tubular specimens. On the other hand, cruciform biaxial test requires special test equipment. Also stress computation is not straightforward due to difficult determination of loaded area [2]. Next issue is proper design of cruciform specimen to be able perform a reliable test.

Biaxial test machine was developed for purpose of biaxial cruciform testing at VÚTS, a.s. Test machine consists of 4 independent actuators with maximal load capacity 10 kN. The stroke of the machine is 350 mm, which allows both composite and elastomer testing. Tests can be performed in displacement or load control mode. Displacements and strains are measured by Digital Image Correlation system Monet 3D. Detail scheme of the equipment is shown in Fig. 1.

Biaxial testing machines with servomotor and ball screw loading system are much cheaper, than the one with hydraulic loading. On the other hand they are limited by maximal loading force. Wider application of biaxial cruciform tests could be adopted if testing machines with small force range could be applied to perform biaxial test on composite materials. For this purpose it is important to assess influence of tab thickness on specimen strength. Numerical simulations with progressive damage and experimental test are performed in this work. Two types of specimen are tested i) CFRP cross-ply specimen with no tabs, ii) CFRP cross-ply specimen with bonded tabs of 2 plies of woven GFRP.

2. Biaxial cruciform tests

Equibiaxial tests with strain ratio $R = 1/1$ are performed in displacement control mode. Type of cruciform specimen geometry is double corner fillet with reduced thickness in the central

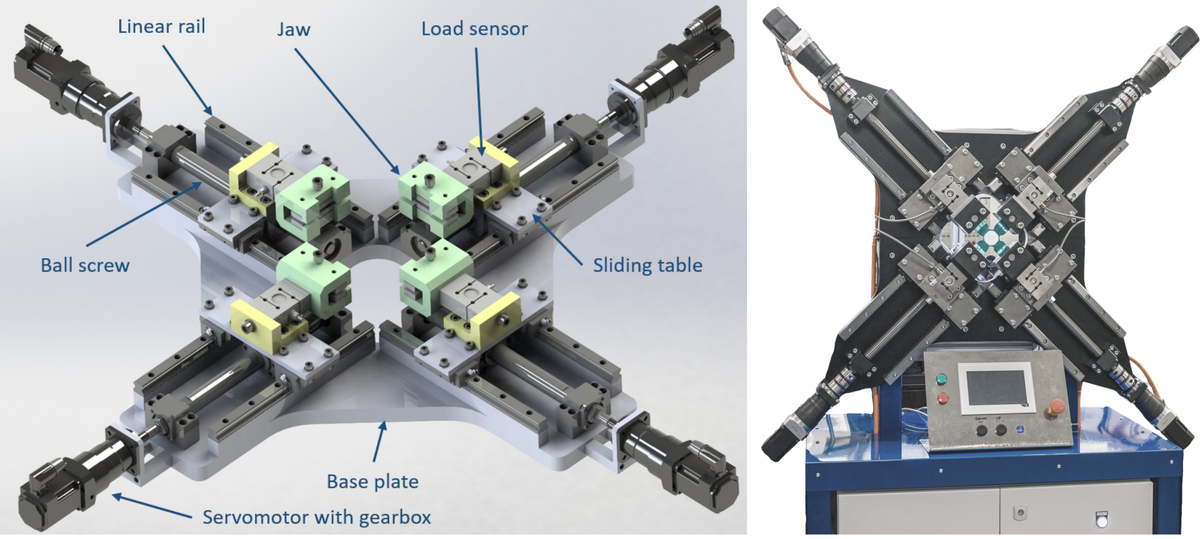

Fig. 1. Biaxial testing machine: CAD model scheme and real machine

area. The geometry arose from the geometry C developed in [3] and several adjustments were made. The specimen is $0.7\times$ scaled down to be able perform measurement at test machine with maximal load 10 kN. And the arms are not straight but towards the clamps they are wider to ensure good grip in the clamps. Cross-ply laminate $[0, 90]_S$ is measured. The material is unidirectional carbon fiber 50K 125 gsm with epoxy resin LH385 manufactured by vacuum infusion process. Glass fiber 200 gsm woven laminate pads are bonded to the CF laminate using Letoxit PL20.

The stress in the central section of the specimen can not be evaluated directly from the area as in the case of uniaxial tests. For linearly elastic materials (carbon fiber laminates) is possible compute stress from equation for plane stress for ortotropic material using measured strains [2]. This approach requires values of E_x, E_y, ν_{xy} and ν_{yx} obtained from uniaxial tests or estimation based on micro-mechanical models.

3. Numerical model

Numerical simulation of biaxial cruciform test is performed to be able validate failure criteria results. Finite element software Ansys 2021R1 with composite module ACP is used. The material model is ortoropic elasticity with progressive damage. The progressive damage model uses Puck failure criterion - when the failure criteria is met, the mechanical properties in the element are degraded. Degradation factor 1 means 100 % reduction and 0 means no reduction of mechanical propertie. Values of degradation factors are set to $E^*_{ft} = 0.99$ (Fiber tensile damage), $E^*_{fc} = 0.99$ (Fiber compression damage), $E^*_{mt} = 0.85$ (Matrix tensile damage) and $E^*_{mc} = 0.5$ (Matrix compression damage). Mechanical properties of specimen and tabs are summarized in Table 1. The boundary conditions are $u = 0.5$ mm in the end of the tabs.

4. Results and discussion

Strains at failure are evaluated as average strain in the 9×9 mm square in the central area of the specimen. Measured values of strain at failure and computed strengths are summarized in Table 2. Specimens with GF tabs achieved higher strains at failure, 0.2 % higher compared to the specimens without tabs.

Table 1. Mechanical properties of unidirectional CF laminate $[0]_4$ 125 gsm and woven GF laminate $[0]_4$ 200 gsm. E and G in [MPa] and ν in [1]

	E_x	E_y	E_z	ν_{xy}	ν_{yz}	ν_{zy}	G_{xy}	G_{yz}	G_{xz}
CF specimen	113 600	4700	4700	0.277	0.42	0.277	4700	3080	4700
GF tabs	22 400	22 400	7500	0.14	0.3	0.3	3300	2700	2700

Table 2. Measured values of strain at failure and computed strength of different specimens

		ϵ_{rx} [%]	ϵ_{ry} [%]	X_t [MPa]	Y_t [MPa]
No pads	Average	1.08	1.06	651	640
	St. Dev.	0.06	0.06	354	360
2 GF plies	Average	1.24	1.28	746	773
	St. Dev.	0.11	0.07	63	45

Measured representative force – strain curves are shown in the Fig. 2 on the left. On the right side of the same figure, there is comparison of experiment (full line) with FEM simulation (dash-dotted line). Complete failure of specimen in simulation is evaluated as first stiffness loss (force decrease). Simulations exhibits stiffer behavior of the specimen but failure is predicted earlier (lower strain and force results) than in experiment. Circle point show first matrix failure (FMF) and square point show first fiber failure (FFF) computed in simulation. This plot shows comparison of design approaches for failure prediction: i) failure criteria (FMF, FFF), ii) failure criteria with progressive damage model and iii) validation of failure criteria by mechanical testing. As the plot shows, cruciform biaxial tests can make failure prediction more precise and therefore accurate safety factor adjustment.

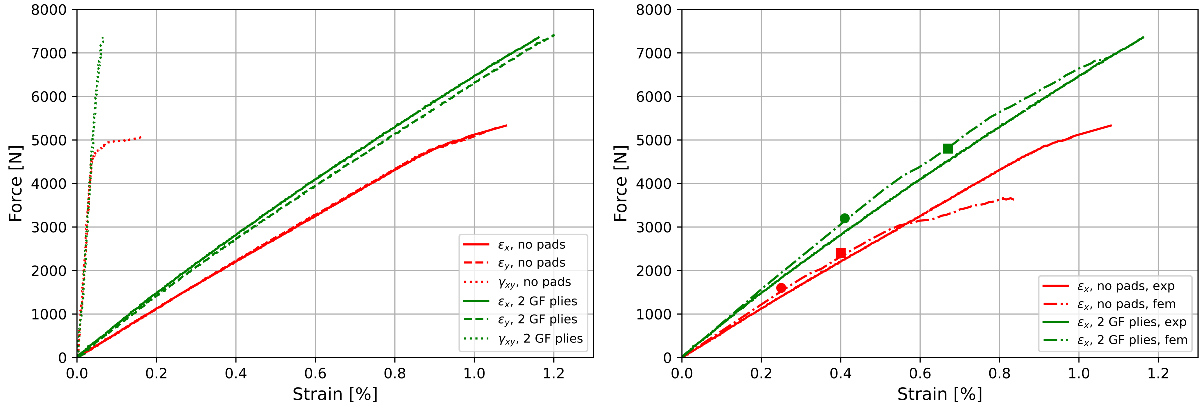

Fig. 2. (*Left*) Experimental results for specimens without tabs and with tabs from 2 GF layers. (*Right*) Comparison of strains in X axis of experiment (full line) with simulation (dash-dotted line)

Specimens without tabs failures prematurely – the failure is observed in the single arm and not in the central area. Typical failure of specimen with tabs of 2 is depicted in Fig. 3. The failure occurs in the central sections near the pads. No delamination between specimen and tabs is observed as reported in [2].

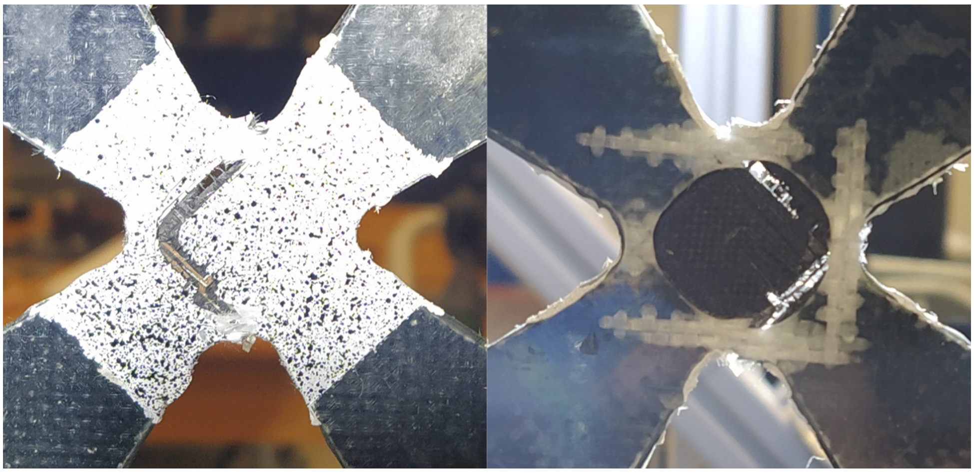

Fig. 3. Typical failure of specimen with tabs of 2 GF plies

Acknowledgement
This publication was supported by the Ministry of Industry and Trade (MPO) within the framework of institutional support for long-term strategic development of the research organization – provider MPO, recipient VÚTS, a. s.

References

[1] Muñoz, H., Moreno, M. del C. S., Advances in cruciform biaxial testing of fibre-reinforced polymers, Polymers 14 (4) (2022) No. 686.

[2] Ramault, C., Guidelines for biaxial testing of fibre reinforced composites using a cruciform specimen, Vrije Universiteit Brussel, 2012.

[3] Smits, A., Van Hemelrijck, D., Philippidis, T. P., Cardon, A., Design of a cruciform specimen for biaxial testing of fibre reinforced composite laminates, Composites Science and Technology 66 (2006) 964-975.

[4] Soden, P. D., Hinton, M. J., Kaddour, A. S., Biaxial test results for strength and deformation of a range of E-glass and carbon fibre reinforced composite laminates: Failure exercise benchmark data, Composites Science and Technology 62 (2002) 1489-1514.

COMPUTATIONAL MECHANICS 2022
37th conference with international participation
Srní
November 7 - 9, 2022

Failure probability estimation of functions with binary outcomes via adaptive sequential sampling

M. Vořechovský

Inst. of Structural Mechanics, Faculty of Civil Engineering, Brno University of Technology, Veveří 331/95, 602 00 Brno, Czech Republic

In many computational models for the performance of an engineering product, which feature random input variables, the outcome may be simply binary information: either safe state or failure event. Moreover, computational models sometimes do not return any answer for a combination of inputs because the computation crashes. While the discrete state nature of the computational model outcome is in general acceptable for Monte Carlo type simulation techniques for estimation of failure probability, the need to use computationally expensive models de facto permits this brute force integration. The reason is that the crude Monte Carlo and also various variance reduction techniques such as Importance Sampling for approximation of probabilistic integrals require a high number of simulations to estimate rare event, which is not feasible for models computing one realization more than a few seconds. The samples drawn in sampling-based techniques are in fact independent of each other which is detrimental to the rate of convergence to the true values with an increasing number of outcomes. The use of quasi Monte Carlo techniques is not of much help in reliability problems as the convergence rate improvement is not sufficient.

The absence of any information about the "landscape" in the case of binary performance function also permits the use of methods designed for estimation of failure probability which use the numerical value of the outcome to compute gradients or to estimate the proximity to the failure surface. Even if the performance provides more than just binary output, the state of the system may be a non-smooth or even a discontinuous function defined in the domain of input variables. In these cases, the classical gradient-based methods typically fail. Even if the approximation of failure probability is so effective that it uses only the location and perhaps the shape of the failure surface in the high probability regions (such as FORM or SORM), they still can not be used, because the discovery of the "most probable points" is usualy based on gradient optimization techniques, be it deterministic (design point search in FORM/SORM) or stochastic gradient optimization (subset simulation, etc.).

This paper promotes the recent paper [1] in which a new simple yet efficient algorithm for sequential adaptive selection of points from the input domain of random variables is presented. The extension of the *experimental design* (ED) is designed to automatically balance global *exploration* of new territories in the input space with local *exploitation* of information in regions containing the failure surface, i.e., the boundary between the failure and safe sets. The extension algorithm sequentially adds new points (one by one) in such a way that the new ψ criterion is maximized. The criterion effectively estimates the amount of *probability* being classified by the evaluation of the expensive computational model in a candidate. The evaluation of the criterion is extremely fast as it uses only the known probability density at a candidate and its nearest previously evaluated point and the distance between them. Therefore, it suffices to offer and evaluate the ψ criterion for a large set of candidates, and select the one with the greatest criterion value. Each evaluation of the function in the winning candidate leads to an update of a simple distance-based surrogate model used to censor our candidates with almost sure model output. Only the predefined set of exploratory points and candidates with two different types of outcome in the nearest points are retained for selection. The result of this sequential adaptive selection is a quick refinement of the failure surface or exploration of a new territory, and this is performed proportionally to the gained probability.

At any stage of sequential sampling, the proposed surrogate model can be used to *estimate the failure probability* via tailored importance sampling scheme and a simple distance-based surrogate model. In cases there are more than just one type of failure event, the method can be automatically generalizes to estimate failure probabilities of all even types. Finally, if there is a possibility to use numerical outcomes from the model to build a smooth surrogate, the algorithm can be use it to improve the estimates.

Let us assume the input random vector is bivariate standard Gaussian and the 2D space is divided into safe and failure domains by the wavy circle; see the blue curve in Fig. 1. The left panel in Fig. 1 shows a stage in which the previously evaluated responses are pictured as red (failure) and green (safe) ED points. The panel also shows a large number of candidates which are excluded from further competition for becoming a winning candidate, because their two nearest neighbor ED points are of the same type. The middle panel shows the retained candidates plus the exploration points (empty cirlces) which are blue-colored depending on the proposed ψ criterion. The light blue cross is the winning candidate in which future performance function will be evaluated. The right panel show importance sampling integration nodes.

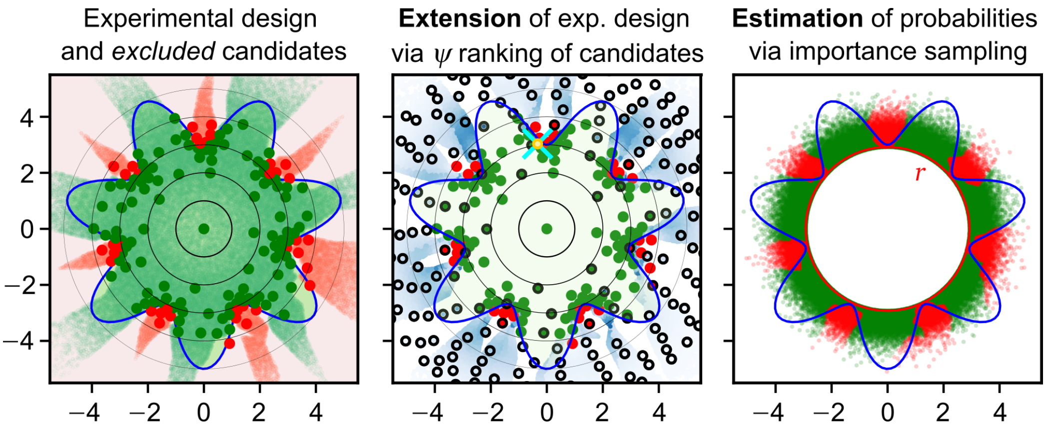

Fig. 1. Illustration of the proposed methodology using a two-dimensional problem with seven effectively disconnected failure domains, each with the same contribution to the probability of failure

Acknowledgement

The work was supported within the framework of research project “Energy dissipation-based approach to stochastic fatigue of concrete considering interacting time and temperature effects” supported by the Czech Science Foundation under project no. 22-06684K.

References

[1] Vořechovský, M., Reliability analysis of discrete-state performance functions via adaptive sequential sampling with detection of failure surfaces, Computer Methods in Applied Mechanics and Engineering, 2022. (in press)
(available via arXiv.org at https://arxiv.org/abs/2208.02475, doi: 10.48550/ARXIV.2208.02475).

COMPUTATIONAL MECHANICS 2022
37th conference with international participation
Srní
November 7 - 9, 2022

Problematic of composite materials with woven reinforcement

J. Žák, J. Ezenwankwo

Faculty of Mechanical Engineering, Technical University of Liberec, Technická 1402/2, Liberec, Czech Republic

Since the beginning of the production of composites, one of the most common forms of reinforcement is woven structure, i.e., fabric. Although accepted for general use without reservation, this form of reinforcement is shown to have its limits in certain areas of application. During the development of deformation members for the automotive industry, we encountered a problem where fibers that seemed very suitable for this purpose lost half of their ability to absorb energy due to weaving in. This led us to a more detailed analysis of the behavior of the fiber structure in the form of a plain weave.

We tried to explain the differences in the behavior of the material in the form of the yarn itself and in the form of a woven structure by the process itself of weaving-in the yarn. So to a certain extent we chose a mezzo scale approach, thus. The first thing we encounter when trying to describe a fabric is determining its geometry. It is of course possible to proceed experimentally, but this approach requires a former knowledge of the specific fabric, either in the form of a laminated composite or in another form. Since viscose fabric is not a common article, we

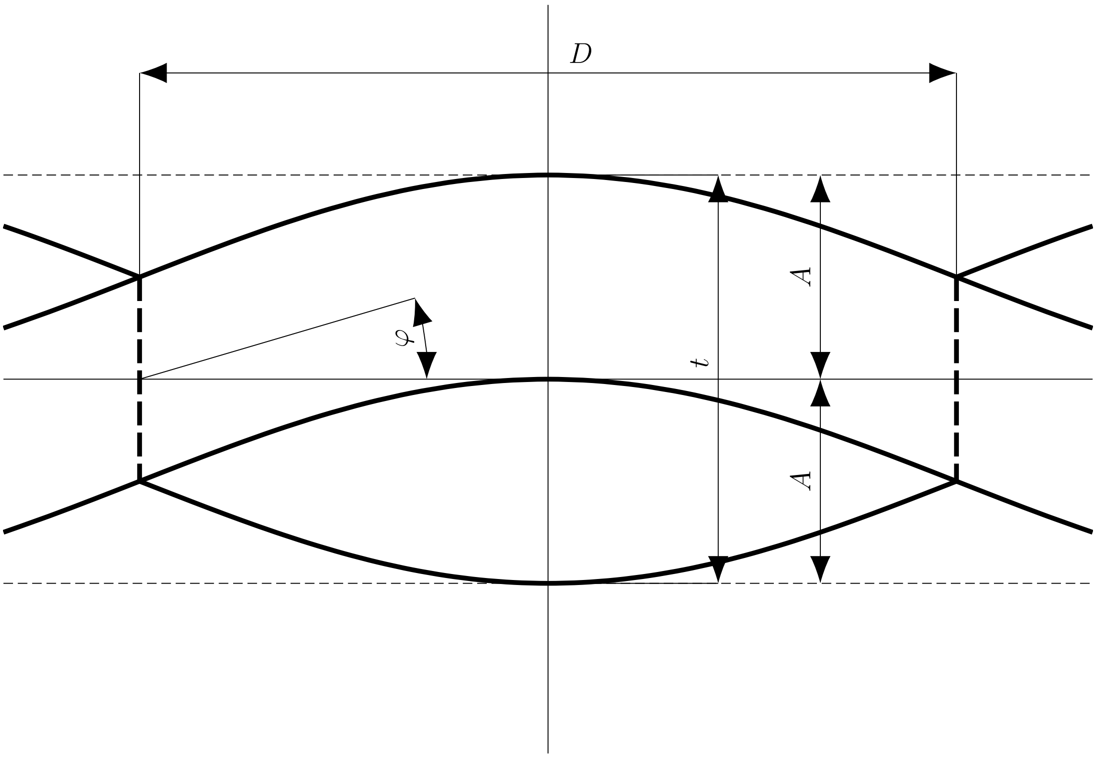

Fig. 1. Description of a plain weave fabric geometry at mezzo scale

did not have this knowledge available, so we proceeded using geometric notions. We modeled the fabric using sine waves with a sinusoidal cross-section, see Fig. 1. This idea is used in the so-called lens model of fabric, however, in general it is not used either to determine the thickness of the fabric neither to determine other parameters that have an effect on the mechanical properties and properties affecting the resulting composite, for example the volumetric ratio of reinforcement.

Let us assume to be known all the characteristic parameters of the fabric in plain balanced weave, i.e., two of following three parameters are given: either the area density γ ($[\gamma] = \frac{\mathrm{kg}}{\mathrm{m}^2}$) or density of weft yarns d_1 ($[d_i] = \frac{1}{\mathrm{m}}$) and that of warp $d_2 = d_1$ or fineness $\lambda_1 = \lambda_2$ ($[\lambda] = \frac{\mathrm{kg}}{\mathrm{m}}$) of both yarns. Let us assume the circular cross section of individual filaments, too; this assumption is well respected for glass or carbon. As the helix angle of the filaments in a yarn is very flat the filaments can *freely* reposition and thus, their most compact layout is in hexagonal mesh, see detail in Fig. 2. Maximum volumetric ratio of filaments in a yarn is then given by geometry of this hexagonal cell

$$v_{f,yarn} = \frac{\pi}{2 \cdot \sqrt{3}} \doteq 0.9. \tag{1}$$

Volume of yarns in the cell bounded by the boundaries of one binding point is (see Fig. 1)

$$V_f = \frac{4}{\pi} \cdot A \cdot D^2.$$

As the thickness is $t = 2 \cdot A$, the volumetric ratio of yarns in the cell then is

$$v_{f,cell} = \frac{V_f}{2 \cdot A \cdot D^2} = \frac{2}{\pi}. \tag{2}$$

Taking into account the relation (1), we get the final formula for the maximal volumetric ratio

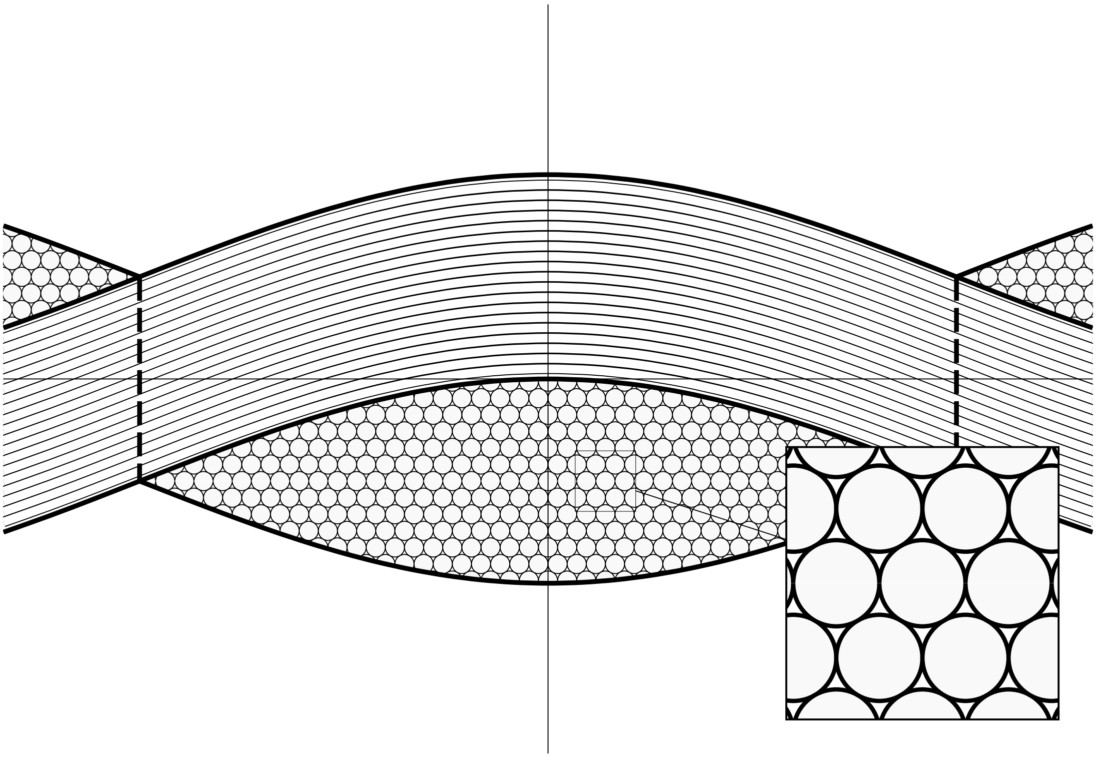

Fig. 2. Description of a plain weave fabric geometry at micro scale

of reinforcement in a plain weave fabric

$$v_{f,max} = v_{f,yarn} \cdot v_{f,cell} = \frac{1}{\sqrt{3}} \doteq 0.58. \tag{3}$$

A few additional notes:

1. This value is valid for fabrics with high density of yarns d_i. It may be higher for very flat yarns (tapes, narrow rovings) in the specially designed fabrics.
2. This value does not depend on the weave (i.e., theoretically it is the same for twill or satin weave), its prove lies outside of the scope of the presented work. However, the weaves other than plain are prone to become more easily flat when under pressure which affects the real value of v_f.
3. In practice it is possible to exceed slightly this limit value by using for example very high pressure to compact the plies in a laminated composite.
4. Higher values of v_f reported by experimenters are not to be necessarily wrong, the measured values depend strongly on the experimental procedure.

The fabric thickness is the key value when modeling a fabric ply, e.g., using FEM. With respect to (3) and using parameters of the fabric, we get

$$t = \frac{\gamma}{\rho} \cdot \sqrt{3}, \tag{4}$$

where γ is the area density of fabric and ρ is density of the yarn material. It is certainly interesting that the value determined following (4) tends to be much closer to the real thickness of the fabric ply in a laminated composite than the value determined experimentally following the ASTM D1777 – 96 (2019) standard [1].

Another phenomenon that relates closely to the woven composite reinforcement is the waveness of the yarn. In fact it was this effect of yarn undulation that has brought us to the problems of the woven reinforcements. Once the geometry based on fabric parameters is known we can easily calculate the real length of the corresponding section of yarn as well as the crossing angle φ of yarns. As the fabrics are relatively flat (the report between t and D is of order 0.1), corresponding elongation of yarn is around 1%. This seems to be very low but in reality it *consumes* non negligible part of available yarn strength. This is all the more important the stiffer the fibers are. Thus the final strength of the fabric is significantly lower than the sum of the strength of individual yarns comprised in the corresponding fabric width.

Even with known (calculated or measured) strength values of a fabric reinforced composite the calculations are complicated by drawbacks of used failure criteria. In a general-use FEM software such bidirectional reinforcement is usually modeled by superposing two unidirectional plies. This is often done internally during preprocessing using classical theory of composites and the resulting values of moduli and strength are used for FEM computations. The most used failure criterion of composites in postprocessing then is that of Tsai-Hill (or its variant Tsai-Wu) which, however, are derived for unidirectional cross isotropic materials [2]. So for a fabric ply it should be used either the full Hill criterion either some of its variations for appropriate material properties. It has to be said that there are dedicated FEM software that offer to take this difference into account. For example, for the balanced fabric working under in-plane stresses and with the same behavior in traction and compression, we have $R_l = R_t$ in-plane strengths, a different value for normal-to-ply direction R_n and of course values for shear strength R_{lt} and $R_{ln} = R_{tn}$. We get the criterion in the following form:

$$\kappa = \frac{(\sigma_l - \sigma_t)^2}{R_l^2} + \frac{\sigma_l \cdot \sigma_t}{R_n^2} + \frac{\tau_{lt}^2}{R_{lt}^2}.$$

As can be seen, the value of such a criterion depends strongly on the out-of-plane *intralaminar* strength R_n (not to be confused with interlaminar strength). This value is unfortunately difficult to measure. One possible way to determine it theoretically could be by using known fabric geometry at mezzo scale with given strengths of yarns and matrix, but this approach has not been explored yet.

While working on the rayon fabric, we faced quite surprising, albeit simple, challenges; just to describe the fabric geometry without time-consuming experiments is not completely obvious. On the other hand, it turned out that the mechanical properties of woven reinforcements are in principle limited and the fabric cannot fully utilize the quality of the yarns. The use of woven reinforcement in composite materials must therefore be strictly justified. In many cases, especially in the one where a pseudo-isotropic stacking is to be used, there is an alternative to using reinforcement fibers in the form of a much cheaper mat.

References

[1] ASTM D1777-96(2019) Standard test method for thickness of textile materials, 2019.

[2] Gay, D., Composite materials, Éditions HERMES, Paris, 1991. (in French)

COMPUTATIONAL MECHANICS 2022
37th conference with international participation
Srní
November 7 - 9, 2022

Determination of the equivalent stiffness of thick-walled composite beams with an inter-circular cross-section using the semi-analytical method

T. Zámečníková, T. Mareš, Z. Padovec, A. Malá, B. Kropík, D. Vondráček

Department of Mechanics, Biomechanics and Mechatronics, Faculty of Mechanical Engineering, Czech Technical University in Prague. Technicka 4, Praha 6, Czech Republic

1. Introduction

The aim of this work is the search for a new analytical method of calculating the stiffness of the wound composite beams with the circular cross-section. The FE models and several analytical calculations were performed for chosen geometry of the composite beam and all results are compared to experimental data. The experiment of three-point bending on fibre-reinforced composite beams with two different composite lay-ups and two different diameters of the tubes was done. The stiffness of all specimens was also calculated. The comparison of a new semi-analytical method with the well-known analytical methods [1] of stiffness calculation and FE models are introduced in this paper.

Composite beams are very variable not only in their shape or cross-section, but also in the layup of the composite material from which they are made. This creates several variables that we must consider when calculating their deformation. It is well known that the available methods for calculating the deformation of composite materials do not provide relevant results for all possible types and shapes of composite beams. It turns out that these methods differ in the results for the same case of a composite beam or are too complex for the initial design of the part. Also, the results of these methods differ from a possible experiment. Analytical, semi-analytical, and numerical methods are known for calculating the deformation of composite beams. The comparison of Timoshenko's and Bernoulli's method of bending calculation, the method of calculation using ABD matrices and the numerical FE method were chosen as the basis for this work. All these methods were applied to an embedded composite beam with an inter-circular cross-section. The aim of this work is to find out in which specific cases the mentioned methods of calculating the effective stiffness of composite beams are valid for the general composition of the composite material.

2. Analytical methods for calculation the equivalent stiffness modulus of the composite tubes

2.1. The stiffness matrix and the compliance matrix

The Hooke's law contains the stiffness matrix $\boldsymbol{S}$,

$$\boldsymbol{\sigma} = \boldsymbol{S} \cdot \boldsymbol{\varepsilon}\,. \tag{1}$$

The modulus of elasticity is expressed for each layer separately by means of the stiffness matrix $\boldsymbol{S}$ in the main coordinate system of the composite material $O(L, T, T')$. An orthotropic material is considered. [1] To express the equivalent modulus of elasticity in the main coordinate system of the whole beam $O(x, y, z)$, it is possible to use the stiffness matrix $\boldsymbol{S_{xy}}$ or an inverse matrix the compliance matrix $\boldsymbol{C_{xy}}$. The stiffness matrix $\boldsymbol{S_{xy}}$ is expressed by the following transformation (2) to the coordinate system $O(x, y, z)$ and the compliance matrix $\boldsymbol{C_{xy}}$ is inverse to it (3),

$$\boldsymbol{S'}_{\boldsymbol{xy}} = \boldsymbol{T_{xy}} \cdot \boldsymbol{S} \cdot \boldsymbol{T'_{xy}}\,, \tag{2}$$

$$\boldsymbol{C'}_{\boldsymbol{xy}} = \boldsymbol{S'^{-1}_{xy}}\,. \tag{3}$$

The modulus of elasticity in the direction of the beam axis E_x can be obtained from the compliance matrix $\boldsymbol{C'_{xy}}$, and also from the stiffness matrix $\boldsymbol{S'_{xy}}$**.** The element S'_{11} is an element of the stiffness matrix $\boldsymbol{S'_{xy}}$ and element C'_{11} is an element of the compliance matrix $\boldsymbol{C'_{xy}}$. The usage of the stiffness matrix $\boldsymbol{S'_{xy}}$ represents the upper estimate of the equivalent stiffness, the use of the compliance matrix $\boldsymbol{C'_{xy}}$ the lower estimate of the stiffness of the composite beam. In the results section, their arithmetic mean is also used.

2.2. Calculation of equivalent elasticity modulus E_{eq} by Classical Laminate Theory

To calculate the deflection of a composite beam with a circular cross-section using method from [1] the following equation is used

$$[N \cdots M\,] = [A \,\vdots\, B \cdots \vdots \cdots B \,\vdots\, D\,][\varepsilon^{\circ}{}_m \cdots k\,]\,. \tag{4}$$

The force loading of the beam can be expressed using the elements of the matrix $\boldsymbol{A}$ [2]. The stress of a composite material using Hooke's law is expressed. To obtain the stress relationship, it is necessary to divide this expression by the total thickness of the composite material t.

$$\sigma_1 = \frac{N_1}{t} = \frac{1}{t}(A_{11} - [A_{12}\, A_{16}\,] \cdot [A_{22}\, A_{26}\, A_{62}\, A_{66}\,]^{-1} \cdot [A_{21}\, A_{61}\,]) \cdot \varepsilon^{\circ}{}_1\,. \tag{5}$$

The equivalent modulus of elasticity is expressed by the following relation.

$$E_{eq} = (A_{11} - [A_{12}\, A_{13}\,] \cdot [A_{22}\, A_{23}\, A_{32}\, A_{33}\,]^{-1} \cdot [A_{21}\, A_{31}\,]) \cdot \frac{1}{t}\,. \tag{6}$$

2.3. A new semi-analytical method

A new semi-analytical approach is based also on the Classical Laminate Theory and tries to calculate the equivalent stiffness of the beam with the combination of the tensile and bending stiffness matrix elements. The assumption for this theory is that the geometry of the composite beam with circular cross-section combines the tensile and bending loading of the material of the composite beam. The combination of the elements of matrix $\boldsymbol{A}$ and matrix $\boldsymbol{D}$ (4) is used in a superposition of the stiffnesses.

$$(EJ)_{equivalent} = (EJ)_{A_{11}} + (EJ)_{D_{11}}. \tag{7}$$

3. Experiment

Composite wound tubes (T700/epoxy matrix) with an inner diameters of 26 mm and 50 mm with the 3 mm (thick) and 1 mm (thin) wall thickness were selected as specimens. The geometrical characteristics of the specimens were chosen to compare the results from the analytical and FE methods in cases of thick and thin-walled beams. The tests were performed for three composite layups. Three-point bending tests were performed on an FPZ 100/1 loading machine. Supports with a span of 400 mm and 750 mm were used for the tests. The beams were loaded with force through the strap with a width of 25 mm. The deflection was measured with a laser extensometer OptoNCDT 1320 and strain with a strain gauge. The sensors were placed in the centre of the beam under the loaded place and one extensometer was placed in the quarter of the span length. Groups of six pieces from each combination of fibres, composite layup, and support span were tested. The average value of the equivalent stiffness EJ_{eq} was evaluated. All specimen types were modelled by available FE methods (in Abaqus) and the equivalent stiffness was calculated. All the mentioned analytical methods were also used to calculate the equivalent stiffness. A comparison of these values is shown in the following section.

4. Results

The results show the deviations of all calculation methods from the experimental data in percentages. The equivalent stiffness EJ_{eq} of beams is compared. The results of two lay-ups are presented. These are results of beams with inner diameter 26 mm, 400 mm span and Diagonal lay-up [90 °, ± 45°] in Fig. 1. The second results are for beams with inner diameter 50 mm, 750 mm span and Typical lay-up [90°, 0°, ± 30°] (Fig. 2) Both results are for the thick and thin variant of composite beams. The average stiffness (EJ_mean in the figures) obtained from the matrix S' and C' shows a good agreement with the experiment, but this method usually predicts higher stiffness compared with experimental data. The new semi-analytical approach shows the constant deviations of less than 25% for the thin variant and less than 7% for the thick variant from experimental data in both cases of specimens. These results are on the safety side of the calculation in most cases compared to the experimental data.

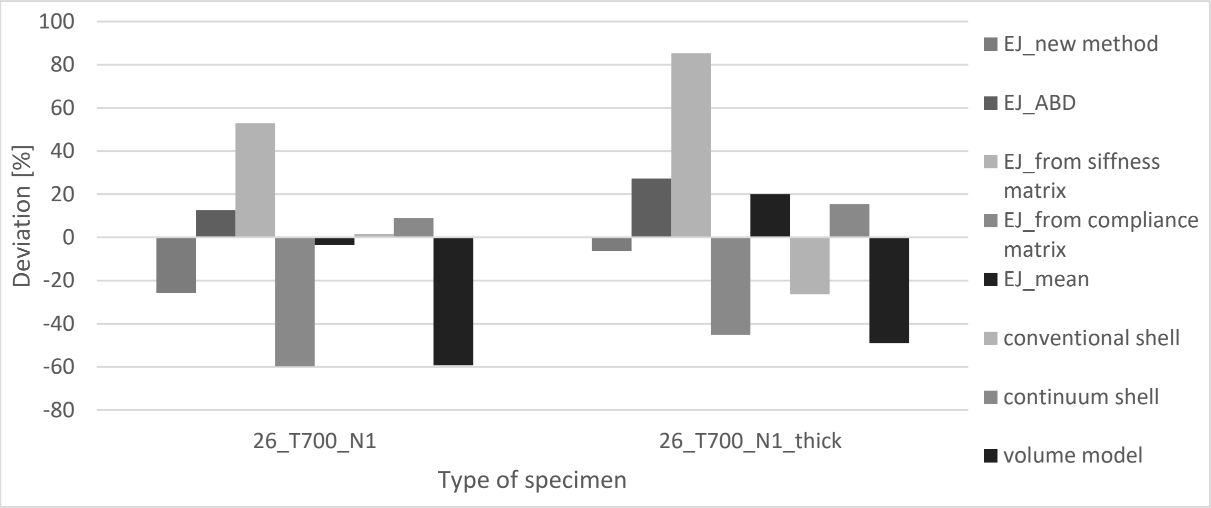

Fig. 1. The deviation from the experiment of equivalent stiffness for beams with ID 26 mm and Diagonal 1 [90°, ±45°]

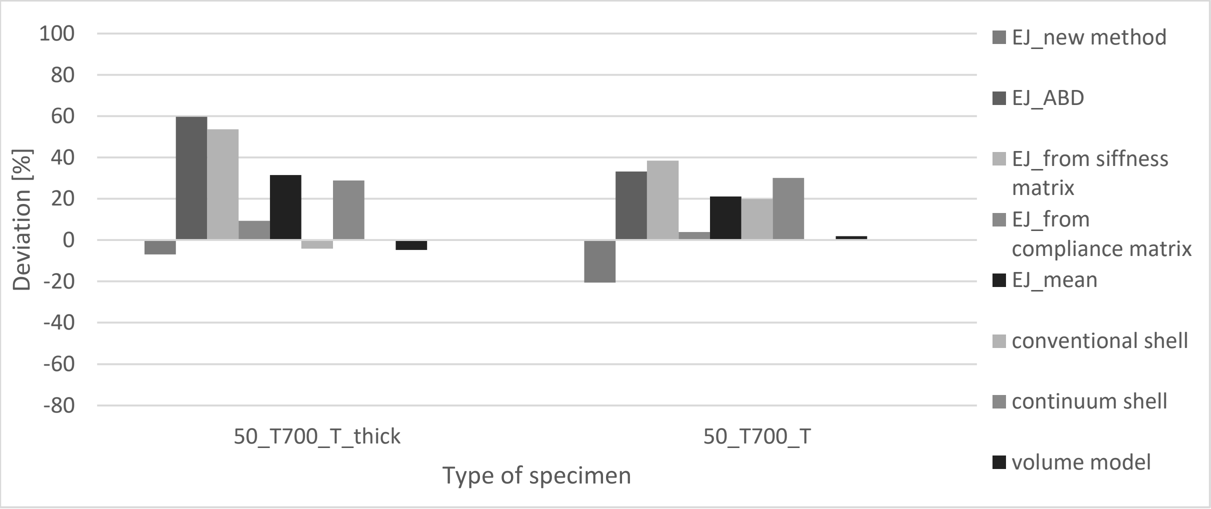

Fig. 2. The deviation from the experiment of equivalent stiffness for beams with ID 50mm and Typical layup [90°, 0°, ±30°]

5. Conclusion

None of the methods described above gives sufficiently accurate predictions of the stiffness of experimentally tested beams. There is still a noticeable problem where the results of different methods show different outcomes of the beam equivalent stiffness EJeq. From the performed comparison, methods with the best results are commented on.

The new semi-analytical approach reached a good agreement with experimental data in both composite lay-ups. A method based on the mean of an upper and lower estimate of the stiffness of the composite lay-up seems to be almost equally suitable, but with the deviation that predicts the greater stiffness than the experiment. In terms of computational complexity, the proposed approaches are less demanding than the FE method and are therefore suitable for fast usage for the preliminary design. The numerical optimization of these approaches is also possible.

Acknowledgements

The work has been supported by the research project of Students grant agency CTU SGS21/151/OHK2/3T/12.

References

[1] Laš, V., Mechanika kompozitních materiálů. 2. vyd., Západočeská univerzita, Plzeň, 2008. (in Czech)
[2] Zavřelová, T., Analysis of composite beam bending, Diploma thesis, Czech Technical University in Prague, Prague, 2015.

COMPUTATIONAL MECHANICS 2022
37th conference with international participation
Srní
November 7 - 9, 2022

Study of the oscillation of a pendulum in a magnetic field

J. Zapoměl[a,b], J. Kozánek[a], J. Košina[a], J. Cibulka[a]

[a] *Institute of Thermomechanics, Czech Academy of Sciences, 182 00 Praha, Dolejškova 5, Czech Republic*
[b] *Faculty of Mechanical Engineering, VŠB-Technical University of Ostrava, 17. listopadu 15, 708 00 Ostrava, Czech Republic*

Realization of some technological processes requires application of rotating machines with a vertical rotor mounted in rolling element bearings. One of the requirements put on their operation is minimization of energy losses in the support elements. The losses have several physical reasons. They rise with increasing loading, speed of the shaft rotation, and kinematic viscosity of the lubricant [1]. Replacement of one or more rolling element bearings with a contactless one represents a significant design alteration making it possible to contribute to cuts of energy losses.

Application of magnetic elements for reducing energy losses in the rotor supports was studied at several working places. A historical review and formulas for designing permanent magnetic bearings are reported in [2]. The approach to determination of stiffness of axial bearings using permanent magnets can be found in [3]. The advanced technological solution based on reducing axial loading of rolling element bearings supporting vertical rotors consists in their lifting by means of annular permanent magnets. The details on application of this design solution are reported in [4]. Efficiency of lifting the rotors was analyzed in [5]. A new concept of a shear magnetic bearing was introduced by Zapoměl et al. in [6]. The intentional change of the bearing stiffness to reduce vibration of a rotor system passing through the critical speed was analyzed by Zapoměl and Ferfecki in [7].

The proposed design variant consists in supporting the vertical rotor by one rolling element bearing placed at its upper part and by one axial magnetic bearing mounted in its lower end. The magnetic bearing is composed of an electric coil coupled with the stationary part and of a permanent magnet attached to the rotating part. The magnetic force attracts the permanent magnet, which reduces radial displacement of the lower end of the rotor. The magnetic field between the magnets represents a force coupling between the rotor and the stationary part, which shows some stiffness and affects the system natural frequencies. The controlled change of the stiffness makes it possible to reduce the rotor lateral oscillations in the resonance area.

Applicability and properties of the proposed design concept was studied by means of analysis of oscillations of a pendulum focusing on construction of the frequency response characteristic of the system for variable magnitude of the applied current.

The investigated pendulum (Fig. 1) is coupled with the frame by a revolute joint at its upper end. The permanent magnet is attached to its lower end. The electric coil is coupled with the stationary part and placed under the pendulum. The system is excited by a moment of harmonic time history, which sets the pendulum into a seesaw motion. The task is to construct the frequency response characteristic in dependence on magnitude of the applied current passing the winding of the coil. Amplitude of the oscillations is assumed to be small. The computational simulations should be used to solve the problem.

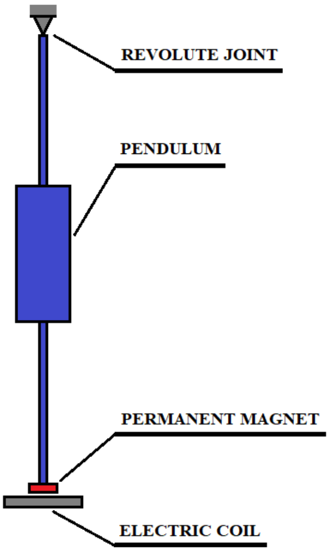

Fig. 1. The investigated system

The introduced coordinate system and the generalized coordinate φ of the pendulum angular position is evident from Fig. 2.

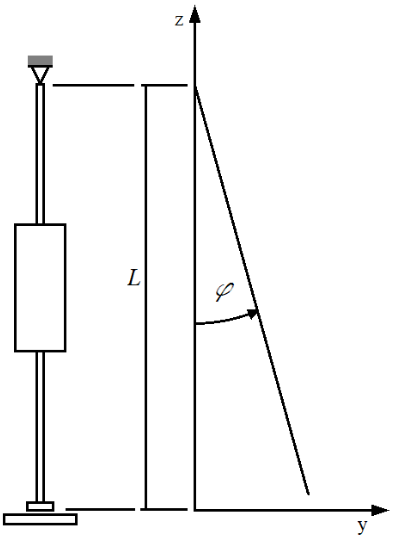

Fig. 2. The introduced coordinate system

In the computational model the pendulum is considered as absolute rigid, the revolute joint as absolute rigid and neutral (with no resistances against motion), and the damping produced by the environment as linear. The coil attached to the stationary part has only one turn. The permanent magnet connected to the pendulum is represented by a magnetic dipole. Because of small displacements, it was assumed that the magnetic field produced by the coil near to its center is homogeneous in the radial direction.

The oscillation of the pendulum is governed by the motion equation

$$J\ddot{\varphi} + b_P\dot{\varphi} + \left[mgL_T + F_{mag}(I)L\right]\varphi + M_{mag}(I) = M_A\sin(\omega_B t)\,, \qquad (1)$$

J is the pendulum moment of inertia relative to the axis of rotation, m is the pendulum mass, b_P is the coefficient of the pendulum external damping, L is the length of the pendulum, L_T is the distance between the pendulum axis of rotation and the center of gravity, g is the gravity acceleration, F_{mag} is the magnetic force acting on the pendulum, M_{mag} is the magnetic moment acting on the pendulum, I is the applied current feeding the coil, M_A is amplitude of the excitation moment, ω_B is the excitation angular frequency, t is the time, φ is the generalized coordinate of the pendulum position, and $(\dot{})$, $(\ddot{})$ denote the first and second derivatives with respect to time.

The magnetic force and the magnetic moment are functions of the applied current I feeding the coil. If the current is constant, the motion equation is an ordinary linear differential equation of the second order with constant coefficients

$$J\ddot{\varphi} + b_P\dot{\varphi} + k_e(I)\varphi = M_A\sin(\omega_B t)\,, \tag{2}$$

because the magnetic moment M_{mag} is proportional to the angle of rotation φ. k_e is the equivalent stiffness of the system.

The motion equation shows that the natural frequency of the system can be controlled by increasing or decreasing magnitude of the magnetic force and moment.

The principal physical and geometric parameters of the analyzed pendulum are: mass 65 g, moment of inertia 0.0016 kgm^2, length 305 mm, the gap between the permanent magnet and the electric coil 0.5 mm, magnetic moment of the permanent magnet 1.26 Am^2, and amplitude of the excitation moment 0.020 Nm.

Application of the current of 200 A rises the natural frequency from 7.15 rad/s to 7.63 rad/s. which corresponds with rising the critical speed as evident from the frequency response characteristic depicted in Fig. 3.

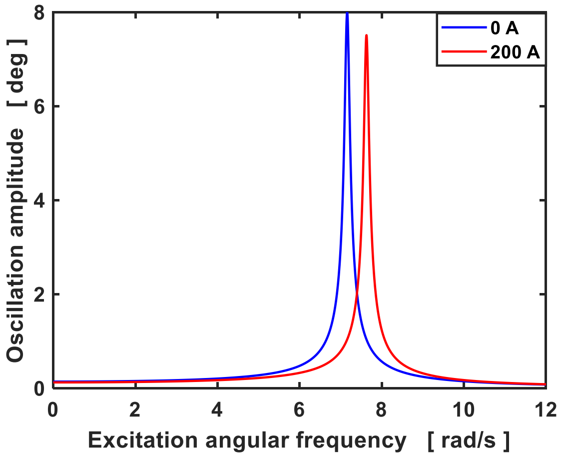

Fig. 3. Frequency response characteristic

The simulation results show that application of the current in the area of sub-critical frequencies and switching the current off in the region of ultra-critical ones makes it possible to reduce amplitude of the pendulum oscillations. This manipulation can be utilized for minimizing the vibration amplitude if the excitation frequency rises and the system passes through the resonance region.

Acknowledgements

The research work has been supported by project RVO: 61388998. The support is highly acknowledged.

References

[1] SKF Rolling bearings catalogue, http://www.skf.com/binary/56-121486/SKF-rolling-bearings-catalogue.pdf

[2] Paden, B., Groom, N., Antaki, J.F., Design formulas for permanent-magnetic bearings, Transactions of the ASME - Journal of Mechanical Design 125 (2003) 734-738.

[3] Ravaud, R., Lemarquand, G., Lemarquand, V., Force and stiffness of passive magnetic bear-ings using permanent magnets, Part 1: Axial magnetization, IEEE Transactions on Magnetics 45 (7) (2009) 1-16.

[4] Jiang, S., Wang, H., Wen, S., Flywheel energy storage system with permanent magnet bear-ing and a pair of hybrid ceramic ball bearing, Journal of Mechanical Science and Technology 28 (12) (2014) 5043-5053.

[5] Zapoměl, J., Ferfecki, P., Kozánek, J., Application of permanent magnetic rings to reducing energy losses in the supports of vertical flywheels, Proceedings of the 30th Nordic seminar on computational mechanics, Lyngby, 2017, pp. 210-213.

[6] Zapoměl, J., Ferfecki, P., Kozánek, J., Košina, J, Cibulka, J., Vibration of a rigid vertical rotor supported by a shear radial magnetic bearing, In: Beran, J., Bílek, M., Václavík, M., Žabka, P. (eds) Advances in Mechanism Design III. TMM 2020, Mechanisms and Machine Science, Vol 85., Springer.

[7] Zapoměl, J., Ferfecki, P., A computational investigation on the reducing lateral vibration of rotors with rolling-element bearings passing through critical speeds by means of tuning the stiffness of the system supports, Mechanism and Machine Theory 46 (5) (2011) 707-724.

COMPUTATIONAL MECHANICS 2022
37th conference with international participation
Srní
November 7 - 9, 2022

Modal synthesis method for vibration analyses of damped mechanical systems

V. Zeman, Z. Hlaváč, Š. Dyk

NTIS – New Technologies for the Information Society, Faculty of Applied Sciences, University of West Bohemia,
Univerzitní 8, 301 00 Plzeň, Czech Republic

1. Introduction

Subsystems of flexible multibody systems are often described by models with many degrees of freedom (DOF) and with proportional damping. Nonlinear couplings between the subsystems make the vibration analyses too time consuming. Then it is desirable to apply one of the DOF number reduction of the whole system. A suitable and established methods is the modal synthesis method (MSM) [1, 3, 5]. The classical approach of the MSM is based on the reduction of the natural modes of conservative models of subsystems respected in dynamic response. The modal properties of damped subsystems are expressed by complex eigenvalues and complex eigenvectors. The main aim of this contribution is to present the new complex MSM with DOF number reduction of each proportionally damped subsystem. A variation of the proposed method modified for rotating mechanical systems with gyroscopic effects has been published in [7].

2. Mathematical model of the multibody system

Let us consider a multibody system composed of N subsystems linked by generally nonlinear couplings. Motion equations can be expressed in the matrix form

$$\boldsymbol{M}_i\ddot{\boldsymbol{q}}_i(t)+\boldsymbol{B}_i\dot{\boldsymbol{q}}_i(t)+\boldsymbol{K}_i\boldsymbol{q}_i(t)=\boldsymbol{f}_i^E(t)+\sum_{j=1,j\neq i}^{N}\boldsymbol{f}_{j,i}^C(\boldsymbol{q}_i,\boldsymbol{q}_j,\dot{\boldsymbol{q}}_i,\dot{\boldsymbol{q}}_j),\; i=1,\dots,N. \tag{1}$$

Let mass, damping and stiffness matrices $\boldsymbol{M}_i,\ \boldsymbol{B}_i,\ \boldsymbol{K}_i$ be symmetric of order n_i. In addition, let the damping matrices meet the proportionality conditions

$$(\boldsymbol{v}_\nu^{(i)})^T\boldsymbol{B}_i\boldsymbol{v}_\nu^{(i)}=2D_\nu^{(i)}\Omega_\nu^{(i)},\; \nu=1,\dots,n_i,\; i=1,\dots,N\,, \tag{2}$$

where $\Omega_\nu^{(i)}$ are the eigenfrequencies and $\boldsymbol{v}_\nu^{(i)}$ are the eigenvectors of the conservative part of subsystem model i. These modal values satisfy the orthonormality conditions

$$(\boldsymbol{v}_\nu^{(i)})^T\boldsymbol{M}_i\boldsymbol{v}_\nu^{(i)}=1,\; (\boldsymbol{v}_\nu^{(i)})^T\boldsymbol{K}_i\boldsymbol{v}_\nu^{(i)}=(\Omega_\nu^{(i)})^2,\; \nu=1,\dots,n_i,\; i=1,\dots,N. \tag{3}$$

Damping factors $D_\nu^{(i)}$ describe the proportional damping of subsystems. The time dependent vector $\boldsymbol{f}_i^E(t)$ expresses excitation of subsystem i. Nonlinear vectors $\boldsymbol{f}_{j,i}^C$ express the nonlinear forces—an action of subsystem $j\in\{1,\dots,N\},\ j\neq i$ on subsystem i in case of mutual contact.

The first-order formulation of the equation of motion (1) in the state space $\boldsymbol{u}_i = [\dot{\boldsymbol{q}}_i^T, \boldsymbol{q}_i^T]^T$ have the form

$$\boldsymbol{N}_i\dot{\boldsymbol{u}}_i(t) + \boldsymbol{P}_i\boldsymbol{u}_i(t) = \boldsymbol{p}_i,\ i = 1, \ldots, N, \tag{4}$$

where

$$\boldsymbol{N}_i = \begin{bmatrix} \boldsymbol{0} & \boldsymbol{M}_i \\ \boldsymbol{M}_i & \boldsymbol{B}_i \end{bmatrix},\ \boldsymbol{P}_i = \begin{bmatrix} -\boldsymbol{M}_i & \boldsymbol{0} \\ \boldsymbol{0} & \boldsymbol{K}_i \end{bmatrix},\ \boldsymbol{p}_i = \begin{bmatrix} \boldsymbol{0} \\ \boldsymbol{f}_i^E(t) + \sum\limits_{j=1, j\neq i}^{N} \boldsymbol{f}_{j,i}^C(\boldsymbol{u}_i, \boldsymbol{u}_j) \end{bmatrix}. \tag{5}$$

Modal properties of each individual subsystem i are expressed by the complex diagonal spectral matrix

$$\boldsymbol{\Lambda}_i = \text{diag}[\lambda_1^{(i)}, \ldots, \lambda_{n_i}^{(i)}, \lambda_1^{(i)*}, \ldots, \lambda_{n_i}^{(i)*}] = \text{diag}[\overline{\boldsymbol{\Lambda}}_i, \overline{\boldsymbol{\Lambda}}_i^*] \in C^{2n_i, 2n_i} \tag{6}$$

and the complex modal matrix

$$\boldsymbol{U}_i = [u_1^{(i)}, \ldots, u_{n_i}^{(i)}, u_1^{(i)*}, \ldots, u_{n_i}^{(i)*}] = \text{diag}[\overline{\boldsymbol{U}}_i, \overline{\boldsymbol{U}}_i^*] \in C^{2n_i, 2n_i}\,. \tag{7}$$

Complex eigenvalues $\lambda_\nu^{(i)}$ with a positive imaginary part and corresponding eigenvectors $\boldsymbol{u}_\nu^{(i)}$ can be expressed in terms of eigenfrequencies $\Omega_\nu^{(i)}$ and eigenvectors $\boldsymbol{v}_\nu^{(i)}$ of the conservative part of subsystem model i in the form

$$\lambda_\nu^{(i)} = -D_\nu^{(i)}\Omega_\nu^{(i)} + \mathrm{i}\Omega_\nu^{(i)}\sqrt{1 - (D_\nu^{(i)})^2},\ \boldsymbol{u}_\nu^{(i)} = \begin{bmatrix} \lambda_\nu^{(i)}\boldsymbol{q}_\nu^{(i)} \\ \boldsymbol{q}_\nu^{(i)} \end{bmatrix}, \nu = 1, \ldots, n_i, i = 1, \ldots, N\,. \tag{8}$$

Eigenvectors $\boldsymbol{q}_\nu^{(i)}$ in the original space of generalized coordinates of the subsystems can be quickly calculated from the relation

$$\boldsymbol{q}_\nu^{(i)} = \frac{1}{\sqrt{\mathrm{i}}} \cdot \frac{\boldsymbol{v}_\nu^{(i)}}{\sqrt{2\Omega_\nu^{(i)}\sqrt{1 - (D_\nu^{(i)})^2}}},\ \nu = 1, \ldots, n_i,\ i = 1, \ldots, N\,, \tag{9}$$

where i is the imaginary unit.

3. Complex modal synthesis method with DOF reduction

Complex MSM with DOF reduction is based on an incomplete transformation of state vectors $\boldsymbol{u}_i(t)$ in (4) into the vectors of complex modal coordinates $\boldsymbol{x}_i(t)$ of the subsystems in the form

$$\boldsymbol{u}_i(t) =^m \boldsymbol{U}_i\boldsymbol{x}_i(t) = \sum_{\nu=1}^{m_i}(\boldsymbol{u}_\nu^{(i)}x_\nu^{(i)} + \boldsymbol{u}_\nu^{(i)*}x_\nu^{(i)*}),\ m_i \leq n_i,\ i = 1, \ldots .N\,. \tag{10}$$

By using orthogonality conditions [1,4]

$${}^m\boldsymbol{U}_i^T\boldsymbol{N}_i\,{}^m\boldsymbol{U}_i = \boldsymbol{E}_{2m_i}\,,\ {}^m\boldsymbol{U}_i^T\boldsymbol{P}_i\,{}^m\boldsymbol{U}_i = -{}^m\boldsymbol{\Lambda}_i \tag{11}$$

and the form of eigenvectors $\boldsymbol{u}_\nu^{(i)}$ in (8), equations (4) can be written as

$$\dot{\boldsymbol{x}}_i(t) -^m \boldsymbol{\Lambda}_i\boldsymbol{x}_i(t) =^m \boldsymbol{Q}_i^T\left[\boldsymbol{f}_i^E(t) + \sum_{j=1, j\neq i}^{N} \boldsymbol{f}_{j,i}^C(\boldsymbol{u}_i, \boldsymbol{u}_j)\right],\ i = 1, \ldots, N\,. \tag{12}$$

Due to the structure of the reduced (master) spectral and modal matrices of the subsystems in the form

$$ {}^m\mathbf{\Lambda}_i = \mathrm{diag}[\lambda_1^{(i)},\dots,\lambda_{m_i}^{(i)},\lambda_1^{(i)*},\dots,\lambda_{m_i}^{(i)*}] = \mathrm{diag}[{}^m\overline{\mathbf{\Lambda}}_i,{}^m\overline{\mathbf{\Lambda}}_i^*] \in C^{2m_i,2m_i}\,, \tag{13} $$

$$ {}^m\boldsymbol{Q}_i = [\boldsymbol{q}_1^{(i)},\dots,\boldsymbol{q}_{m_i}^{(i)},\boldsymbol{q}_1^{(i)*}\dots,\boldsymbol{q}_{m_i}^{(i)*}] = [{}^m\overline{\boldsymbol{Q}}_i,{}^m\overline{\boldsymbol{Q}}_i^*] \in C^{n_i,2m_i} \tag{14} $$

and vector of complex modal coordinates in the form

$$ \boldsymbol{x}_i = [x_1^{(i)},\dots,x_{m_i}^{(i)},x_1^{(i)*},\dots,x_{m_i}^{(i)*}]^T = \begin{bmatrix} \overline{\boldsymbol{x}}_i \\ \overline{\boldsymbol{x}}_i^* \end{bmatrix}, \tag{15} $$

equations (12) can be divided to

$$ \dot{\overline{\boldsymbol{x}}}_i(t) -{}^m\overline{\mathbf{\Lambda}}_i\overline{\boldsymbol{x}}_i(t) ={}^m\overline{\boldsymbol{Q}}_i^T\left(\boldsymbol{f}_i^E(t)+\sum_{j=1,j\neq i}^{N}\boldsymbol{f}_{j,i}^C\right), \tag{16} $$

$$ \dot{\overline{\boldsymbol{x}}}_i^*(t) -{}^m\overline{\mathbf{\Lambda}}_i^*\overline{\boldsymbol{x}}_i^*(t) ={}^m\overline{\boldsymbol{Q}}_i^{*T}\left(\boldsymbol{f}_i^E(t)+\sum_{j=1,j\neq i}^{N}\boldsymbol{f}_{j,i}^C\right). \tag{17} $$

The global form of these equations is

$$ \dot{\overline{\boldsymbol{x}}}(t) -{}^m\overline{\mathbf{\Lambda}}\overline{\boldsymbol{x}}(t) ={}^m\overline{\boldsymbol{Q}}^T(\boldsymbol{f}^E(t)+\boldsymbol{f}_C)\,, \tag{18} $$

$$ \dot{\overline{\boldsymbol{x}}}^*(t) -{}^m\overline{\mathbf{\Lambda}}^*\overline{\boldsymbol{x}}^*(t) ={}^m\overline{\boldsymbol{Q}}^{*T}(\boldsymbol{f}^E(t)+\boldsymbol{f}_C)\,, \tag{19} $$

where

$$ {}^m\overline{\mathbf{\Lambda}} = \mathrm{diag}[{}^m\overline{\mathbf{\Lambda}}_1,\dots,{}^m\overline{\mathbf{\Lambda}}_N] \in C^{m,m}\,,\ {}^m\overline{\boldsymbol{Q}} = \mathrm{diag}[{}^m\overline{\boldsymbol{Q}}_1,\dots,{}^m\overline{\boldsymbol{Q}}_N] \in C^{n,m}\,, \tag{20} $$

$$ \overline{\boldsymbol{x}}(t) = \begin{bmatrix} \overline{\boldsymbol{x}}_1(t) \\ \vdots \\ \overline{\boldsymbol{x}}_N(t) \end{bmatrix},\ \boldsymbol{f}_E(t) = \begin{bmatrix} \boldsymbol{f}_1^E(t) \\ \vdots \\ \boldsymbol{f}_N^E(t) \end{bmatrix},\ \boldsymbol{f}_C = \begin{bmatrix} \sum\limits_{j=2}^{N}\boldsymbol{f}_{j,1}^C(\boldsymbol{u}_1,\boldsymbol{u}_j) \\ \vdots \\ \sum\limits_{j=1}^{N-1}\boldsymbol{f}_{j,N}^C(\boldsymbol{u}_N,\boldsymbol{u}_j) \end{bmatrix}. \tag{21} $$

Reduced DOF number $m = \sum_{i=1}^{N} m_i$ corresponds to the dimension of vector $\overline{\boldsymbol{x}}(t)$ and full DOF number $n = \sum_{i=1}^{N} n_i$ correspond to the dimension of vectors $\boldsymbol{f}^E(t)$ and $\boldsymbol{f}_C$. According to (10) and the structure of eigenvectors $\boldsymbol{u}_\nu^{(i)}$ in (8), the dynamic response of the arbitrary subsystem i in the original generalized coordinates is real in the form

$$ \boldsymbol{q}_i(t) ={}^m\overline{\boldsymbol{Q}}_i\overline{\boldsymbol{x}}_i(t) +{}^m\overline{\boldsymbol{Q}}_i^*\overline{\boldsymbol{x}}_i^*(t) = 2\mathrm{Re}[{}^m\overline{\boldsymbol{Q}}_i\overline{\boldsymbol{x}}_i(t)]\,, \tag{22} $$

$$ \dot{\boldsymbol{q}}_i(t) ={}^m\overline{\boldsymbol{Q}}_i\,{}^m\overline{\mathbf{\Lambda}}_i\overline{\boldsymbol{x}}_i(t) +{}^m\overline{\boldsymbol{Q}}_i^*\,{}^m\overline{\mathbf{\Lambda}}_i^*\overline{\boldsymbol{x}}_i^*(t) = 2\mathrm{Re}[{}^m\overline{\boldsymbol{Q}}_i\,{}^m\overline{\mathbf{\Lambda}}_i\overline{\boldsymbol{x}}_i(t)]\,. \tag{23} $$

The presented method is illustrated by numerical experiments on the impact-vibration of two nuclear fuel assemblies in the reactor core excited by coolant pressure fluctuations. The model of the single FA (see Fig. 1) is created using simple beam-type finite elements [6] and the computational model of FAs interaction is described in detail in [2].

4. Conclusions

The new modal synthesis method enables dynamic analysis of the large multibody systems composed from linear damped subsystems mutually coupled by nonlinear discrete couplings. The method is suitable especially for dynamic analysis of the systems with clearances between subsystems characterised by impact and friction forces in contact surfaces.

Consideration of the chosen master complex natural modes of each subsystem improves approximation of the reduced model in comparison with classical approach of the MSM. Calculation of complex modal values of the subsystems models with proportional damping based on real modal values of their conservative part and the damping ratios greatly speeds up the calculation time. These facts have been illustrated by means of numerical experiments with the nuclear fuel assemblies in mutual interactions excited by the coolant pressure pulsations. The concept of fuel assembly modelling is detailed in [2].

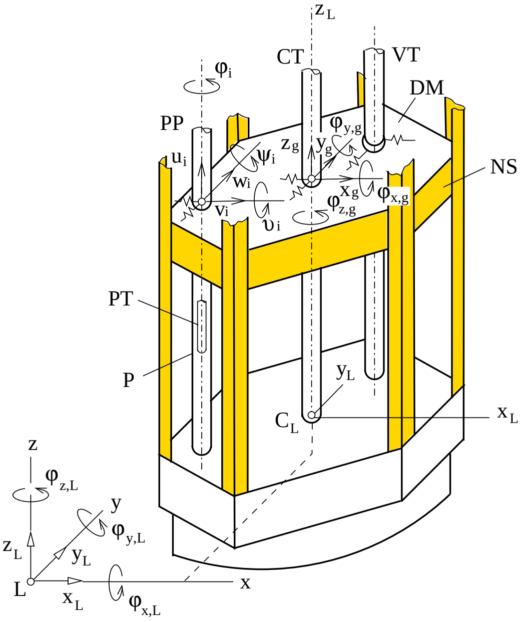

Fig. 1. Detailed FA model

Acknowledgement

This work was developed under the research project Fuel cycle of NPP coordinated by Nuclear Research Institute Řež.

References

[1] Byrtus, M., Hajžman, M., Zeman, V., Dynamics of rotating systems, University of West Bohemia, Pilsen, 2010. (in Czech)

[2] Dyk, Š., Zeman, V., Hlaváč, Z., Mechanical interaction of bowed hexagonal fuel assemblies in PWR core, Progress in Nuclear Energy, 2022. (under review)

[3] Irretier, H., A modal synthesis method with free interfaces and residual flexibility matrices from frame structures, Building Journal 37 (9) (1989) 601-610.

[4] Sui, Y., Zhong, W., Eigenvalue problem of a large scale indefinite gyroscopic dynamic system, Applied Mathematics and Mechanics 27 (1) (2006) 15-22.

[5] Zeman, V., Vibration of mechanical systems by the modal synthesis method, ZAMM - Journal of Applied Mathematics and Mechanics 74 (4) (1994) 99-101.

[6] Zeman, V., Dyk, Š., Hlaváč, Z., Two-stage modelling of hexagonal fuel assemblies vibration considering mechanical nonlinearities, Progress in Nuclear Energy 138 (2021) No. 103825, 1-12.

[7] Zeman, V., Hlaváč, Z., Generalized modal reduction method for the dynamic analysis of rotating mechanical systems, Applied Computational Mechanics 14 (2020) 81-98.